Modern Solid-State NMR on Amorphous Materials: Ultrahard Glasses and Polyacrylonitrile

Dissertation

zur Erlangung des akademischen Grades

Dr. rer. nat.

eingereicht an der

Mathematisch-Naturwissenschaftlich-Technischen Fakultät

der Universität Augsburg

von

Alina Nizamutdinova

Augsburg, Dezember 2020

Erster Gutachter: Prof. Dr. Leo van Wüllen

Zweiter Gutachter: Prof. Dr. Henning Höppe

Tag der mündlichen Prüfung: 30. März 2021

“Knowledge rests not upon truth alone, but upon error also.”

— Carl Gustav Jung

Table of Contents

Table of Figures

Table of Tables

Introduction

Modern science and technology consist of many important elements: simulations and modeling, high-tech equipment, processing and manufacturing to name a few. One of the most important questions with which developers are confronted is choosing the proper material for a certain application. Which components should be used and if it is possible to engineer the properties of the final object to obtain the best-suited solution? Here is where material science, physics, chemistry, characterization methods and chemical engineering must be combined to achieve the best results. Understanding organization of material is an indispensable part of this process. There are many techniques available to investigate the structural organization, such as IR (infrared) spectroscopy, XANES (X-ray absorption near-edge fine structure) spectroscopy or XPS (X-ray photoelectron) spectroscopy. However, all of them are difficult to apply to the broad range of amorphous materials due to absence of periodicity. Solid-state NMR (nuclear magnetic resonance) plays a leading role in the research of amorphous materials. It is of particular importance for structural research because it does not only allow to characterize structural units on short (1-2 Å) length scales by employing MAS (magic angle spinning) and MQMAS (multiple quantum MAS)[1,2] but also able to estimate the connectivity of these units utilizing dipolar-based NMR techniques such as REDOR (rotational echo double resonance)[3–5] and REAPDOR (rotational echo adiabatic passage double resonance)[3,6,7]. Furthermore, *in-situ* experiments at high temperatures provide insight into the dynamic of the structural network. In this work, two classes of amorphous materials, one which is known to mankind for many thousand years and one which mainly found many important applications in the last century – glasses and carbon fibers are investigated by means of solid-state NMR spectroscopy.

In our everyday life we are surrounded by glass-based materials: in lenses, in touchscreens, in windows and many others. At the same time glasses are one of the materials known to the humankind since the ancient ages. For example, glazed beads found in Egypt are estimated to be produced around 12000 BC[8]. Originally, glasses were mostly reserved for jewelry and decoration and only later they have become commodity products. The crucial step towards industrial glass development was caused by their applicability in optics. The scientists Schott und Abbe were first to start the systematic scientific research of glass properties depending on their composition back in 1882[9]. One of the key advantages of glass-based materials is the

adjustability of their properties through variation of the initial composition of oxide melts. Initial oxide melts are not bound by stoichiometric restrictions opening a wide range of optical, chemical and physical properties.

The importance of the currently trending fields of glass applications, especially phosphosilicate, aluminosilicate and phospho-aluminosilicate glasses, for modern science can be barely underestimated. One of the major areas of usage is optics where glasses can play a role of laser hosts[10]. Other important application domains are biomaterials[11–14], sealing glasses[15] or separators of nuclear waste storage[16–19]. Mechanical properties of these glasses are governed by their short and medium-range arrangement. The arrangement of short-range structural motifs correlate with hardness and Tg (glass transition temperature)[20,21]. The crack resistance on the other hand is rather governed by Poisson's ratio as derived by Rouxel[22]. The latter one depends on atomic packing density and, consequently, on coordination numbers (CN)[23]. That is why high-strength glasses normally contain high-coordinated species. Besides aluminum, presence of high-coordinated silicon units (SiO_6) leads to increased hardness[24,25] and fictive temperatures[26]. Nevertheless, the correlation is not unequivocal and, hence, deeper understanding of the correlation of mechanical properties *w.r.t*. structure and topology of the glass network is needed. Hence, NMR investigation is an indispensable step in the glass engineering. Better understanding of glass structure and its effect to macroparameters might allow developing of ultrahard glasses for various range of applications and to propose the most promising compositions for further applicability research. Furthermore, it might help to save time and energy costs if the most promising composition are identified and are not searched randomly across glass-forming region which has a positive effect for economy and environment.

When glasses are known and applied since several thousand years, there are new group of amorphous materials, appearance and development of which is caused by the recent progress in science and technology. More and more spheres of our life require application of high-strength, temperature-resistant but at the same time lightweight materials. This often could be reached by blending of two or more components to obtain new materials with unique combination of properties which is not possible for individual constituents. These blendings are called composite materials. A particular type of composite materials, carbon fiber reinforced materials (CFR) where carbon fibers are combined with matrix often consisting of

some epoxy resin found their way to many domains of high-demanding applications – automotive, aerospace, renewable energy and sport equipment to name a few. Carbon fibers could be made from three major precursors – polyacrylonitrile (PAN), rayon or petroleum pitch, when the first one is the most widespread and studied[27]. The manufacturing process of carbon fibers from PAN consists of two major steps – stabilization in air and carbonization in inert atmosphere at the higher temperatures. Despite many efforts to investigate the reaction path of carbonization step with IR (infrared radiation) spectroscopy[28,29], DSC (differential scanning calorimetry)[30], ^{13}C MAS NMR (magic angle spinning nuclear magnetic resonance)[29,31,32] and other methods, the exact mechanism is still not completely understood[33,34]. It is of essential importance to gain more information to be able to fine-tune process parameters and to optimize costly manufacturing cycle. Furthermore, more efficient production strategies might allow to decrease costs and energy needs, which has a positive effect to gas emission and atmosphere pollution. Methods of NMR suit perfectly for the investigation of the non-ordered structure of polymerization of PAN on different stages and hence were used in the current work.

In the beginning of this thesis, first, theoretical introduction into principles of NMR is given. It is followed by the description of mechanisms of NMR techniques used in this work. After that, an overview of materials studied (high-strength glasses and PAN) and their structural organization and synthesis are described.

Part 4 of this work, where the results of measurements are described and analyzed, starts with discussion of two phosphorus aluminosilicate glass systems chosen for this work. First, alkali silicophosphate system (two experimental series having 50 and 60 m. p. of P_2O_5 were chosen for this investigation) and the effect of aluminum incorporation on the structural organization is investigated by means of NMR. The aim of this study was to find out if it is possible to improve mechanical and thermal properties of the glasses where six-coordinated silicon or a mixture of six-coordinated and four-coordinated silicon units is already present by adding aluminum into the system. Structural investigations of the network connectivity were further extended by *in-situ* investigations using novel heating technique[28] which allowed spectral deconvolution of phosphorus units at high temperatures (up to 700°C). Network dynamics was studied to find out if there is a correlation with trends in macro properties.

In part 4.2 of this work another glass system, alkali aluminosilicate glasses, was investigated by means of solid-state NMR. Aluminosilicate glasses with small amount of phosphorus in the glass composition are of special interest for geological studies because their composition is similar to those of magma. Furthermore, addition of phosphorus to aluminosilicate glasses-leads to their improved processability. Base glass system with 50-70 m. p. of SiO_2 and the rest equally divided between aluminum and sodium oxides and the change of the structural network upon addition of phosphorus were investigated. Changes in the structure upon addition of phosphorus were followed together with trends in macro properties. Additionally, the studies were complimented by high-temperature in-situ MAS NMR[28] of base glasses where sodium and aluminum dynamics in the glasses were researched.

Parts 4.3-4.7 of this work are devoted to investigation of carbon fibers from PAN precursor. First, in the part 4.3 NMR was attempted on the samples which went through different production steps to understand where its application could be the most promising. It was identified that investigations of fibers before high-temperature treatment seems to be the most promising which became a focus of further studies. In the part 4.4 the structure of PAN precursors and several test samples were investigated. This was an indispensable step which allowed further analysis of PAN which underwent thermal treatment. In the part 4.5 the reaction path during stabilization step was investigated by means of NMR spectroscopy on the samples with selectively enriched ^{15}N atoms. These samples underwent different temperature treatments which allowed to follow the mechanism of polymerization which is still not fully understood[34–45]. To our best knowledge it is a first solid-state NMR study including the investigation of ^{15}N-enriched PAN during thermal treatment. The results obtained by $^{13}C\{^{15}N\}$ REDOR NMR helped to support one of the reaction mechanisms proposed in literature.

In the part 4.6 of this work special attention was paid to the role of copolymers in the reaction. It is known that addition of copolymers is indispensable for commercial production of the carbon fibers[46] and results in better processability[27,47,48]. However, their effect to the reaction mechanism is not fully understood. Polymerization mechanism of PAN-MA (methacrylate) copolymers with selectively enriched ^{15}N, ^{13}C and ^{2}H was followed during stabilization step by means of wide range of dipolar-based NMR techniques. To our best knowledge, it is the first study devoted to ^{15}N and ^{2}H-selectively enriched copolymers investigations of the stabilization

step. This allowed selective following PAN-MA copolymerization and proposing a role of MA in the reaction scheme.

In the part 4.7 different NMR methods including MAS NMR, cross-polarization NMR (CP NMR)[49,50] and hyperpolarized continuous flow ^{129}Xe NMR[51–53] were applied to the industrially produced fibers having different surface treatment and to recycled carbon fibers. This allowed to track changes of the signal complexity upon surface treatment. Although it was not possible to correlate chemical environments of the highly overlapping peaks if ^{1}H MAS spectra, NMR allowed to qualitatively compare which recycle treatment is less damaging to the surface functionalities which are important for the production of carbon fiber reinforced plastics (CFRP). Additionally, hyperpolarized continuous flow ^{129}Xe NMR allowed to track pore surface distribution upon surface treatment.

1. NMR Technique

NMR is a physics-based method for investigation the structure of materials based on the interaction of the nuclei, which have non-zero spin, with external magnetics field. It is very important for structural research because it allows to characterize structural units on both short (1-2 Å) and intermediate (2-5 Å) length scales. Furthermore, solid state NMR plays the leading role in the research of amorphous materials where other characterization methods are difficult to apply. First foundations for NMR were developed by Edward Mills Purcell and Felix Bloch who were awarded the Nobel Prize in physics for that in 1952[54,55]. In this chapter, the theoretical foundations of NMR-spectroscopy including magnetic moment and spin, energy splitting in the external magnetic field, macroscopic magnetization and nuclei spin interaction are introduced. Then essential measurement techniques such as MAS, spin-echo, CPMAS, MQMAS, MAT and INADEQUATE and dipolar-based experiments REDOR and REAPDOR used in this work will be described and discussed in the following chapters. The theoretical foundation is based on compilation of NMR basics based on books from M. Duer, M. Levitt, P. Atkins, S. Slichter and J. Keeler[56–60] complemented with indicated in the text references.

1.1. Theoretical Base

1.1.1. Magnetic Moment and Spin

NMR is based on interaction of a nuclear spin I with an external magnetic field. If a nucleus has an odd number of protons or neutrons, it possesses a non-zero spin (see Table 1). It is an intrinsic property of a nucleus.

Number of protons	Number of neutrons	Nuclei spin
Even	Even	Zero
Even	Odd	Half-integer
Odd	Even	Half-Integer
Odd	Odd	Integer

Table 1. Dependence of the nuclei spin number on the number of protons and neutrons.

Nuclei spin is described mathematically by spin operator $\hat{\boldsymbol{I}}$. Each nucleus has an angular momentum $\hat{\boldsymbol{J}}$ and magnetic moment $\hat{\boldsymbol{\mu}}$ which are described by:

$$\hat{\boldsymbol{\mu}} = \gamma\hat{\boldsymbol{J}} = \gamma\hbar\hat{\boldsymbol{I}},$$

where γ is the gyromagnetic ratio which is specific for the given type of nuclei and $\hbar$=1.054 x 10^{-34} J s is the reduced Planck's constant $h/2\pi$.

Magnitude of the spin vector $\hat{\boldsymbol{I}}^{\boldsymbol{2}}$ and its z-component $\hat{\boldsymbol{I}}_{\boldsymbol{z}}$ are connected by following relationships:

$$\langle I, m|\hat{I}^2|I, m\rangle = I(I+1)\ where\ I = 0, \frac{1}{2}, 1 \ldots$$

$$\langle I, m|\hat{I}_z|I, m\rangle = m, where\ m = -I, -I+1, \ldots I-1, I$$

This results in *2I+1* eigenstates. In the absence of an external magnetic field, these eigenstates have degenerated energy levels.

The components of spin operator $\hat{\boldsymbol{I}}$ commute by following commutation equations with the norm of the operator and only a square of a spin and one of its components can be defined exactly at the same time:

$$\left[\hat{I}^2, \hat{I}_x\right] = 0 \quad \left[\hat{I}^2, \hat{I}_y\right] = 0 \quad \left[\hat{I}^2, \hat{I}_z\right] = 0$$

$$\left[\hat{I}_z, \hat{I}_x\right] = i\hat{I}_y \quad \left[\hat{I}_x, \hat{I}_y\right] = i\hat{I}_z \quad \left[\hat{I}_y, \hat{I}_z\right] = i\hat{I}_x$$

1.1.2. Energy Splitting in the External Magnetic Field

If an external magnetic field is applied along z-axis, the energy states described above are not equal anymore due to Zeeman interaction. The separation of the energy levels on the example of a nucleus having *I*=1/2 is represented in Figure 1.

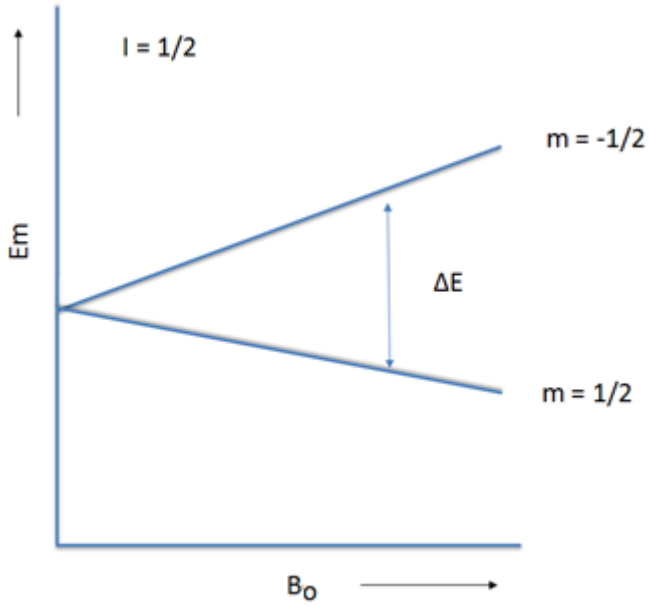

Figure 1. Scheme of energy splitting depending on magnetic field strength.

The interaction of magnetic field and nuclei spin is described with Zeeman operator:

$$\hat{H}_z|I,m>=E_m|I,m>$$

The solution of this equation are eigenvalues of energy values of the states $|I,m>$:

$$E_m = -\gamma\hbar m B_0$$

Which means that the equidistant *2I+1* energy levels are formed when an externa magnetic field is present. By rules of quantum mechanics, transitions between energy levels having Δm=±1 are allowed. The energy difference between these two energy levels is then:

$$\Delta E = \gamma\hbar B_0$$

By irradiation with electromagnetic wave (in the radio frequency range) with a suitable resonance frequency, a transition between neighboring Zeeman levels can be introduced. The interaction between the dipole moments and the external magnetic field results in a precessional motion of these moments around the direction of the magnetic field with the so-called LARMOR frequency, ω_L:

$$\omega_L = \gamma B_0 = \frac{\Delta E}{\hbar}$$

1.1.3. Macroscopic Magnetization

Since in NMR spectroscopy macroscopic samples with an ensemble of nuclei are measured, it is necessary to make an assumption about the distribution of the nuclear spins on the Zeeman levels. In the thermal equilibrium, the different energy levels are populated according to Boltzmann distribution. For example, for spin I=1/2 system, the population of energy states might be calculated as:

$$N_{-1/2}/N_{+1/2} = exp[-\Delta E/k_B T] = exp[-\gamma\hbar B_0/k_B T]$$

By using a linear Taylor development this term can be simplified even further and then so-called "high-temperature approximation" is valid (T>4 K):

$$N_{-1/2}/N_{+1/2} \approx 1 - \gamma\hbar B_0/k_B T$$

As might be seen, population difference is very low and depends on external magnetic field, specific nucleus and temperature. Still, despite inherent low population difference, net magnetic moment along z axis of the external Bo field might be calculated using Curie's law:

$$M = \frac{N\gamma^2\hbar^2 I(I+1)}{3k_B T} B_0$$

1.1.4. Pulse NMR

If a polarized electromagnetic wave having frequency equal to the energy difference between the Zeeman levels is applied to the nuclei, oscillating magnetic field of the wave interacts with nuclear magnetic moment. This process might be described using following Hamiltonian (for a wave applied along y-axis):

$$H_{rf} = -\gamma\hbar B_1 cos[\omega_0 t]\hat{I}_y$$

Where B_1 is the amplitude of the magnetic field caused by the electromagnetic wave and ω_0 is the frequency of the oscillating magnetic field component. By irradiating the electromagnetic wave, a torque is applied to the macroscopic magnetization M_0, deflecting it from z-axis into the xy-plane where it precesses with frequency ω_0.

The effect of the electromagnetic pulses to the system is easier to describe using a system of coordinates which is rotating with the frequency ω_o along z-axis with which B_1 becomes

stationary magnetic field. In this coordinate system the macroscopic magnetic moment would be deflected from the z-axis by the angle α which is defined by:

$$\alpha = \gamma B_1 t_p$$

Where t_p is the length of applied electromagnetic pulse.

After the application of electromagnetic pulse, the system will return to the thermal equilibrium, naming, it regenerates to Boltzmann distribution. Recovery of the magnetic moment along z-axis happens due to energy exchange between nuclei spins and its surrounding, lattice. This process is called spin-lattice or longitudinal relaxation and is characterized by spin-lattice relaxation T_1. In solids T_1 constants might vary from seconds to several hours. Addition of paramagnetic impurities might decrease longitudinal relaxation times.

$$M_z(t) = M_0 \left[1 - e^{-\frac{t}{T_1}}\right]$$

The time constant T_2^* (spin-spin relaxation constant), reflects the decrease of magnetization in the plane perpendicular to the z-axis. This is caused by energy exchange between different spins and results in their dephasing through spatially and temporally fluctuating magnetic fields:

$$M_{xy}(t) = M_{xy,0} e^{-\frac{t}{T_2^*}}$$

The decaying precession of magnetization induces alternating current in the detection coil located perpendicular to external magnetic field B_0 (often the same coil that produces the electromagnetic pulse). The detected amplitude of the current is time-dependent, and the phenomena is called free induction decay (FID):

$$FID(t) = \cos\left((\omega_L - \omega_0)t\right) e^{-\frac{t}{T_2^*}}$$

It then transformed from time-domain to frequency domain with Fourier transformation:

$$S(\omega_L - \omega_0) = \frac{1}{2\pi} \int_{-\infty}^{\infty} FID(t) exp[-i(\omega_L - \omega_0)t] dt$$

Spin-spin relaxation constant is mostly smaller than spin-lattice relaxation constant and is less dependable on the magnetic field strength.

1.1.5. Internal Interaction

Apart from Zeeman interaction, there are several further interactions with local magnetic field which affect the shape of NMR signal. They could be represented with Hamiltonian operator $\hat{H}^{tot}$, which is defined as:

$$\hat{H}^{tot} = \hat{H}^{Z} + \hat{H}^{RF} + \hat{H}^{CS} + \hat{H}^{D} + \hat{H}^{J} + \hat{H}^{Q}$$

Where $\hat{H}^{Z}$ (Zeeman interaction) and $\hat{H}^{RF}$ (interaction with applied electromagnetic wave) are external interactions and $\hat{H}^{CS}$ (chemical shift), $\hat{H}^{D}$ (direct dipole-dipole interaction), $\hat{H}^{J}$ (indirect dipole-dipole interaction) and $\hat{H}^{Q}$ (quadrupole interaction) are internal interactions. Contrary to the liquid-state NMR, where most of interactions are averaged due to Brown's motion, several interaction Hamiltonians effect the shape of resulting NMR spectra and might be selectively approached by corresponding NMR experiments. It allows to extract information about local structure. The dominant interaction in solid-state NMR is the Zeeman interaction and sometimes strong quadrupolar interaction. The other interaction could often be simplified as the first-order interactions.

In general, all interaction Hamiltonians might be described by means of the tensor operator formalism. Generally, two kinds of interaction can be introduced. First, magnetic dipole interacts with a magnetic field B:

$$\hat{H}_x = \sum_{i}^{spins} \hat{H}_x(i) = \sum_{i}^{spins} C_i \hat{I}(i)\, \overleftrightarrow{A}(i)\, B$$

Second, two magnetic dipole spins interact with each other:

$$\hat{H}_x = \sum\nolimits_{i}^{spins} \sum_{i>j}^{spins} \hat{H}_x(i,j) = \sum_{i,j}^{spinpairs} C_{i,j} \hat{I}(i)\, \overleftrightarrow{A}(i,j)\, \hat{I}(j)$$

Where constant factor C represents the magnitude of the interaction and the tensor $\overleftrightarrow{A}$ represents the information about anisotropy.

In the next chapters, constituents of Hamilton operator are introduced and discussed,

1.1.6. Chemical Shift

An applied external magnetic field affects not the nuclei energy levels but also the surrounding electrons: applied magnetic field induces a current in the electron shell causing an additional magnetic field in the opposite direction of the applied field. The nucleus is thus "shielded" from the external magnetic field ("diamagnetic effect"). Additionally, external magnetic field distorts the electron distribution around nucleus which causes the appearance of the additional magnetic field along z-direction leading to the "deshielding" of the nucleus ("paramagnetic effect"). Both effects are proportional to B_0 and contribute to the effective magnetic field B_{eff}. Therefore, the local magnetic field around nucleus is defined by two components: external magnetic field B_0 and the local magnetic field B_{ind} caused by the local electron configuration of the nucleus. The resulting magnetic field B_{eff} is the vector sum of those components:

$$B_{eff} = B_0 + B_{ind}$$

Therefore, the resonance frequency of nuclei depends on the local electron density. This dependence is called "chemical shift" and is used in solid state NMR to identify structural moieties. To be able to compare chemical shift, it is normally given in ppm with respect to known resonance frequency of certain reference material, ω_{ref}:

$$\delta = \frac{\omega - \omega_{ref}}{\omega_{ref}} 10^6$$

The Hamiltonian of the chemical shift interaction, $\hat{H}^{CS}$, is defined as:

$$\hat{H}^{CS} = \hbar \sum_{i}^{spins} \gamma_i \hat{I}(i)\, \overleftrightarrow{\sigma}(i)\, B_0$$

Where $\overleftrightarrow{\sigma}(i)$ is the magnetic shielding tensor defined as:

$$B_{ind} = -\overleftrightarrow{\sigma}(i)\, B_0$$

In global coordination system (labor coordination system) chemical shift tensor is given as:

$$\overleftrightarrow{\sigma}^{L}(i) = \begin{bmatrix} \sigma_{xx} & \sigma_{xy} & \sigma_{xz} \\ \sigma_{yx} & \sigma_{yy} & \sigma_{yz} \\ \sigma_{zx} & \sigma_{zy} & \sigma_{zz} \end{bmatrix}$$

For a better description and easier solution of the eigenvalue problem, the equation can be transformed from the laboratory coordinate system into the principal axis system (PAS). Thereby, the tensor is diagonalized and could be written in principal coordinate system as:

$$\overleftrightarrow{\sigma}^{P}(i) = \begin{bmatrix} \sigma_{x^*x^*} & 0 & 0 \\ 0 & \sigma_{y^*y^*} & 0 \\ 0 & 0 & \sigma_{z^*z^*} \end{bmatrix}$$

Conventionally, PAS is chosen to fulfill:

$$|\sigma_{z^*z^*} - \sigma_{iso}| \geq |\sigma_{x^*x^*} - \sigma_{iso}| \geq |\sigma_{y^*y^*} - \sigma_{iso}|$$

Isotropic chemical shift, σ_{iso}, is defined as one-third of the trace of the chemical shift tensor:

$$\sigma_{iso} = \frac{1}{3} Tr\{\overleftrightarrow{\sigma}^{P}(i)\} = \frac{1}{3}(\sigma_{xx} + \sigma_{yy} + \sigma_{zz})$$

Furthermore, chemical shift anisotropy, $\Delta\sigma$, and asymmetry parameter, η_{CS}, are needed to fully describe chemical shift tensor:

$$\Delta\sigma = \sigma_{z^*z^*} - \frac{1}{2}(\sigma_{x^*x^*} + \sigma_{y^*y^*})$$

$$\eta_{CS} = \frac{\sigma_{y^*y^*} - \sigma_{x^*x^*}}{\sigma_{z^*z^*} - \sigma_{iso}}$$

Chemical shift tensor in PAS might be then written in terms of isotropic and anisotropic part:

$$\overleftrightarrow{\sigma}^{P} = \begin{bmatrix} \sigma_{x^*x^*} & 0 & 0 \\ 0 & \sigma_{y^*y^*} & 0 \\ 0 & 0 & \sigma_{z^*z^*} \end{bmatrix} = \sigma_{iso} \begin{bmatrix} 1 & 0 & 0 \\ 0 & 1 & 0 \\ 0 & 0 & 1 \end{bmatrix} + \Delta\sigma \begin{bmatrix} -\frac{1}{2}(1+\eta) & 0 & 0 \\ 0 & -\frac{1}{2}(1+\eta) & 0 \\ 0 & 0 & 1 \end{bmatrix}$$

Resonance frequency could be derived with the help of first order perturbation theory. In case of axially symmetric chemical shift tensor ($\eta = 0$), the resonance frequency is defined as:

$$\omega(\theta) = \gamma B_0 (1 - \sigma_{iso} - \Delta\sigma \frac{1}{2}(3cos^2\theta - 1))$$

Where polar angle θ is the angle between z-axis of PAS and the external magnetic field.

If the tensor is non-axially symmetric, the chemical shift frequency is

$$\omega(\theta) = -\omega_0\sigma_{iso} - 1/2\omega_0\Delta\sigma(3cos^2\theta - 1 + \eta_{CS}sin^2\theta cos2\varphi)$$

Where φ is the second polar angle between PAS and the external magnetic field, specifically, between the plane with z-axis of PAS and Bo and x-axis of PAS.

The resulting shape of the spectra depends on the properties of the chemical shift tensor. Due to this dependency on orientation, randomly located crystallites in powder samples usually lead to the broadening of the spectra (see Figure 2).

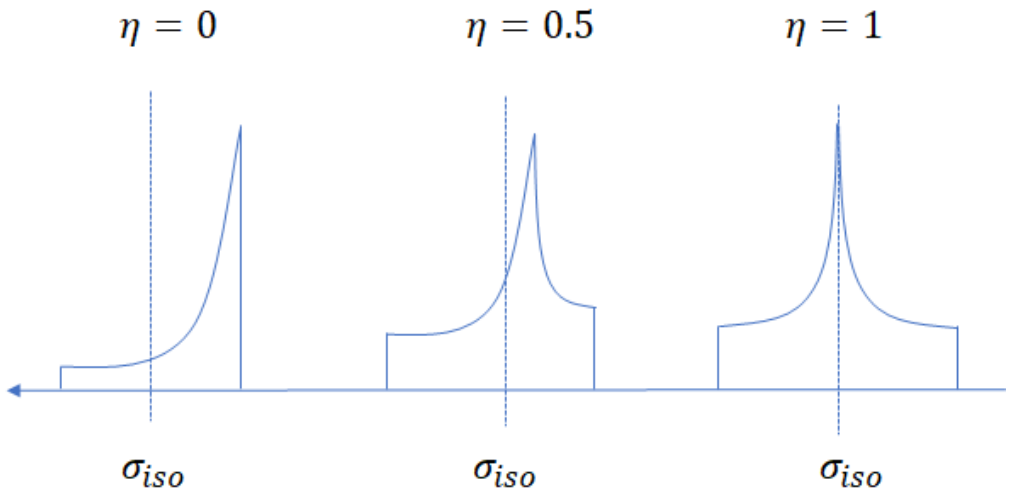

Figure 2. Theoretical powder spectra with different asymmetry parameters.

1.1.7. Direct Dipole-Dipole Interaction

Apart from interaction with external magnetic field and chemical shift, nuclei interact with each other directly as magnetic dipoles. The magnitude of this interaction depends on gyromagnetic ratios, distance between the coupled nucleus $\vec{r}$ and relative directions of the magnetic moment of the nuclei. This interaction Hamiltonian could be written as a sum of all spin pairs:

$$\hat{H}^D = -\frac{\mu_0}{4\pi}\sum_{i}^{spins}\sum_{j>i}^{spins}\frac{\gamma_i\gamma_j\hbar}{r_{ij}^3}\left[\hat{I}(i)\hat{I}(j) - \frac{3(\hat{I}(i)\vec{r})(\hat{I}(j)\vec{r})}{r^2}\right]$$

After introducing the so-called shift operators

$\hat{I}^+ = \hat{I}_x + i\hat{I}_y$ and $\hat{I}^- = \hat{I}_x - i\hat{I}_y$

And transformation of the operator into the polar coordination system (r, θ, ϕ), the Hamiltonian for two spin system might be written as a sum of six terms (“Dipolar Alphabet”):

$$\hat{H}^D(i) = -d\left[\hat{A} + \hat{B} + \hat{C} + \hat{D} + \hat{E} + \hat{F}\right]$$

Where d is dipolar constant (in rad s^{-1}):

$$d = \frac{\mu_0 \gamma_i \gamma_j \hbar}{4\pi r_{ij}^3}$$

And the other terms are, each corresponding with a transition:

$$\hat{A} = \hat{I}_z(i)\hat{I}_z(j)(1 - 3cos^2\theta)$$

$$\hat{B} = -\frac{1}{4}\left(\hat{I}^+(i)\hat{I}^-(j) + \hat{I}^-(i)\hat{I}^+(j)\right)(3\cos^2\theta - 1)$$

$$\hat{C} = \frac{3}{2}\left(\hat{I}_z(i)\hat{I}^+(j) + \hat{I}^+(i)\hat{I}_z(j)\right)\sin\theta\cos\theta\, e^{-i\varphi}$$

$$\hat{D} = \frac{3}{2}\left(\hat{I}_z(i)\hat{I}^-(j) + \hat{I}^-(i)\hat{I}_z(j)\right)\sin\theta\cos\theta\, e^{+i\varphi}$$

$$\hat{E} = \frac{3}{4}\left(\hat{I}^+(i)\hat{I}^+(j)\right)\sin^2\theta\, e^{-2i\varphi}$$

$$\hat{F} = \frac{3}{4}\left(\hat{I}^-(i)\hat{I}^-(j)\right)\sin^2\theta\, e^{+2i\varphi}$$

The term $\hat{A}$ describes classical magnetic dipole-dipole interaction in a two-spin system. The term $\hat{B}$ is so-called “flip-flop” term. It is responsible for energy exchange (change of state) of the same isotopes having nearly equal resonance frequencies. Terms $\hat{C}$ and $\hat{D}$ describe energy exchange when only one of the coupled nuclei changes its state ($\Delta m = \pm 1$). Terms $\hat{E}$ and $\hat{F}$ describe energy exchange where two parallel oriented nuclei change theirs state together ($\Delta m = \pm 2$).

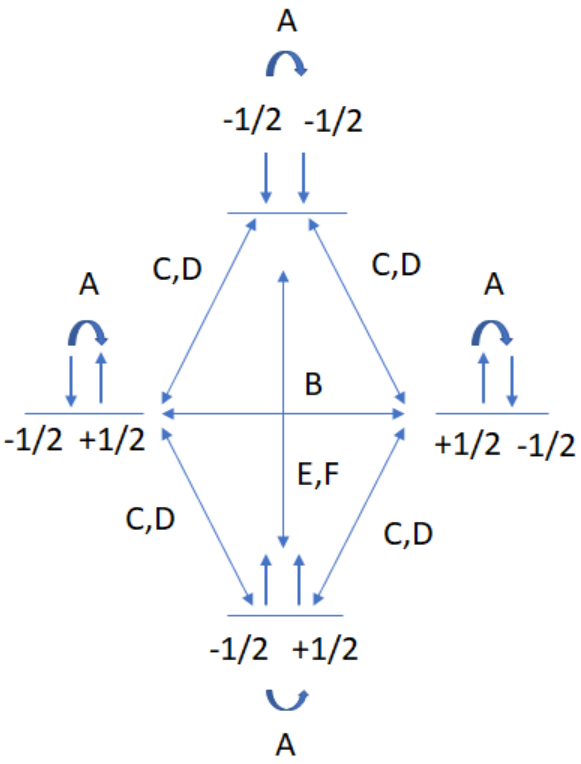

Figure 3. Schematic presentation of transitions and corresponding terms of direct dipole-dipole interactions which could affect these transitions.

The magnitude of direct dipole-dipole interaction is several magnitudes smaller than Zeeman interaction. Therefore, first-order perturbation only suffices for the description of the secular terms commuting with $\hat{H}^z$, which are $\hat{A}$ und $\hat{B}$ for homonuclear dipole-dipole coupling and only $\hat{A}$ for heteronuclear dipolar coupling (term $\hat{B}$ is only important when the xy component of the spin S rotates with the frequency close to the resonance frequency of the spin I, namely, when spins S and I are similar nuclei with similar chemical shifts):

$$\hat{H}_{D,homo} = d\frac{1}{2}(1 - 3\cos^2\theta)\left(3\hat{I}_z(i)\hat{I}_z(j) - \hat{I}(i)\hat{I}(j)\right)$$

$$\hat{H}_{D,hetero} = d(1 - 3\cos^2\theta)\,\hat{I}_z(i)\hat{I}_z(j)$$

Mostly in solid state NMR there is no separated interacting dipoles but an ensemble of spins interacting with each other. Van Vleck developed a method[61] to describe dipole-dipole interaction in many-spin systems – magnetic moments might be calculated without information of the eigenvalues of full Hamiltonian. Following this model, FID f(t) of NMR experiment is approximated as Taylor-series of moments:

$$f(t) = f(0)\left[1 - \frac{M_2 t^2}{2!} + \frac{M_4 t^4}{4!} - \frac{M_6 t^6}{6!} + \cdots\right]$$

Where M_n is defined as:

$$M_n = \frac{\int_0^\infty (\omega - \omega_0)^n f(\omega) d\omega}{\int_0^\infty f(\omega) d\omega}$$

This allows to investigate the intensity of homonuclear dipolar coupling with simple spin-echo experiments (see 1.2.2). The second moment is an important metric used to characterize dipole-dipole interaction in many-spin systems such as it dominates decay of FID at smaller t:

$$M_{2,homo}^I = \frac{3}{4}\left(\frac{\mu_0}{4\pi}\right)^2 \gamma_I^4 \hbar^2 I(I+1) \sum_{i \neq j} \frac{(1 - 3\cos^2 \theta_{ij})^2}{r_{ij}^6}$$

$$M_{2,hetero}^I = \frac{1}{3}\left(\frac{\mu_0}{4\pi}\right)^2 \gamma_I^2 \gamma_S^2 \hbar^2 S(S+1) \sum_{S} \frac{(1 - 3\cos^2 \theta_{IS})^2}{r_{IS}^6}$$

Or in case of the powder samples averaging over possible orientations:

$$M_{2,homo}^i = \frac{3}{5}\left(\frac{\mu_0}{4\pi}\right)^2 \gamma_I^4 \hbar^2 I(I+1) \sum_{i \neq j} \frac{1}{r_{ij}^6}$$

$$M_{2,hetero}^I = \frac{4}{15}\left(\frac{\mu_0}{4\pi}\right)^2 \gamma_I^2 \gamma_S^2 \hbar^2 S(S+1) \sum_{S} \frac{1}{r_{IS}^6}$$

Such as second moment decays proportional to $\frac{1}{r_{ij}^6}$, it allows to investigate local environment around nuclei.

1.1.8. Indirect Dipole-Dipole Interaction

Two nuclei might be also coupled through electron cloud. This interaction can take place to the extent of several chemical connections. The Hamiltonian for indirect dipole-dipole coupling is defined as:

$$\widehat{H}_J = 2\pi \hat{I} \overleftrightarrow{J_{lk}} \hat{K}$$

Where interaction tensor $\overleftrightarrow{J_{lk}}$ has both isotropic and anisotropic components. After transformation to the principal system, the isotropic part of this tensor is given as:

$$J_{iso} = \frac{1}{3}(J_{xx} + J_{yy} + J_{zz})$$

Where J is the coupling constant. Depending on the coupled nuclei, indirect dipole-dipole coupling might lead to the appearance of multiples in the spectrum. Two J-coupled atoms lead to appearance of a duplet having peaks intensity in an NMR spectrum where the distance between multiples reflects the coupling constant, J. Three coupled atoms lead to triplet with intensities ratios of 1:2:1 (see Figure 4).

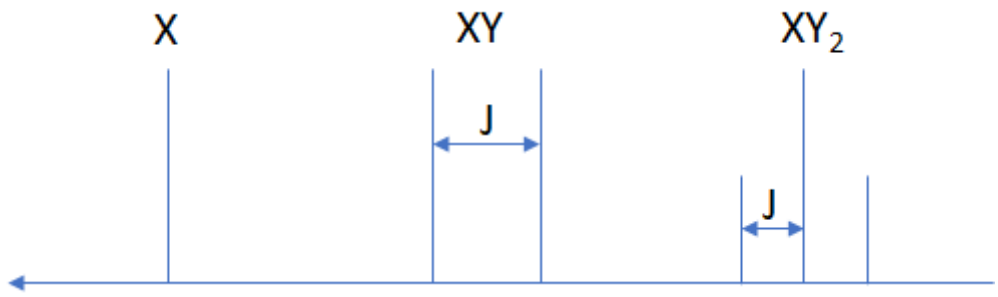

Figure 4. Effect of indirect dipolar coupling to the spectrum of the nucleus (I=1/2) with two coupled atoms (middle) and three coupled atoms (right).

1.1.9. Quadrupole Interaction

74% of all NMR-active spins have a nuclear spin quantum number $I > \frac{1}{2}$ which leads to appearance of a quadrupole moment eQ due to asymmetrical charge distribution within the nucleus. If an electric field around the nucleus has an electric field gradient (EFG), it will interact with quadrupolar moment resulting in quadrupolar interaction.

The electric field gradient around a nucleus is defined as the second derivative from electric potential V:

$$\overleftrightarrow{V}_{\alpha,\beta} = \frac{\partial^2 V}{\partial\alpha\partial\beta}$$

Where $\alpha, \beta = x, y, z$. Transformed to the PAS ($|V_{zz}^P| \geq |V_{yy}^P| \geq |V_{xx}^P|$), only two independent parameters are required to describe the EFG in regard to Laplace convention ($|V_{zz}^P| + |V_{yy}^P| + |V_{xx}^P| = 0$):

$$\eta_Q = \frac{|V_{yy}^P| - |V_{xx}^P|}{|V_{zz}^P|} \text{ and } eq = V_{zz}^P$$

Where eq is the magnitude of the EFG along the main axis in PAS and η_Q is the asymmetry parameter.

In NMR quadrupole coupling constant, C_Q, and quadrupole frequency, v_Q, are often used to characterize quadrupole interaction:

$$C_Q = \frac{e^2qQ}{\hbar}$$

$$v_Q = \frac{3e^2qQ}{2I(2I-1)\hbar}$$

If the quadrupolar coupling constant is small (Hz to kHz range), then the quadrupolar Hamiltonian might be written using first order perturbation only:

$$H_Q^{(1)} = \frac{1}{12}\omega_Q\hbar\left[3\hat{I}_z^2 - I(I+1)\right]\left(3\cos^2\theta - 1 + \eta_Q\cos(2\varphi)\,sin^2\,\theta\right)$$

Where angles θ and φ are the angles between principal and laboratory coordinate systems. In a simple case when EFG is axially symmetric, the energy correction caused by quadrupolar interaction might be written as:

$$E_Q^{(1)} = \frac{1}{12}\omega_Q\hbar[3m^2 - I(I+1)](3\cos^2\theta - 1)$$

Where quadrupole interaction influences not the central transition ($m = +\frac{1}{2} \leftrightarrow m = -\frac{1}{2}$) but satellite transitions ($m = \pm\frac{1}{2} \leftrightarrow m = \pm\frac{3}{2}$) – see Figure 5.

If quadrupole interaction is of the same order as the magnitude of the Zeeman interaction (typically in MHz range), all transitions are strongly effected, and the energy levels are in complex dependency on $I,\ m,\ \eta_Q,\ C_Q,\ \theta,\ \varphi$ (see Figure 5):

$$E_Q^{(2)} = -\left(\frac{e^2qQ}{4I(2I-1)}\right)^2\frac{m}{\hbar\omega_0}\left(-\frac{1}{5}(I(I+1)-3m^2)\left(3+\eta_Q^2\right)+\right.$$

$$+\frac{1}{28}(8I(I+1)-12m^2-3)\left(\left(\eta_Q^2-3\right)(3\cos^2\theta-1)+6\eta_Q\,sin^2\,\theta\cos(2\varphi)\right)+$$

$$\left.+\frac{1}{8}(18I(I+1)-34m^2-5)\left(\frac{1}{140}\left(18+\eta_Q^2\right)(35\,cos^4\,\theta-30\,cos^2\,\theta+3)+\right.\right.$$

$$+\frac{3}{7}\eta_Q \, sin^2\,\theta\,(7\,cos^2\,\theta - 1)\cos(2\varphi) + \frac{1}{4}\eta_Q^2 \, sin^4\,\theta\cos(4\varphi)))$$

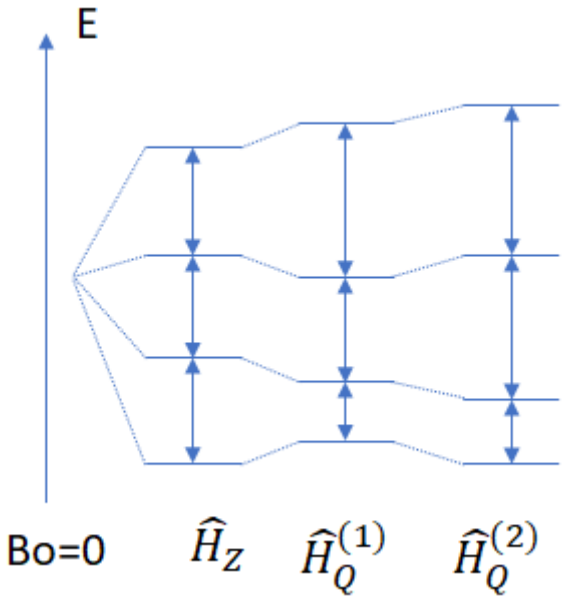

Figure 5. Splitting of energy levels of quadrupolar nucleus (I=3/2) due to Zeeman interaction and quadrupolar interaction of the first and second order.

The probability of allowed 2I transition depends strongly on the magnitude of B1 field and the length of electromagnetic pulse. This opens an opportunity for non-selective and selective excitations. Non-selective excitations are realized through short strong pulses with nutation frequency in solids equal to those in liquids ($\omega_1(solids) = \omega_1(liquids)$ which excite all possible transitions ($\omega_1 \gg \omega_q$). For selective excitation long soft pulses ($\omega_1 \ll \omega_q$) are applied which excite only central transition. For selective excitation, the nutation frequency is changes as: $\omega_1(solids) = \left(I + \frac{1}{2}\right)\omega_1(liquids)$

1.2. Techniques Used in Current Work

1.2.1. Magic Angle Spinning (MAS)

As described in 1.1, there are several interactions which could affect the shape of NMR spectrum. On the one side, NMR spectrum of 4 powder sample might therefore deliver information about isotropic and anisotropic interactions, on the other side, when many interactions are present at the same time on the same sample, it could make the spectrum too complicated to interpret. In liquid samples, Brownian motion averages out anisotropic interactions which results in narrow peaks. To reach the same effect in solid powder spectra, Andrew and Lowe proposed the Magic Angle Spinning (MAS)[62,63] technique, where the sample is rotated around the axis having the angle θr to the direction of the external magnetic field, where $\theta r = 54{,}7°$, also called "magic angle" (see Figure 6). Such as many interaction Hamiltonians are dependent on $(3\cos^2\theta - 1)$:

$$(3\cos^2\theta - 1) = 1/2(3\cos^2\theta r - 1)(3\cos^2\alpha - 1)$$

Where θ and α are the angles between PAS and laboratory axis system, if the system is rotated under θr and the term $(3\cos^2\theta r - 1)$ is equal to zero and these anisotropic contributions are averaged out.

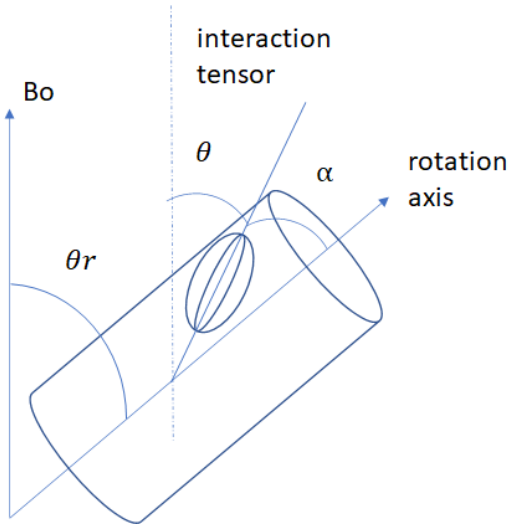

Figure 6. Illustration of MAS experiment.

To achieve the effect, a sample has to be rotated with the frequency higher than the width of the static spectrum. Otherwise, dipole-dipole interaction and chemical shift anisotropy are

not completely averaged out which results in appearance of so-called spinning sidebands – multiples located at spinning intervals across the linewidth of static spectrum (see Figure 7). The quadrupolar interaction of the first order is also proportional to $(3\cos^2\theta - 1)$ and might be averaged out by this technique.

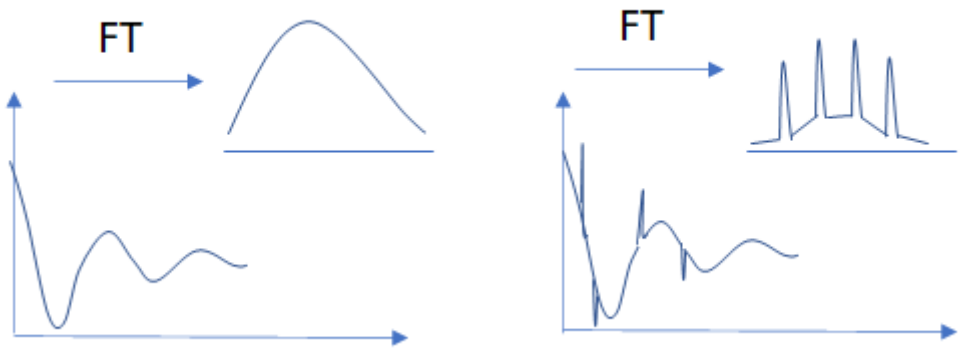

Figure 7. Illustration of FID obtained through Fourier-transformation without applying MAS (left) and with MAS applied (right).

Applying of MAS to powder sample leads to loosing information about anisotropic components. Multiple techniques were proposed to regain information about e. g. dipolar coupling with the help of REDOR (Rotation Echo Double Resonance) which would be discussed later in the chapter 1.2.3.

1.2.2. Spin Echo

Normally, in NMR spectrometers the same coil is used to apply electromagnetic pulses and to detect the signal. This complicates the detection of the signal immediately after applying pulse (so-called dead time delay). If the signal decay is relatively slow, the loss of the information in the beginning of FID might be compensated by first-order phase correction. If the signal decays fast, too much information is lost during the dead time and an alternative approach is needed (see Figure 8).

Figure 8. Effect of the dead time to fast (left) and slow (right) decaying FID.

One way to overcome this problem is the spin echo pulse sequence $90^{\circ}_{x} - \tau - 180^{\circ}_{y} - \tau$ developed by Hahn[64]. As might be seen in Figure 9, first, 90° pulse first applied to the system to bring magnetization from z-axis to the transverse plane of x'y' in the rotational coordinate system. During time evolution spins are losing their phase. After time evolution period τ, a 180°_{y},-pulse rotates the magnetization components around the y-axis, spins continue to precess and are refocused after a second τ period and FID can be completely recorded.

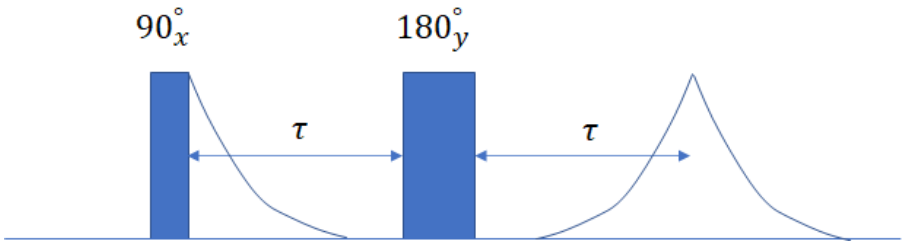

Figure 9. Pulse sequence of Hahn-echo experiments.

Only the interactions which are commute with $\hat{I}_z$ are refocused with 180°_{y},-pulse: chemical shift anisotropy and heteronuclear dipole-dipole interaction. In contrary, homonuclear dipole-dipole interaction and quadrupole interactions are not refocused. This is very important and opens an opportunity to obtain information about homonuclear dipole-dipole coupling by measuring of the signal intensity depending on the evolution time τ (see Figure 10). The intensity decay of the FID signal, $I_{2\tau}/I_0$ for spins I = 1/2, is then connected with $M_{2,homo}$ (see 1.1.7) through a Gauss-equation as a function of evolution time τ:

$$\frac{I_{2\tau}}{I_0} = \exp\left(-\frac{M_2}{2}(2\tau)^2\right)$$

Where $I_{2\tau}$ is the signal intensity after 2τ and I_0 is the initial intensity.

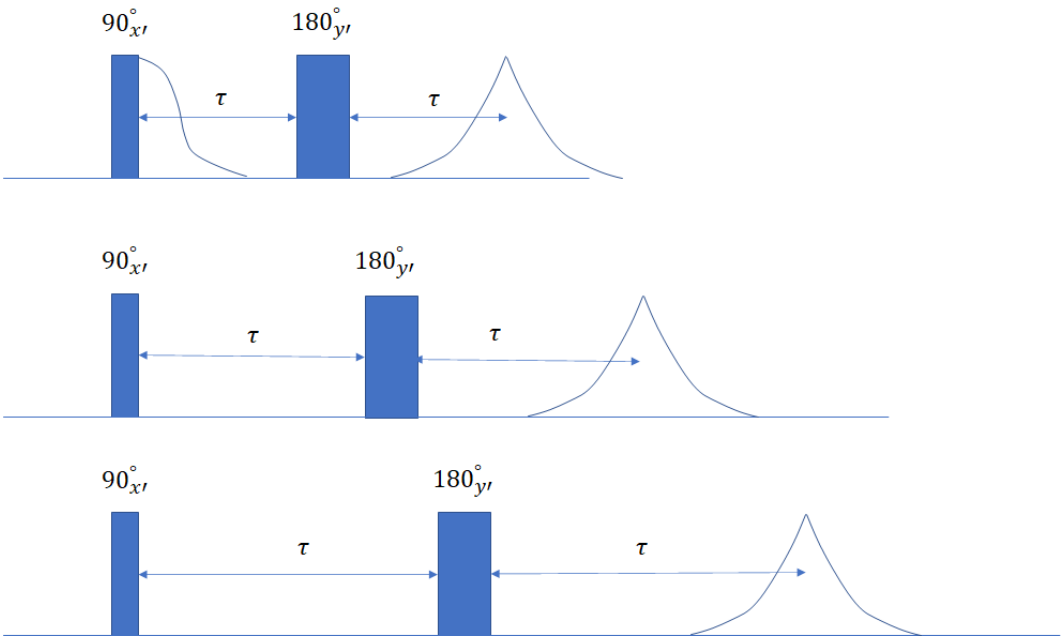

Figure 10. Evolution of the signal intensity in Hanh-Experiment depending on the evolution time τ.

1.2.3. REDOR and REAPDOR

Rotational Echo Double Resonance (REDOR) experiment was developed by Gullion and Schaeffer in 1989 based on Hahn-echo experiment from earlier Spin Echo Double Resonance (SEDOR) experiment[4,5]. It is used for quantitative determination of heteronuclear dipolar coupling. REDOR is of essential importance for understanding of structure of materials because the dipolar couplings reflect the distances between nuclei. The general scheme or REDOR pulse sequence and the development of Hamilton operator for heteronuclear dipolar coupling $\widehat{H}_D$ is represented in Figure 11 where I is the channel of an observed nucleus.

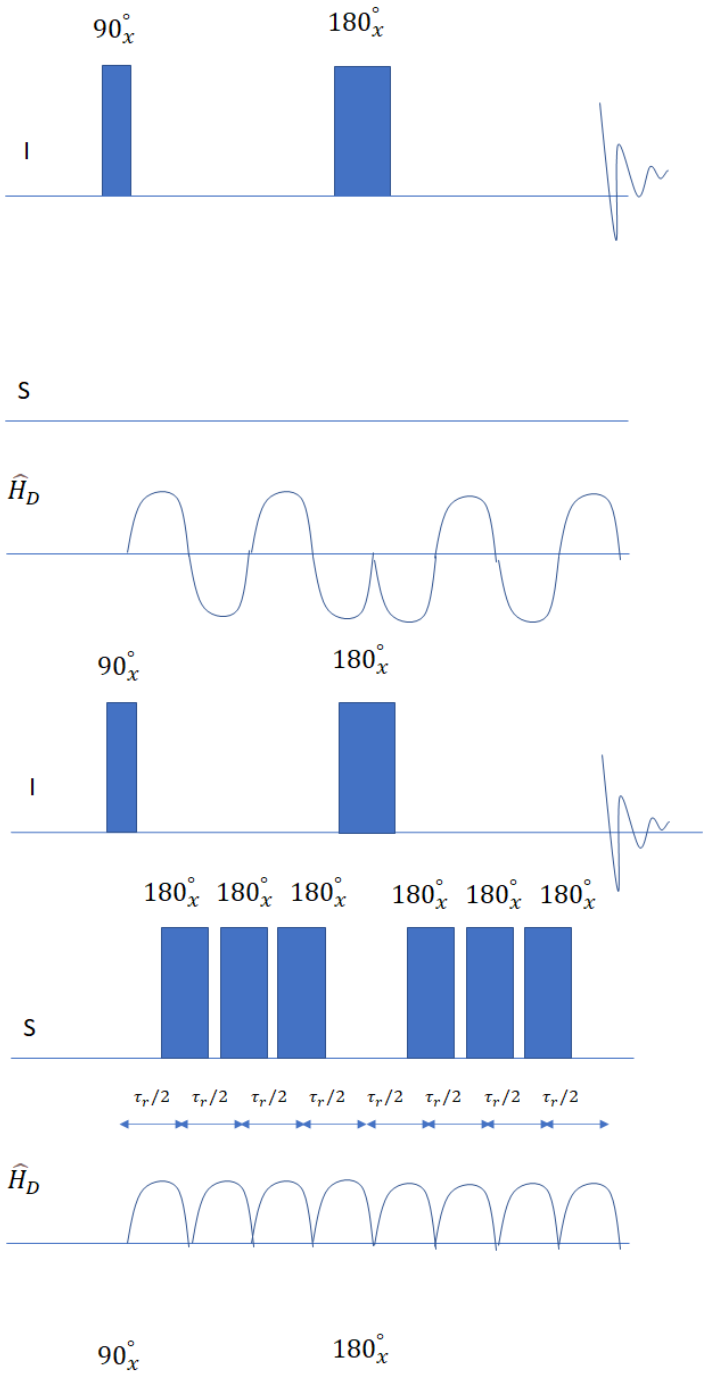

Figure 11. Pulse sequence of REDOR experiment without (top) and with pulses on S channel (bottom) for four rotor cycles.

The interaction Hamiltonian between two spins I and S under MAS condition is:

$$\widehat{H}_D(t) = -2C_{IS}(\beta, \gamma, t) I_Z S_Z$$

Where C_{IS} is the dependence of dipolar interaction on time (t) and orientation of the crystalline to the magnetic field (β, γ) which can be written using depending on rotational frequency ω_r:

$$C_{IS}(\beta,\gamma,t) = d(-\frac{1}{\sqrt{2}} sin2\beta cos(\omega_r t + \gamma) + \frac{1}{2} sin^2\beta cos(2\omega_r t + 2\gamma))$$

REDOR-experiment consisting of two parts. First, reference rotor-synchronized spin-echo experiment is carried out. The Hamiltonian of heteronuclear dipolar coupling over a rotor period is then:

$$\langle \hat{H}_D \rangle = \frac{1}{T_R} \int_0^{T_R} \hat{H}_D(t) dt$$

Which is zero due to periodic time dependance of the term C_{IS} (see Figure 11). Therefore, in the first part of REDOR experiment a reference signal So which is not changed through heteronuclear decoupling and only decays with T_2 relaxation is obtained.

In the second part of the experiment 180° pulses on the second channel synchronized with halves of the rotor periods, $\frac{1}{2T_R}$ are applied (except of the time when a 180° pulse is applied to I channel), which leads to the inversion of the sign of $\hat{H}_D$ after each 180° pulse. Then the Hamiltonian operator over rotor period is:

$$\langle \hat{H}_D \rangle = \frac{1}{T_R} (\int_0^{\frac{T_R}{2}} \hat{H}_D(t) dt - \int_{\frac{T_R}{2}}^{T_R} \hat{H}_D(t) dt)$$

The average Hamiltonian is then not averaged out and the intensity of the signal is then decreased to the value S which is affected not only by T_2 relaxation but also by heteronuclear dipolar coupling. $S_0 - S$ might then be compared with the intensity of the reference signal S_0 to obtain information about heteronuclear dipolar coupling.

The weakening of the signal caused by heteronuclear dipolar interaction might be quantified using the dependence of the normalized difference signal versus the length of evolution time NT_R which is for a powdered sample equal to:

$$\frac{\Delta S}{S_0} = 1 - \frac{1}{4\pi} \int_0^{2\pi} d\gamma \int_0^{\pi} \cos(\Delta\phi)\, sin\beta d\beta$$

Where $\Delta\phi$ is the dipolar de-phasing depending on evolution time NT_R:

$$\Delta\phi = 4\sqrt{2}NT_R d sin\beta cos\beta sin\gamma$$

For a two-spin system Mueller proposed a solution using k-th order J_k Bessel functions (J_0 and J_0)[65]:

$$\frac{\Delta S}{S_0} = 1 - \left(J_0(\sqrt{2}\lambda_N)\right)^2 + 2\sum_{k=1}^{\infty} \frac{1}{16k^2 - 1}\left(J_k(\sqrt{2}\lambda_N)\right)^2$$

Where $\lambda_N = NT_R d$

It is challenging to apply this solution to glasses and other disordered systems due to multi-spin interactions where REDOR curves depend strongly on the geometry of the studied system which is often not known exactly. Nevertheless, in case of glass systems this dependence on geometry might be neglected for short evolution times and the dependence might be approximated as[66,67]:

$$\frac{\Delta S}{S_0} \approx \frac{16}{15}(NT_R)^2 \sum_{i=1}^{n} d_i^2$$

Where the sum of dipolar couplings d is related to the heteronuclear dipolar moment $M_{2,hetero}$ (see above) and the normalized difference for the spin I=1/2 might be written as:

$$\frac{\Delta S}{S_0} \approx \frac{4}{3\pi^2}(NT_R)^2 M_{2,hetero}$$

REDOR cannot be applied to evaluate dipolar coupling between ½-spin and a quadrupolar nucleus in most of the systems because it is difficult to apply pi-pulses to broad satellite transitions, e. g. of several MHz. REAPDOR-experiment (rotational echo adiabatic passage double resonance sequence) [3,6,7] was developed by Gullion for such systems. The typical pulse sequence of REAPDOR is represented in Figure 12. In the upper part of the Figure the multispin-echo reference measurement of S_0 and in the lower part of the figure the pulse sequence leading to reintroduction of dipole-dipole interaction is represented.

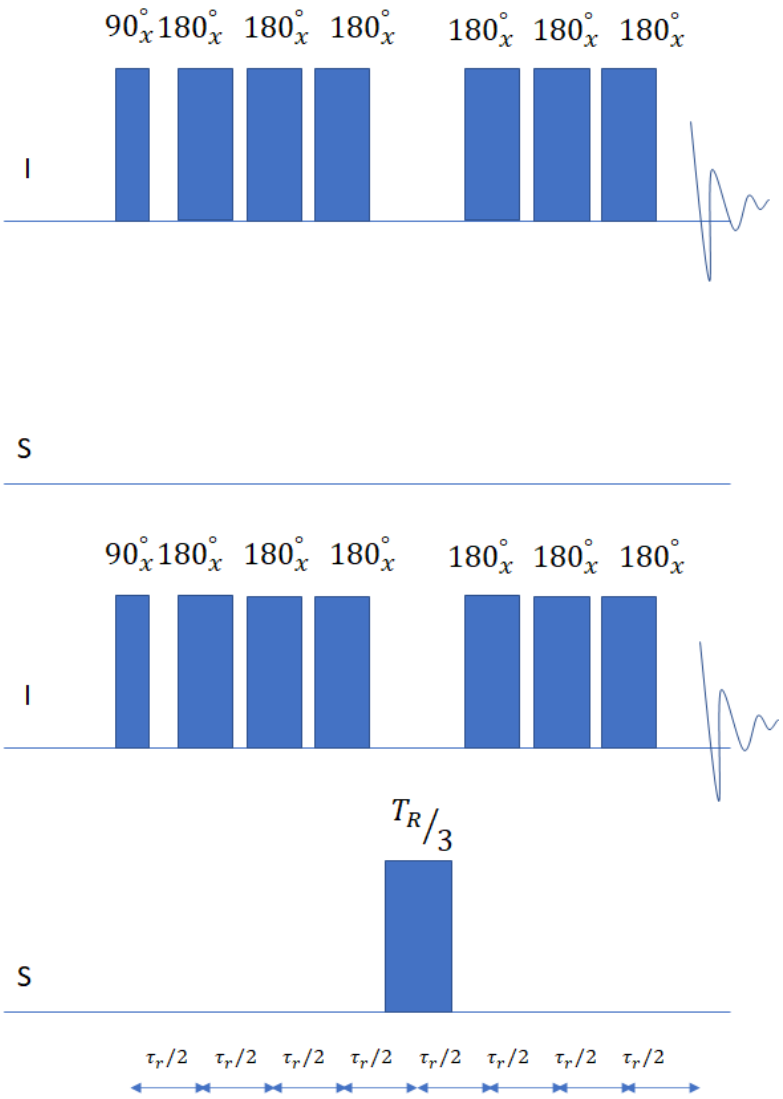

Figure 12. Pulse sequence of REAPDOR experiment for four rotor periods.

To explain how the pulse on S channel works (on the example of the spin S=1 system), first-order perturbation level approximation of Hamiltonian of the quadrupolar interaction is introduced[7]:

$$\widehat{H}_Q(t) = \frac{Q(t)}{2}\left(\hat{S}_z^2 - \frac{S(S+1)}{3}\right) + \Delta\omega_S\hat{S}_z + \omega_{1,S}\hat{S}_x$$

Where the first term $Q(t)$ is time-dependent spatial component of the quadrupolar interaction:

$$Q(t) = 1/2\omega_Q(3cos^2\theta_Q - 1 - \eta_Q sin^2\theta_Q cos2\phi_Q)$$

Where θ_Q and ϕ_Q are instantaneous values of the polar angles of the B_0 field in the principal axis system of the quadrupolar tensor and ω_Q is connected with quadrupolar frequency ν_Q with:

$$\omega_Q = 2\pi\nu_Q$$

Where ν_Q is connected with quadrupolar coupling constant defined as $\chi = e^2qQ/h$ through following equation:

$$\nu_Q = \frac{3\chi}{2S(S-1)}$$

The other two terms in the equation of $\widehat{H}_Q(t)$ represent the effect of the offset and application of rf pulse.

The term $Q(t)$ oscillates between large negative and positive values. If it is much higher or much lower than ω_1, the spins exist in |m> states and the applied rf pulse does not have much effect as shown in Figure 13. When $Q(t)$ crosses zero, the states are mixed. If an adiabatic rf pulse is applied to the system ($Q(t)$ passes slowly through zero-crossing), avoided level crossings occur leading to the change of the spin states need for dipolar decoupling as depicted in Figure 13 (|01> to |+1>, |+1>to |-1> and |-1> to |0>). The nature of transition is defined by the parameter $\alpha = \frac{v_1^2}{v_r v_Q}$, where v_1 is RF-frequency and v_r and v_Q are MAS frequency and quadrupolar frequency, respectively. If α is greater than 1, adiabatic passage occurs.

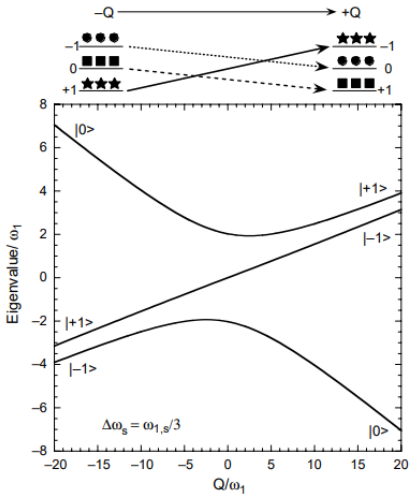

Figure 13. Eigenvalues of the Hamiltonian $\widehat{H}_Q(t)$ depending on ω_1 and Q_t (from [7]).

Such as sample rotates further, $Q(t)$ changes from positive to negative values changing the spin states again. Therefore, the length of rf pulse should be chosen in the way that the system experiences one or three of such transitions. The fraction of crystallites experiencing crossings depending on the rotor time is represented in Figure 14. As might be seen, the majority of the spins experience one crossing after a third of the rotor period which is used as a pulse length in REAPDOR.

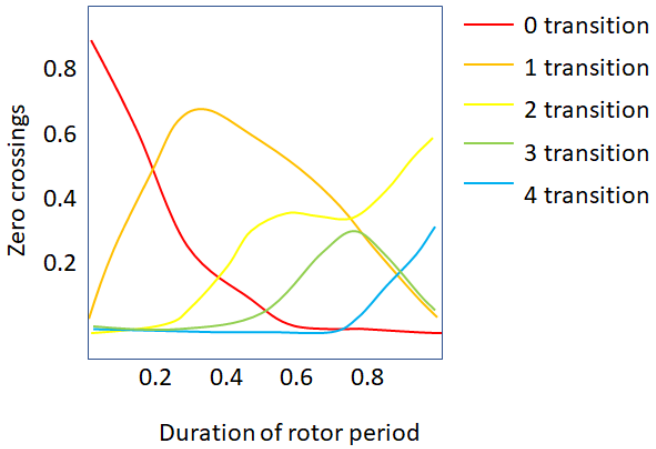

Figure 14. Amount of spins experienced zero to four zero crossings during rotor period[7].

1.2.4. CPMAS and HETCOR NMR

Low-abundant nuclei with low gyromagnetic ratios often pose a challenge for solid-state NMR resulting in low signal intensity. Furthermore, these obstacles are often complicated by long relaxation times. To solve this problem and to facilitate acquisition of NMR spectra, Cross-polarization MAS NMR (CPMAS) was developed[68]. During sequence of pulses the magnetization is transferred from abundant nuclei with high gyromagnetic ratio (e. g. protons) to low-abundant nuclei (e. g. ^{13}C, ^{15}N). Additionally, the advantage of typically lower relaxation times of abundant nuclei is employed.

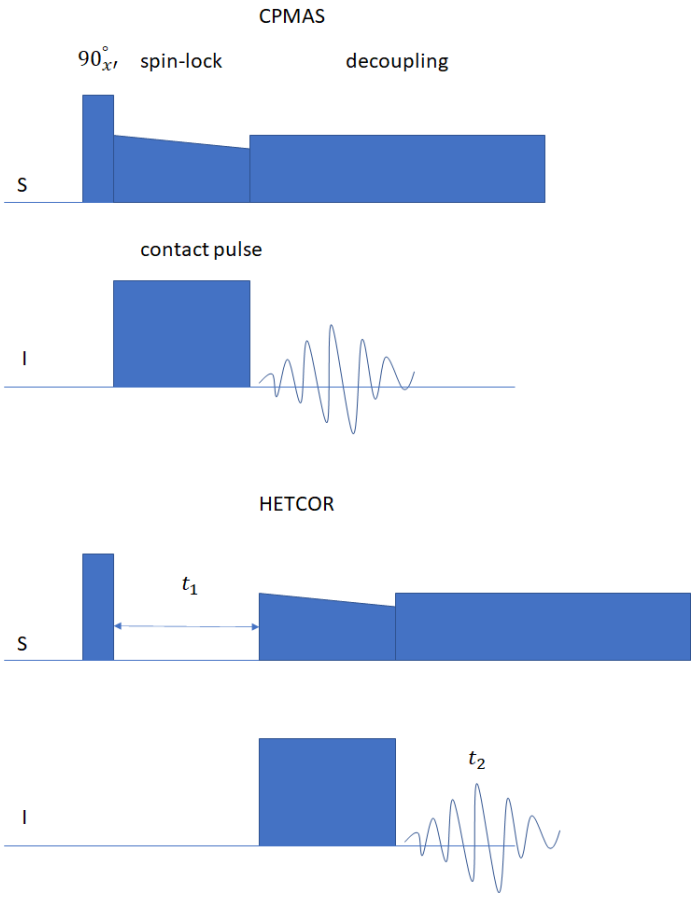

Figure 15. Pulse sequence of CP-experiment and HETCOR-experiment.

Pulse sequence of a typical CP experiment is represented in Figure 15. As the first step, the magnetization of the spins S is aligned with y'-axis with a $90^{\circ}_{x'}$-pulse. In the second part of the experiment, called 'spin-lock' where the magnetization is being transferred through dipolar coupling. Both I and S spins rotate together around y' axis. For magnetization transfer the following condition must be fulfilled (Hartmann-Hahn matching):

$$\gamma_S B_{1S} = \gamma_I B_{1I}$$

The spin-lock pulse might often have a variation of the amplitude along the pulse to ensure that Hartmann-Hahn conditions are satisfied also under MAS conditions where an additional term appears due to rotation:

$$\gamma_S B_{1S} = \gamma_I B_{1I} \pm n\omega_{rot}$$

Often then heteronuclear dipolar coupling of I-spins to the abundant S-spins is reduced by decoupling techniques during FID recording.

The magnetization transfer might be explained using thermodynamic concepts. The S-spins have a very high temperature after $90^{\circ}_{x'}$-pulse because there is no magnetization in z-direction. On the contrary, I-spins are distributed according to Boltzmann distribution and have low temperature. During the contact pulse the energy is transmitted from the hotter spin basin to the colder spin basin ('flip-flop'-transitions) leading to the magnetization transfer from S-spins to I-spin along -y'-axis.

Furthermore, CPMAS experiments opens an opportunity to gain information about dipolar coupling between S and I spins[49,50]. This is done by measuring the intensity of a signal against the duration of contact pulse:

$$M(t) = \frac{1}{1 - {T_{IS}}/{T_{1\rho}}}\left(\exp\left(-{t}/{T_{1\rho}}\right) - exp\left(-{t}/{T_{IS}}\right)\right)$$

Where $T_{1\rho}$ is the relaxation time constant of a spin I in the rotating frame and ${1}/{T_{IS}}$ is the cross-polarization rate which is directly connected with the value of dipolar coupling.

More information might be obtained from NMR experiments if they are developed to involve several dimensions. In the simple case of a 2D NMR experiment, a one-dimensional experiment is extended by a varied time t_1, also called an evolution time. First, the magnetization of S-spins is transferred to xy-plane by a simple 90°-pulse or by more sophisticated methods, e. g. CP-MAS techniques. This step is called a preparation period. After this, the magnetization of the spins S evolves during t_1, so-called evolution period step. This later allows to detect a shift of the second nucleus in the F1. The time t_1 is not fixed but is incremented during the experiment. After that, the so-called mixing period follows, where the coherence after t_1 is transferred to a detectable signal on I-channel employing e. g. dipolar coupling between S and I nuclei. The detection takes place during the detection period t_2. The resulting signals is dependable on t_1 and t_2 and Fourier-transformed to ω_1 and ω_2 frequency domains for spins S and I, respectively (see Figure 16).

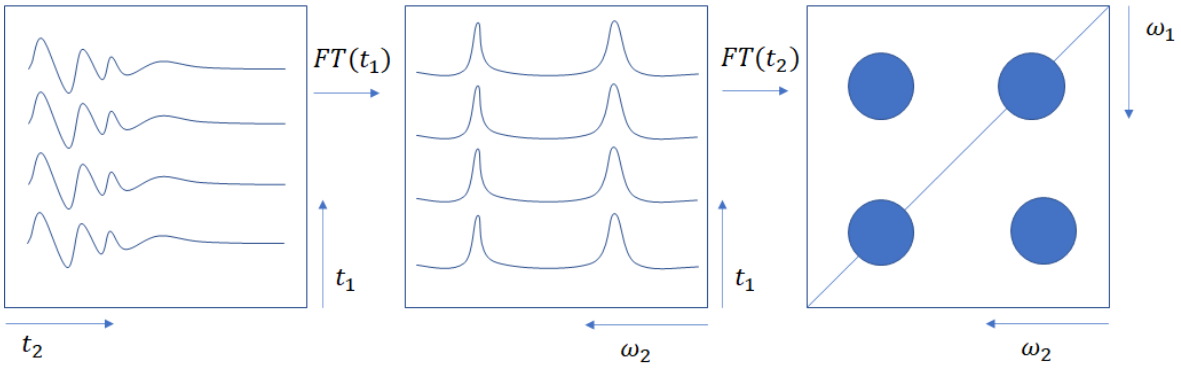

Figure 16. General scheme of two-dimensional Fourier-transformation.

HETCOR NMR (heteronuclear correlation) is two-dimensional version of CP experiment. The general scheme is represented in Figure 15. It allows to identify connectivity between the nuclei. As seen in Figure 15 in HETCOR incremented evolution time t_1 is added between $90^{\circ}_{x'}$-pulse and contact pulse. The FID is than detected during t_2. If the two-dimensional Fourier-Transformation is then applied to FID, the resulting spectrum allows to identify I and S spins which are coupled with each other through spin-spin coupling: it leads to appearance of cross-peaks in two-dimensional spectrum.

1.2.5. MQMAS

MQMAS (multiple angle quantum spinning)[1,2] is a technique which allows to collect isotropic chemical shift of quadrupolar nuclei which have severely broadened spectra due to the quadrupolar interaction of the second order which cannot be reduced by MAS NMR. In MQMAS multi-quantum coherence is transformed to single-quantum coherence.

To describe how MQMAS works, first, the transition frequencies for the central transition are introduced:

$$\omega_{1/2,-1/2} = \frac{\omega_q^2}{\omega_0}\left[I(I+1) - \frac{3}{4}\right][A_0 + 8A_2(\theta,\phi)P_2(cos\beta) + 18A_4(\theta,\phi)P_4(cos\beta)]$$

Where A_0 term depends on isotropic shift and A_2 and A_4 are the angle-dependent terms which cause line broadening. Terms P_2 and P_4 are Legendre-polynomes of the second- and forth-order:

$$P_2 = (3cos^2\beta - 1)/2$$

$$P_4 = (35cos^4\beta - 30cos^2\beta + 3)/8$$

P_2 equals to 0 under MAS-rotation. Then the quadrupolar interaction of the second order depends on A_4 and P_4 and the line broadening is proportional to C_Q^2.

The general description of |±m>↔ |∓m> transitions:

$$\omega_{m,-m} = \frac{\omega_q^2}{\omega_0}[A_0 C_0^I(m) + 8A_2(\theta,\phi)C_2^I(m)P_2(cos\beta) + A_4(\theta,\phi)C_4^I(m)P_4(cos\beta)]$$

Where the terms $C_0^I(m)$, $C_2^I(m)$ and $C_4^I(m)$ depends on I and m:

$$C_0^I(m) = 2m[I(I+1) - 3m^2]$$

$$C_2^I(m) = 2m[8I(I+1) - 12m^2 - 3]$$

$$C_4^I(m) = 2m[18I(I+1) - 34m^2 - 5]$$

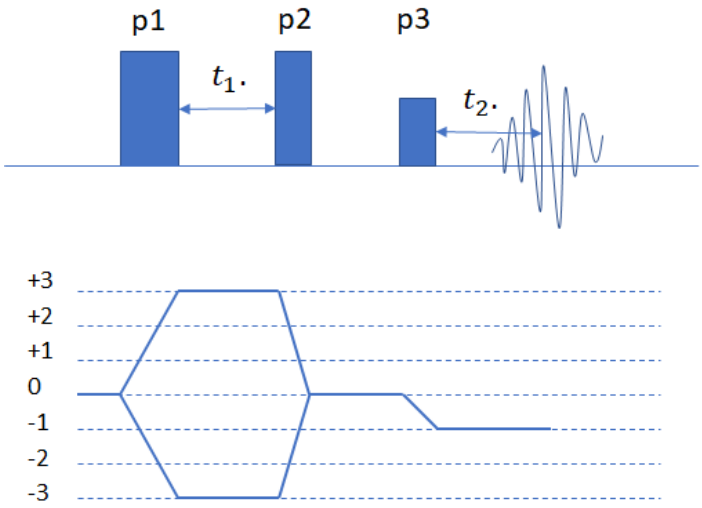

Figure 17. Pulse sequence of MQMAS and corresponding coherence path of triple-quantum NMR for spin 3/2 nucleus.

The additional broadening of quadrupolar nuclei might be removed if the different coherences (states where spins oscillate between between different energy levels with the same phase and speed) of the spins evolve during different evolution times. In Figure 17 MQMAS pulse sequence with applied Z-filter is shown. After the first pulse where all coherences are exited the system is allowed to evolve during evolution time t_1. The second pulse (so-called 'hard pulse') converts multiple-quantum coherence to zero-quantum coherence. Desired coherences are selected using detection phase cycling[69]. The third selective pulse ('soft pulse') transforms zero-quantum coherence to single quantum coherence which could then be detected after t_2. The prerequisite for isotropic echo is:

$$C_4^I(m)t_1 + C_4^I(-1)t_2 = 0, \text{ or } t_2 = \left|\frac{C_4^I(-1)}{C_4^I(m)}\right| t_1 = Rt_1$$

Where R is 7/9 for the spin 3/2. After that the spectrum is Fourier-transformed in both dimensions. To obtain an isotropic F1 dimension, shearing has to be carried out

$$\delta_{F1} = \delta_{F1'} + \delta_{F2'}R$$

In case of 3/2-nucleus corresponding isotropic and anisotropic chemical shifts in F1 and F2 dimensions are:

$$\delta_{F1} = \frac{34\delta_{cs}^{iso} - 60\delta_Q}{9}$$

$$\delta_{F2} = \delta_{cs}^{iso} + 3\delta_Q$$

Where:

$$\delta_Q = \frac{4\pi^2(SOQE)^2}{3\omega_0^2[2I(2I-1)]^2}$$

Where SOQE is the second order quadrupolar effect $C_Q(1 + \frac{\eta_Q^2}{3})^{1/2}$

1.2.6. MAT

As described above in 1.2.1, under MAS rotation parts of Hamiltonians are averaged out. Relevant for e. g. phosphorus investigation in glasses, the information about CSA is, therefore, lost under MAS. To prevent this, several NMR techniques were developed – for example, magic angle hopping (MAH) by Bax[70] or magic angle turning by Gan (MAT)[71]. In MAH the probe is rotated in 120° steps around the magic angle which is quite challenging to implement with standard NMR equipment. MAT allows to obtain information about CSA while using commercially available NMR rotation probes. In MAT the magnetization is deflected from Z-axis to XY plane and then saved again in Z-direction after short evolution time when sample is rotated slowly (50-200 Hz) as shown in Figure 18. This allows to regain information e. g. about CSA tensors lost under rotation. The pi-pulses transfer the magnetization to XY plane and are separated by 1/3 of the rotor period. The time between transferring to XY plane and returning to Z-axis (shaded pulses) is being incremented in this 2D pulse sequence. The very last pulse is used to transfer the magnetization to XY plane to acquire the signal. Only information about the cos or the sin of 1/3 of the signal frequency ($\omega_A/3, \omega_B/3, \omega_C/3$) is stored in the z-direction

between flipping to the XY plane. If the correct phase cycling is used, the summation over all information obtained over the whole cycle delivers full information ($exp\left(\frac{i(\omega_A+\omega_B+\omega_C)}{3}\right)$) about isotropic chemical shift of the sample. After Fourier transformation, in the second dimension the CSA of the powder pattern of the corresponding unit is presented [70,72].

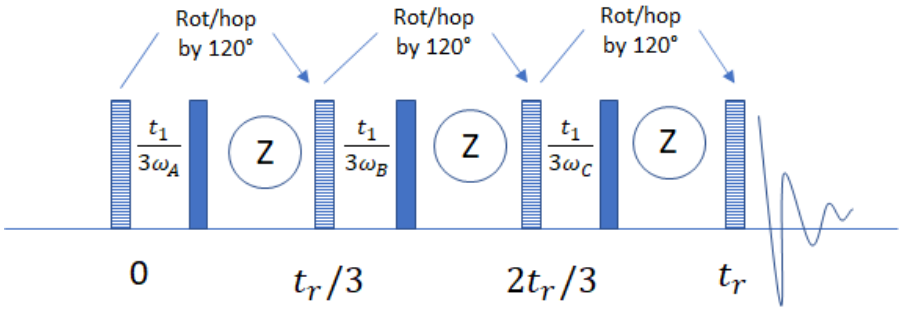

Figure 18. Schematic representation of magic angle turning sequence. Hatched pulses bring the magnetization to XY plane and are separated by 1/3 of rotor period. Shaded pulses return the magnetization to z-axis [73].

MAT probe and sequenced used in this work were developed and carried out by Gerrit Schiffmann using the pulse sequence published by Gan in 1992 [71].

2. Materials

This chapter is devoted to information about materials investigated in this thesis. First, typical characteristics of glasses and their difference to ordered materials are described. After that specific for this work phosphate, aluminophosphate and silicoaluminophosphate systems are described. In the second part manufacturing of PAN, different finishing treatment as well as recycling techniques are introduced.

2.1. Glasses

Network structure of the glasses has no symmetry and periodicity in contrast to crystals. Glasses also can be described as undercooled liquids which exist in metastable condition. Although many alternative techniques such as sol-gel methods are used to obtained glassy materials, quenching is the most popular synthesis methods. Oxide melts are quenched into air, copper plates or other mediums, which leads to the cooling speeds high enough that crystalline structures do not have enough time to form. If the melt is cooled fast enough, increasing viscosity of the liquid hinders formation of crystallization seeds which is resulted in metastable glass structure (see Figure 19).

One of the characteristics of the glass network is its glass temperature transitions (Tg) which is also shown in Figure 19. At this temperature many properties of the glass structure, such as thermal expansion coefficients and heat capacity experience significant change. Unlike in crystals, it is not an exact temperature but rather a continuous process.

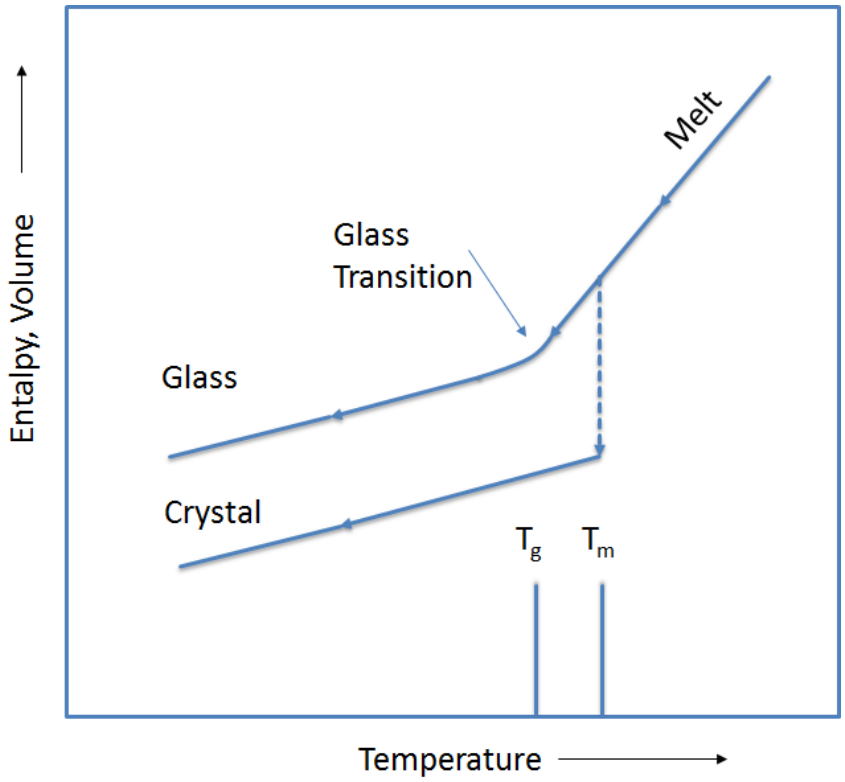

Figure 19. General scheme of melt-to-glass and melt-to-crystal transition.

Zachariasen's Random Network Theory (1932)[74] defined glasses as consisting from glass-forming polyhedral elements surrounded by oxygen and corners of those units connected to each other through oxygen bridges. Coordination numbers of forming atoms are small and oxygen is connected to only two forming elements. Although many stable glasses violating Zachariasen's glass theory were found since 1932 (e. g shared edges in nitride glasses or oxygen bound to three atoms in Al-Si triclusters), his theory has practical importance and can be used to describe a broad range of glass system.

Elements by which the glasses are formed might be broadly divided into two main categories: network formers and network modifiers. The division is made based on the values of dissociation energy E_d of element oxides. If E_d is higher than 80 kcal/mol then the element is called a glass network former. Glass network formers can form glass networks where they are connected by bridging oxygen (e.g. Si^{4+}, Ge^{4+} or P^{5+}). The elements having dissociation energy of oxides lower than 60 kcal/mol are called glass network modifiers. Glass modifiers do not build glass network. They are distributed in the network and reduce connectivity by destroying bonds between network formers leading therefore to appearance of non-bridging oxygen (NBO) (e.g. Na^+). Apart of this there are conditional glass formers which cannot form glasses

by their own but can act as network modifiers as or glass formers when there are already enough glass modifiers present in the structure. Typical example of a conditional network former is aluminum.

2.1.1. Phosphate Glasses

Phosphate glasses are important for optic applications due to their low dispersion and refractive indices and high transparency for ultraviolet light[75]. Other important application areas are, for example, sequestering agents for hard water treatments and dispersant for clay processing and pigment manufacturing[76]. Low thermal expansion coefficients lead to their applications as laser hosts[10]. Biocompatibility of phosphate glasses allowed them to be used in medical applications[14].

Basis theory of phosphorus-based glasses was first formulated by Van Wazer[76]. Structural units of phosphate glasses consist of connected phosphorus tetrahedra formed by sp^3 hybridized orbitals of outer electrons of phosphorus atoms. According to Van Wazer[76], alkali ions act as network modifiers when added to glass composition. They decrease polymerization of glass network by destroying P-O-P bonds, which leads to formation of non-bridging oxygen (NBO). This might be illustrated using pseudo-reaction scheme:

$$2Q^x + M_2O \rightarrow 2Q^{x-1} + 2M^+$$

Phosphorus units are distinguished using Q^x notation, where x indicates amount of phosphorus bonding oxygen. They are shown in Figure 20. It is supposed that alkali ions first connect to Q^3 phosphorus, forming Q^2 phosphorus units. Only when all Q^3 phosphorus units are transformed, the transformation of Q^2 to Q^1 units starts[77]. However, there are glasses with more than two phosphorus units coexisting at the same time, which might be described with "reorganization theory" of Van Wazer.

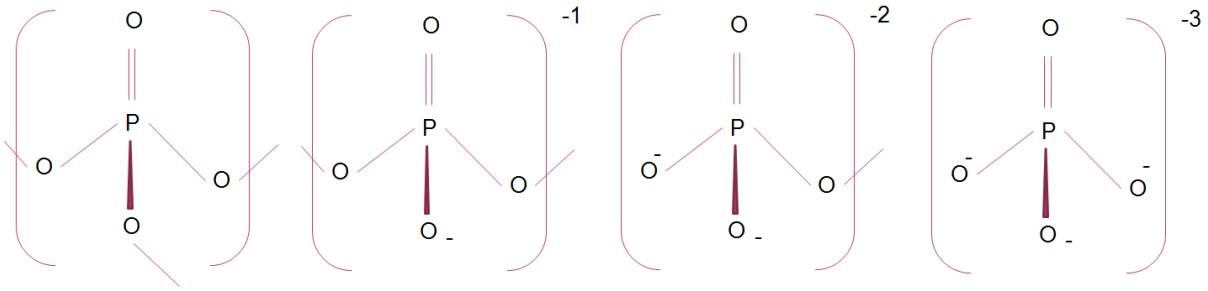

Figure 20. Phosphors structural units Q^x where x represents the amount of bridging oxygen and decreases from 3 to 0 from left to the right.

Q^3 phosphorus species possess large axially symmetric chemical shift anisotropy (CSA) tensors, Q^2-phosphorus tensors are not axially symmetric and CSA tensors of Q^1 units are nearly axially symmetric. Typical isotropic chemical shifts of phosphorus units and shapes of their CSA tensors are represented in Figure 21. It is changing from positive to negative ppm values along depolymerization of phosphorus units due to increasing ionicity of NBO bonds[78], thus, making NMR an important tool in glass structure investigations. Nature of network modifier has significant effect to mechanical properties of the glasses and to the chemical shift of phosphorus units: network modifiers with high cation potential shift peaks to more negative ppm[79]. Furthermore, isotropic chemical shift of individual phosphorus units are shifted to less negative (more positive ppm) under addition of network modifiers[75].

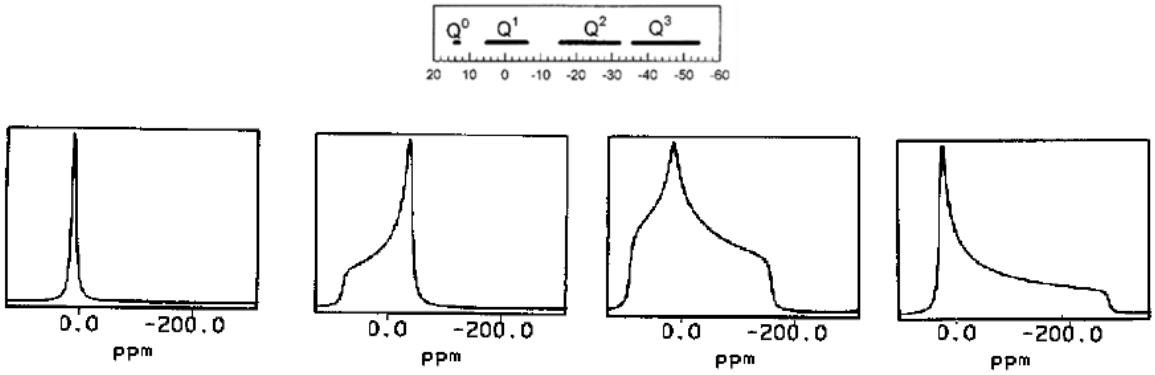

Figure 21. Typical isotropic chemical shifts and shapes of CSA tensors of phosphorus units in phosphate glasses [75,80].

2.1.2. Aluminophosphate glasses

Although phosphorus glasses possess many important technical characteristics, their low chemical resistance restricts possible application domains. Especially important issue is their hydrophilic nature which makes them unsuitable for many applications. Addition of aluminum

tends to decrease reactivity of phosphorus glasses[81] with water, lower their thermal expansion coefficients and increase their transition temperatures[82,83].

Aluminum can play a role of network former (in tetrahedral position) or network modifier (in octahedral position). If a small amount of aluminum is added to the glass composition, it becomes six-coordinated. It might be explained by the stable local charge environment. Each six-coordinated Al^{3+} donates 0.5 Valence units (VU) to phosphorus it is connected with, which leads to the stable structure (see an example in Figure 22). If aluminum would be four-coordinated (or five), then it would donate 0.75 or 0.6 VU, which together with phosphorus contributing 1.5 VU to P-O-Al bonds and 1.0 VU to P-O-P bonds would lead to overbound oxygen (VU more than 2). When the amount of aluminum is increasing and more aluminum-phosphorus bridges are created, four-coordinated aluminum is preferred (P contributes 1.25 VU and Al contributes 0.75 VU). An example of such charge-balanced structures is given in Figure 22. Aluminum coordination also might be discussed in terms of O/P ratio. In glasses where O/P ratio is close to 3 (pyrophosphate region), octahedral aluminum is charge-stabilized and preferred. If O/P=4 (orthophosphate glasses), aluminum is four-coordinated because AlO_6 units would be overbounded[83,84].

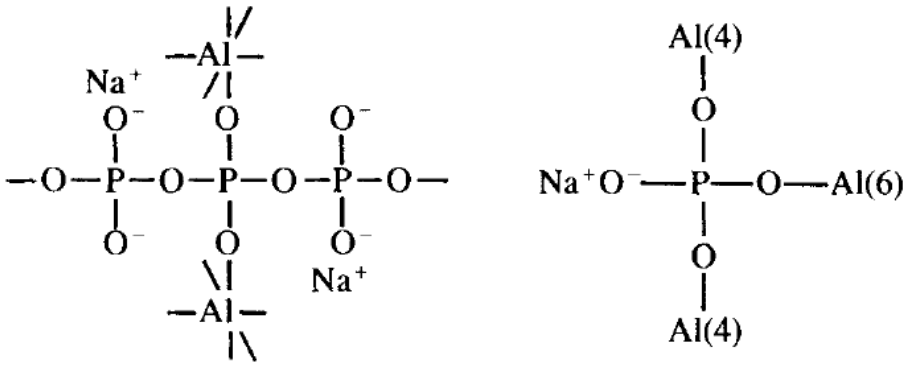

Figure 22. Stable charge-balanced Al-P environments with AlO_6 (left) and ALO_4 (right)[83].

Assignment of phosphorus peaks in solid state NMR spectra in alkali aluminophosphate glasses might be complicated because position of phosphorus peak depends on the amount and type of aluminum units in the second coordination sphere[83–87]. Generally, when P-O-P bonds are replaced by P-O-Al bonds, the peaks are shifted to less negative ppm. Further effect is decreasing CSA values upon appearance of aluminum in the second coordination sphere. When more aluminum is added to the glass composition, many overlapping peaks from

different aluminum-phosphorus environment might appear which make it difficult to assign individual units based on the chemical shift alone[83].

AlO_4, AlO_5 and AlO_6 units give rise to peaks located at about +40, +15 and -10 ppm in alkali aluminophosphate systems. The position of the peak shifts slightly to more negative (less positive) ppm upon addition of aluminum[84]. Often there are problems with exact estimation of peaks positions and their fractional areas due to highly distorted and anisotropic shape of the signals. Furthermore, if a peak is severely broadened due to high second-order quadrupole effect, it sometimes cannot be distinguished by ^{27}Al MAS NMR. Measurements in higher field using high spinning speeds or multiple-quantum MAS (MQMAS - see 1.2.5) are then needed[84] to identify aluminum species.

2.1.3. Aluminophosphosilicate Glasses

Aluminosilicate glasses are of special importance for modern industry such as they are used as base for high-strength glasses such as car windows and smartphone screens. Addition of phosphorus to aluminosilicate glasses leads to their better processability. The structure of glasses is complicated and understanding of interplay of roles of silicon and phosphorus, nature of aluminum as network former and network modifier and the distribution of alkali ions in glass structure is an important step in finding optimal composition for glass applications.

Aluminosilicate Glasses. Pure aluminosilicate glasses are not possible to synthesize by melt-quenching technique (although it is possible to produce them by sol-gel method) and they require an addition of some alkali metals to the glass composition. Chemical shift of silicon units is strongly affected by the presence of aluminum in the second coordination sphere. Differentiation of different $Si(OAl)_x(OSi)_{4-x}$ signals are often difficult due to their strong overlapping. Indirectly, linewidth of silicon signal may also indicate diversity of adjacent atoms.

In alkali aluminosilicate glasses with Si/Al ratio more than one and enough alkali ions to charge-balance aluminum, the glass network consists of tetrahedral aluminum units avoiding each other in accordance with Löwenstein rule distributed in the network of tetrahedral silica. Addition of alkali metals to these glasses leads to depolymerization of silicon while aluminum

remains four-coordinated. If there is not enough alkali metals to charge-balance aluminum, formation of oxygen threeclusters is possible[80].

Alkali phosphosilicate Glasses and Role of Aluminum. Pure glassy SiO_2 consists of tetrahedral connected units. They lead to appearance of NMR peak centered around -112 ppm. Bridging oxygen of silicon units can connect to alkali metals and get depolymerized (one Si-O-Si connection is replace by two NBO). Addition of small percentage (till 8 mol %) of phosphorus to alkali silicate glasses leads to repolymerization of phosphate network: alkali ions leave silicon, which gets higher-coordinated (this is visible in NMR spectra as a shift to more negative frequency). It leads to appearance of Q^0 and Q^1 phosphorus units and indicates P-alkali ions affinity. When more phosphorus is added, it forms metaphosphate network and alkali ions are partially connect back to silicon. With even more phosphorus is present in the composition, the amount of lower-coordinated silicon is decreasing and some Si-O-P linkage occurs, which is visible from the shift of the position of Q^4 silicon signal to more negative ppm. If there is more than 35 m. p. of phosphorus in the structure, octahedral silicon units appear[26,88]. These high-coordinated silicon units are otherwise found only in high-pressure silicates (for example, stishovite). Amount of octahedral phosphorus increases with the amount of alkali metal ions in the composition (because two alkali ions are needed to charge-balance octahedral silicon units[89,90]) and an exact amount depend on the synthesis procedure (fraction of octahedral silicon is higher when oxide melt is cooled slower[26,88]). In alkali phosphosilicate glasses aluminum being added to the glasses is initially six-coordinated and gets four-coordinate upon further addition. Further on, added aluminum decreases amount of octahedral silicon[26].

2.2. Carbon Fibers

Carbon fibers play an important role in modern composite materials. They are anisotropic materials which contain 92-100 wt% of carbon after production[27]. Their combination of strength and low density are especially important for aerospace, automotive and sport industries. The production of carbon fibers is a complex, very energy-demanding process which is still not fully understood. Better understanding of the reaction mechanism might not only allow to produce higher-quality fibers but also adjust the production process to be more efficient and to demand less energy and. In this chapter the manufacturing of carbon fibers and typical comonomers and their proposed role in the polymerization reaction are described.

2.2.1. Carbon Fibers Manufacturing

First carbon fibers were produced by Edison by dissolving cellulosic materials and extruding the resulting mixture through a liquid bath. The resulting filament were then carbonized in the absence of air[46]. Modern carbon fibers production is similar to this and in principle also a process of transformation of carbon-containing precursor into carbonized fibers.

Carbon fibers manufacturing consists of three major steps. First, fibers are formed from a suitable precursor (also so-called precursor-fibers). Then these filaments are stabilized at the temperatures up to 300 °C. Carbonization or/and graphitization is the last step in the production to remove all other elements apart from carbon. Additionally, fibers then might be coated to protect them from environment or to ensure better bonding to the matrix. The process is schematically represented in Figure 23. The production of precursor fibers is responsible for approximately 50% of the resulting costs, stabilization – for about 20% and carbonization for about 15%[46].

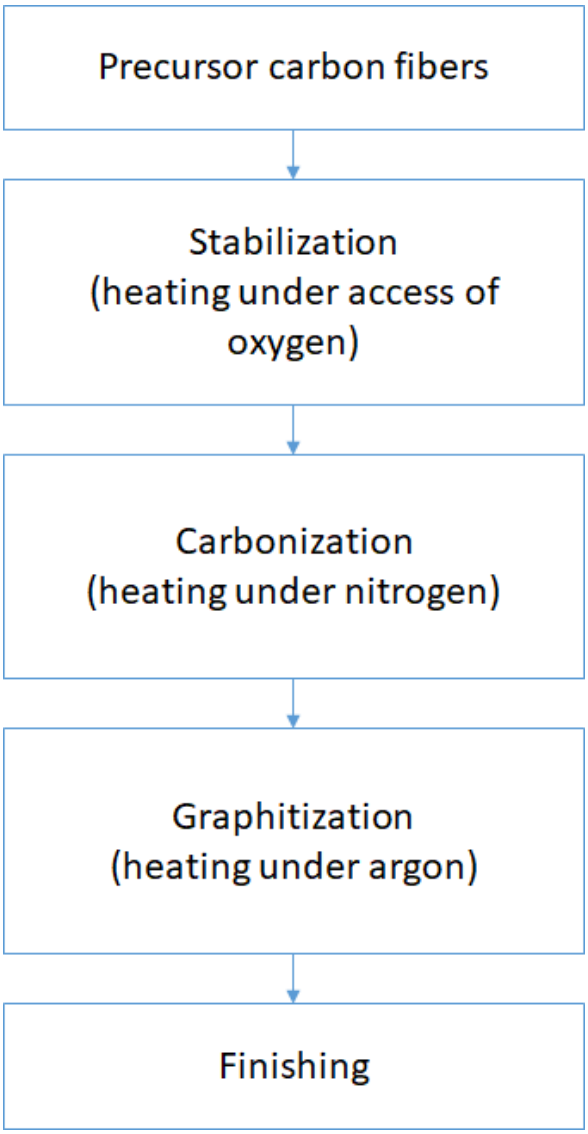

Figure 23. Carbon fibers manufacturing process.

2.2.2. Precursor Carbon Fibers and Comonomers.

Several precursors are used in modern carbon fibers manufacturing industry including petroleum pitch, rayon and polyacrylonitrile (PAN – see Figure 24) with the last taking the highest market share – around 90 %[27,46]. Its popularity is caused by the combination of high carbon yield (above 60 %) and processability, and, subsequently higher quality of the resulting fibers[46,91,92].

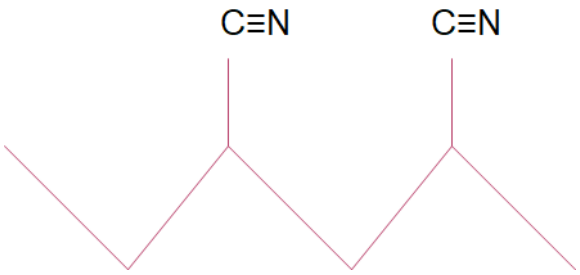

Figure 24. Structure of polyacrylonitrile (PAN).

Different comonomers are added to acrylonitrile to reach better technical properties of the resulting fibers. Its typically contribute up to 5 wp% of the polymer precursor[46]. If the amount of acrylonitrile is lower than 85%, the properties of the resulting fibers are inferior[46]. Pure PAN is not used in the carbon fibers production because the stabilization of the fibers starts rapidly at the high temperature and rather difficult to control[46]. Chosen copolymer mixture is then dry or wet-spun to form precursor carbon fibers to be processed further in the stabilization step. Precursor fibers are semi-crystalline after spinning[46].

Copolymers could be roughly subdivided into neutral and acidic copolymers and have different affect to the final structure. Acidic comonomers such as acrylic acid or itaconic acid are incorporated to the structure via solution or suspension polymerization. They are believed to facilitate reactions in the stabilization step[46]. Another group of copolymers are so-called neutral copolymers such as vinyl acetate, methyl acrylate (MA) or methyl methacrylate[46] which are included by radical polymerization with acrylonitrile[27]. They are believed to not participate much in the polymerization reaction and rather work as plasticizers[46] although an exact role of them is not understood. The resulting properties of the fibers depend strongly on the chosen copolymer mixture[27,47,48].

2.2.3. Stabilization Step

Stabilization of the precursor fibers is the least understood of the production steps. At the same time, it is of crucial importance for the whole production and the properties of the resulting fibers are strongly affected by this step. Stabilization of precursor carbon fibers is a low-temperature heating (up to 300 °C) typically with an air access (although it also could be carried under inert atmosphere[35]) when the fibers are also stretched. It stabilizes the fibers structure so it could later be carbonized at higher temperatures without melting. In practice stabilization might be carried out by applying a constant temperature or by using an oven with

different temperature zones with increasing temperatures. Second way is more widespread in the industry[46].

Although the carbonization step was investigated staring from 1950[93], there is still a lack of the full understanding of the stabilization process[27,33,34,48]. The most widespread theory is decreasing of amount of nitrile group parallel to the appearance of so-called ladder structure of conjugated -C=N-C=N- structures proposed by Burlan and Parson[94] in 1956 based on IR-investigations.

There are many possible reaction mechanisms which can lead to the formation of the ladder structure, intramolecular and intermolecular. They include cyclization, partial and complete tautomerization, isomerization and dehydration. Possible reaction products are represented in Figure 25. Despite many efforts devoted to the investigation of stabilization step[34–45] it is still not clear which reaction mechanism(s) may be dominating and how the polymerization is started – through radicals present in the precursor fibers or through copolymer.

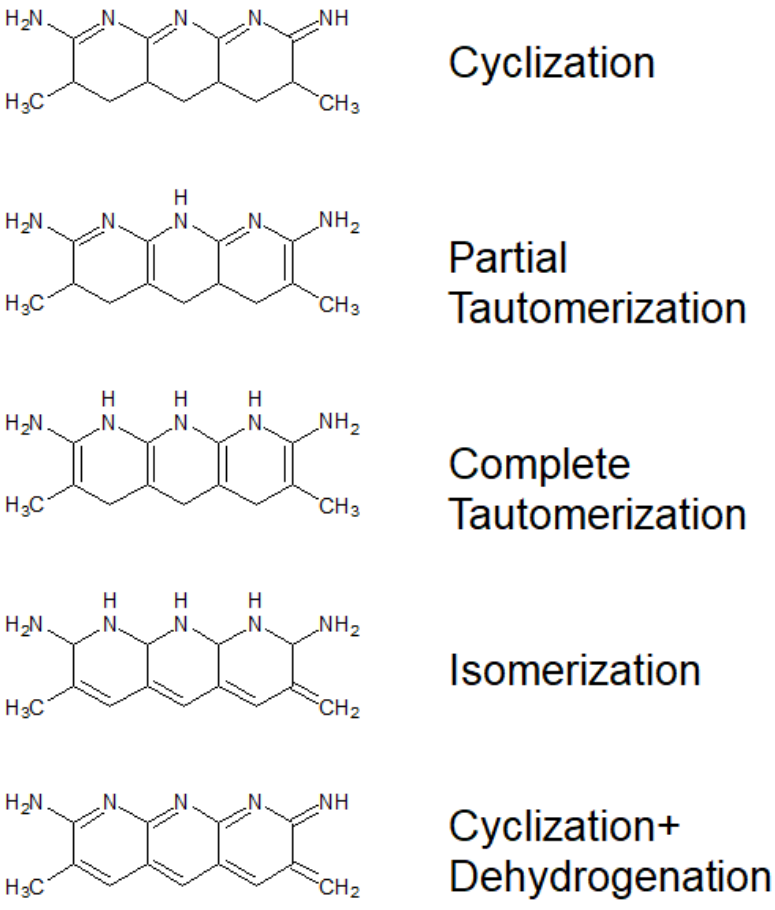

Figure 25. Proposed molecular motifs (right) resulting from different possible PAN polymerization mechanisms (tight).

2.2.4. Carbonization and Graphitization

The aim of carbonization step is to delete all elements except of carbon from the structure. The process is carried out under inert atmosphere. Normally, argon or nitrogen are used. Such as carbonization step requires high temperature in inert atmosphere, it is often carried out consequently in two different ovens – low temperature oven (up to 1000 °C) and the high temperature oven (up to 1500 °C). To obtain high modulus fibers, further heating up to 2500 °C is needed. The graphite crystallites are getting more and more ordered after heating which leads to improved mechanical properties.

The properties of the fibers depend strongly on the ordering and, therefore, temperatures applied during carbonization and graphitization step. Carbon fibers might be divided into high-tensile-strength (HT), intermediate-modulus (IM), high-modulus (HM) and ultrahigh-modulus (UHM) fibers. Their ordering according to the temperatures used is represented in Table 2.

Carbon fiber type	Heat treatment temperature (°C)	Crystallite orientation	Long-distance order	
Type I high modulus	>2,000	Mainly parallel to the fiber axis	High	UHM
				HM
Type II high strength	≈1,500	Mainly parallel to the fiber axis	Low	IM HT
Type III isotropic	<1,000	Random	Very low	Isotropic

Table 2. Classification of carbon fibers[95].

The fibers obtained after the final heat treatment consist mostly of carbon (92-100 wp). In crystalline part it is arranged sp^2-hybridized carbon atoms. Although many different characterization techniques were used to define the functional groups on the surface of carbon fibers including X-ray photoelectron spectroscopy (XPS)[96], X-ray diffraction (XRD)[97], Raman spectroscopy[98], Augler electron spectroscopy (AES) it is still not clear which functional groups might cover the surface of the carbon fibers.

2.2.5. Finishing Treatment

After heat treatment the oxidation of the fibers follows. This is important for further better adhesion of fibers to the matrix. Gas phase oxidation using mixture of inert gases and oxygen, liquid phase oxidation using different substances or anodic oxidation might be applied. The

last one is the most wide-spread currently in the industry[46]. Alternatively, fibers might be treated with plasma or crystals might be grown on the surface of the fibers to ensure better adhesion to the matrix[46].

After oxidation the surface of the fibers is washed and covered by a thin layer of lubrication or/and epoxy resin to improve mechanical properties, protect from environment and to ensure better bonding with the matrix. This might be done by solution deposition, electrodeposition, electropolymerization or by using plasma when solution deposition is the most wide-spread technique[46]. The choice of the sizing coverage might affect further bonding with the matrix and, subsequently, resulting properties of composite materials.

2.2.6. Recycling of Carbon Fibers

Such as the production of carbon fibers is very energy and time-demanding process, recycling and re-use of carbon fibers might open new ways to save financial expenses and to reduce waste being released during manufacturing. Such as carbon fibers are mostly used in combination with matrix, mostly with thermoset resins, one of the main challenges is the separation of the matrix from the fibers. The fibers might be then used in further applications. Many different separation procedures including thermal, mechanical, chemical and inductive were proposed and attempted although industry-scale recycling process is still under development[99,100]. Mechanical recycling involves crushing of CRFP and division of the resulting fragments into matrix phase and carbon phase[101,102]. Thermal decomposition or pyrolysis involves heat treatment of CFRP in an inert atmosphere[103,104]. In chemical method the matrix is attacked by reactive compounds (e. g. benzyl alcohol) at medium (up to 350 °C) temperatures[105,106]. Inductive recycling is the novel method allowing retaining of an original geometry[107]. Recycled fibers might then be used as aligned, chopped or milled fibers. The quality of recycling is mostly controlled by microscopy to find out how effective the separation of fibers from the matrix was and by mechanical tests although with this method it is difficult to define how the functionalities on the surface of the fibers have changed with recycling process which might be crucially important for the following adhesion with the new matrix[100,108,109].

3. Experimental

In this chapter first the details to the synthesis of two investigated glass system are given. Then the important parameters of relevant nuclei and the details of solid-state NMR experiments and pulse sequences used in this work are described.

3.1. Synthesis

3.1.1. Phosphorus-Rich System

Two glass series $60P_2O_5$-$30Na_2O$-$10SiO_2$ (P60 glasses) and $50P_2O_5$-$16.6Na_2O$-$33.3SiO_2$ (P50 glasses) were prepared. About 6 g of appropriate amounts of SiO_2, $Al(PO_3)_3$, $NH_4H_2PO_4$ and $NH_4H_2PO_4$ were mixed before heating. To facilitate acquisition of NMR spectra $MnCO_3$ (0.01 w. p.) was added to the glass compositions to decrease relaxation times. The mixtures were then slowly heated to 800 °C in platinum crucible to decompose the ammonium dihydrogen phosphate precursor. Then the mixtures were melted at 1200 °C for 1 h and quenched to room temperature between two copper plates. Due to high phosphorus content, these glasses might react with water in the atmosphere despite of high aluminum content. The samples therefore were stored inside a desiccator and solid state NMR measurements were carried out using nitrogen as bearing and driving gas. The compositions of investigated glasses are shown in Table 3.

P60 Series				
Glass	**P_2O_5**	**Na_2O**	**SiO_2**	**Al_2O_3**
P60_noAl	60.00	30.00	10.00	0.00
P60_3Al	58.20	29.10	9.70	3.00
P60_6Al	56.40	28.20	9.40	6.00
P60_8Al	55.20	27.60	9.20	8.00
P60_10Al	54.00	27.00	9.00	10.00
P60_13Al	52.20	26.10	8.70	13.00
P60_15Al	51.00	25.50	8.50	15.00

P50 Series				
Glass	**P_2O_5**	**Na_2O**	**SiO_2**	**Al_2O_3**
P50_noAl	50.00	16.67	33.33	0.00
P50_0.25Al	49.88	16.63	33.25	0.25
P50_1Al	49.50	16.50	33.00	1.00
P50_3Al	48.50	16.17	32.33	3.00
P50_6Al	47.00	15.67	31.33	6.00
P50_8Al	46.00	15.33	30.67	8.00
P50_10Al	45.00	15.00	30.00	10.00
P50_13Al	43.50	14.50	29.00	13.00
P50_15Al	42.50	14.17	28.33	15.00

Table 3. Nominal compositions of two series of phosphorus-rich glasses.

To carry out dipolar based NMR experiments between silicon and other nuclei, five samples with 100%-enriched $^{29}SiO_2$ using total initial oxide mixture of 1.5 g were prepared following the procedure explained above. Names and nominal composition of these glasses are represented in Table 4.

Glass	**P_2O_5**	**Na_2O**	**SiO_2**	**Al_2O_3**
P60_3Al_Si	58.20	29.10	9.70	3.00
P60_15Al_Si	51.00	25.50	8.50	15.00
P50_noAl_Si	50.00	16.67	33.33	0.00
P50_3Al_Si	48.50	16.17	32.33	3.00
P50_10Al_Si	45.00	15.00	30.00	10.00

Table 4. Nominal compositions of the glasses prepared with 100%-enriched ^{29}Si.

To prove whether the structural units of the enriched glasses are similar to the corresponding units in glasses of P50 and P60 series and that the results obtained from enriched glasses could be generalized, *ex-situ* ^{27}Al, ^{31}P and ^{29}Si single pulse excitation experiments were carried out on enriched glasses (see Appendix 1). The glasses prepared with enriched silicon exhibit the same structural units as non-enriched glasses in one-dimensional NMR spectra.

3.1.2. Silicon-Rich System

Synthesis. Series of glasses with 50, 55.5, 60 and 70 molar percent of SiO_2 and the rest evenly divided between Al_2O_3 and Na_2O were synthesized at the University of Jena. To these base compositions, 2.5-7.5 % of P_2O_5 was added by substituting equal amount of aluminum and sodium oxides to investigate the effect of phosphorus incorporation into glass structure. The nominal compositions of the glasses are shown in Table 5. SiO_2, $NaPO_3$, Na_2CO_3 and $Al(OH)_3$ were used as precursors for the glasses and were ground together with help of Al_2O_3 balls. The mixtures then were slowly heated and melted in aluminum crucible to 1600 °C for 1 h and then rapidly cooled down in air. Prepared glasses were subsequently annealed at 740 °C (below Tg) to decrease mechanical stresses resulting from rapid cooling.

Probe Name	**SiO_2**	**P_2O_5**	**Al_2O_3**	**Na_2O**
Si50_P0	50	0	25	25
Si50_P7.5	50	7.5	21.25	21.25
Si55.5_P7.5	55.5	7.5	18.5	18.5
Si60_P0	60	0	20	20
Si60_P2.5	60	2.5	18.75	18.75
Si60_P5	60	5	17.5	17.5
Si60_P6.25	60	6.25	16.875	16.875
Si60_P7.5	60	7.5	16.25	16.25
Si70_P0	70	0	15	15

Si70_P7.5	70	7.5	11.25	11.25

Table 5. Nominal compositions of investigated glasses of silicon-rich system.

To decrease relaxation times and facilitate the acquisition of NMR spectra a sample with nominal composition $60SiO_2$-$7.5P_2O_5$-$16.25Al_2O_3$-$16.25Na_2O$ and $MnCO_3$ (0.01 w. p.) was prepared in aluminum crucible at 1600 °C using total of 6 g of SiO_2, $NH_4H_2PO_4$, Na_2CO_3 and Al_2O_3 as precursors (Si60_P7.5(A) glass). To prove whether addition of manganese and annealing affect the local environment of structural units, *ex-situ* ^{27}Al, ^{31}P and ^{29}Si single pulse excitation experiments were carried out on this glass (see Figure 128 in Appendix 1).

To be able to carry out dipolar-based NMR experiments between silicon and other nuclei the glass with nominal composition $60SiO_2$-$5P_2O_5$-$17.5Al_2O_3$-$17.5Na_2O$ (Si60_P5_Si glass) and $MnCO_3$ (0.01 w. p.) was prepared in aluminum crucible at 1600 °C using total of 0.75 g of 100%-enriched $^{29}SiO_2$, $NH_4H_2PO_4$, Na_2CO_3 and Al_2O_3 as precursors. To check whether the local environment of aluminum, phosphorus and silicon nuclei is similar those in non-enriched glasses, *ex-situ* ^{27}Al, ^{31}P and ^{29}Si single pulse excitation experiments were carried out on this enriched glass (see Figure 131 in Appendix 2). The glasses prepared with enriched silicon exhibit the same structural units as non-enriched glasses in one-dimensional NMR spectra.

3.1.3. Industrially Produced Carbon Fibers

Preparation row. To probe the applicability of NMR to the investigation of carbon fibers, industrially produced samples of carbon fibers at different production stages named A410-A419 were obtained from the group of Prof. Dr. Horn starting from precursor PAN fibers to finished carbon fibers (Table 6). The samples are shown in Figure 26.

Sample	**Manufacturing Step**
A410	PAN-Fibers
A 411	Stabilization step 1
A 412	Stabilization step 2
A 413	Stabilization step 3
A 414	Stabilization step 4

A 415	Stabilization step 5
A 416	Stabilization step 6
A 417	Carbonization step 1
A 418	Carbonization step 2
A 419	Final fibers

Table 6. Industrially produced carbon fibers used for NMR investigations.

Figure 26. Industrially produced carbon fibers from A410 (left) to A419 (right).

Fibers having different surface treatment. Industrially produced carbon fibers having different finishing treatment – untreated, oxidized and oxidized and sized fibers were obtained from the group of Prof. Dr. Horn to attempt solid-state NMR.

Recycled Fibers. To investigate application of NMR to the analysis of recycling process, samples of original carbon fibers and the fibers recycled chemically and inductively were obtained from the group of Prof. Dr. Horn.

3.1.4. ^{15}N enriched PAN and test substances

Low natural abundance of N^{15} isotopes (0.4%) and low gyromagnetic ratio of N^{15} nuclei (19.4 γ 10^6 rad s^{-1} T^{-1}) make it rather difficult nuclei to study by means of solid state NMR. That is why our cooperation partner in the team of Dr. Klaus Ruhland prepared N^{15}-enriched PAN copolymer and N^{15} enriched Test substances (TS1 and TS2 - 1-Amino-2,4-dicyano-6-methylcyclohexene), the structure of which is represented in Figure 27.

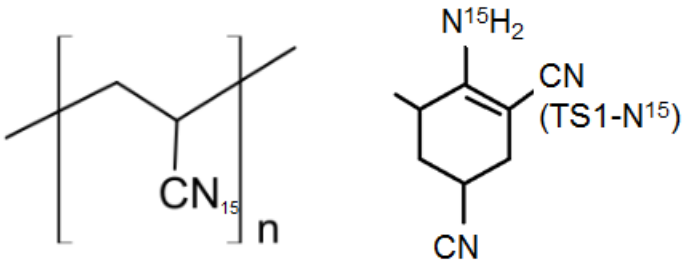

Figure 27. Structure of PAN (left) and test substances 1-Amino-2,4-dicyano-6-methylcyclohexene (right).

Polyacrylonitrile was synthesized using free radical solution polymerization procedure. The details of synthesis of ^{15}N-enriched PAN can be found in the literature[110]. As proved by IR, the resulting degree of enrichment of ^{15}N atoms is as least 98%[110].

After synthesis, PAN copolymers were heated using Simultaneous Thermal Analysis (STA) 449 F3 Jupiter. The TG-DTA sample carrier with 0.3 ml Al_2O_3 crucibles was used to heat the PAN powder samples with a rate of 5 K/min under inert atmosphere of helium. Samples heated to 268 °C, 295 °C and 395 °C were called PAN 268, PAN 295 and PAN 395, respectively. The samples were transferred to a Schlenk tube immediately after heating, transferred to argon glove box and then packed to rotors in the glove box. Dry N_2 gas was used as driving and bearing gas during NMR experiments.

The details of synthesis of the test substances, produced by cooperation partner in the team of Dr. Klaus Ruhland and the exact details might be found in the literature[110].

3.1.5. Deuterated Samples

Copolymers for deuterated samples were produced by cooperation partner in the team of Dr. Klaus Ruhland. Polymerization of copolymers was done by using free radical solution polymerization procedure[111].

3.1.6. Double-Enriched PAN-MA Copolymer

Copolymers for double enriched PAN-MA samples were produces by cooperation partner in the team of Pr. Dr. Klaus Ruhland[111]. Polymerization of copolymers was carried by using free radical solution polymerization procedure.

3.1.7. AN-co-AAM Sample

AN-co-AAM (acrylonitrile copolymer with 9 mol % of acrylamide) with ^{15}N-enriched AAM samples were produces by cooperation partner in the team of Dr. Klaus Ruhland[111].

3.2. NMR Analysis

In Table 7 and Table 8 the overview of the nuclei, measured in this work, is given. The measurements were performed on a Bruker Avance III 300 MHz (operating at 7 T) or Varian VNMRs 500 (operating at 11 T) spectrometers using double or triple resonance probes. Typically, 1.6 mm rotors made from zirconium oxide were used for the measurements in 11 T field and 4 mm zirconia rotors were used for the measurements in 7 T field. Glass samples were milled to fine powder and then filled in the rotors. Vespel caps were used to close the rotors tightly. The rotors were rotated by applying nitrogen as bearing and driving gas to prevent contact of hydrophilic phosphorus glasses with water in the air. The sample were stored in desiccator or in the glove box.

	^{31}P	^{27}Al	^{29}Si	^{23}Na
Spin number, I	1/2	5/2	1/2	3/2
Gyromagnetic ratio, 10^{-7} T s^{-1}	10.8	6.9	-5.3	7.0
Natural abundance, %	100	100	4.7	100
Reference	85% H_3PO_4 (0 ppm)	1 molar $Al(NO_3)_3$ (0 ppm)	TMS (tetramethylsilane) (0 ppm) using TTMS (tetrakis(trimethylsilyl)silane) as external standard	1 molar NaCl (0 ppm)

			(-9.8 ppm)	
Larmor frequency in 7 T, MHz	121.4	78.2	59.6	79.3
Larmor frequency in 11 T, MHz	202.4	130.3	99.3	132.3

Table 7. Overview of the important characteristics of nuclei measured in the glass system.

	^{13}C	^{15}N	^{1}H	^{2}D
Spin number, I	1/2	1/2	1/2	3/2
Gyromagnetic ratio, 10^{-7} T s^{-1}	67.3	-27.1	267.5	41.2
Natural abundance, %	1.1	0.4	99.98	0.02
Reference	adamantane ($\delta(CH_2)$ 38.5 ppm)	Glycine ($\delta(N)$ -346.8 ppm)	adamantane ($\delta(CH_2)$ 1.75 ppm)	Acetone-d_6 (2 ppm)
Larmor frequency in 7 T, MHz	75.4	30.4	300.0	46.1
Larmor frequency in 11 T, MHz	125.7	50.7	500.0	76.7

Table 8. Overview of the important characteristics of nuclei measured in the PAN fibers, precursors, test substances and comonomers.

Simulation of NMR spectra. To define fractional areas and values of chemical shift, the spectra were simulated with DMFIT NMR software[112]. Isotropic chemical shifts and fractional areas of

silicon and phosphorus signal were estimated by modelling the spectra using Gaussian/Lorentzian peaks and considering all spinning sidebands. For aluminum, isotropic chemical shift was defined by simulating spectra with Czjzek model[113] using DMFIT program (a model where the spread of quadrupolar parameters is considered through a joint probability density function of the parameters C_q and η_q). Static phosphorus spectra were fitted using "CSA static" model.

REDOR and REAPDOR Measurements[3,6,7]. In REDOR-measurements, the echo-pulses were applied on S channel and in REAPDOR-measurements on I-channel to ensure maximal reintroduction of dipole-dipole coupling as described in 1.2.3. In REAPDOR, a pulse having length of $T_r/3$ was used on S-channel. RF amplitudes for this pulse were defined on liquid standards. The results of REDOR and REAPDOR experiments were then analyzed using SIMPSON simulation software[114].

Exemplary simulation of ^{29}Si{^{31}P}-REDOR curves with SIMPSON software showed that, although high deviation of pulse lengths from π-values and high offsets on both channels may strongly effect the results of ^{29}Si{^{31}P}-REDOR, CSA values and offset on the observed channel have the highest effect in REDOR evolution curves (see Appendix 3). Therefore, if these parameters were known, they were considered in SIMPSON simulations.

Such as an exact geometry of spins was not known, two-spin approximation was used for SIMPSON simulations: effective dipolar coupling was calculated using $D_{eff} = \sqrt{n}D_{ind}$, where D_{ind} is dipolar coupling between one pair of nuclei and n is the amount of S nuclei around a measured I nucleus[66]. This approximation delivers results close to multiple-dipole simulation until $\frac{\Delta S}{S_0}$ values of approximately 0.5 as shown by exemplary simulations of ^{19}Si{^{31}P}-REDOR on 4-spin system (one silicon atom and three phosphorus atoms) and 6-spin system (one silicon atom and five phosphorus atoms) with SIMPSON software (see Appendix 4).

3.2.1. Phosphorus-Rich System

Standard *ex-situ* single pulse acquisition (Bloch decay) ^{27}Al-, ^{29}Si- and ^{31}P-MAS NMR experiments were performed on a Bruker Avance III 300 MHz (7 T) spectrometer or a Varian VNMRs 500 (11 T) spectrometer at MAS spinning frequencies of 10 kHz. As probes a Bruker 4 mm triple or double resonance probe and a Varian 1.6 mm T^3 MAS probe were used. The spectra were recorded with repetition times of typically 60 s, 1 -3 s and 20 s for ^{29}Si, ^{27}Al and

^{31}P with typical pulse lengths of 7 µs, 1.25 µs and 5 µs, respectively. Relaxation delays of ^{31}P and ^{27}Al were defined by inversion recovery and saturation recovery experiments, respectively. For the detection of the ^{29}Si signals, the acquisition was preceded by a 15-20*π/2-saturation comb. DMFIT software was used to deconvolute individual peak contributions as discussed above[112].

^{31}P MAT spectra were measured by Dr. Schiffmann at 200 Hz with typical flipping-pulses lengths of 4 us for ^{31}P using the pulse sequence published by Gan in 1992 [71] as shown in Figure 28. The spectrum was sheared after the measurement.

^{27}Al{^{31}P}-REDOR-[3–5] and ^{31}P{^{27}Al}-REAPDOR NMR experiments were performed at the Varian VNMRs spectrometer employing a 1.6 mm T^3 MAS probe with typical spinning speeds of 10 kHz. Typical π-pulse lengths of 6 µs for ^{27}Al and 5.5 µs for ^{31}P were used in REDOR, in REAPDOR the adiabatic passage pulse length (^{27}Al) was set to 33 µs, employing a RF amplitude of 42 kHz.

The ^{27}Al{^{29}Si}-REDOR, ^{29}Si{^{27}Al}-REAPDOR, ^{31}P{^{29}Si}-REDOR and ^{29}Si{^{31}P}-REDOR NMR were performed on a Bruker Avance 300 MHz (7 T) spectrometer at typical spinning speeds of 10 kHz. Typical π-pulse lengths of 10-12 us for ^{31}P and ^{27}Al and 16 us for ^{29}Si were used in REDOR, in REAPDOR the adiabatic passage pulse length (^{27}Al) was set to 33 µs employing typical RF amplitudes of 47 kHz. For the dipolar based experiments where silicon signal was obtained on the observed channel, relaxation times of ^{29}Si were defined on the samples with the smallest amount of aluminum in the structure (P50_noAl_Si - about 30 s) and then 3-5 of relaxation time was used as waiting time for the sample series.

For the high temperature *in situ* MAS NMR experiments, a novel home-build setup was used. Controlled continuous-wave irradiation on ^{1}H channel was used to induce an inductive heating of platinum inserts inside a 4 mm rotor. Power of ^{1}H radiation was calibrated using chemical shift of ^{79}Br of KBr[115]. That allowed MAS NMR at temperatures of up to 770 °C at MAS frequencies of up to 10 kHz[116]. For the high temperature ^{27}Al- and ^{31}P-MAS NMR experiments reported here, typically spinning frequencies of 6 – 8 kHz were used. Repetition times of 1 s (^{31}P) and 0.1 s (^{27}Al) were used for the samples at temperatures above T_g to underline glass part of the network and to filter out, if there, crystalline part (crystalline part, if there, tends to have longer relaxation times).

3.2.2. Silicon-Rich System

Standard *ex-situ* single pulse acquisition (Bloch decay) ^{27}Al-, ^{23}Na ^{29}Si- and ^{31}P-MAS NMR measurements were carried out on a Bruker Avance III 300 MHz (7 T) respectively at typical MAS spinning speeds of 10 kHz. The spectra were recorded with typical pulse lengths of 1 us, 1 us, 7 us and 6 us and repetition times of 1 s, 1 s, 200 s and 200 s for ^{27}Al-, ^{23}Na ^{29}Si- and ^{31}P, respectively. Relaxation delays of ^{31}P and ^{27}Al and ^{23}Na were defined by inversion recovery and saturation recovery experiments, respectively. For the detection of the ^{29}Si signals, the acquisition was preceded by a 15-20*π/2-saturation comb. Due to the low molar percentage and long relaxation times, it was difficult to measure T_1 of individual components of phosphorus signals and all signals were treated as one peak when defining relaxation times in inversion-recovery experiment.

The ^{31}P{^{23}Na}-REAPDOR NMR experiment was performed at Bruker Avance III 300 MHz (7 T) at MAS speeds of 10 kHz. π-pulse lengths of 9 µs for ^{31}P were used; the adiabatic passage pulse length (^{23}Na) was set to 33 µs, employing RF amplitude of 42 kHz.

^{31}P MAT spectrum was measured by Dr. Schiffmann at 200 Hz with typical flipping-pulses lengths of 4 us for ^{31}P using the pulse sequence published by Gan in 1992 [71] as shown in Figure 28. The spectrum was sheared after the measurement.

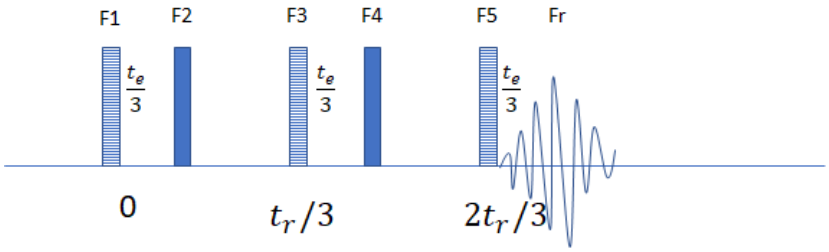

F1	F2	F2	F4	F5	Fr
-Y	Y	-Y	Y	-Y	X
-Y	-X	-Y	-X	-Y	-X
-Y	Y	-Y	-X	-Y	-X
-Y	X	Y	-Y	-Y	X

Figure 28. Pulse sequence and phases of MAT sequence.

^{31}P M_2 measurements were carried out by measuring static spin echo on at Bruker Avance III 300 MHz (7 T) using π-pulse lengths of 10 us with delays times of 350 s (typical relaxation delays of about 60-75 seconds were measured for several probes in this row).

^{27}Al MQMAS [1,2] measurements were carried out at Varian VNMRs 500 (11 T spectrometer) at MAS spinning frequency of 25 kHz applying Z-filtering [69]. Two preparation pulses having pulse lengths 1 and 3 us and "soft" selective pulse having length of 22 us were used in the pulse sequence. Such as MQMAS experiments are very susceptible to the magic angle settings, magic angle was optimized bevor each measurement using potassium bromide.

The $^{27}Al\{^{31}P\}$-REDOR-[3–5] and $^{31}P\{^{27}Al\}$-REAPDOR [3,6,7] NMR experiments were performed at Bruker Avance III 300 MHz (7 T) at MAS speeds of 10 kHz. Typical π-pulse lengths of 10 µs for ^{27}Al and 11 µs for ^{31}P were used in REDOR, in REAPDOR the adiabatic passage pulse length (^{27}Al) was set to 33 µs, employing typical RF amplitudes of 45 kHz.

The $^{29}Si\{^{31}P\}$-REDOR-[3–5] and $^{31}P\{^{29}Si\}$-REDOR[3,6,7] NMR experiments of Si-rich glasses were performed at Bruker Avance III 300 MHz (7 T) at MAS speeds of 10 kHz employing relaxation delays of 75 s and 40 s for ^{29}Si and ^{31}P, respectively. π-pulse lengths of 14.5 µs for ^{29}Si and 11.5 µs for ^{31}P were used. Relaxation delays for ^{29}Si were defined by inversion recovery experiment to be about 20 s and 3-5 multiple od this time was used in experiment as waiting time between scans.

The $^{29}Si\{^{27}Al\}$-REAPDOR-[3–5] and $^{27}Al\{^{29}Si\}$-REDOR[3,6,7] NMR experiments of Si-rich glasses were performed at Bruker Avance III 300 MHz (7 T) using XY8 phase cycling at MAS speeds of 10 kHz employing relaxation delays of 75 s and 1 s for ^{29}Si and ^{27}Al, respectively. π-pulse lengths of 17 µs for ^{29}Si and 11.5 µs for ^{27}Al were used REDOR, in REAPDOR the adiabatic passage pulse length (^{27}Al) was set to 33 µs, employing RF amplitudes of 44 kHz.

For the high temperature *in situ* MAS NMR experiments, a novel home-build setup developed by H. Kirchhain was used[116]. Typically spinning frequencies of 6 – 8 kHz were used. Repetition times of 1 s for ^{27}Al and ^{23}Na were used for the samples as defined by saturation recovery experiment. Occasionally, longer relaxation times were used to be able to detect, if present, crystalline phases.

3.2.3. ^{15}N labelled PAN and Test Substances

^{1}H-{^{13}C}, ^{1}H-{^{15}N} cross polarization (CPMAS) of PAN and model compounds TS1 and TS2 were performed at the Varian VNMRs spectrometer operating at 11.7 T, employing a 1.6 mm T^{3} MAS probe. Recycle delays of 10-20 s for were used as 3-5 multiple of relaxation times measured with inversion recovery experiments.

^{15}N-MAS-NMR spectra and ^{1}H-{^{13}C} and ^{1}H-{^{15}N} CPMAS NMR spectra of PAN, PAN300 and PAN400 were recorded on a Bruker Advance III 300 MHz spectrometer employing a 4-mm MAS probe with resonance frequencies of were 30.4 MHz, 75.7 MHz and 300.23 MHz for ^{15}N, ^{13}C and ^{1}H, respectively. Recycle times of 10 - 20 s (as 3-5 multiple of T1 time measured with inversion recovery) and 300 s (as supposed by saturation recovery experiments) were used for the CPMAS experiments and ^{15}N single pulse experiments, respectively. Chemical shifts are referenced to adamantane ($\delta(CH_2)$ = 38.5 ppm) for ^{13}C and glycine (δ(N) = -346.8 ppm) for ^{15}N. Typical spinning speeds of 8.0 to 10.0 kHz were used in all experiments. Deconvolution of the spectra was performed employing the DMFIT software package by Massiot et al[112].

^{13}C{^{15}N} REDOR measurements of PAN, TS1 and TS2, PAN300 and PAN400 were performed on a Varian VNMRs spectrometer employing recycle delays of 10-20 s under typical spinning speeds of 8-16 kHz. Typical π-pulse lengths of 6 µs for ^{15}N and 4.4 µs for ^{13}C were used. Spectra were simulated using SIMPSON software [114]. To facilitate acquisition of NMR spectra, the magnetization of carbon nuclei was prepared by magnetization transfer from proton nuclei.

3.2.4. Industrially Produced Carbon Fibers

When investigation of carbon fibers before carbonization could be carried without dilution (they are not conductive) the samples of conductive fibers must be diluted with non-conductive material to enable spinning in high magnetic field. Therefore, conductive fibers (A416-A419) have been diluted with silicon dioxide which was previously calcined at 800 °C for 24 h to remove water. Zirconia cap and rotor were used to avoid ^{1}H and ^{13}C signal from the rotor or the cap. To eliminate background signal spin-echo pulse sequence (4 rotor cycles) was used to record ^{1}H spectra. Typical π-pulse lengths of conductive fibers differ much from the π-pulse lengths of non-conductive materials and therefore were define individually for each conductive sample. ^{1}H spectra were recorded at a Bruker Advance III 300 MHz employing recycle delays of 10-20 s under typical spinning speeds of 5-10 kHz with typical π-pulse lengths

of 10-15 us. Relaxation times of hydrogen were obtained using inversion-recovery experiments.

^{1}H-{^{13}C} CPMAS spectra were recorded at a Bruker Advance III 300 MHz employing recycle delays of 3-5 s as 3-5 multiple of t1 measured with inversion recovery under spinning speeds of 10 kHz with typical π-pulse lengths of 10-15 us.

Spin-echo ^{13}C MAS NMR were recorded using on a Varian VNMRs spectrometer employing recycle a 5-mm MAS probe. Recycle delays of 30 s (implied by saturation recovery test measurements) under typical spinning speeds of 5-10 kHz were used.

3.2.5. Deuterated Samples

^{1}H-{^{13}C} and ^{1}H-{^{2}H} CPMAS NMR were performed at Bruker Advance III 300 MHz spectrometer employing a 4-mm MAS probe. Recycle delays of 10-20 s and typical spinning speeds of 6-10 kHz were used. Cq values were fitted using DMFIT software [112].

One pulse ^{2}H measurements and ^{1}H-{^{2}H} and ^{1}H-{^{13}C} CPMAS NMR measurements of heated and unheated D4 sample were done on a Varian VNMRs spectrometer employing recycle delays of 20-50 s and 10-20 s (3-5 of T1) under typical spinning speeds of 25 kHz and 6-10 kHz, respectively.

3.2.6. Double-Enriched PAN-MA Copolymer

^{1}H-{^{13}C} and ^{1}H-{^{15}N} CPMAS NMR were performed on at a Varian VNMRs spectrometer operating at 11.7 T, employing a 1.6 mm T^{3} MAS probe. Recycle delays of 10-20 s were used. Recovery times were defined by inversion recovery experiments. Lowest possible spinning speeds of 6-7 kHz were used to observe maximum spinning sidebands to define CSA tensors. For ^{1}H-{^{13}C} and ^{1}H-{^{15}N} CPMAS typical spinning speeds of 8-12 kHz were used (spinning speeds were varied to distinguish signals from possible sidebands.

^{13}C and ^{15}N single pulse quantitative experiments were carried out at a Varian VNMRs spectrometer operating at 11.7 T, employing a 1.6 mm T^{3} MAS probe with spinning speeds of 12 kHz and recycle delays of 200 s to obtain quantitative spectra.

^{1}H-{^{15}N} CPMAS HETCOR was carried out at a Varian VNMRs spectrometer operating at 11.7 T, employing a 1.6 mm T^{3} MAS probe. Recycle delays of 10-20 s were used. The contact time in ^{1}H-{^{15}N} HETCOR was varied to ensure that only direct ^{1}H-^{15}N connections are seen.

$^{13}C\{^{15}N\}$ REDOR measurements of PAN-MA samples were performed on a Varian VNMRs spectrometer employing recycle delays of 10-20 s under typical spinning speeds of 8-16 kHz. Typical π-pulse lengths of 5.25 μs for ^{13}C and 9 μs for ^{15}N were used. Spectra were simulated using SIMPSON software [114]. To facilitate acquisition of NMR spectra, the magnetization of carbon nuclei was prepared by magnetization transfer from proton nuclei.

$^{13}C\{^{15}N\}$ CPMAS HETCOR was carried out at a Varian VNMRs spectrometer operating at 11.7 T, employing a 1.6 mm T^3 MAS probe. Recycle delays of 10-20 s were used. The mixing time in $^{13}C\{^{15}N\}$ CPMAS HETCOR was varied and optimized on test samples (double-enriched glycine) to ensure that only direct ^{13}C-^{15}N connections are seen. To facilitate acquisition of NMR spectra, the magnetization of carbon nuclei was prepared by magnetization transfer from proton nuclei.

3.2.7. AN-co-AAM Sample

^{1}H-$\{^{13}C\}$, ^{1}H-$\{^{15}N\}$ CPMAS were performed at a Bruker Advance III 300 MHz spectrometer employing a 4-mm MAS probe. Recycle delays of 10-20 s (as 3-5 multiple of T1 times defined by inversion recovery experiments) and typical spinning speeds of 6-10 kHz were used.

3.2.8. NMR of Fibers Having Different Treatment and of Recycled Fibers

Conductive nature of industrially produced carbon fibers hindered their rotation in spectrometer if not milled to a powder. Although for the fibers which are already conductive the finer size of the powder leads to the higher resulting signal, there is a danger of too fine milling when the investigated sample does not retain its morphology. With electron microscopy it was found that the samples should be milled by hand to retain fiber-like shape.

To eliminate background signal spin-echo pulse sequence (4 rotor cycles) was used to record ^{1}H spectra. ^{1}H MAS spectra were recorded at a Bruker Advance III 300 MHz spectrometer employing a 1.3-mm MAS probe. Recycle delays of 10-20 s and typical spinning speeds of 35 kHz were used to decrease homonuclear dipole-dipole coupling.

Spin-echo ^{13}C MAS NMR were recorded using on a Varian VNMRs spectrometer employing a 5-mm MAS probe. Recycle delays of 30 s under typical spinning speeds of 5-10 kHz were used.

^{1}H-$\{^{13}C\}$ CPMAS spectra were recorded at a Bruker Advance III 300 MHz employing recycle delays of 35 s under spinning speeds of 10 kHz with typical π-pulse lengths of 10-15 us.

^{1}H-{^{13}C} HETCOR was carried out at a Bruker Advance III 300 MHz, employing a 4 mm MAS probe. Recycle delays of 10-20 s were used.

4. Results and Discussion

In this chapter, the results of structural characterization of two investigated alkali phosphoaluminosilicate glass systems are shown and discussed. It is known that the addition of aluminum to alkali phosphate glasses leads to higher chemical and mechanical stability. On the other side, addition of silicon to phosphate glasses with a certain composition may result in formation of SiO_5 and SiO_6 which also leads to better mechanical properties. Effect of aluminum addition incorporation in the phosphor silicate glass system already having SiO_6 is studied in the first part of this chapter. First, alkali silicophosphate system with high phosphorus constituent (50-60 molar percent) and its structural transformation upon addition of aluminum at room temperature is discussed. Then dynamics of glass network is observed and analyzed using high-temperature MAS NMR.

In the second part of this chapter alkali aluminosilicate system and its transformation upon addition of small amount of phosphorus is described. These glasses are important for geological studies due to the similarity of the chemical composition to those of magma. Furthermore, added phosphorus increases processability of the glasses. Structural units of phosphorus and role of aluminum as network former and network modifier was followed upon addition of phosphorus (up to 7.5 m. p.) at several base glasses with 50 to 70 m. p. of SiO_2 and the rest equally divided between Al_2O_3 and Na_2O. Additionally, the dynamics of glasses was investigated by high-temperature in-situ MAS NMR.

4.1. Phosphorus-Rich System

In this part two alkali silicophosphate glass systems with high molar percentages of phosphorus (50-60 m. p.) and their structural transformation upon addition of aluminum are investigated. From previous research, it is known that presence of six-coordinated silicon, which normally appears only in high-pressure glasses, is expected in this glass-forming region[25,26,88,117]. Furthermore, it is known that small amount of aluminum added to phosphate glasses leads to aluminum being mostly six-coordinated (see 2.1.2). We hoped that the addition of aluminum to the structure will lead to the increase of the overall amount of high-coordinated species, which therefore might increase hardness and Tg of the glass system. To prove this hypothesis, first, glass structure is characterized by ex-situ single pulse excitation experiments and dipole-dipole based NMR. Structural organization of the glass network and its transformation upon addition of aluminum was followed. Then the effect of addition of aluminum to thermal stability of the glass is investigated by means of *in-situ* high-temperature MAS NMR. The results were compared with the trends in macro characteristics (Tg, hardness) observed in the glasses with the same nominal compositions by our cooperation partners.

4.1.1. EDX Results

Such as some part of phosphorus may evaporate from the oxide mixture during the heat treatment, compositional analysis of several samples was carried out to check whether real and nominal compositions of two glass series are similar. Results of EDX analysis of the glasses performed at the Universität Jena are represented in Table 9. It might be seen that some phosphorus indeed is being evaporated during preparation process. The only exception is P60_15Al glass, which might be related to higher visually perceived viscosity of this melt during quenching.

43esd		**P_2O_5**	**Na_2O_3**	**SiO_2**	**Al_2O_3**
P60_3Al	Nominal composition	58.2	29.1	9.7	3.0
	EDX results	47.3±0.1	37.5±0.0	11.6±1.3	3.7±0.0
P60_15Al	Nominal composition	51.0	25.5	8.5	15.0

	EDX results	49.3±0.1	24.8±0.0	8.8±1.6	17.1±0.0
P50_3Al	Nominal composition	48.5	16.2	32.3	3.0
	EDX results	40.0±0.1	20.6±0.0	35.4±0.2	4.1±0.0
P50_15Al	Nominal composition	42.5	14.2	28.3	15.0
	EDX results	37.1±0.1	14.7±0.0	28.2±0.2	20.1±0.0

Table 9. Comparison of nominal glass composition and EDX results of phosphorus-rich glasses.

4.1.2. Glass Transition Temperature Measurements

Parallel to our investigation, glass series with nominal base compositions $60P_2O_5$-$30Na_2O$-$10SiO_2$ and $50P_2O_5$-$16.6Na_2O$-$33.3SiO_2$ without added manganese with different amount of Al_2O_3 were synthesized at the University of Jena. The results of Tg measurements of these glasses are represented in Table 10. From the table it might be seen that incorporation of Al_2O_3 to P60 glasses leads to noticeable changes of Tg. The Tg of P50 glasses first slightly increases and then decreases with added aluminum and varies only slightly comparing with increasing Tg of P60 glasses. Furthermore, the results of EDX analysis of the glass series with the same nominal composition prepared without addition of Mn also show some loss of phosphorus during synthesis.

Glass composition	**Crucible**	**Tg (°C)**	**Composition according to EDX analysis**			
			P_2O_5	**Na_2O_3**	**SiO_2**	**Al_2O_3**
$60P_2O_5$-$30Na_2O$-$10SiO_2$	Silica	301.2	53.8±1.9	33.6±2.0	12.6±0.7	-
$60P_2O_5$-$30Na_2O$-$10SiO_2$	Alumina	277.1	57.8±1.3	29.1±1.2	8.8±0.2	4.3±0.2
$5Al_2O_3$-$0.95(60P_2O_5$-$30Na_2O$-$10SiO_2)$	Alumina	424.9	55.6±1.3	28.5±1.1	9.3±0.3	6.7±0.4
$10Al_2O_3$-$0.95(60P_2O_5$-$30Na_2O$-$10SiO_2)$	Alumina	487.3	51.2±1.8	28.5±1.7	9.3±0.5	11.0±0.6
$15Al_2O_3$-$0.85(60P_2O_5$-$30Na_2O$-$10SiO_2)$	Alumina	488.5	47.7±1.4	29.5±1.2	8.5±0.2	14.3±0.7
$50P_2O_5$-$33,3SiO_2$-$16,6Na_2O$	Silica	448.5	45.9±1.6	18.0±1.1	36.1±1.6	-

$50P_2O_5$-33,3SiO_2-16,6Na_2O	Alumina	480.5	45.3±1.4	18.0±1.1	34.7±1.3	2.0±0.2
$5Al_2O_3$-0.95(50P_2O_5-33,3SiO_2-16,6Na_2O)	Alumina	466.1	45.2±1.6	17.8±1.1	32.6±1.1	4.4±0.3
$10Al_2O_3$-0.95(50P_2O_5-33,3SiO_2-16,6Na_2O)	Alumina	429.7	42.1±1.5	16.2±1.1	30.9±1.3	10.8±0.6

Table 10. Glass compositions and glass transition temperatures.

4.1.3. ^{31}P, ^{27}Al, ^{29}Si *ex-situ* MAS NMR Results

To obtain the information about structural motifs of the glass network at the length scales of 1-2 Å, the samples were characterized by single pulse excitation ^{31}P, ^{27}A, and ^{29}Si ex-situ MAS NMR experiments. As described in 2.1, isotropic chemical shifts of these nuclei depend strongly on their coordination numbers. Octahedral and tetrahedral silicon units and tetrahedral, pentavalent and octahedral aluminum units could be assigned based on their isotropic chemical shift. Phosphorus units might be assigned in the samples where individual peaks are resolved in the spectrum. There are different conventions regarding designation of different phosphorus units having different amount of bridging oxygen, silicon and aluminum in the surrounding. Phosphorus species are named using Q^x notation, where x is the amount of bridging oxygen without differentiation of the nucleus to which this oxygen is bound. For example, Q^2 means that the phosphorus species has one charge-compensating sodium in the vicinity and two oxygen bridges to other phosphorus, aluminum or silicon atoms (alkali ions act as network modifiers decreasing polymerization of glass network by destroying P-O-P bonds).

P60 series. The ^{31}P MAS spectra of P60 series are compiled in Figure 29. In the samples P60_noAl and P60_3Al two distinct peaks centered at -23 ppm and -35 ppm can be distinguished. Based on the known ranges of chemical shifts of phosphorus species (see Figure 21) and previous works these two signals are attributed to Q^2 and Q^3 phosphorus sites. In the samples with higher molar percent of Al_2O_3 phosphorus peaks get broader and only an unresolved broad peak centered at -31 ppm can be distinguished. Broader lines of phosphorus spectra are most probably caused by aluminum addition and might indicate phosphorus-aluminum affinity. To prove it and find out whether aluminum causes line broadening, measurements on test glass system without silicon (see Appendix 5) and dipolar-based experiment were carried out. The results of simulation of ^{31}P spectra of the samples P60_noAl and P60_3Al with DMFIT software show that the amount of Q^2 group decreases from 37 % to

25 % upon addition of Al_2O_3. It must be noticed that the unambiguous spectrum deconvolution in the sample P60_3Al was difficult due to severe line broadening of the signals and that the results should be treated with caution. Further addition of aluminum (6-15 m. p. of Al_2O_3) leads to the shifting of the center of gravity of the phosphorus which is also probably caused by appearance of P-O-Al connections, which supported by the measurements on the test system and dipolar-based experiments (*vide infra)* and general tendency to of signal shift to less negative ppm under addition of aluminum (e. g. P-O-P-O-P and P-O-P-O-Al units having chemical shift of -20 and -6 ppm, repectively[118]). Chemical shift anisotropy (CSA) decreases with increasing aluminum content which has already been observed in aluminosilicate glasses[82,83] and in the test system (see Appendix 5) and is also probably caused by increasing amount of aluminum in the second coordination sphere. The range of chemical shift of phosphorus is more negative than might be expected for Q^2 or Q^3 phosphorus having one or two aluminum in the second coordination sphere[118]. A possible explanation might be presence of silicon in the second coordination sphere which is investigated further by the means of dipolar-based experiments.

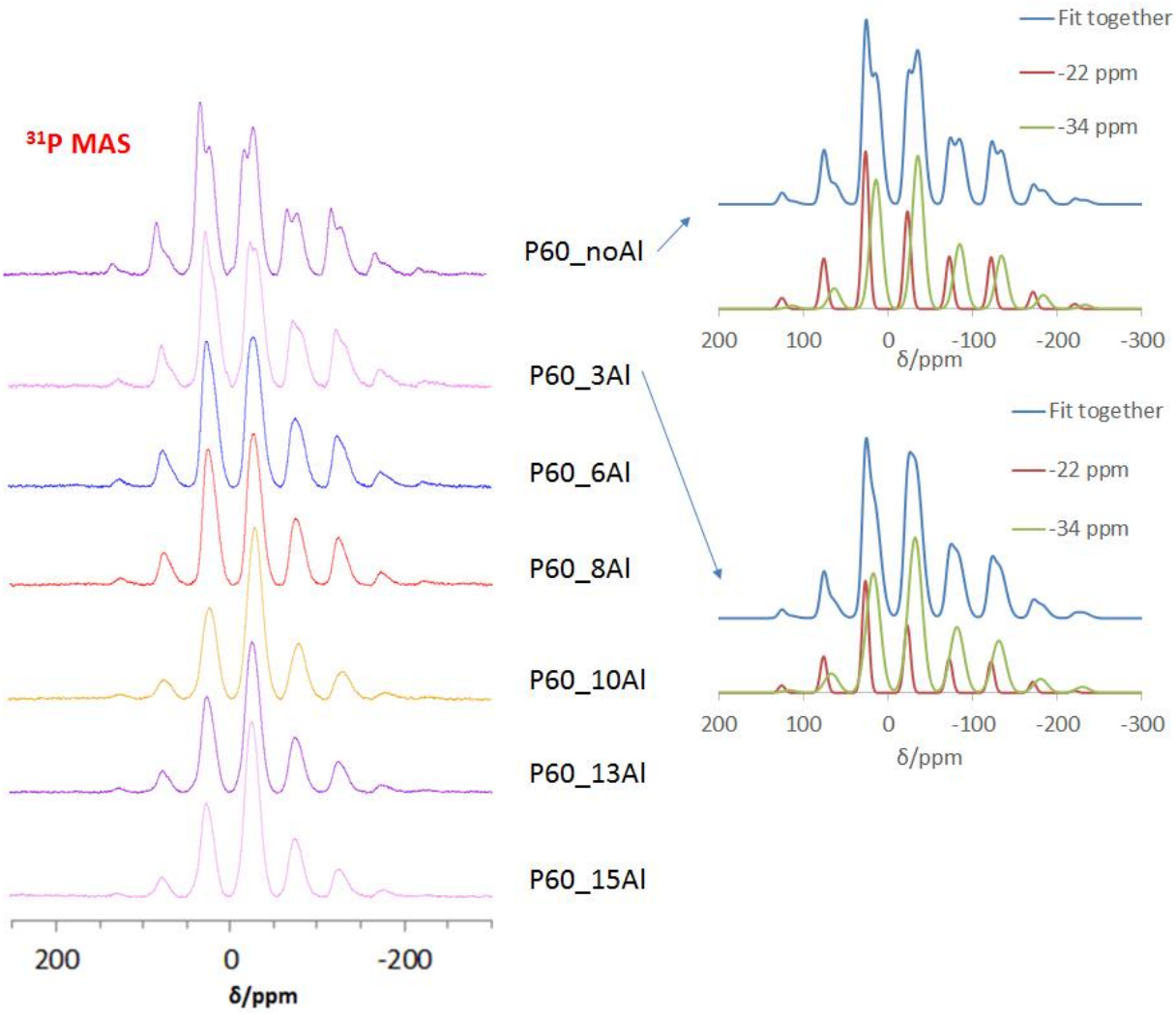

Figure 29. ^{31}P-MAS NMR spectra of glasses of series P60 ((100-x)(0.6P_2O_5-0.3Na_2O-0.1SiO_2)-xAl_2O_3) obtained at B_0 = 11 T.

To prove whether line broadening of the phosphorus signals and the shift of the unresolved peak to less negative frequency is caused by presence of aluminum, a test sodium phosphate system with different aluminum content was prepared and single excitation ^{31}P MAS NMR was performed on this system. As might be seen in Appendix 5, both Q^2 and Q^3 phosphorus signals experience severe line broadening, CSA of alkali phosphate glasses decreases upon addition of aluminum and the center of gravity of the unresolved peak shifts from -31 ppm to -27 ppm from the sample PNa_6Al to the sample PNa_15Al. The same spectra changes are observed in ^{31}P MAS NMR spectrum of P60 glasses, which speaks strongly for Al-P affinity and formation of high amount of P-O-Al bonds upon addition of aluminum.

Ratio of fractional areas of Q^3/Q^2 peaks in sample P60_noAl provides us with complimentary to EDX possibility of comparing nominal and experimental amounts of phosphorus in the glass. Assuming that each SiO_6 species needs two sodium cations for charge-compensation and that

each Q^2 phosphorus unit needs one sodium ion for charge-compensation, the expected Q^3/Q^2 ratio for P60_noAl sample is 2:1. The results of DMFIT deconvolution of phosphorus signal indicate real composition of $54P_2O_5$-$33Na_2O$-$11SiO_2$. This is in accordance with results of EDX spectroscopy (see 4.1.1) showing that some amount of phosphorus is being evaporated during synthesis. Exact calculations of the composition of P60_3Al glass were difficult due to severe signal broadening which led to different possibilities of simulating the spectra and, subsequently, different fractional areas of Q^2 and Q^3 phosphorus signals depending on parameters used.

^{29}Si and ^{27}Al MAS spectra of P60 series are represented in Figure 30. ^{29}Si MAS NMR spectra have low signal-to-noise ratio due to low natural abundance, low gyromagnetic ratio, long relaxation times and low molar percentage of SiO_2 in the oxide melt. The signal around -120 ppm could be attributed to SiO_4 units and the signal around -212 ppm to SiO_6 units. It might be seen that incorporation of aluminum provokes significant changes in the glass structure. In the absence of aluminum, silicon is present only as SiO_6. The amount of SiO_6 species decreases and the amount of SiO_4 species increases with increased amount of added Al_2O_3. In the glass P60_3Al small amount of five-coordinated silicon is observed. Starting from the samples with 8 m. p. of Al_2O_3, only four-coordinated silicon is found in the structure.

Values of the chemical shifts of SiO_4 units might indicate high amount of phosphorus in the second coordination sphere: Chemical shifts of SiO_4 and SiO_6 are close to those observed in phosphosilicate glasses, where silicon is predominantly coordinated with phosphorus[119]. This also might speak for Si-P affinity and high amount of phosphorus in the second coordination sphere of both silicon units. This might be supported by $^{29}Si\{^{31}P\}$-REDOR (see 4.1.6).

^{27}Al MAS NMR spectra show that if the amount of added aluminum is low, the AlO_6 species prevail. With increased Al_2O_3 percentage the amount of AlO_6 species decreases and the amount of AlO_5 and AlO_4 species increases. This corresponds well with observed effect of aluminum incorporated into phosphate glasses[75,82,83,118,120]. It might be explained by increasing O/P ratio along the series (2.9 to 3.4) which favors four-coordinated aluminum (see 2.1.2). Must probably aluminum substitutes six-coordinated silicon and is preferred to remain six-coordinated until charge-balancing leads part of it to become four-coordinated (see 2.1.2).

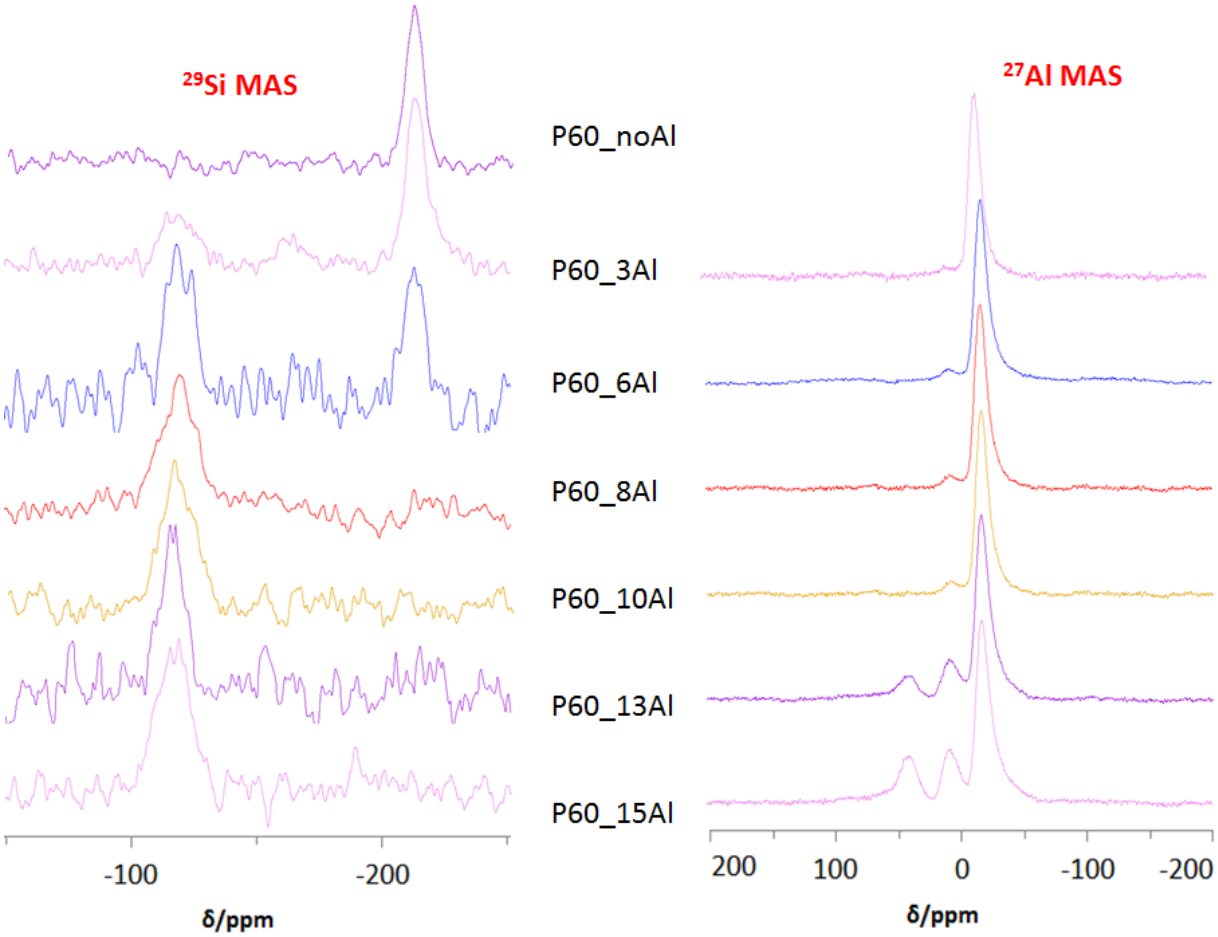

Figure 30 ^{27}Al and ^{29}Si spectra of the glasses P60_noAl-P60_15Al obtained at B_0 = 11 T.

Corresponding evaluated chemical shifts and fractional areas of P60 glass series are summarized in Table 11. Isotropic chemical shifts of silicon and phosphorus signals were found by simulating the spectra with Lorentzian/Gaussian curves with DMFIT software[112]. For aluminum, isotropic chemical shift was defined by simulating spectra with Czjzek model using DMFIT program. It must be noted that exact estimation of fractional areas and isotropic chemical shifts of aluminum might be difficult due to overlapping distorted isotropic shapes of quadrupole distribution patterns and the results should be treated with caution. The same is applicable to chemical shift and fractional areas of silicon species due to noisy spectrum. Such as it was not possible to discriminate between different phosphorus environments in the

samples with high percentage of aluminum, only centers of gravity of phosphorus peaks are given in Table 11.

Glass	δ_{iso}/ppm AlO_4	δ_{iso}/ppm AlO_5	δ_{iso}/ppm AlO_6	δ_{iso}/ppm SiO_4	δ_{iso}/ppm SiO_5	δ_{iso}/ppm SiO_6	δ_{grav}/ppm P
P60_noAl	-	-	-	-	-	-212 (100%)	-32
P60_3Al		16 (14%)	-12 (85%)	-119 (28%)	-163 (11%)	-213 (61%)	-31
P60_6Al		16 (18%)	-13 (82%)	-119 (69%)		-212 (31%)	-31
P60_8Al		16 (16%)	-13 (84%)	-119			-29
P60_10Al	42 (9%)	13 (16%)	-12 (75%)	-117			-27
P60_13Al	44 (12%)	14 (20%)	-12 (68%)	-116			-27
P60_15Al	44 (19%)	14 (20%)	-12 (61%)	-117			-27

Table 11. ^{27}Al-, ^{29}Si- and ^{31}P chemical shift values for the glasses of series P60. Values in brackets correspond to the fractional areas. Due to the limited resolution, for the ^{31}P spectra, only the center of gravity of the isotropic line is listed. Values for ^{27}Al and ^{29}Si were obtained from a simulation of the spectra using the DMFIT software.

Contrary to the changing shift of phosphorus signal, chemical shift of aluminum and silicon units stay relatively constant in all the samples. Such as chemical shift might be affected by the nuclei in the second coordination sphere, it might indicate stable environment of

aluminum and silicon units which is not affected much by chemical composition. This might be proved by dipole-based NMR experiments which are described later.

The amount on six-coordinated cations N6 per (100-x)(0.6P_2O_5-0.3Na_2O-0.1SiO_2)-xAl_2O_3 as a function of molar percentage of incorporated Al_2O_3 is plotted in Figure 31. Corresponding calculations of N6 are shown in Appendix 6. It can be seen that the overall amount of six-coordinated cations growths with increased Al_2O_3 percentage. At small Al_2O_3 percentage (1-3%) SiO_6 brings the major contribution to the growth of 6-coordinated cations. Starting from six molar percent of Al_2O_3, aluminum is the main and from eight molar percent the exclusive contributor to the number of six-coordinated cations is AlO_6. General tendency of increasing number of six-coordinated cations upon addition of aluminum correlates well with increase of Tg (see 4.1.2).

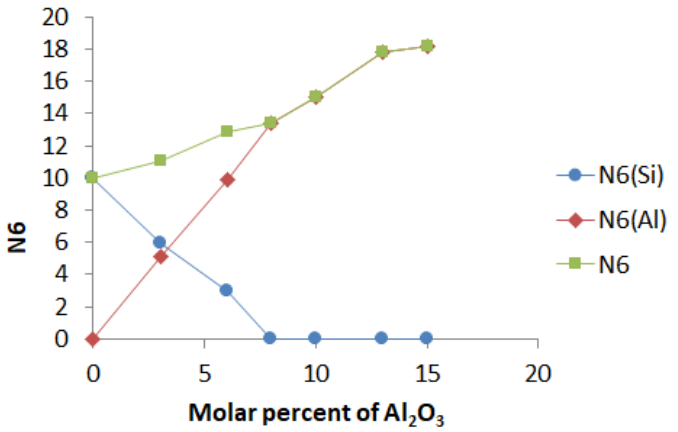

Figure 31. Number of 6-coordinated network former cations (N6) per (100-x)(0.6P_2O_5-0.3Na_2O-0.1SiO_2)-xAl_2O_3 (series P60) as a function of the Al_2O_3 content x. Blue circles: amount of six-coordinated silicon cations; orange squares: amount of six-coordinated aluminum cations; grey squares: overall amount of six-coordinated network former cations.

P50 series. ^{31}P, ^{27}Al and ^{29} Si spectra of P50 glass row are represented in Figure 32 and Figure 33. Similar to P60 series, two peaks which can be attributed to Q^2 and Q^3 phosphorus species are observed. In ^{31}P MAS NMR, the same tendencies as in P60 series might be observed: CSA of phosphorus signal decreases, Q^2 and Q^3 peaks are getting broader upon addition of aluminum. This might speak for aluminum being incorporated into the structure. To find out to which atoms phosphorus atoms are connected through oxygen bridges, dipolar-based experiment were carried out and are described further. The fraction of Q^2 signal growth from 17 to 19 to 21 % in the samples P50_noAl-P50_0.25Al-P50_1Al. Assuming that each SiO_6 unit

requires two sodium ions to be charge-balanced and using the results of simulations of ^{31}P spectra with DMFIT software, the compositions of P50_noAl and P50_1Al glass based on NMR studies are $43P_2O_5$-$38SiO_2$-$19Na_2O$ and $41P_2O_5$-$39SiO_2$-$20Na_2O$-$1Al_2O_3$, respectively. This corresponds with the results of EDX measurements indicating loss of phosphorus during synthesis.

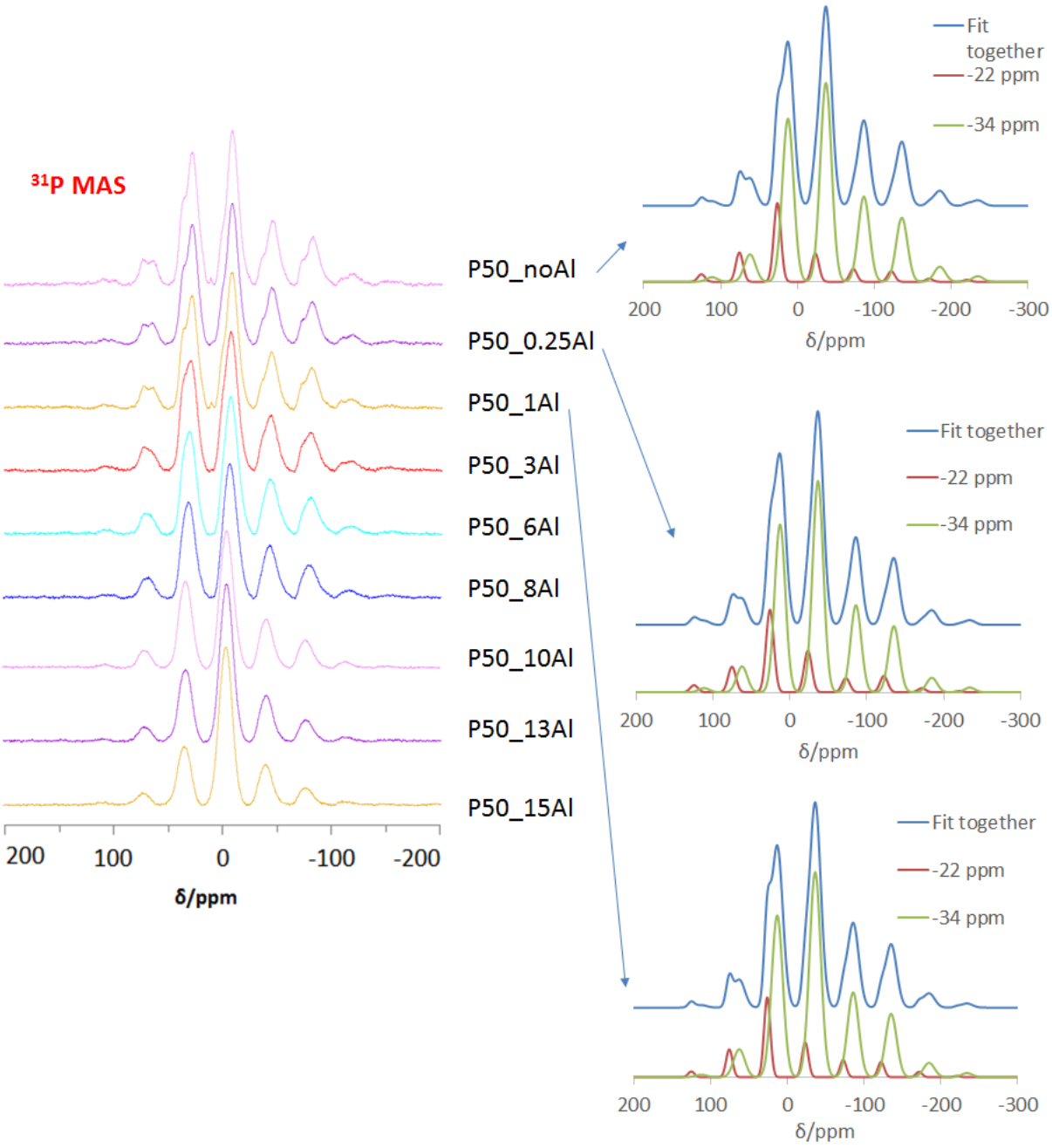

Figure 32. ^{31}P-MAS NMR spectra of glasses of series P50 ((100-x)(0.5P_2O_5-0.33SiO_2-0.17Na_2O)-xAl_2O_3), obtained at B_o = 11.74 T.

In correspondence with previous research[121] there are SiO_4 and SiO_6 units observed in ^{29}Si MAS NMR spectra of the glass without aluminum. Upon addition of aluminum the amount of six-coordinated silicon is decreasing until only four-coordinated silicon is observed in the sample with six or more percentage of Al_2O_3. Amount of six-coordinated aluminum decreases with increased Al_2O_3 content parallel to the appearance and growth of AlO_5 and AlO_4 species which correlates with increasing O/P ration (3.3 to 3.9)[75,83]. Chemical shift of silicon and aluminum units again do not change much upon addition of aluminum. Chemical shift of silicon units also might indicate presence of phosphorus in the second coordination sphere which is investigated further by the means of dipolar-based experiments. The spectra of P50 glasses were simulated with DMFIT software and the results of these simulations are summarized in Table 12.

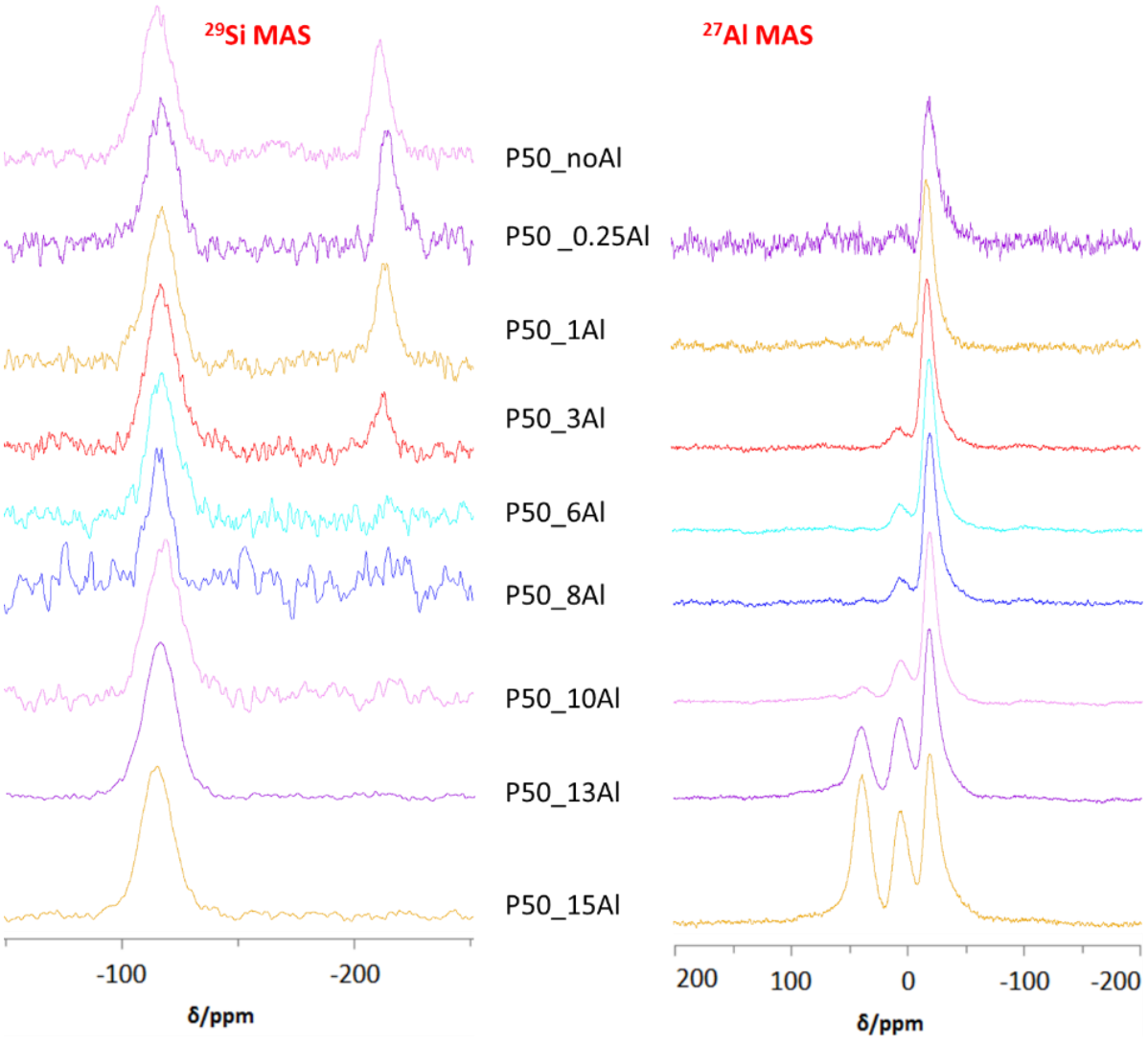

Figure 33 ^{27}Al and ^{29}Si spectra of the series P50 ((100-x)(0.5P_2O_5-0.33SiO_2-0.17Na_2O)-xAl2O3), obtained at B0 = 11.74 T.

	δ_{iso}/ppm AlO_4	δ_{iso}/ppm AlO_5	δ_{iso}/ppm AlO_6	δ_{iso}/ppm SiO_4	δ_{iso}/ppm SiO_6	δ_{grav}/ppm P
P50_noAl				-115 ppm (69%)	-210 ppm (31%)	-36.1
P50_0.25Al		14 (9%)	-14 (91%)	-117 (68%)	-214 (32%)	-35.5
P50_1Al		-14 (16%)	-14 (84%)	-117 (72%)	-212 (28%)	-32.7
P50_3Al		14 (16%)	-14 (84%)	-117 (87%)	-211 ppm (13%)	-34.4
P50_6Al		14 (17%)	-14 (83%)	-117		-35.3
P50_8Al		14 (16%)	-14 (84%)	-117		-35.7
P50_10Al	40 (5%)	14 (25%)	-14 (70%)	-118		-32.5
P50_13Al	43 (26%)	13 (27%)	-14 (47%)	-115		-30.6
P50_15Al	42 (35%)	12 (27%)	-14 (38%)	-116		-29.5

Table 12. ^{27}Al-, ^{29}Si- and ^{31}P chemical shift values for the glasses of series P50. Values in brackets correspond to the fractional areas. Due to the limited resolution, for the ^{31}P spectra, the center of gravity of the isotropic line is listed. Values for ^{27}Al and ^{29}Si were obtained from a simulation of the spectra using the DMFIT software.

Figure 34 represents the amount of six-coordinated species N6 per (100-x)($0.5P_2O_5$-$0.33SiO_2$-$0.17Na_2O$)-xAl_2O_3 in P50 glasses. For that molar percent of aluminum oxide was multiplied by the fractional area of AlO_6 peak and then by two and molar percent of silicon dioxide was multiplied by fractional area of SiO_6 peak. Detailed calculations of N6 are represented in Appendix 6. Contrary to the P60 series, the amount of six-coordinated species does not growth significantly and only oscillates around 12 for all measured samples. That might be connected with initial lower P/(Si+Al) ratio compared with P60 glasses. Probably, there is not enough phosphorus in the system to high-coordinated aluminum units. This is in agreement with O/P ratio which growths from 3.3 to 3.9 requiring existence of AlO_4 units for charge-balance of oxygen. Again, small variance of amount of six-coordinated species correlates well with moderate changes in Tg of glasses with similar nominal composition (see 4.1.2).

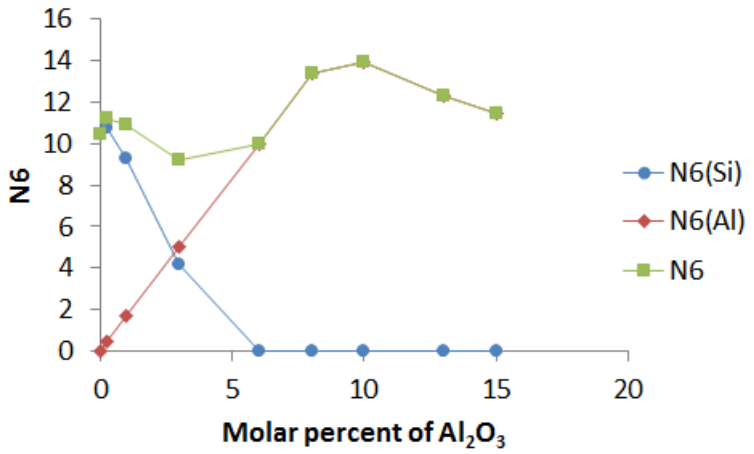

Figure 34. Number of 6-coordinated network former cations (N6) per (100-x)($0.5P_2O_5$-$0.33SiO_2$-$0.17Na_2O$)-xAl_2O_3 (series P50) as a function of the Al_2O_3 content x. Blue circles: amount of six-coordinated silicon cations; orange squares: amount of six-coordinated aluminum cations; grey squares: overall amount of six-coordinated network former cations.

4.1.4. Effect of Aluminum to CSA Tensors of Phosphorus

Although MAS NMR allows the estimation of the width of the CSA tensor and to some degree its shape, most of the valuable information about CSA tensor is lost under rotation. To retrieve this information, different techniques such as CT-2DCSA (constant Time 2D CSA), ROSCA (Recoupling of CSA), SUPER (separation of undistorted powder patterns by effortless recoupling) or MAT (magic angle turning) might be used. In this study MAT spectra (see 1.2.6) were performed by Dr. Schiffmann on P60 series glasses to investigate the changes of phosphorus signal upon addition of aluminum. 2D MAT spectrum and corresponding slices of the spectrum (taken at the chemical shift of individual phosphorus signals measured with ^{31}P NMR: -22 ppm and -34 ppm) of P60_noAl glass are represented in Figure 35. The CSA tensor

of the peak at -34, which is caused by a phosphorus, that is surrounded by three bridging oxygen atoms, has an asymmetry parameter of 0.3 and the CSA tensor of the signal at -22 ppm, caused by a phosphorus, that is surrounded by two bridging oxygen atoms, has an asymmetry parameter of 0.4. Contrary to the axially symmetric shape of Q^3 phosphorus observed in pure alkali phosphate glasses, non-axially symmetric shape of the signal at -34 ppm might be caused by the presence of silicon in the second coordination sphere or by overlapping of the phosphorus signals with and without silicon in the second coordination sphere. Furthermore, due to the high width of the phosphorus peaks in the indirect dimension the peaks can contribute some intensity to each other in slices and the results are to be treated with caution.

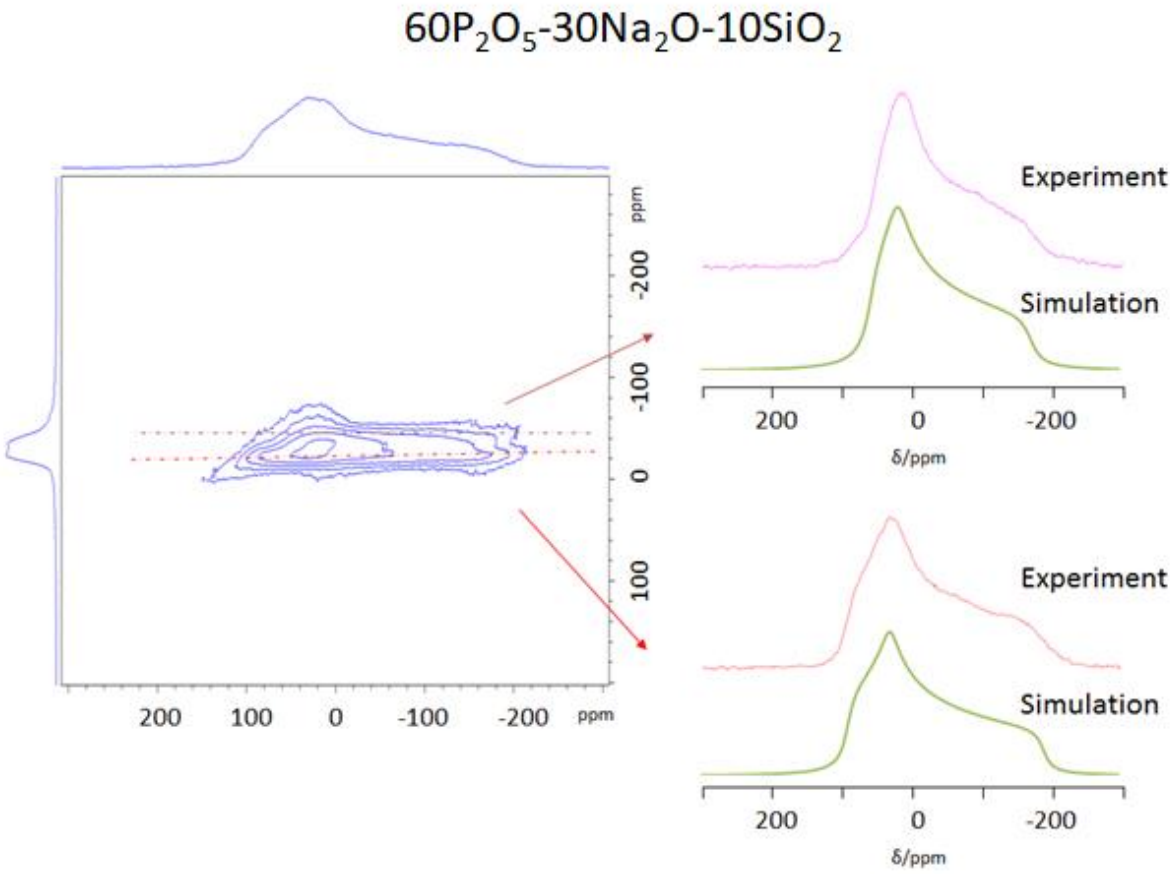

Figure 35. ^{31}P sheared MAT spectrum of the glass with nominal composition $60P_2O_5$-$30Na_2O$-$10SiO_2$ measured at 200 Hz in the field B_o=7 T.

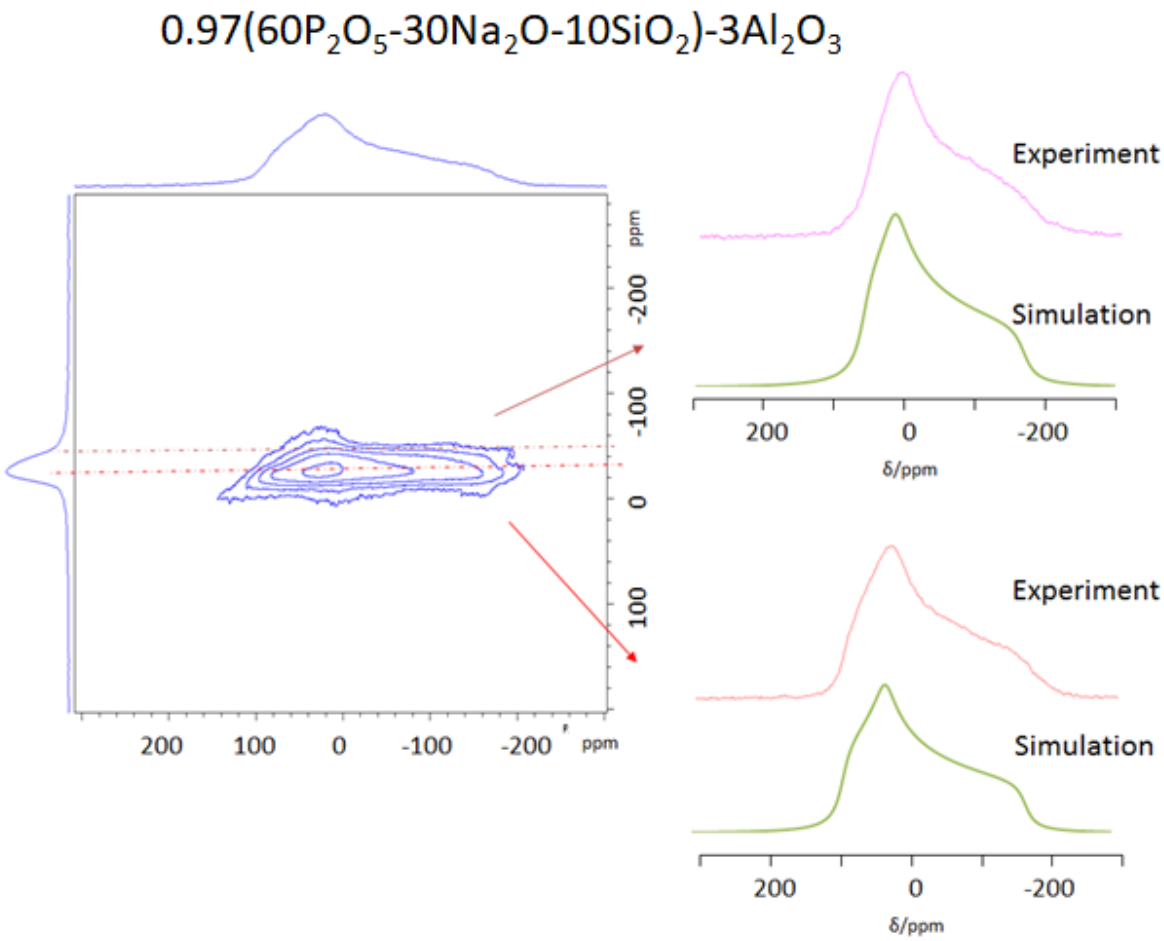

Figure 36. ^{31}P sheared MAT spectrum of the glass with nominal composition $0.97(60P_2O_5\text{-}30Na_2O\text{-}10SiO_2)\text{-}3Al_2O_3$ measured at 200 Hz in the field B_o=7 T.

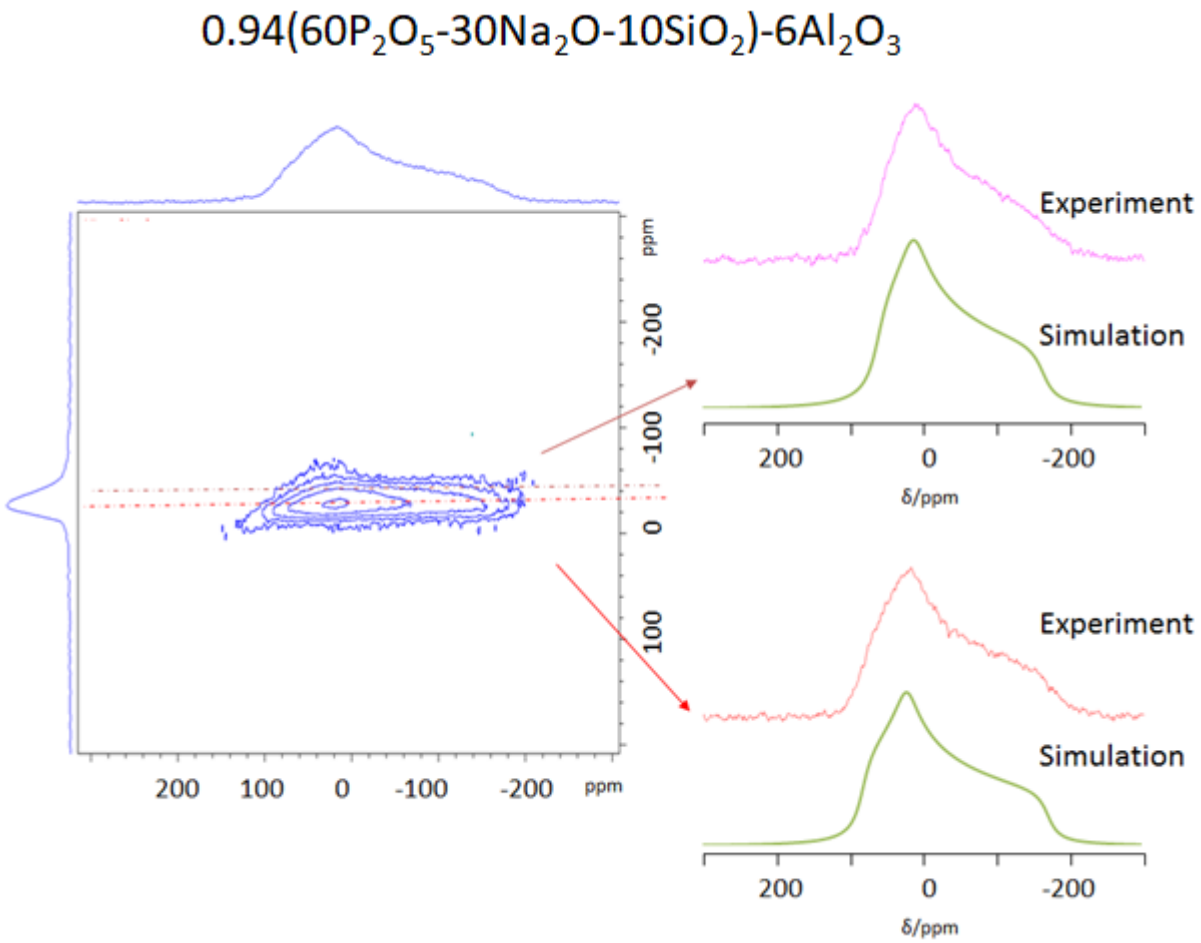

Figure 37. ^{31}P sheared MAT spectrum of the glass with nominal composition $0.94(60P_2O_5\text{-}30Na_2O\text{-}10SiO_2)\text{-}6Al_2O_3$ measured at 200 Hz in the field B_o=7 T.

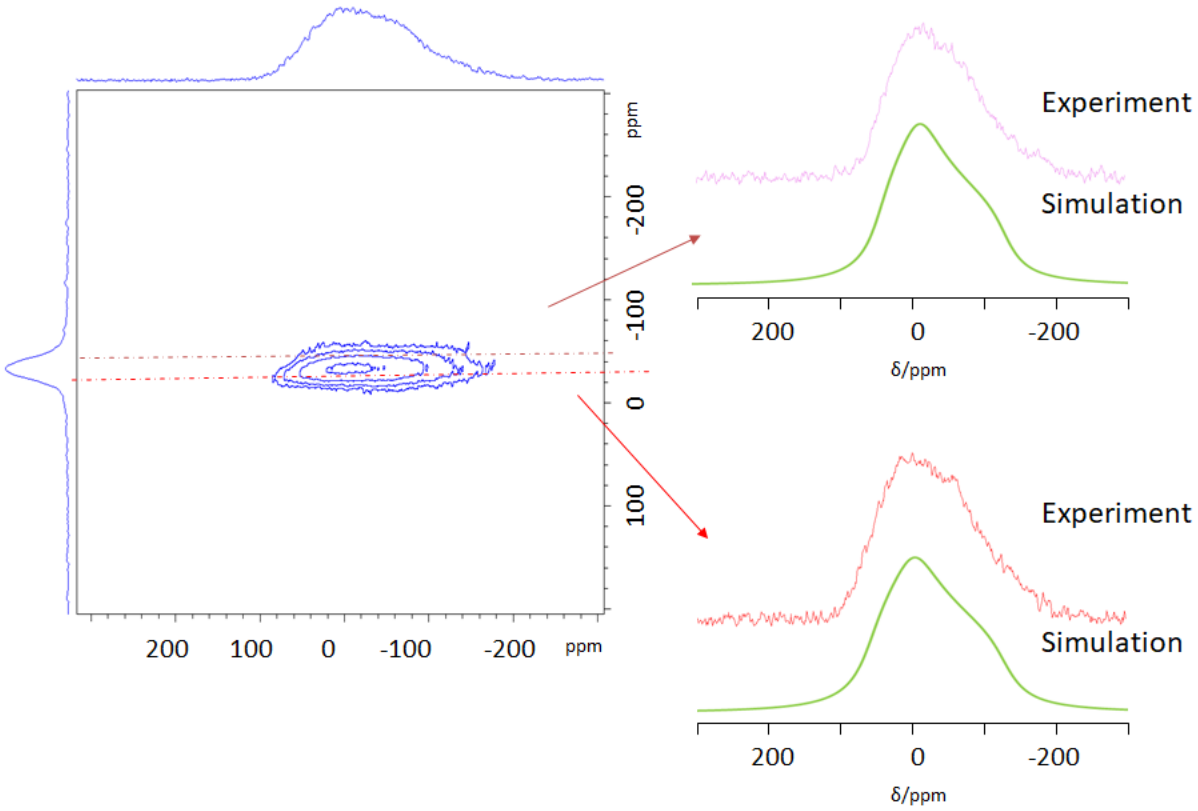

Figure 38: ^{31}P sheared MAT spectrum of the glass with nominal composition $0.90(60P_2O_5\text{-}30Na_2O\text{-}10SiO_2)\text{-}10Al_2O_3$ measured at 200 Hz in the field B_o=7 T.

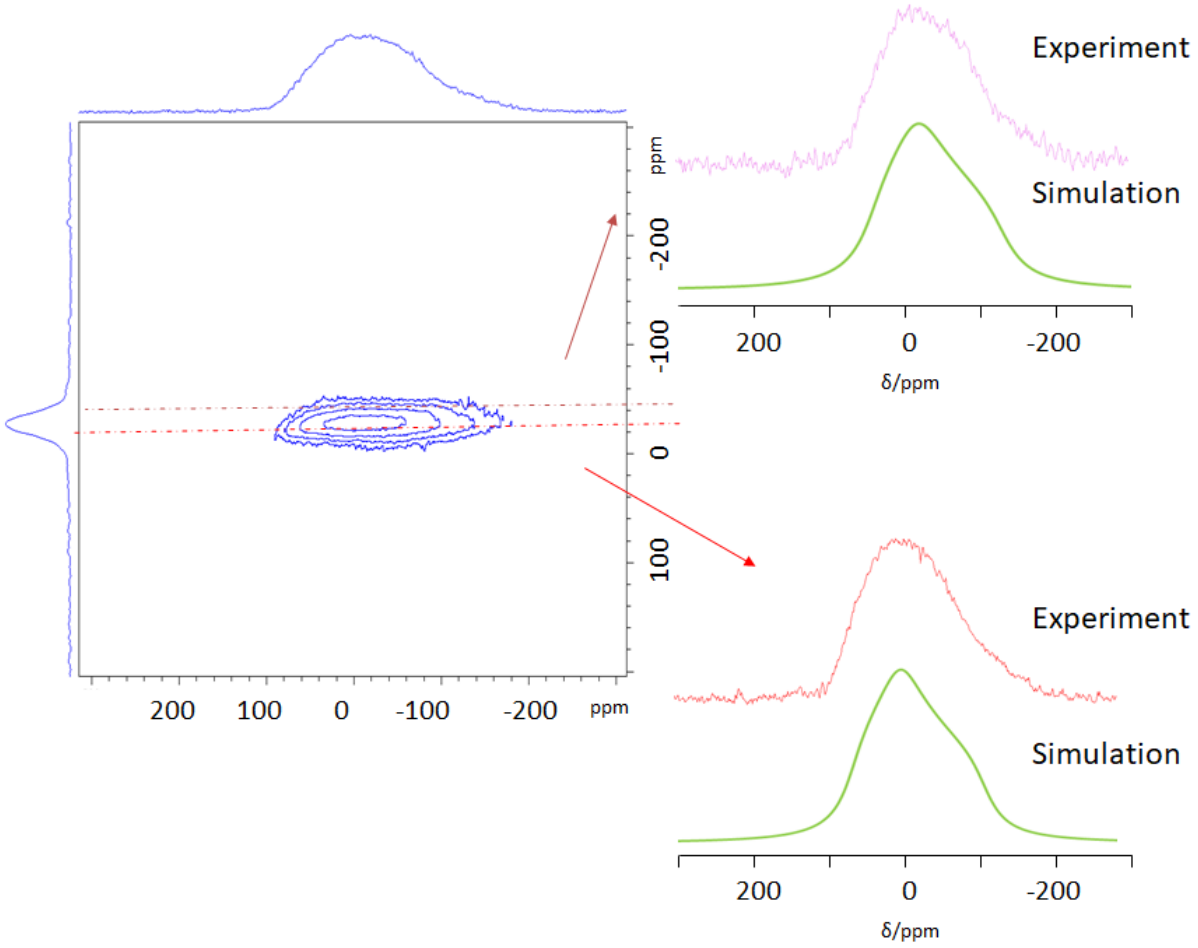

Figure 39. ^{31}P sheared MAT spectrum of the glass with nominal composition $0.85(60P_2O_5\text{-}30Na_2O\text{-}10SiO_2)\text{-}15Al_2O_3$ measured at 200 Hz in the field Bo=7 T.

The results of 2D MAT measurements and resulting spectra (extracting of corresponding slices) of the glasses P60_3Al, P60_6Al, P60_10Al and P60_15Al are represented in Figure 36-Figure 39. In Table 13 the results of the simulations of slices of MAT spectra in P60 series are represented. The results are to be treated with caution because the signals are broader in the indirect dimension and can contribute to the intensity of each other. The signals of both extracted slices might be simulated with one peak. The width of the tensor decreases continually for the peak around -20 ppm and increases first slightly and then decreases for the peak around -35 ppm which might indicate incorporation of aluminum in the second coordination sphere. Chemical shift of the signal at -22 ppm stays nearly constant and the chemical shift of the signal at -34 ppm shifts first to less negative values (-30 ppm for P60_3Al and P60_6Al) and rises then again with increasing aluminum amount. This effect is also must probably connected with different Si/Al ratio of neighboring atoms. In the sample with high

aluminum content asymmetry parameter of both peaks in indirect dimension increases to 0.6-07.

	Peak 1			Peak 2		
	Position, ppm	Width of CSA tensor, ppm	η (asymmetry of CSA tensor)	Position, ppm	Width of CSA tensor, ppm	η (asymmetry of CSA tensor)
P60_noAl	-23	167	0.4	-32	140	0.3
P60_3Al	-22	154	0.4	-30	157	0.2
P60_6Al	-23	150	0.4	-30	158	0.2
P60_10Al	-24	104	0.6	-34	97	0.6
P60_15Al	-22	97	0.7	-35	94	0.6

Table 13. CSA parameters and fractional area of CSA tensor contributions of the glasses of P60 series simulated by DMFIT software to fit the results of MAT experiments.

4.1.5. $^{27}Al\{^{31}P\}$-REDOR and $^{31}P\{^{27}Al\}$-REAPDOR NMR

Having identified coordination numbers with one-pulse MAS NMR experiment, more information can be derived by employing dipolar-based NMR methods. The values of heteronuclear dipolar coupling deliver information about structural organization at intermediate (2-8 Å) length scales which allows to learn more about the connectivity of different structural polyhedral.

P60 series. From single pulse excitation experiments and from CSA tensor evolution upon addition of aluminum we suppose that there is a substantial amount of P-O-Al connections present in the glass. Furthermore, from relatively constant chemical shift of aluminum units it is expected that aluminum, once being incorporated into the structure, retains stable environment. $^{27}Al\{^{31}P\}$-REDOR experiments were performed to analyze the amount of phosphorus connected to AlO_x polyhedra. The results of $^{27}Al\{^{31}P\}$-REDOR measurements

carried out on the glasses P60_3Al, P60_6Al, P60_10Al and P60_15Al are represented in Figure 40. Noticeable effect is observed for all three aluminum species, which means that phosphorus groups are connected to all three aluminum species. It can also be seen that the experimental curves are not affected much by the amount of incorporated Al_2O_3. This agrees with relatively constant isotropic chemical shift of aluminum units observed in single excitation experiments (see Table 11).

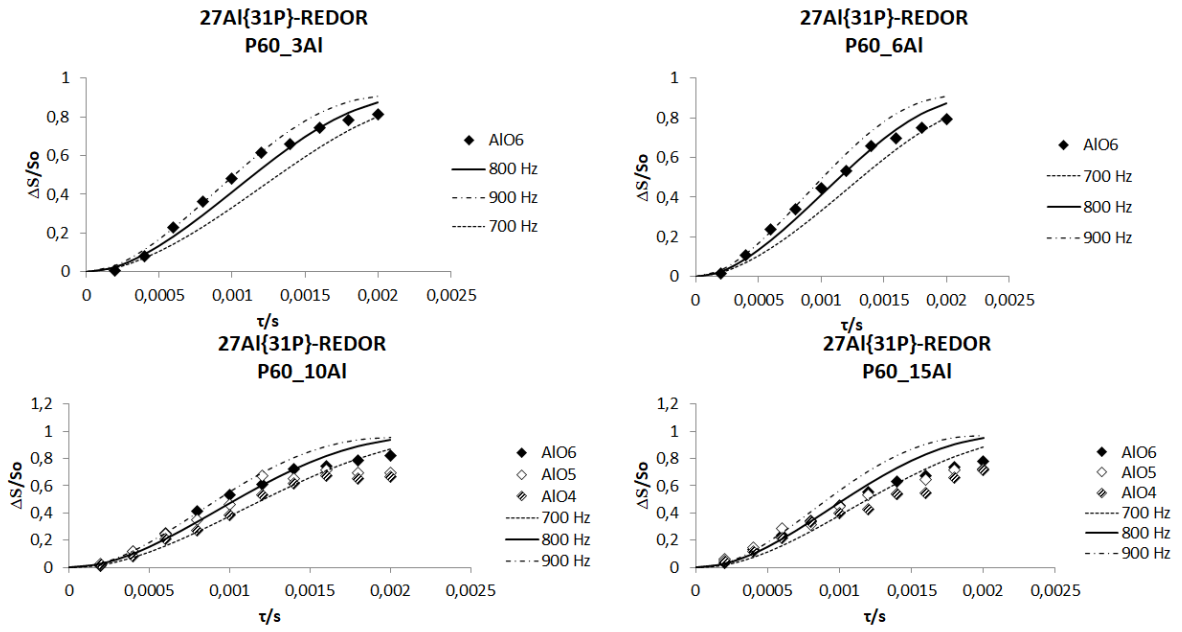

Figure 40. $^{27}Al\{^{31}P\}$ REDOR-NMR data for glasses P60_3Al, P60_6Al, P60_10Al and P60_15Al, obtained employing 11.7 T Varian magnet. Filled diamonds: AlO6; open diamonds: AlO5; patterned diamonds: AlO4. The lines represent results of SIMPSON simulations assuming effective dipolar couplings of 700 Hz (dashed line), 800 Hz (solid line) and 900 Hz (dashed dotted line).

Using two-spin approximation (see 3.2) and considering CSA values and instrumental parameters, $^{27}Al\{^{31}P\}$ REDOR experimented were simulated using SIMPSON software (see Figure 40). Such as it is known that CSA values have significant effect to REDOR measurements and in particular to $^{27}Al\{^{31}P\}$ REDOR experiments (see Appendix 3), CSA values were first simulated in DMFIT program and set as average of weighted CSA values of Q^2 and Q^3 phosphorus peaks in the sample without Al addition and as CSA values of phosphorus peak treated as one signal in SIMPSON program (-140, -135, -105 and -105 ppm for the samples P60_3A, P60_6Al, P60_10Al and P60_15Al, respectively). It must be noted that from MAT experiments we know that phosphorus signals has two different constituents in the sample with high amount of aluminum having drastically different widths of CSA tensor which was

not considered in the SIMPSON simulation and that it might have affected the results of the numerical simulation.

The results show Al-P coupling of 850-900 Hz for aluminum in AlO_6 units, 800 Hz for aluminum in AlO_5 units and 800 Hz for aluminum in AlO_4 units. Assuming Al-P distances of 3.2 Å, for aluminum in AlO_6 units and 3.1 Å for aluminum in $AlPO_5$ and AlO_4 units depending on coordination of involved aluminum species[122,123] and using two-spin approximation (see 3.2), the results of $^{27}Al\{^{31}P\}$ REDOR experiment indicate full or nearly full coordination of all aluminum units by phosphorus. The fact that measured dipolar couplings are getting slightly smaller upon addition of aluminum might be explained by slightly less phosphorus in the surrounding, smaller observed bulk effect of phosphorus or might be caused by not considering smaller CSA values of phosphorus fraction: in SIMPSON simulations only high CSA of the phosphorus signal constituent was considered and from the test measurements it is known that the simulation curves having lower CSA values are more steep that the curves having higher CSA values (see Appendix 3). Full or nearly full coordination of aluminum with phosphorus implies Al-O-Al avoidance and no or very small amount of Al-O-Si connections.

$^{31}P\{^{27}Al\}$ REAPDOR curves and corresponding SIMPSON simulations[114] of P60_3Al, P60_6Al, P60_10Al and P60_15Al glasses are shown in Figure 41. Due to the poor resolution, Q^2 and Q^3 phosphorus signals were treated as one peak when simulating with DMFIT software. P-Al dipolar coupling increases gradually along addition of Al_2O_3 until the system is saturated in the sample with 10% of added Al_2O_3. Gradual change of dipolar coupling upon addition of aluminum supposes that aluminum polyhedral are distributed in the phosphorus network. There is no additional increase of aluminum around phosphorus species in the sample with 15% of added Al_2O_3. This implies that the amount of P-O-Al connections stays constant. Assuming P-Al distance of 3.2 Å[122,123] and two-spin approximation (see 3.2), maximum observed P-Al dipolar coupling of 500 Hz corresponds with 1.5 aluminum in the second coordination sphere of phosphorus.

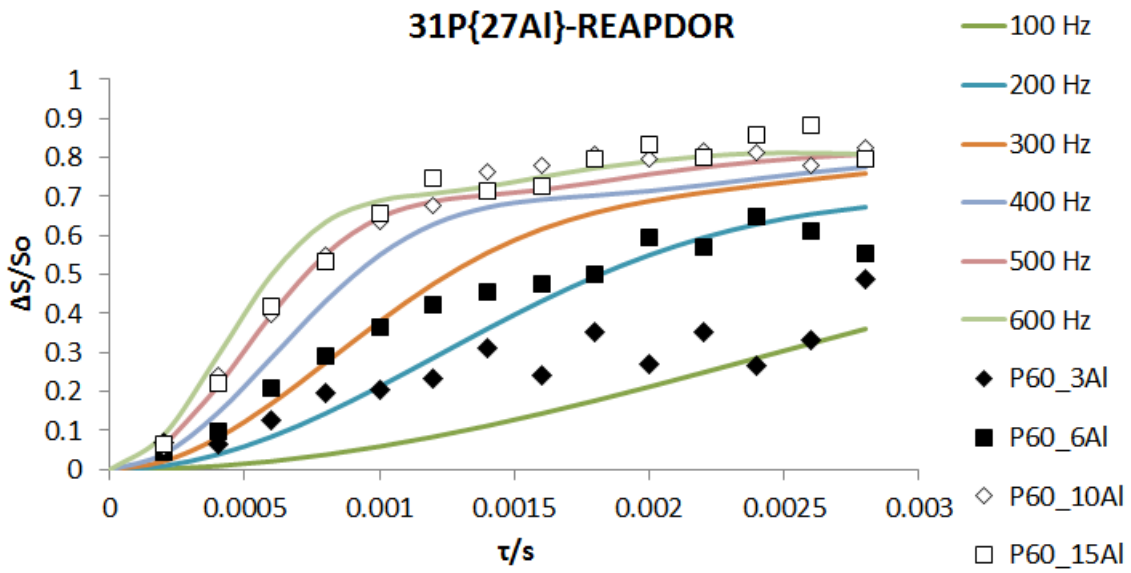

Figure 41. $^{31}P\{^{27}Al\}$ REAPDOR NMR data for glasses of series P60. Filled diamonds: P60_3Al, filled squares: P60_6Al; open diamonds: P60_10Al; open squares: P60_15Al. The lines represent results of SIMPSON simulations assuming the indicated effective dipolar couplings.

P50 series. The results of $^{27}Al\{^{31}P\}$-REDOR experiment carried out on P50_3Al, P50_6Al, P50_10Al and P50_15Al glasses are shown in Figure 42. Similar to P60 series, the results were simulated with SIMPSON software considering instrumental setups and using CSA values of 130 ppm, 125 ppm, 115 ppm and 95 ppm for the glasses P50_3Al, P50_6Al, P50_10Al and P50_15Al, respectively (defined by the procedure described above). Assuming Al-P distances of 3.2 Å, for aluminum in AlO_6 units and 3.1 Å for aluminum in $AlPO_5$ and AlO_4 units depending on coordination of involved aluminum species[122,123] and using two-spin approximation (see 3.2), the results for AlO_6 and AlO_5 units are similar to those obtained for P60 series: they are fully or nearly fully surrounded by phosphorus. Al-P dipolar coupling of aluminum in AlO_4 units is lower than the one observed in P60 glasses. It might be caused by lower initial amount of phosphorus which makes it impossible to fully coordinate all aluminum species. Instead of phosphorus aluminum might be partially coordinated by silicon or, less probable, other aluminum units which might be proved by Si-Al dipolar-based experiments.

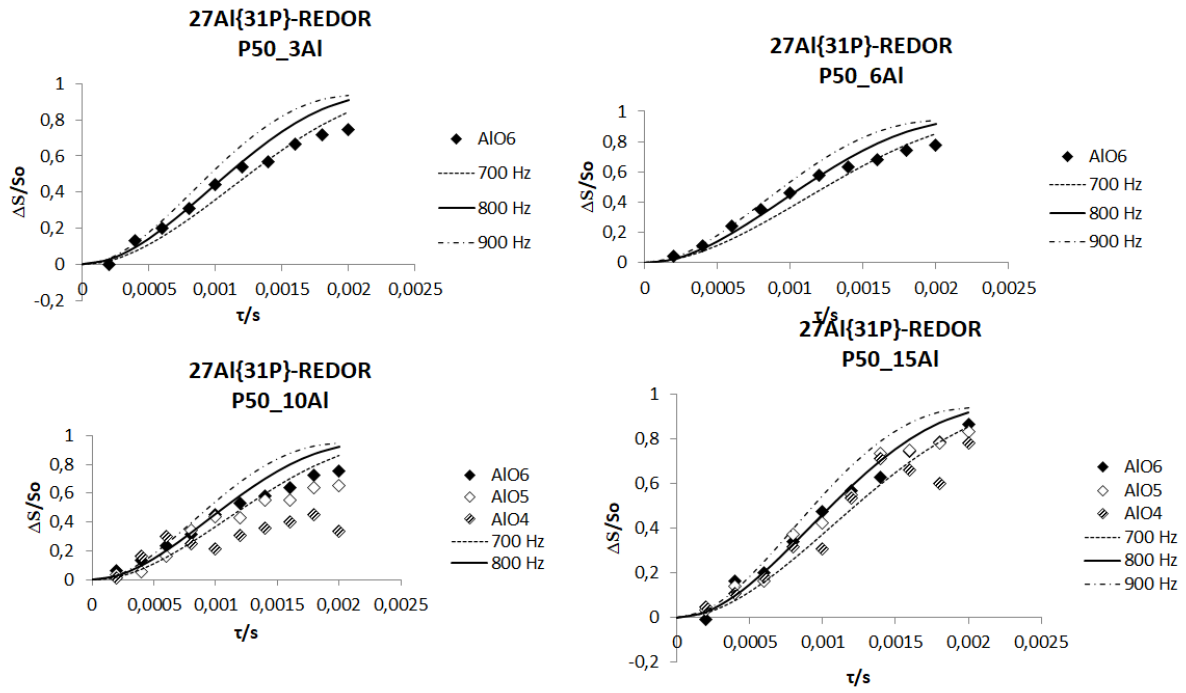

Figure 42. $^{27}Al\{^{31}P\}$ REDOR-NMR data for glasses P50_3Al, P50_6Al, P50_10Al and P50_15Al, obtained employing 11.7 T Varian magnet. Filled diamonds: AlO_6; open diamonds: AlO_5; patterned diamonds: AlO_4. The lines represent results of SIMPSON simulations assuming effective dipolar couplings of 700 Hz (dashed line), 800 Hz (solid line) and 900 Hz (dashed dotted line).

$^{31}P\{^{27}Al\}$ REAPDOR curves and corresponding SIMPSON simulations of P50_3Al, P50_6Al, P50_10Al and P50_15Al glasses are shown in Figure 43. Due to poor resolution Q^2 and Q^3 phosphorus peaks were treated as one peak when fitting with SIMPSON and DMFIT software. Contrary to the effect observed in P60 glasses, added aluminum gradually connects to more and more phosphorus in all tested samples until every phosphorus has about two connected aluminum in the surrounding. The results indicate aluminum polyhedral being distributed in phosphorus network.

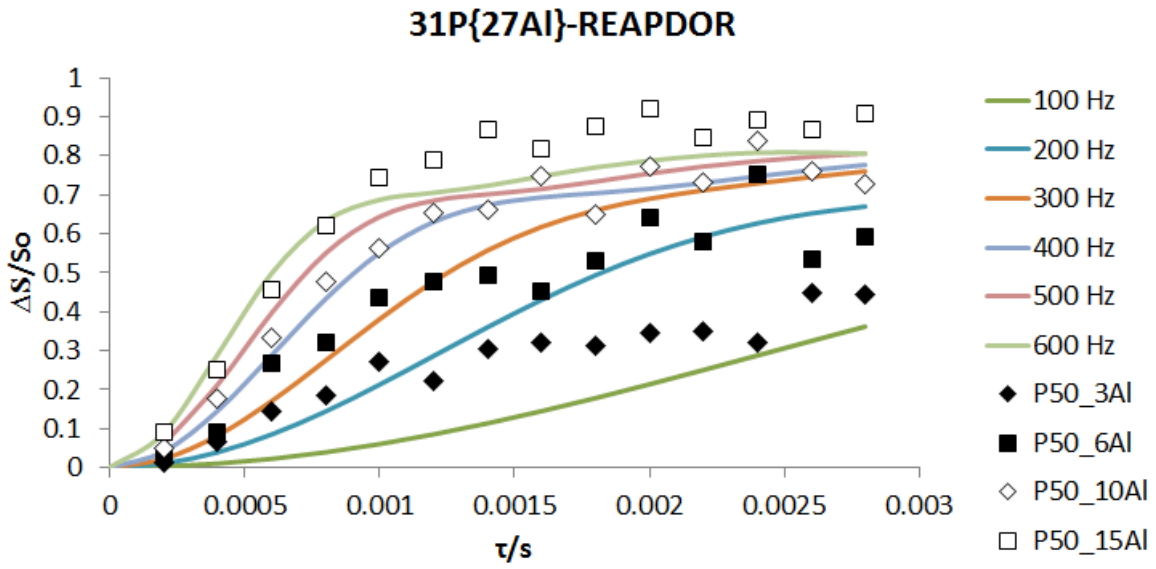

Figure 43. $^{31}P\{^{27}Al\}$ REAPDOR NMR data for glasses of series P50. Filled diamonds: P50_3Al, filled squares: P50_6Al; open diamonds: P50_10Al; open squares: P50_15Al. The lines represent results of SIMPSON simulations assuming the indicated effective dipolar couplings.

4.1.6. $^{31}P\{^{29}Si\}$-REDOR NMR and $^{29}Si\{^{31}P\}$-REDOR NMR

From the previous research it is known that the amount of phosphorus and aluminum in the second coordination sphere of silicon effects its chemical shift. From the results obtained in $^{27}Al\{^{31}P\}$-REAPDOR experiment it is supposed that silicon is most probably surrounded by phosphorus or other silicon units and not by aluminum. From constant chemical shift of the silicon signal we can expect constant amount of phosphorus in the second coordination sphere. To quantify this and to gain more information about the distribution of silicon units in phosphorus network, $^{29}Si\{^{31}P\}$-REDOR and $^{31}P\{^{29}Si\}$-REDOR were carried out. Such as dipolar-based experiments involving silicon are either impossible or difficult to carry out due to low abundance and long relaxation times of ^{29}Si atoms (in case of silicon being used on decoupling and receiving channel, respectively), samples enriched with 100 % of ^{29}Si were used to investigate silicon environment.

P50 series. The results of $^{29}Si\{^{31}P\}$-REDOR NMR on the enriched glasses of P50 series (P50_noAl_Si, P50_3Al_Si, P50_10Al_Si) are represented in Figure 44. The lines are guides to the eyes and represent theoretical curves obtained with simulation using SIMPSON software. "n-spin" notation in the graphs indicates the result of simulation of n-spin system (1 silicon nuclei and n-1 phosphorus nucleus) using 2-spin approximation taking P-Si distance of 3.22 Å[124], and considering the effect of CSA tensor as described in $^{27}Al\{^{31}P\}$-REDOR (4.1.5).

Again, it must be noted that the fact that phosphorus units have two different components with different CSA widths was not considered in SIMPSON simulation and might have affected the numerical results.

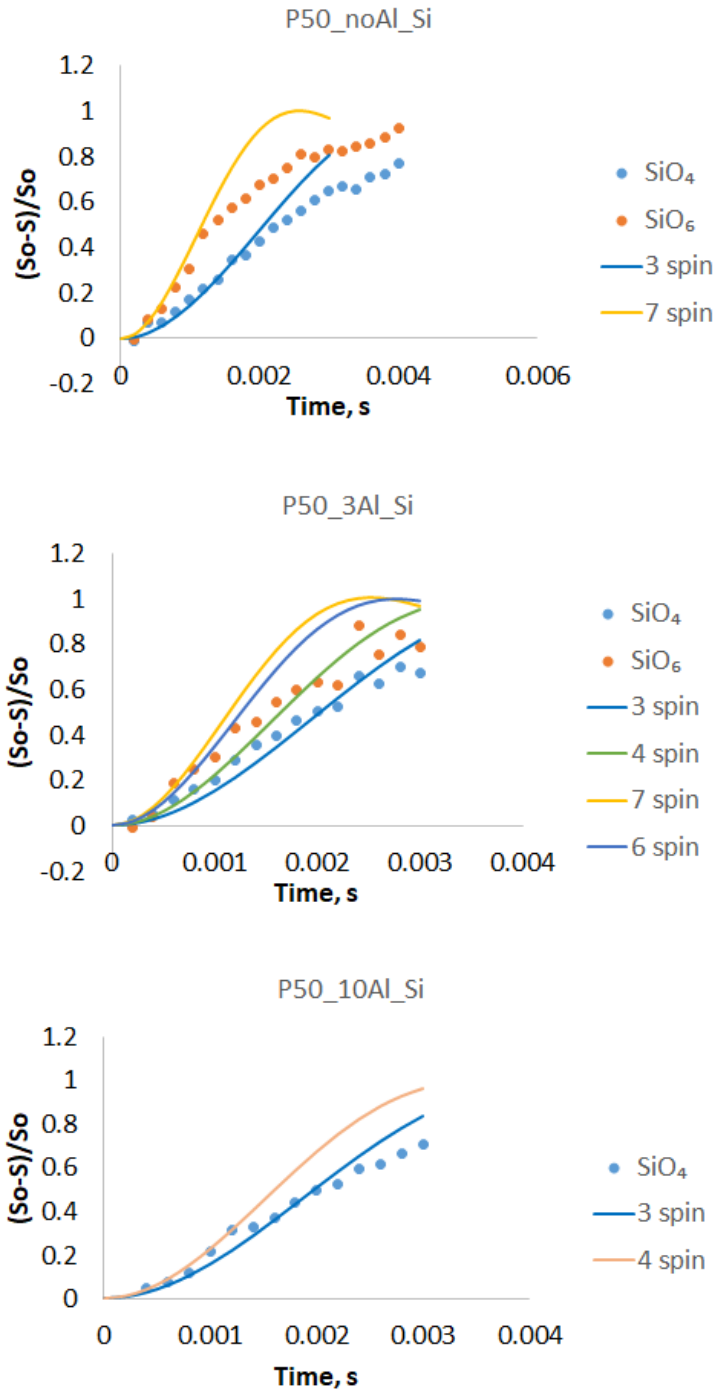

Figure 44. $^{29}Si\{^{31}P\}$ REDOR-NMR data for glasses P50_noAl_Si, P50_3Al_Si and P50_10Al_Si, obtained employing 7 T magnet. Blue circles: SiO_4; orange circles: SiO_6. The lines are guides for the eyes and represent results of SIMPSON simulations of n-spin system (1 silicon nuclei and n-1 phosphorus nucleus) taking P-Si distance 3.22 Å[124].

According to the results of simulations, in P50_no Al glass six-coordinated silicon units are fully surrounded by phosphorus and half of the bridging oxygen around SiO_4 units are occupied by phosphorus which is in agreement with previous results[119]. The rest of the bridging oxygen of SiO_4 units might be connected to other silicon units or to aluminum, which is less probable due to full or nearly full coordination of aluminum units by phosphorus. To support this assumption, Al-Si dipolar based experiments we carried out and are discussed in 4.1.7.

In the sample P50_3Al six-coordinated silicon has five to six phosphorus in the second coordination sphere and is still nearly fully phosphorus-coordinated. SiO_4 units in the glasses P50_3Al and P50_10 Al also still have two phosphorus in the surrounding. Therefore, upon addition of aluminum, coordination of silicon by phosphorus does not change much. This corresponds well with stable chemical shift of silicon units upon addition of aluminum (see Table 12).

In Figure 45 the results of $^{31}P\{^{29}Si\}$-REDOR NMR of P50 enriched series are represented. The lines are guides to the eyes and represent theoretical curves obtained with simulation using SIMPSON software. “n-spin” notation in the graphs indicates the result of simulation of n-spin system (1 silicon nuclei and n-1 phosphorus nucleus) using 2-spin approximation taking P-Si distance of 3.22 Å[124], and considering the effect of CSA tensor. Due to severe broadening of phosphorus signals upon addition of aluminum, site-resolved evaluation was only possible for the sample without aluminum.

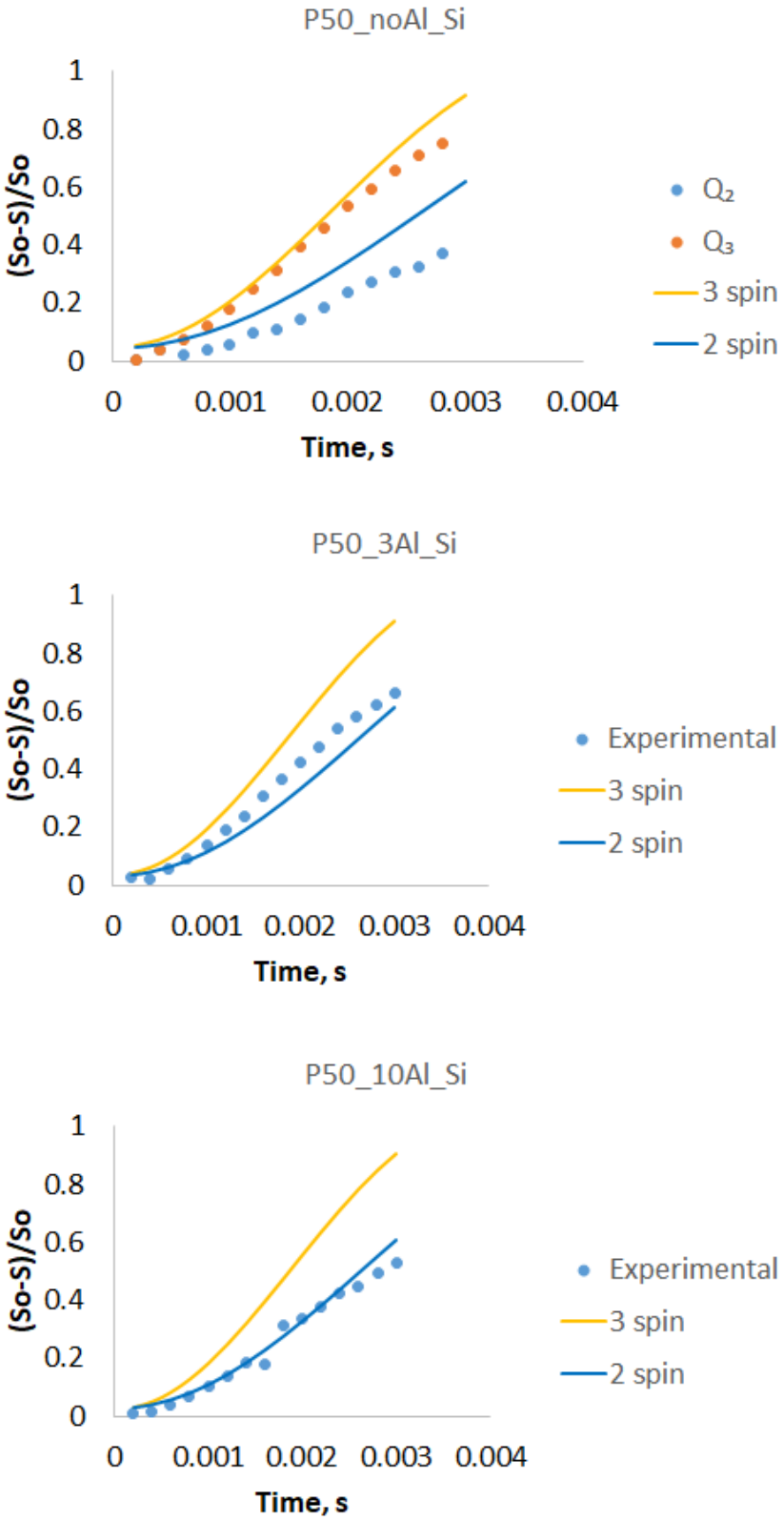

Figure 45. $^{31}P\{^{29}Si\}$ REDOR-NMR data for glasses P50_noAl_Si, P50_3Al_Si and P50_10Al_Si, obtained employing 7 T magnet. Top: blue circles: Q^2; orange circles: Q^3, middle and bottom: blue circles represent superposition of two peaks. The lines are guides for the eyes and represent results of SIMPSON simulations for 2-spin (one phosphorus and one silicon) and 3-spin systems (one phosphorus and two silicon nuclei using two-spin approximation) taking P-Si distance 3.22 Å[124].

As might be seen from the comparison of experimental results with theoretical SIMPSON simulations of $^{31}P\{^{29}Si\}$-REDOR of P50_noAl_Si glass, Q^3 phosphorus has in averaged almost two and Q^2 phosphorus almost one silicon neighbor in the second coordination sphere. Although experimental dipolar coupling are slightly smaller than observed previously in the literature[119], the results are in agreement with previous theoretical simulation and experimental results[89,119,125]. As might be see, measured dipolar couplings are getting smaller upon addition of aluminum and decreasing nominal amount of phosphorus in the oxide mixture. This speaks for distribution of silicon units in the phosphate network. This also corresponds with the fact that more and more phosphorus is connected to aluminum upon addition of aluminum.

P60 series. The results of $^{29}Si\{^{31}P\}$-REDOR NMR experiments for enriched P60 series are represented in Figure 46. The lines are guides to the eyes and represent theoretical curves obtained with simulation using SIMPSON software. "n-spin" notation in the graphs indicates the result of simulation of n-spin system (1 silicon nuclei and n-1 phosphorus nucleus) using 2-spin approximation taking P-Si distance of 3.22 Å[124], and considering the effect of CSA tensor. The intensity of the signal from SiO_4 unit in P60_3Al_Si glass was too low to quantify the $^{29}Si\{^{31}P\}$-REDOR effect. The experimental results were compared with the results of SIMPSON simulations as outlined above for P60 glasses. SiO_6 silicon units are fully or nearly fully surrounded with phosphorus as in P50 series. Experimental results obtained on P60_15Al_Si glass were difficult to estimate due to the noisy experimental data resulting from very low percentage of silicon in this glass and, therefore, should be treated carefully. Nevertheless, the results indicate that SiO_4 units in P60_15Al_Si have between two and three phosphorus in the second coordination sphere. The rest might be connected to other silicon units or to aluminum, which is less probable due to full or nearly full coordination of aluminum units by phosphorus. To support this assumption, Al-Si dipolar based experiments we carried out and are discussed in 4.1.7.

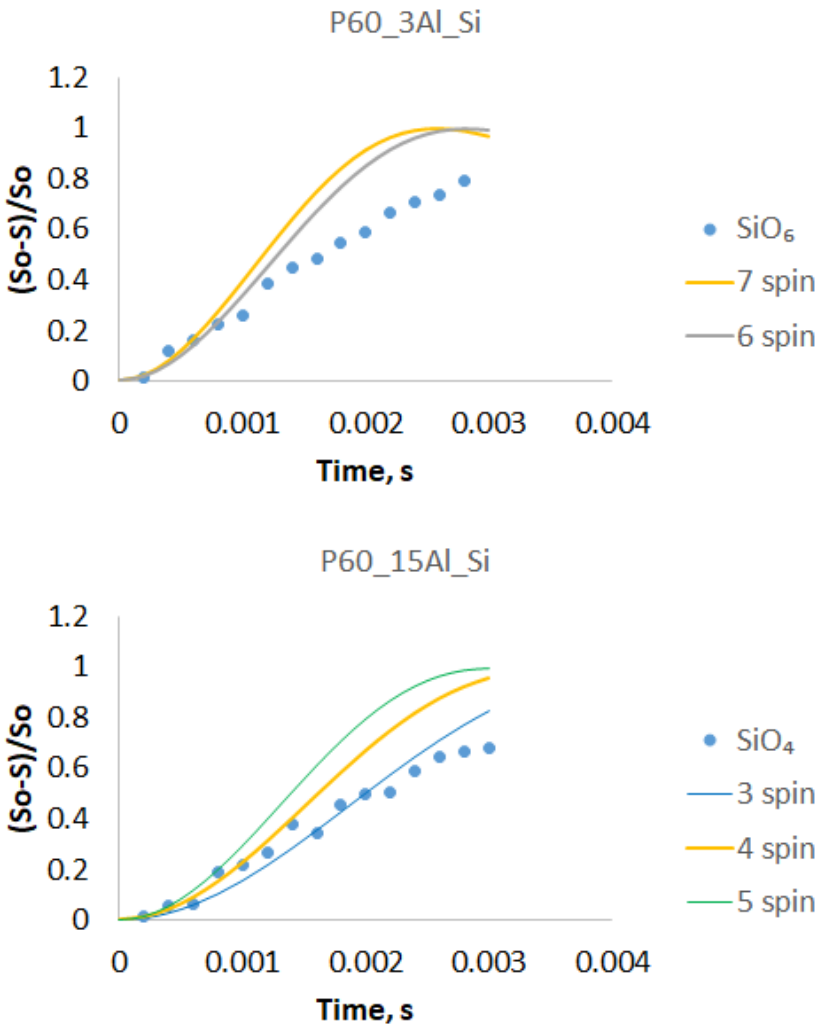

Figure 46. $^{29}Si\{^{31}P\}$ REDOR-NMR data for glasses P60_3Al_Si and P60_15Al_Si, obtained employing 7 T magnet. Top: orange circles: SiO6; bottom: blue circles: SiO4. The lines are guides for the eyes and represent results of SIMPSON simulations of n-spin system (1 silicon nuclei and n-1 phosphorus nucleus) taking P-Si distance 3.22 Å[124].

The results of $^{31}P\{^{29}Si\}$-REDOR NMR and are represented in Figure 47. The lines are guides to the eyes and represent theoretical curves obtained with simulation using SIMPSON software. "n-spin" notation in the graphs indicates the result of simulation of n-spin system (1 silicon nuclei and n-1 phosphorus nucleus) using 2-spin approximation taking P-Si distance of 3.22 Å[124], and considering the effect of CSA tensor. The results of $^{31}P\{^{29}Si\}$-REDOR NMR experiments show decreasing P-Si dipolar coupling upon addition of aluminum indicating distribution of silicon units in phosphorus network.

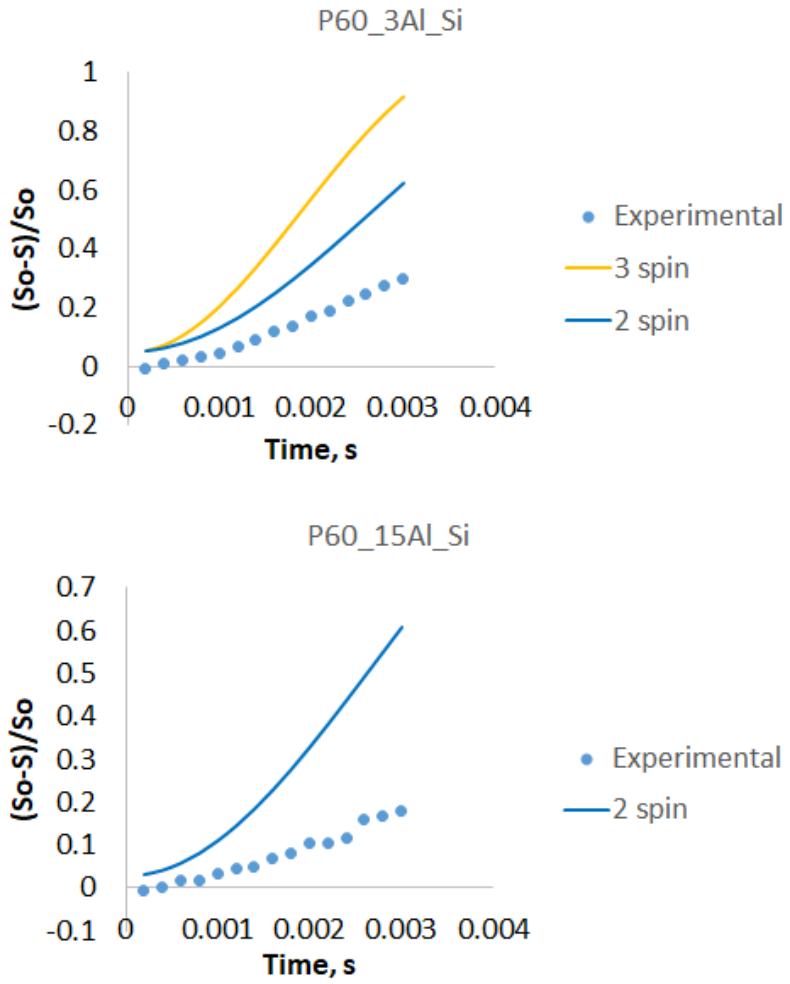

Figure 47. $^{31}P\{^{29}Si\}$ REDOR-NMR data for glasses P60_3Al_Si and P60_15Al_Si, obtained employing 7 T magnet. Blue circles: experimental data. The lines are guides for the eyes and represent results of SIMPSON simulations for 2-spin (one phosphorus and one silicon) and 3-spin systems (one phosphorus and two silicon nuclei using two-spin approximation) taking P-Si distance 3.22 Å[124].

4.1.7. $^{27}Al\{^{29}Si\}$-REDOR NMR and $^{29}Si\{^{27}Al\}$-REAPDOR NMR

The results of $^{27}Al\{^{31}P\}$ REAPDOR show that aluminum units are fully or nearly fully surrounded by phosphorus. It means that no Al-Si connections is expected in the investigated system. The results of $^{29}Si\{^{31}P\}$-REDOR indicate that SiO_4 units have two and two to three phosphorus in the second coordination sphere in P60 and P50 glasses, respectively. This leaves an open question if the remaining oxygen bridges are connected to silicon or aluminum. To clear out these uncertainties, $^{27}Al\{^{29}Si\}$-REDOR NMR and $^{29}Si\{^{27}Al\}$-REAPDOR we carried out on enriched samples.

Such as the observed dipolar couplings were small and difficult to quantify, the results are discussed qualitatively in this section using an exemplary $^{27}Al\{^{29}Si\}$ REDOR and $^{29}Si\{^{27}Al\}$ REAPDOR spectra. In Figure 48 exemplary spectra of P50_3Al_Si glass is shown. As might be

seen, there is low or negligible $^{27}Al\{^{29}Si\}$ REDOR and $^{29}Si\{^{27}Al\}$ REAPDOR effects on aluminum and silicon units even at higher rotor cycles. This implies Si-O-Al avoidance and supposes presence of Si-O-Si connections. However, upon an addition of aluminum some $^{27}Al\{^{29}Si\}$ REDOR and $^{29}Si\{^{27}Al\}$ REAPDOR effect are observed on P50_10Al_Si glasses as shown in Figure 49. This effect is small and difficult to quantify but it is clearly observable in contrast with P50_3Al_Si. It might be caused by the bulk effect or may indicate some small amount of Al-O-Si connections.

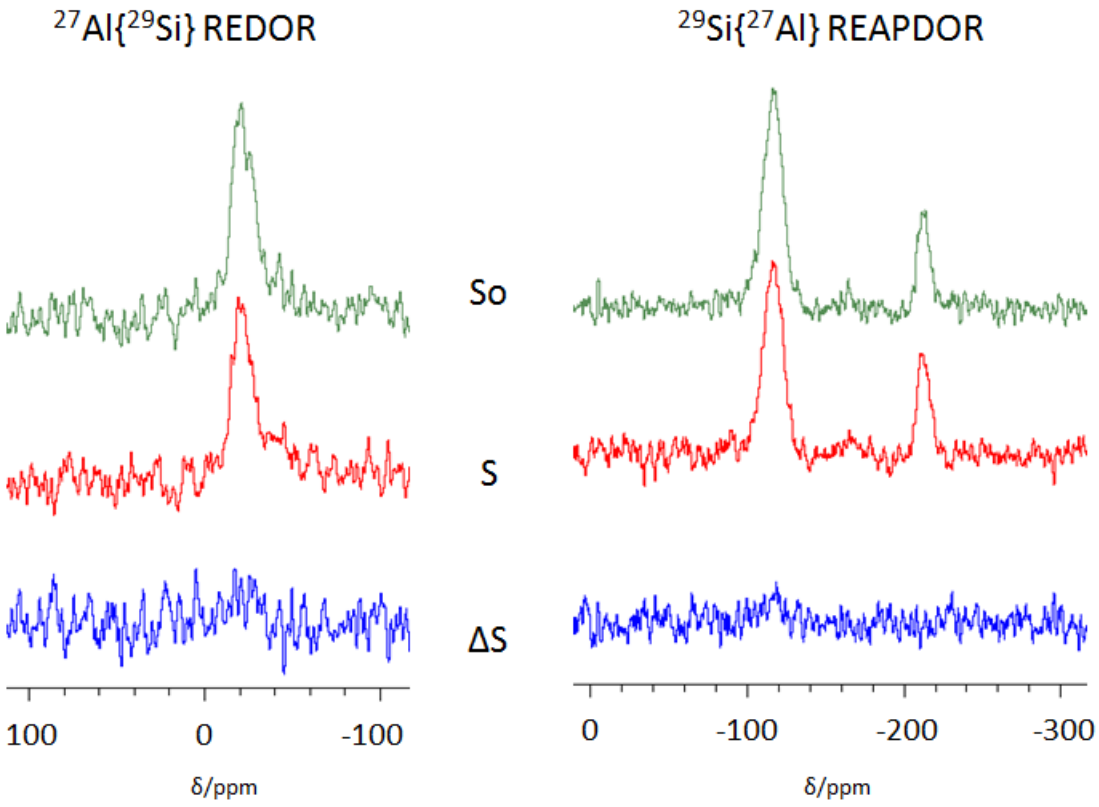

Figure 48. Exemplary $^{27}Al\{^{29}Si\}$ REDOR-NMR spectra recorded at 40th rotor cycle (left) and $^{29}Si\{^{27}Al\}$ REAPDOR-NMR spectra recorded at 30th rotor cycle for P50_3Al_Si glasses.

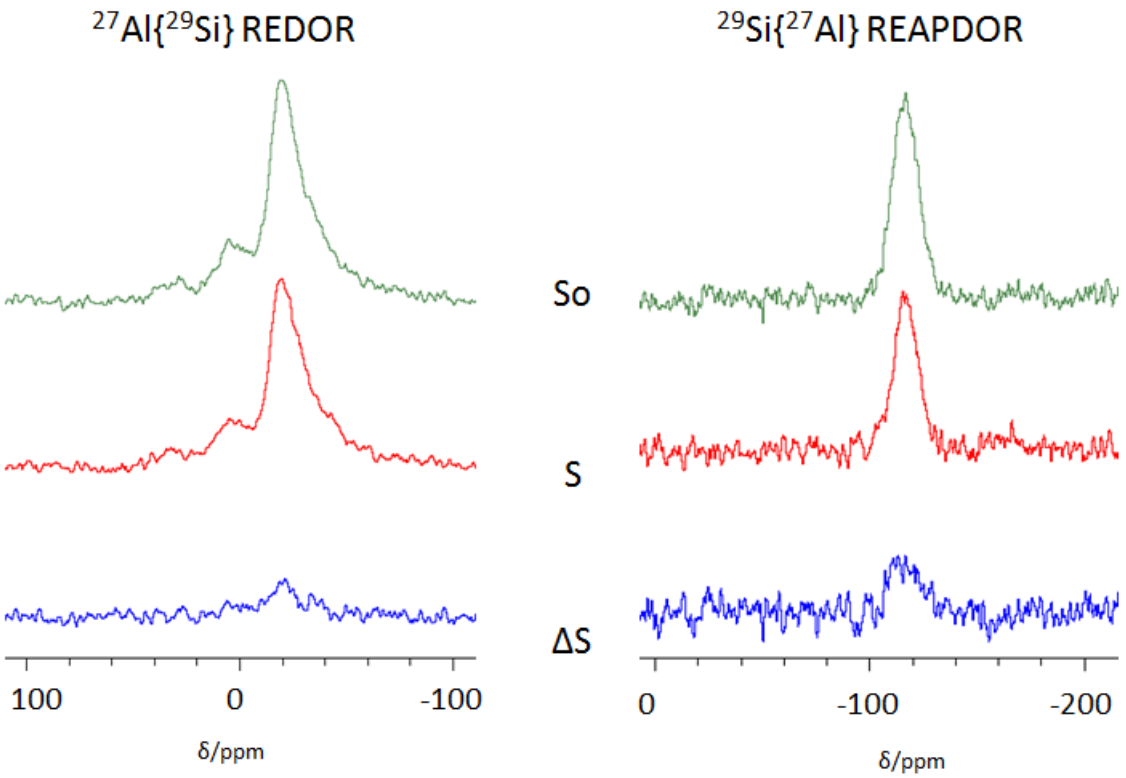

Figure 49. Exemplary $^{27}Al\{^{29}Si\}$ REDOR-NMR spectra recorded at 40th rotor cycle (left) and $^{29}Si\{^{27}Al\}$ REAPDOR-NMR spectra recorded at 30th rotor cycle for P50_10Al_Si glasses.

$^{27}Al\{^{29}Si\}$ REDOR and $^{29}Si\{^{27}Al\}$ REAPDOR exemplary spectra of P60_3Al_Si glass and P60_15Al_Si glass are represented in Figure 50 and Figure 51, respectively. Similar to P50_Si series, there is no observable effect in the glass with low aluminum percentage and some unquantifiable effect in the glass with 15 percent of Al_2O_3. The results speak for Al-O-Si avoidance in the glasses where the amount of aluminum is low. Some effect observed in the sample P60_15Al_Si may be caused by some Al-O-Si connections or by bulk effect. The results of $^{27}Al\{^{29}Si\}$ REDOR and $^{29}Si\{^{27}Al\}$ REAPDOR experiments indicate that there should be some Si-O-Si connections of SiO_4 units in the glasses with high aluminum percentage because measured $^{29}Si\{^{27}Al\}$ REAPDOR effect is not high enough for aluminum to fill free from phosphorus connections around SiO_4 units.

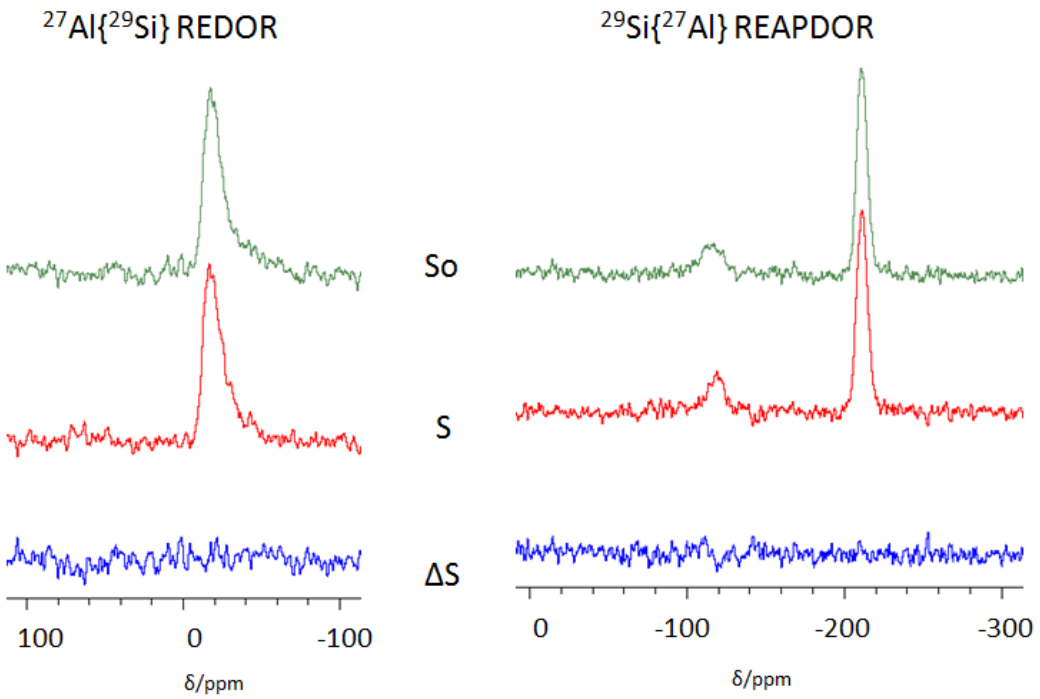

Figure 50. Exemplary $^{27}Al\{^{29}Si\}$ REDOR-NMR spectra recorded at 40th rotor cycle (left) and $^{29}Si\{^{27}Al\}$ REAPDOR-NMR spectra recorded at 16th rotor cycle for P60_3Al_Si glasses.

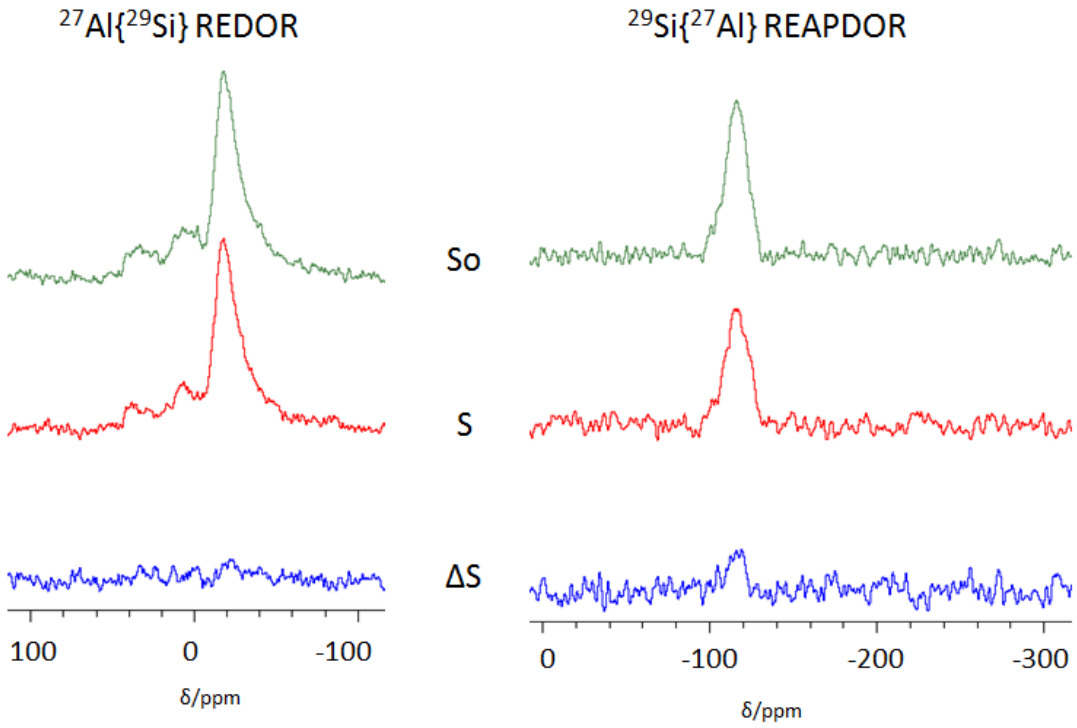

Figure 51. Exemplary $^{27}Al\{^{29}Si\}$ REDOR-NMR spectra recorded at 40th rotor cycle (left) and $^{29}Si\{^{27}Al\}$ REAPDOR-NMR spectra recorded at 22nd rotor cycle for P600_15Al_Si glasses.

4.1.8. Q^2 and Q^3 Affinity to Silicon and Aluminum

In 4.1.6 when discussing the site-resolved results of $^{31}P\{^{29}Si\}$-REDOR NMR for P50_noAl_Si glass it was noticed Q^3 units have higher $^{31}P\{^{29}Si\}$-REDOR effect than Q^2 units in the glass

without aluminum. It was also mentioned that site-resolved quantitative estimations were not possible for other sample due to broadening of phosphorus signals. Still, in the samples with three percentage of aluminum, two signals, although severely overlapping and not suitable for individual deconvolution, are distinguished and the results might be discussed qualitatively.

In Figure 52 the exemplary spectra $^{31}P\{^{29}Si\}$-REDOR spectra of enriched glass P60_3Al_Si are represented. As might be seen, the effect is much higher on Q^3 signal then on Q^2 signal. This indicate that Q^3 units have more P-O-Si connections than Q^2 units. Although both SiO_4 and SiO_6 species are present in this sample and the effect might be also explained by Q^3 units grouping around both silicon units, the previous research[89,119,125] suppose that Q^3 phosphorus units are mostly connected to SiO_6 species and SiO_4 units are surrounded by both Q^3 and Q^2 species. This might indicate that the observed difference of $^{31}P\{^{29}Si\}$-REDOR effects is mostly caused by the presence of SiO_6-O-P(Q^3) connections. The tendency of SiO_6 units to be coordinated with Q^3 phosphorus is explained in previous research by the bond valence gradient of SiO_6-O-P(Q^3) linkage which leads to charge redistribution around SiO_6 units which is favorable for presence of two sodium units needed for charge-compensating of SiO_6[125].

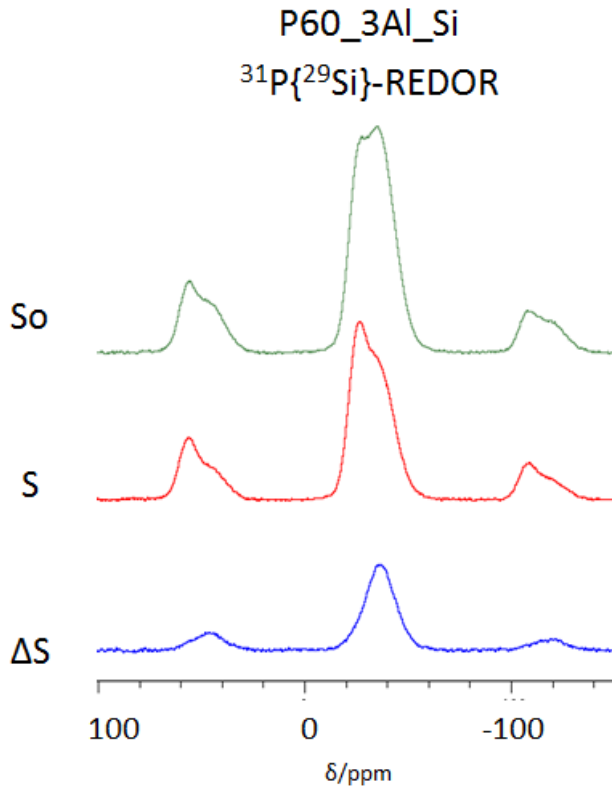

Figure 52. Exemplary $^{31}P\{^{29}Si\}$ REDOR-NMR spectra recorded at 30th rotor cycle for P50_3Al_Si and P60_3Al_Si glasses.

In Figure 53 exemplary results of $^{31}P\{^{27}Al\}$-REAPDOR are represented for the same enriched glasses. In contrast to $^{31}P\{^{29}Si\}$-REDOR, $^{31}P\{^{27}Al\}$-REAPDOR effects are similar for both Q^2 and Q^3 phosphorus peaks. It indicates that AlO_6 is probably surrounded evenly by both phosphorus species. Probably, this indiscrimination toward bridged phosphorus might explain why six-coordinated aluminum is preferred over six-coordinated silicon: coordination of silicon with mostly Q^3 phosphorus is energetically more demanding than coordination of aluminum by random phosphorus species.

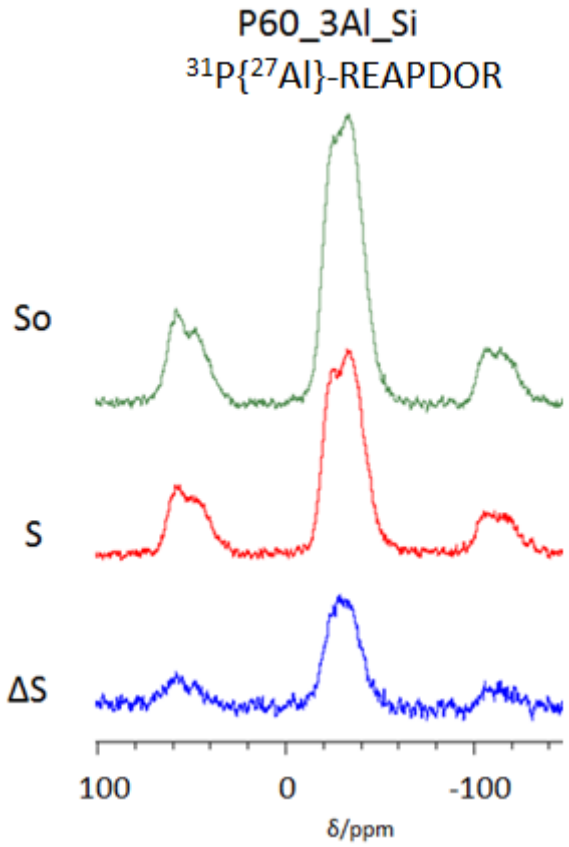

Figure 53. Exemplary $^{31}P\{^{27}Al\}$ REAPDOR-NMR spectra recorded at 40th rotor cycle for P50_3Al_Si and P60_3Al_Si glasses.

Coordination of aluminum by Q^3 and Q^2 phosphorus species is also in a good correlation with the changes observed in ^{31}P spectra: in P50 series in the samples P50_noal-P50_1Al where ^{31}P signals could be unambiguously simulated with dmfit software (contrary to P60_3Al spectrum) growth of the amount of Q^2 phosphorus units is observed. If six-coordinated aluminum, which is surrounded evenly by Q^2 and Q^3 phosphorus, substitutes six-coordinated silicon which prefers Q^3 units, the amount of Q^2 fraction in ^{31}P spectra should initially increase upon addition of aluminum.

4.1.9. Glass Structure at Ambient

Based on combined results of ^{31}P, ^{27}Al, ^{29}Si, $^{31}P\{^{27}Al\}$-REAPDOR and $^{27}Al\{^{31}P\}$-REDOR, ^{31}P-MAT, $^{29}Si\{^{31}P\}$-REDOR and $^{31}P\{^{29}Si\}$-REDOR, $^{27}Al\{^{29}Si\}$-REDOR and $^{29}Si\{^{31}P\}$-REDOR experiments and observations made by previous researches the structure of the glasses network might be described. Phosphate network consists of Q^2 chains connected through Q^3 phosphorus elements. Silicon is either present as SiO_6 in P60 base glass or as mixture of SiO_4 and SiO_6 in P50 base glass in accordance with previous research. Incorporated aluminum substitutes six-coordinated silicon, which gets four-coordinated. At low amounts of incorporated Al_2O_3 six-coordinated aluminum species prevail. With more added Al_2O_3 the amount of AlO_6 species decreases and the amount of AlO_5 and later AlO_4 species increases. In both series, incorporated aluminum and silicon units are distributed in phosphorus network.

Dipolar-based NMR experiments showed that SiO_6, AlO_4, AlO_5 and AlO_6 are fully or nearly fully coordinated by phosphorus, which makes Al-O-Al and Al-O-Si connections improbable. SiO_4 units are surrounded by two to three silicon and the rest of the bonding oxygen is connected to other Si units and might build minor amount of SiO_4-O-AlO_4 connections. The proposed structure of alkali phosphorus aluminosilicate glass is shown in Figure 54.

SiO_6 units are preferred to be surrounded by Q^3 rather than by Q^2 phosphorus units. Q^2 and Q^3 units have the same amount of AlO_6 in the surrounding. This might explain why six-coordinated silicon is preferred over six-coordinated aluminum. Tendency of SiO_6 units to be coordinated with Q^3 phosphorus species might be explained by the charge distribution in SiO_6-O-Q^3 bonds favorable for presence of sodium ions needed to charge-balance SiO_6.

In the P50 row, when P/(Al+Si) ratio is low and the system is already so saturated with silicon that there is not enough phosphorus to six-coordinate all initially available silicon, incorporation of aluminum does not lead to increase in the overall amount of six-coordinated species. SiO_6 units are replaced by AlO_6 and silicon becomes 4-coordinated. Moderate changes of the amount of six-coordinated units correspond well with the trends observed in Tg. On the contrary, in the P60 row with high P/(Al+Si) ratio there is enough available phosphorus to six-coordinate added aluminum. Due to high initial P/(Al+Si) ratio the overall amount of six-coordinated species increases with added Al_2O_3 and, subsequently, stability of the glass and Tg increases.

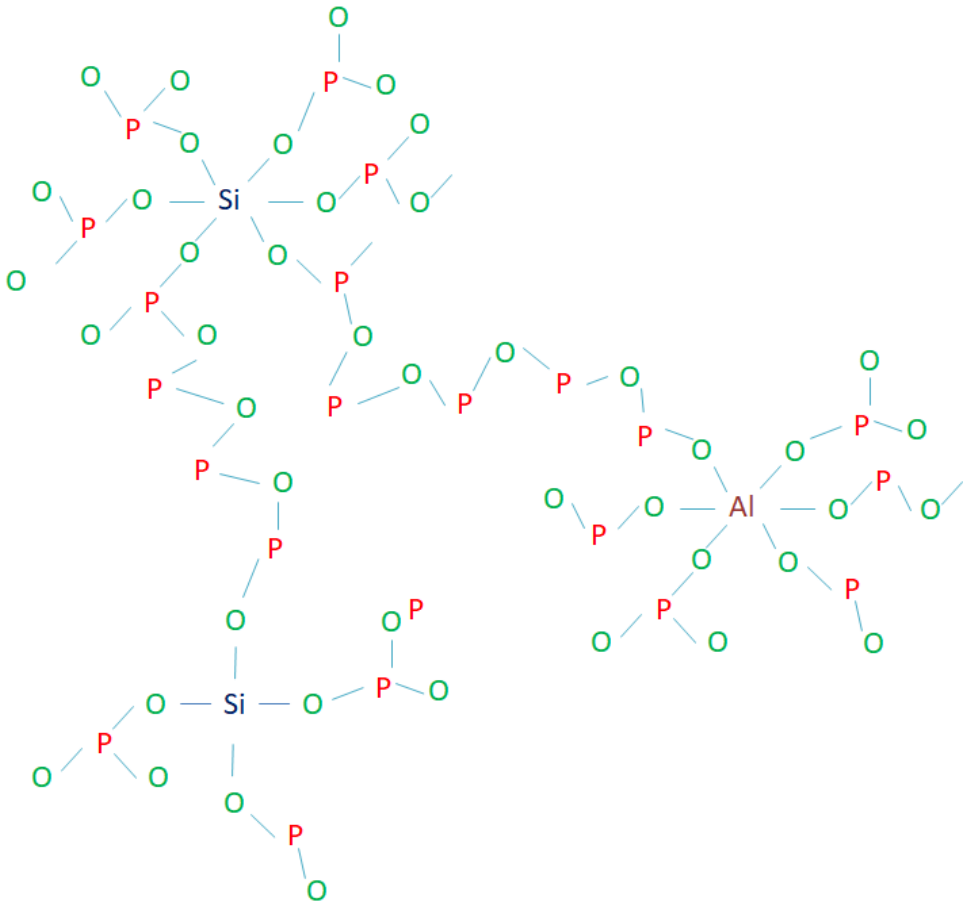

Figure 54. Proposed structure of sodium phosphoraluminosilicate glasses.

4.1.10. In-situ High Temperature Measurements

In previous sections of this chapter, the structure of phosphosilicate glasses and its transformation upon addition of aluminum was discussed based on the results of *ex situ* experiments at room temperature. Other way might be undertaken to investigate network connectivity, namely, *in-situ* NMR. This allows to follow glass organization around and above glass temperature transition, glass dynamics, relaxation processes and crystallization. This was possible due to novel method of induction heating developed by Holger Kirchhain[116] which enables to carry out *in-situ* NMR experiments at higher temperatures under high rotation speeds. This, subsequently, allows to distinguish an effect of high temperature to e. g. distinct phosphate units. In this chapter, the results of *in-situ* ^{27}Al and ^{31}P MAS NMR performed on P60_noAl and P60_10Al glasses are represented and discussed. The experiments were carried out together with the author of the novel method.

Figure 55 shows the evolution of ^{31}P spectra of the glass P60_noAl with increasing temperature. At the room temperature, the spectrum is similar to ^{31}P spectra obtained in the

field of 11 T. When the temperatures increase, phosphorus signal is first getting narrower which is most probably caused by thermal motion. From the spectra, the overall offset of dynamics resulting in less intense sidebands at the temperature around 400 °C can be seen. From the temperatures of about 600 °C, the intensity of the spinning sidebands is decreasing further. The dynamics of the phosphorus nuclei is so fast that NMR measurements time scale is too long to observe CSA tensors which are averaged out by thermal motion.

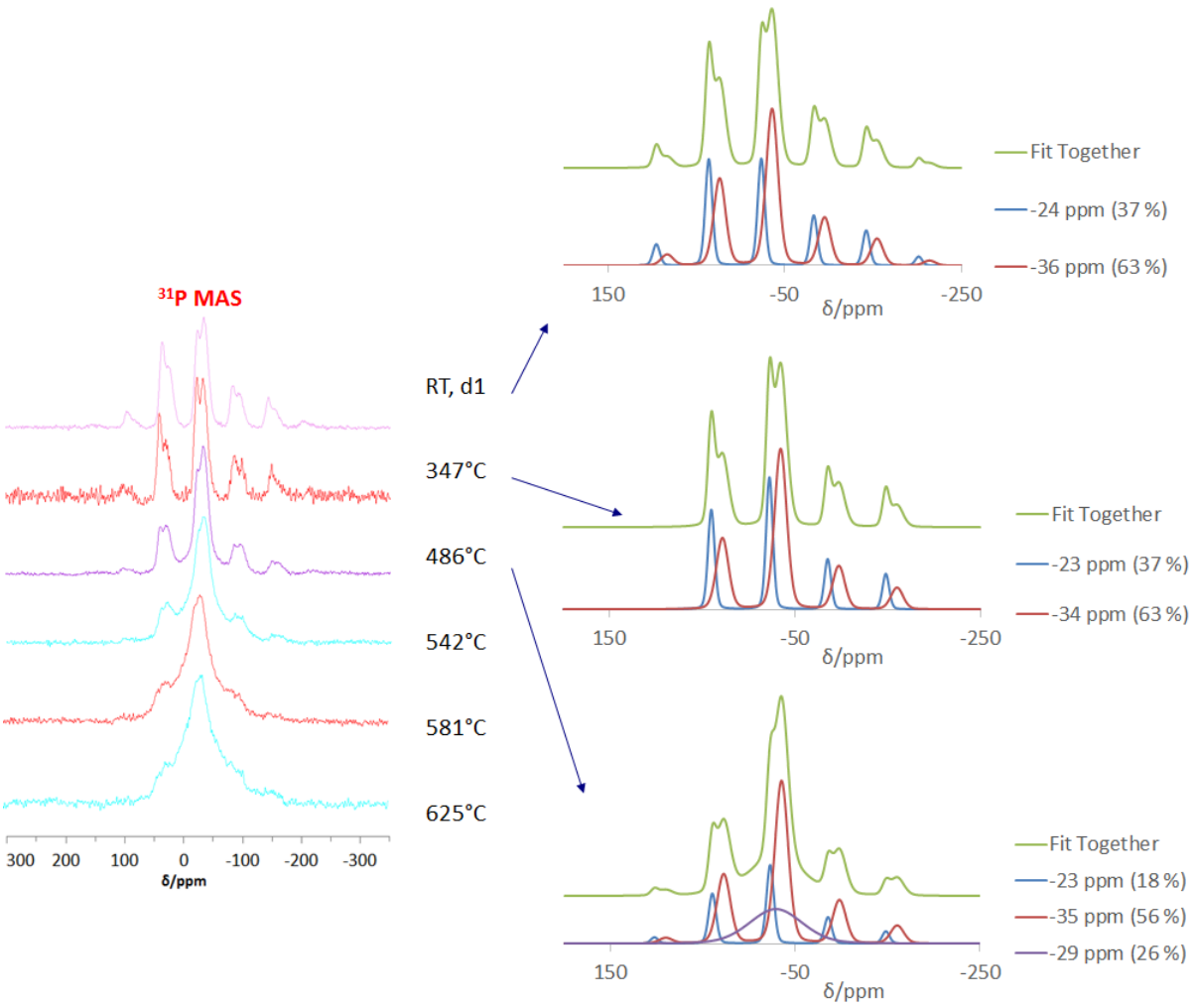

Figure 55. Left: In situ ^{31}P-MAS NMR spectra of glass P60_noAl, obtained at B0 = 7.04 T and employing repetition times of d1 = 1 s. Right: in situ ^{31}P-MAS NMR spectra together with the deconvolution into Q^2 and Q^3 contributions.

The novel methods of inductive heating allowed to increase spinning speeds, so that the estimation of contributions of Q^2 and Q^3 units to phosphorus spectra became possible. In Figure 55 on the right the deconvolutions of spectra at room temperature, at 347 °C, and at 486 °C are shown. At room temperature, 37 % of signal area is attributed to Q^2 phosphorus and 63% is attributed to Q^3 phosphorus. At 486 °C only 18% of the signal is attributed to Q^2 phosphorus and 56% to Q^3 phosphorus. The rest is assigned to the broad peak centered between Q^2 and Q^3 signals coming from dynamic processes in the glass. This indicates that Q^2 phosphorus gets mobile first or higher part of it gets mobile followed by Q^3 at higher temperatures which is in accordance with previous findings[119]. At even higher temperature of 625 °C the coalescence of two signals is observed. It means that the speed of exchange between these two groups is close to the frequency difference of the corresponding signals. From the previous research[119] we know that SiO_6 is connected through phosphorus bridges to Q^3 phosphorus and these constellation are connected further through cross-linked phosphorus chains. Combining this with observation made during *in-situ* experiments, one might propose that SiO_6-O-Q^3 clusters are more stable and that connecting phosphorus chains are destroyed first, followed by leave of Q^3 species from SiO_6 surrounding.

^{31}P and ^{27}Al spectra of P60_10Al Glasses are represented in Figure 56. It might be immediately seen that added aluminum significantly increased stability of the glass structure. The dynamic processes marked by reduced intensity of spinning sidebands and the broad peak in phosphorus spectra first appear at the temperatures above 700 °C. Around the same temperature transformation of AlO_x species starts which has already been observed in aluminophosphate and aluminosilicate glasses[119,126,127]. Center of gravity of aluminum peak shifts from -17 to -11 ppm from RT to 771 °C. This shift is not probable to be caused by the changing temperature of the shim coil, which is affected only slightly in this novel inductive heating in-situ NMR method ([128] and exemplary typical changes of the shim coil temperature shown in Figure 144 in Appendix 8) and is must probably induced by the changes in the glass network. Similar effects were already observed in aluminophosphate glasses[126,127,129]*. However, it is not possible to say if these changes reflect exchange processes between different aluminum species or are caused by structural relaxations because higher *in-situ* measurement temperatures were not possible.

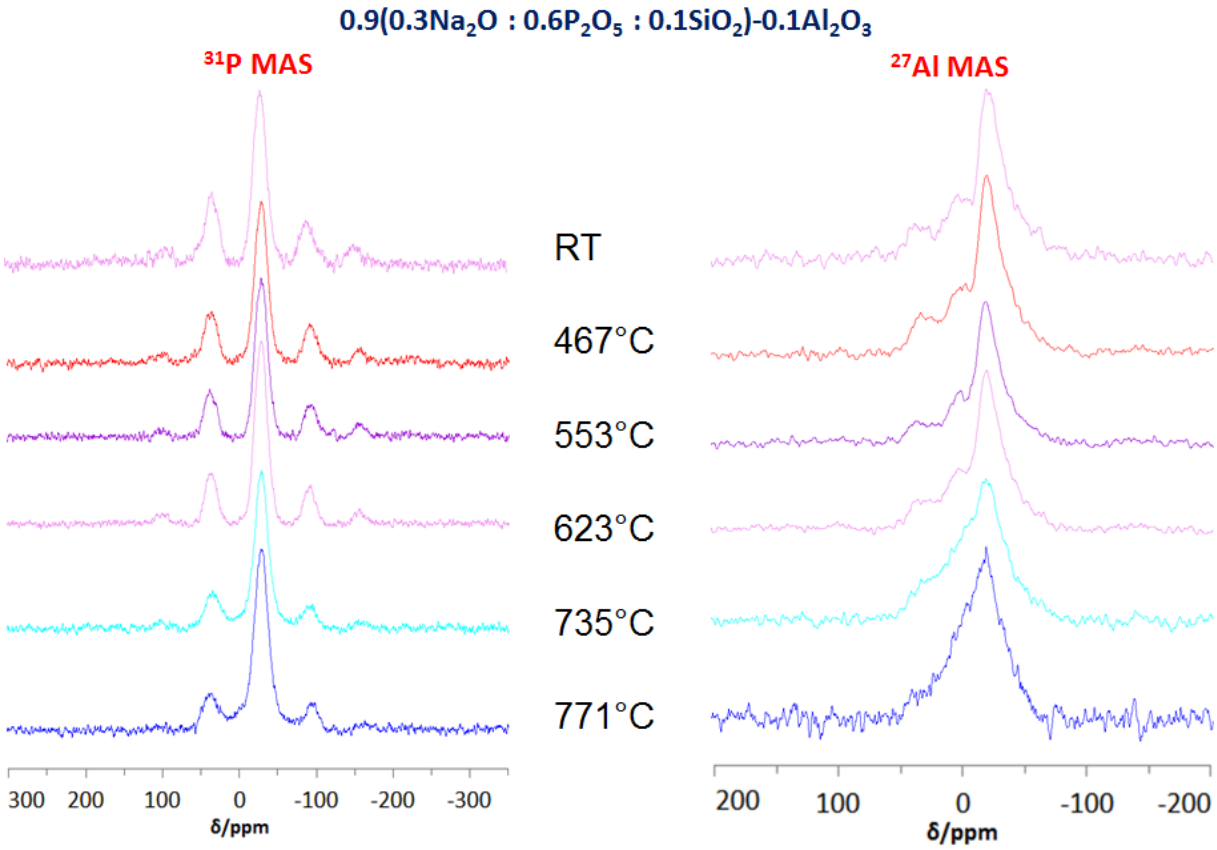

Figure 56. In situ ^{31}P-MAS (left column) and ^{27}Al-MAS (right column) NMR spectra of glass P60_10Al obtained at B0 = 7.04 T, employing repetition times of 1 s (31P) and 0.1 s (^{27}Al).

4.2. Silicon-Rich System

Alkali aluminosilicate glasses are important for modern science and technology such as they found their way in a wide range of technological applications. Aluminosilicate glasses are used in optical telecommunication[130,131], as nuclear waste hosts[132], glass composites seals and as catalyst for petroleum[133]. Pure glassy silica consists of four-coordinated silicon units (Si^4) giving rise to a peak centered about -112 ppm. Addition of alkali ions to the composition leads to depolymerization of the network, so, that different silicon units with three to zero bridging oxygens might be formed. Aluminum added to these glasses in principle can work as network former and network modifier. Previous studies on Na_2O-A_2O_3-SiO_2 system (NAS) system concentrated on the question of the nature of aluminum and silicon units in the alkali silicon glasses, their connectivity and distribution of sodium ions. Structural units of the glass network depend strongly on the ratio of alkali ions to aluminum. If their amount is equal, sodium is used to charge-balance aluminum and the network consists of silicon and aluminum interconnected four-coordinated units. In the glasses with Na/Al ratio > 1, sodium ions are used to charge-balance tetrahedral aluminum and the excess of them depolymerizes phosphorus units. In the glasses with Na/Al ratio < 1, available sodium connects to aluminum and the rest of aluminum species are existing as of AlO_5 and AlO_6 species[134] leading to depolymerization of silicon network. Furthermore, charge-balance might be also reached if triclusters are formed in the glass network which is supported by ^{17}O NMR[135,136].

Additions of small amount of phosphorus to aluminosilicate glasses decreases their glass transition temperatures and, therefore, improves their processability. They are of special interest or glass making and ceramics[137] an also for geological studies[138] because addition of small percentage of phosphorus changes their viscosity[139]. Whereas the structure of phosphorus-free aluminosilicate glasses was subjected to the wide range of research, there are not many studies devoted to the investigation of phosphorus units in alkali aluminosilicate glasses. Previous NMR and Raman studies of the glass systems focused on addition of small percentage of phosphorus to aluminosilicate systems with different alkali/aluminum ratios suggest different roles of phosphors incorporation depending mainly on Na(K)/Al ratio. The proposed mechanisms are not consistent. For example, there is lack of cogency regrading formation of P-O-Si bonds, or amount of $AlPO_4$ formed. In the glasses with alkali/Al ratio > 1

(peralkaline glasses) in potassium aluminosilicate systems system Raman and ^{31}P NMR studies propose that excess of alkali cations connect to phosphorus leading to appearance of monomers, dimers and phosphorus chains (with increasing amount of phosphorus) and that potassium ions are taken from $Si^{(3)}$ units increasing the polymerization of the network[140]. Raman study on sodium aluminosilicate proposes coexistence of PO_4 units and P_2O_7 units together with $AlPO_4$ as charge-compensating mechanism[139]. NMR-based studies of similar same system propose existence of some phosphate dimers and phosphate tetrahedra with tree oxygen bridges attached prevailing to one sodium and two aluminum atoms[85]. In lithium aluminosilicate glasses ^{31}P and $^{27}Al\{^{31}P\}$ D-HMQC (Dipolar Heteronuclear Multiple-Quantum Coherence) studies propose coexistence of PO_4^{3-} and $P_2O_7^{4-}$ species surrounding by lithium together with PO_4^{3-} species where lithium is substituted by one or two aluminum atoms whereas the latter is dominant phosphorus structural unit at higher aluminum content[141]. In the glasses with alkali/aluminum ratio equal to one (sub aluminous), Raman-based and ^{31}P studies on potassium aluminosilicate systems propose coexistence of $AlPO_4$ and potassium phosphate KPO_3 units[140]. Other Raman studies on sodium aluminosilicate propose incorporation of phosphorus in form of $AlPO_4$ as major units in coexistence with $P2O_7$ unis[139]. NMR-supported investigations imply phosphorus incorporation mainly as monomeric phosphorus tetrahedra connected to three four-coordinated aluminum atoms[85]. In the glasses with Al/alkali ratio more than one (peraluminous glasses) Raman and ^{31}P NMR studies on potassium aluminosilicate system propose mainly formation of $AlPO_4$ units residing mostly outside of the aluminosilicate network and no evidence for P-O-Si bonds[140]. Raman studies on mixed alkali aluminosilicate also imply $AlPO_4$ as major phosphorus units but linked to the network through P-O-Si bridges and small amount of ortho and pyrophosphates[142]. Other Raman studies on potassium aluminosilicate system propose $AlPO_4$ as major structural units although some small amount of P_2O_7 was proposed for glasses with high Na amount[139]. Multinuclear NMR study on similar system proposes phosphorus units with four oxygen bridges is a major phosphorus unit[85]. Other NMR investigations propose general scheme of phosphorus incorporation implying existence of Na_3PO_4 and $Na_4P_2O_7$ as major units at low Al/Na ratio and appearance of oxygen tetrahedra with one to four bonding atoms having more bonding oxygen as relative to sodium amount of aluminum increases[143].

In attempt to clear these ambiguities, several starting base compositions with 50-70 m. p. of SiO_2 and equal amount of sodium and aluminum oxides were chosen for this study. In these

glasses, aluminum is expected to be charge-balanced by sodium ions and the glass network to consist of interconnected aluminum and silicon tetrahedra. The evolution of the glass network under addition of 2.5-7.5 m. p. of P_2O_5, redistribution of alkali ions, structural units of aluminum and silicon, nature of aluminum as network former and network modifier and phosphorus environment were investigated first by means of ^{31}P, ^{27}Al and ^{29}Si MAS NMR. To gain more information about nature of aluminum as network former and network modifier, ^{27}Al MQMAS was carried out. To obtain information about CSA tensor of individual phosphorus units and investigate polymerization of phosphorus units, ^{31}P MAT NMR and $^{31}P\{^{23}Na\}$-REAPDOR were performed. To support or reject assumptions about presence of $AlPO_4$ and triclusters units as charge-compensating mechanisms, gain more information about connectivity of aluminosilicate network, to understand better how phosphorus units are connected to the network and found out more information about absence and presence of P-O-Si bridges, dipolar-based experiments were carried out (experiments involving silicon were performed on a glass enriched with ^{29}Si). Additionally, dynamics of the sodium ions was investigated *in-situ*. Correlation between network organization and macro properties were observed and discussed.

4.2.1. EDX Results

Results of EDX analysis of some glasses carried out at the University of Jena are represented in Table 14. It might be seen, that in silicon-rich glasses there is no significant loss of phosphorus during heating. It might be explained by very high visually perceived viscosity of silicon-rich melts comparing with phosphorus-rich melts. Slightly elevated percentage of aluminum might be explained by aluminum leaching from Al_2O_3 crucible.

Probe Name		**SiO_2**	**P_2O_5**	**Al_2O_3**	**Na_2O_3**
Si60_P0	Nominal composition	60.0	-	20.0	20.0
	EDX results	59.6±2.1	-	20.7±1.0	19.8±1.3
Si60_P5	Nominal composition	60.0	5.0	17.5	17.5
	EDX results	58.8±2.2	4.7±0.2	19.3±1.0	17.2±1.1

Si60_P7.5	Nominal composition	60	7.5	16.25	16.25
	EDX results	59.4±2.2	7.3±0.3	16.9±0.8	16.3±1.1
Si70_P7.5	Nominal composition	70	7.5	11.25	11.25
	EDX results	70.2±2.7	7.3±0.3	11.6±0.6	10.9±0.8

Table 14. Comparison of nominal glass composition and EDX results of silicon-rich glasses.

4.2.2. Glass Transition Temperature and Density Measurements

Results of density and Tg measurements carried out by cooperation partners at the University of Jena are represented in Figure 57. It can be seen that in all three glass series addition of phosphorus leads to lower density values and decreases Tg. Furthermore, Tg increases and the density decreases with increasing silicon contents in phosphorus-free glasses and density decreases in the glasses with 7.5 m. p. of P_2O_5 with growing silicon content.

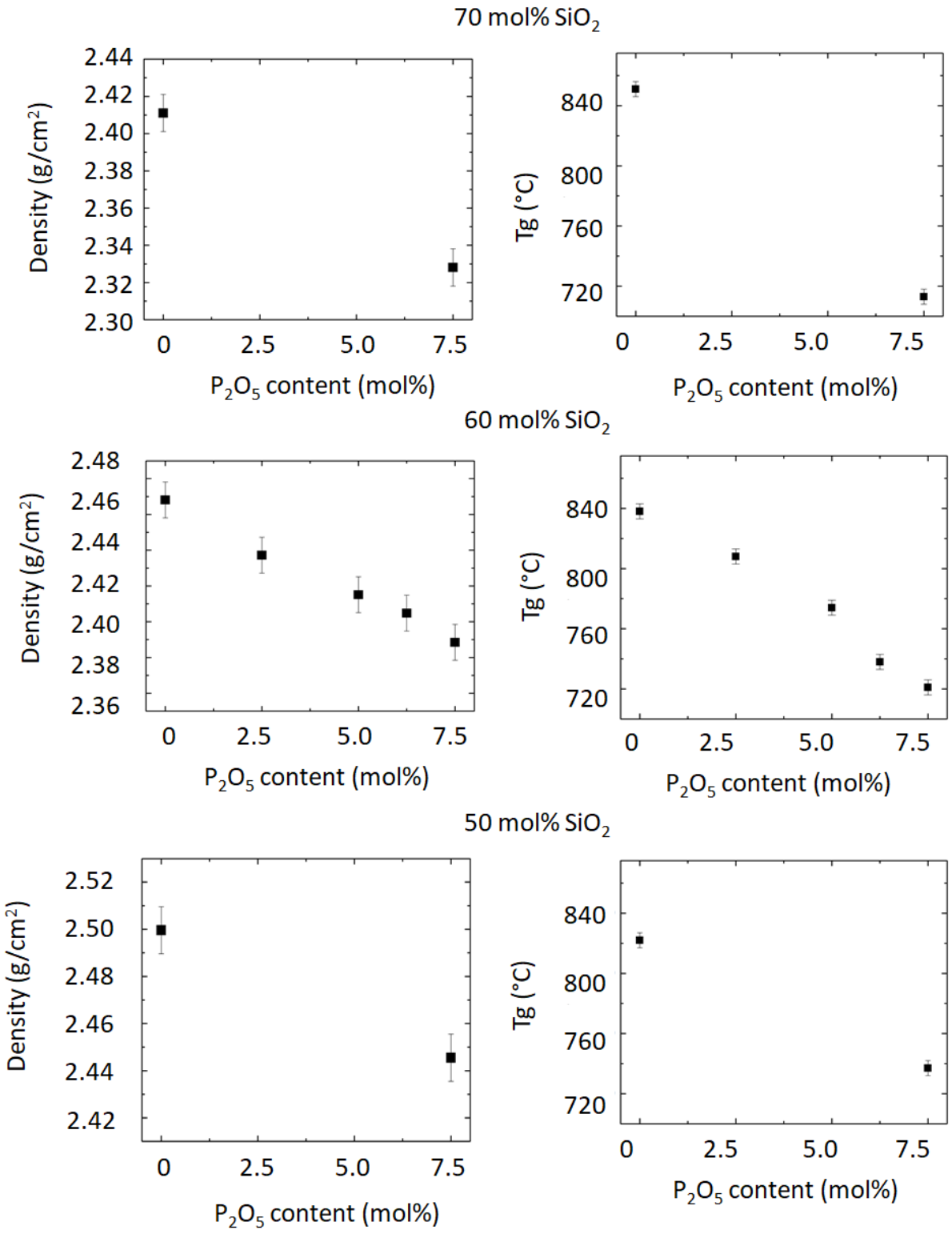

Figure 57. Measured and Tg density of investigated glasses depending on phosphorus content.

4.2.3. ^{27}Al-MAS and MQMAS NMR

In this systems in the glasses with no phosphorus was added to base composition (Si50-Si70 glasses), each four-coordinated aluminum atom is expected to be charge-balanced by one sodium atom. To understand structural reorganizations of the system upon addition of phosphorus it is essential to understand the nature of aluminum units and their distribution. That is why MAS NMR, MQMAS NMR and dipolar-based experiments were carried out on silicoaluminate system.

^{27}Al MAS NMR. To identify coordiantion of aluminum, ^{27}Al MAS NMR was carried out on the availiable samples. The results of ^{27}Al-MAS NMR for Si50(5), Si60 and Si70 series are represented in Figure 58. In all samples one signal broadened by second order quadrupolar interaction and centered around 50 ppm is observed. The shape of the observed signals (tailing to the lower frequencies) is probably due to the distribution of quadrupolar parameters which is characteristic for glasses. Chemical shift of the signal (summarized in Table 15) suggests that aluminum is present mostly in form of tetrahedral units. Increasing phosphorus content leads to the broadening of the spectra probably indicating higher diversity of adjacent units which might be proved by dipolar-based experiments (see 4.1.5-4.1.7). Figure 59 reveals isotropic chemical shift of ^{27}Al depending on ^{29}Si and ^{31}P content. For aluminum, isotropic chemical shift was defined by simulating spectra with Czjzek model using DMFIT program. With higher Si/Al ratio, the signal is shifted to the more negative ppm and with higher P/Al ratio to more positive ppm which might indicate substitution of –Al-O-P- bonds by –Al-O-Si bonds or, less probable, by Al-O-Al bonds[144–147]. Because AlO_4 signal has highly anisotropic shape of the peak, other aluminum signals (AlO_5 and AlO_6) could be present but not seen. Therefore, we cannot state the absence of other units present but not distinguishable in the tail of broad AlO_4 peak based on results from single pulse experiment alone. Such as the nature of aluminum units is crucial for understanding of sodium ions distribution in the glass upon addition of phosphorus, ^{27}Al MQMAS was performed and the results are discussed in the next section.

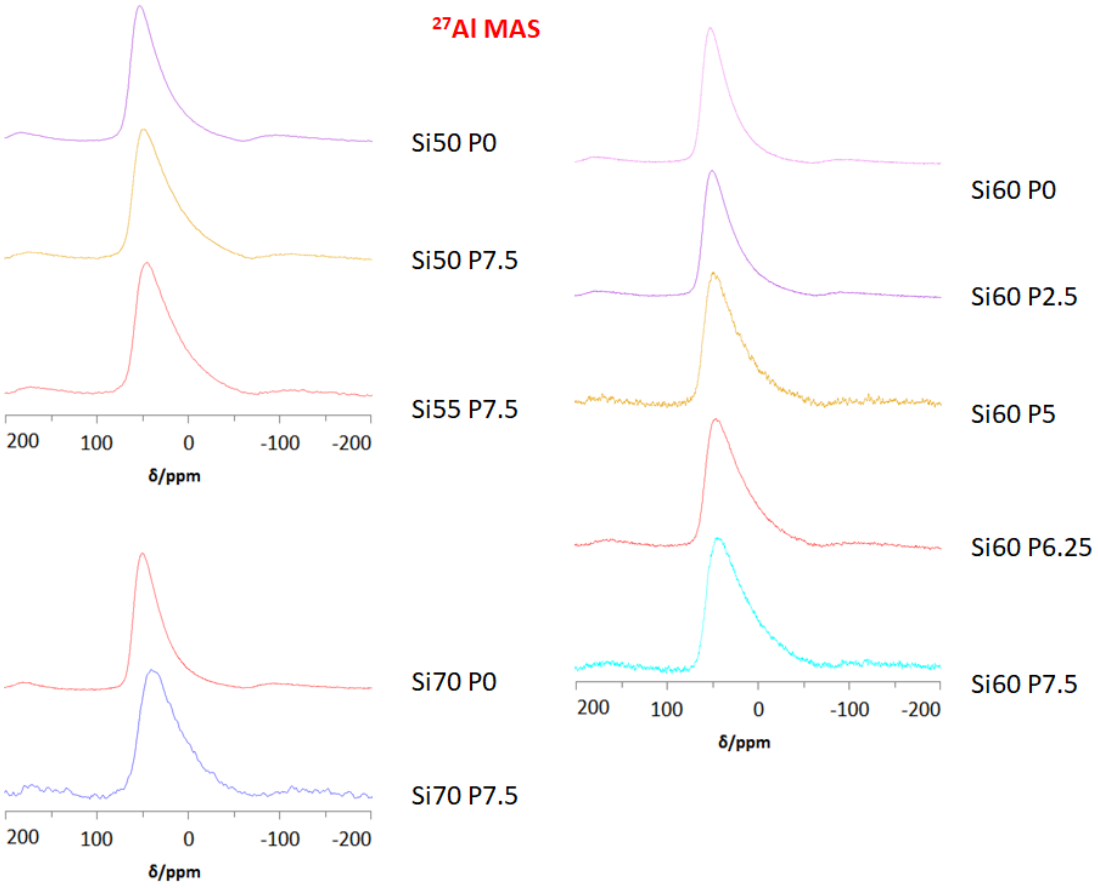

Figure 58. ^{27}Al-MAS spectra of Si50 and Si55 series (top left), Si70 (bottom left) and Si60 series (right) glasses obtained at Bo = 7 T.

		Si, m. p.			
		50	55	60	70
P, m. p.	0	65		63	60
	2.5			62	
	5			61	
	6.25			60	
	7.5	62	60	59	55

Table 15. ^{27}Al chemical shift values obtained from a simulation of the spectra using the DMFIT software

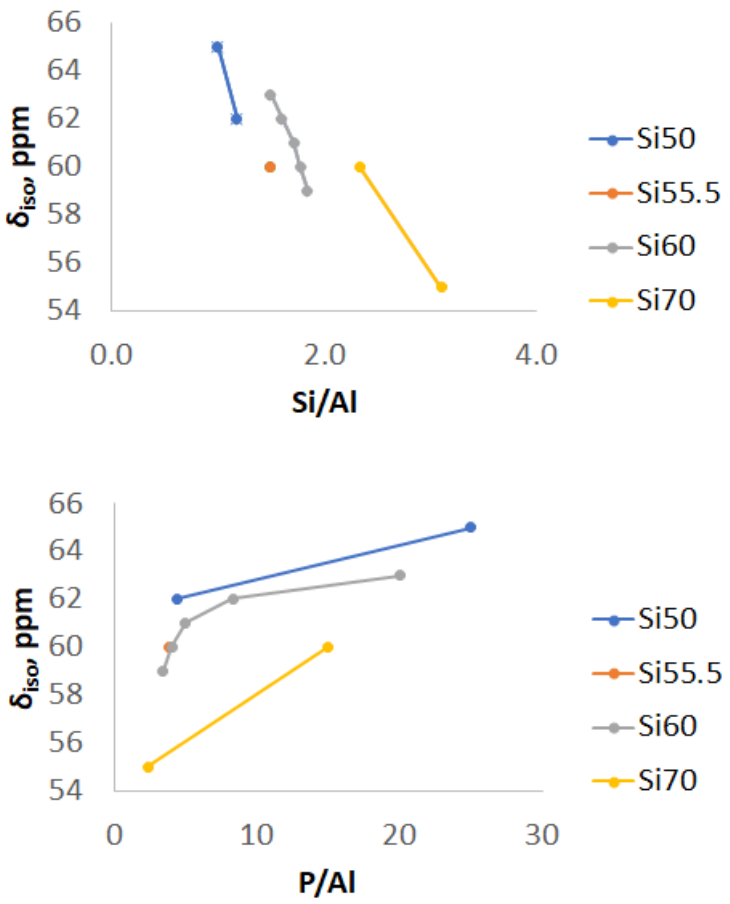

Figure 59. ^{27}Al chemical shift values depending on Si/Al and P/Al ratio.

^{27}Al MQMAS. Such as aluminum AlO_4 signal is broadened by second order quadrupolar interaction, AlO_5 and AlO_6 signals might be present but not distinguishable in ^{27}Al MAS NMR spectra. To identify individual aluminum units having different isotropic chemical shift, MQMAS[1,2] measurements were carried out on the samples Si60_P2.5 and Si60_P7.5. The results are represented in Figure 60. As might be seen, MQMAS spectra clearly show only AlO_4 as structural units. Therefore, aluminum is a network former independent of glass composition.

^{27}Al MQMAS

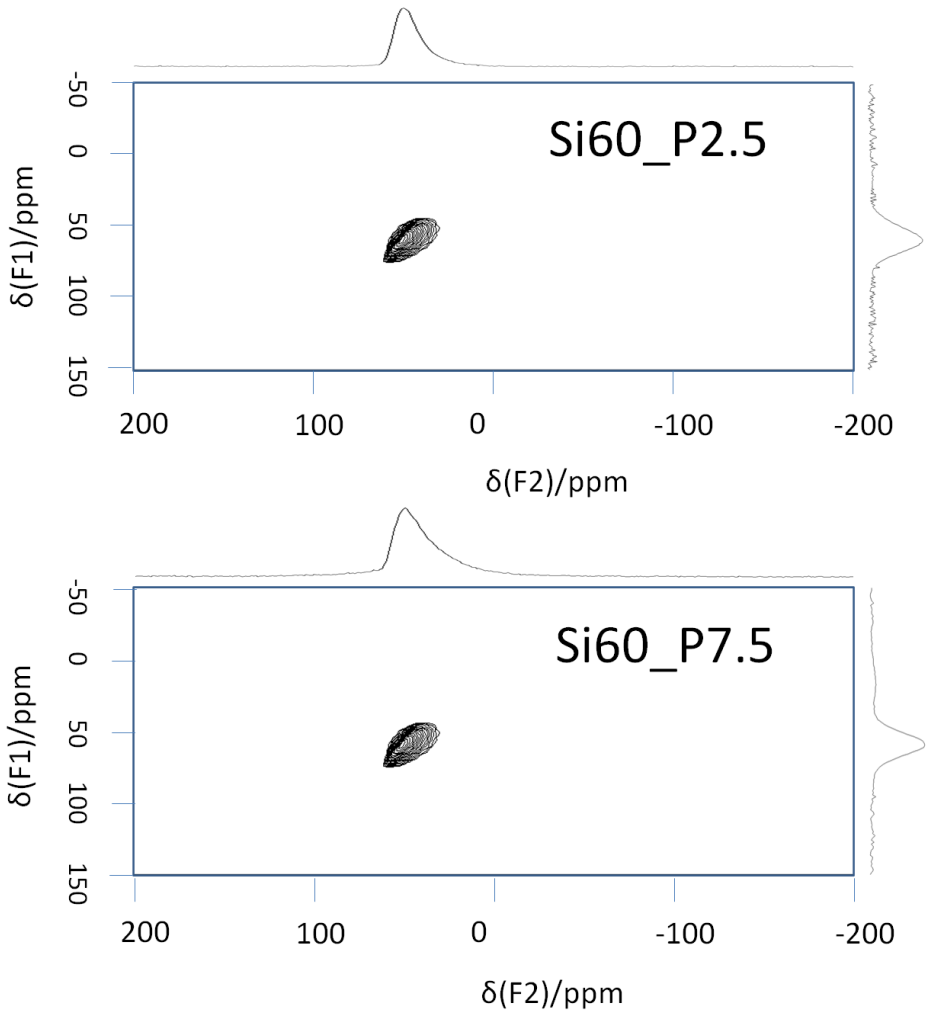

Figure 60. MQMAS spectra of Si60_P2.5 (top) and Si60_P7.5 glasses (bottom) measured in 11.7 T magnet.

Values of isotropic chemical shift δ_{iso} and second order quadrupolar (SOQE) effect were calculated using the results of ^{27}Al MQMAS carried out on Si60_P2.5 and Si60_P7.5 samples: $\delta_{iso} = \delta_{F2} + \frac{17}{27}(\delta_{F1} - \delta_{F2})$ and $SOQE = 1.0244 \times 10^{-2} \times \vartheta_0 \sqrt{\delta_{F1} - \delta_{F2}}$, where δ_{F1} and δ_{F2} are the centers of gravity of the signal in the first and second dimensions and ϑ_0 is the Larmor frequency. SOQE delivers a good estimation of quadrupole coupling constant C_q because they are connected by the equation: $SOQE = C_q \sqrt{1 + \frac{\eta^2}{3}}$, where η is quadrupolar asymmetry parameter taking values from 0 to 1. Estimations of the results of ^{27}Al MQMAS deliver δ_{iso} of 57 and 54 ppm and SOQE of 4.9 and 4.6 for the glasses Si60_P2.5 and Si60_P7.5, respectively.

Although it is not possible to generalize the results of MQMAS experiments to all samples, they suggest that aluminum is exclusively or mostly four-coordinated. Aluminum being present only in tetrahedral coordination immediately raises the question of charge-compensation mechanisms playing role in this glass structure. As no AlO_5 or AlO_6 units were identified in the samples with different phosphorus percentage, some other charge-compensating mechanisms must be at work in this system. One possibility might be an appearance of Al-Si constellations connected through partially three-coordinated oxygen as observed previously (oxygen thriclusters)[124,135,148,149]. Another probable charge-compensation mechanism might be realized through $AlPO_4$ units. To support one of these hypothesis, investigation of phosphorus environment and phosphorus-silicon connections is needed.

4.2.4. ^{29}Si-MAS NMR

To identify coordination of the silicon units and to obtain information about distribution of phosphorus and aluminum ions in the vicinity of silicon, ^{29}Si MAS NMR and dipolar-based experiments (see 4.1.6 and 4.1.7) were carried out. Spectra of ^{29}Si MAS NMR of the glasses from Si50(5) (left), Si60 (middle) and Si70 (right) series are represented in Figure 61. Position of the peaks propose that silicon units are four-coordinated regardless of Al/Si ratio and the amount of phosphorus added. Chemical shift of ^{29}Si signal moves to the lower frequencies with increasing Si/Al and to higher frequencies with increasing Al/P ratio (exact values are given in Table 16 and Figure 62). This might imply changes in the second coordination sphere of the silicon and substitution of –Si-O-Al-bonds by –Si-O-Si- or Si-O-P- bonds. Which nuclei is causing the shift of the silicon signal might be defined by ^{29}Si{^{31}P}-REDOR and ^{29}Si{^{27}Al}-REAPDOR experiments on ^{29}Si-enriched samples (see 4.1.5 - 4.1.7).

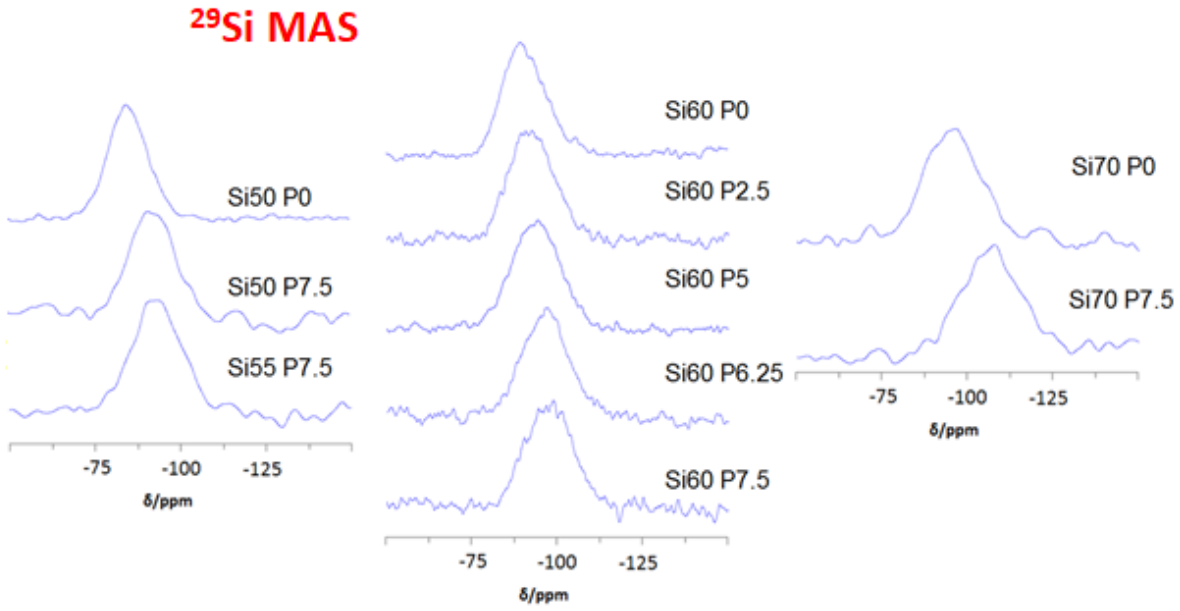

Figure 61. ^{29}Si-MAS NMR spectra of Si50, Si55, Si60 and Si70 series glasses obtained at Bo = 7.04 T.

		Si, m. p.			
		50	55	60	70
P, m. p.	0	-85		-90	-95
	2.5			-92	
	5			-94	
	6.25			-97	
	7.5	-93	-93	-97	-106

Table 16. ^{29}Si chemical shift values obtained from a simulation of the spectra using the DMFIT software.

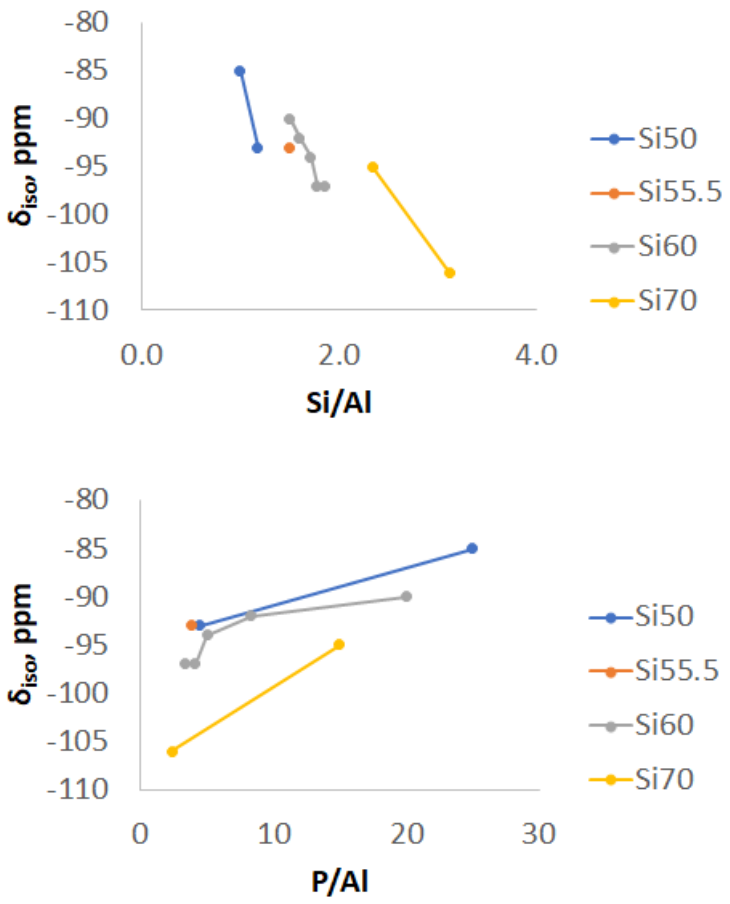

Figure 62. ^{29}Si chemical shift values depending on Si/Al and P/Al ratio.

4.2.5. ^{31}P MAS, MAT and ^{31}P{^{23}Na}-REAPDOR NMR

Knowing how phosphorus nuclei are being integrated into aluminosilicate network is of fundamental importance for current studies. Without it, it would be not possible to understand the rearrangement of the glass network and, especially redistribution of the sodium ions upon addition of phosphorus. Definition of amount of bridging oxygen of phosphorus and its local environment is a challenging task. Chemical shifts of phosphorus units depend not only on coordination number but strongly on the presence or absence of aluminum/silicon in the second coordination sphere and also on the exact type of neighboring species as shown in the previous works (e. g. AlO_4 or AlO_6)[6,85–87,118,121,124,145–147,150,151]. In this part, the results of manifold of NMR characterization experiments carried out to investigate phosphorus coordination environment starting from MAS NMR, MAT and to dipole-based experiments are represented and discussed.

^{31}P-MAS NMR. In Figure 63 ^{31}P spectra of Si60 series (left) and Six_P7.5 series (right) are represented. Several overlapping signals centered around -1, -11 and -15 ppm are observed

in all samples. Low intensities of the spinning sidebands indicate low CSA values and might speak for presence of aluminum in the vicinity of phosphorus units. To find more information about phosphorus environment, deconvolution of the signal with DMFIT software was attempted.

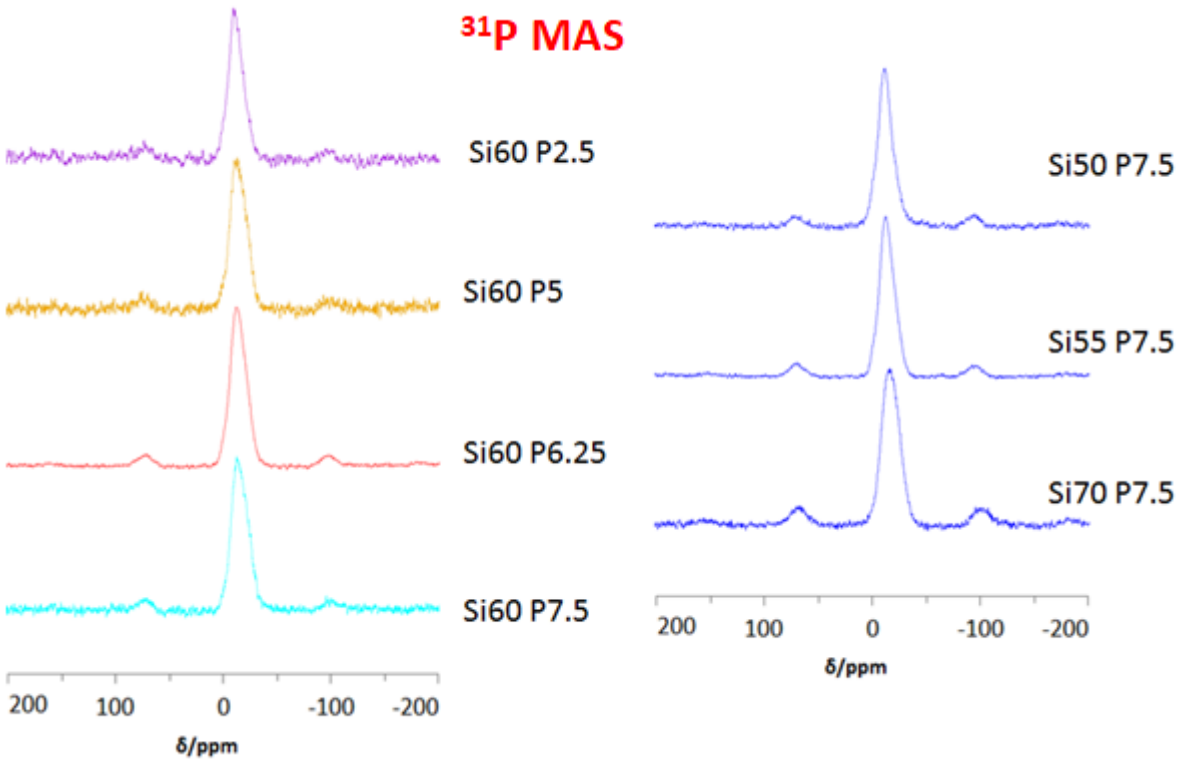

Figure 63. ^{31}P-MAS spectra of Si60 (left) and P7.5 series (right) series obtained at Bo = 7.04 T.

The central peaks of ^{31}P spectra of Si60 series (left) and Six_P7.5 series (right) together with the results of simulations with DMFIT software are represented in Figure 64. Due to low intensity of spinning sidebands only central transitions were simulated with DMFIT software. Due to heavily overlapping signals many approaches could have been used to simulate ^{31}P spectra and the results should be treated with caution. In this study three Gaussian/Lorentzian peaks (with Gaussian/Lorentzian ratio of 0.8) initially set at -1, -10 and -20 ppm with all parameters allowed to be varied freely were used in DMFIT simulations. Table 17 represents isotropic chemical shifts and fractional areas of individual components of phosphorus peak. Exact assignment of the signals to Q^n units from the chemical shift alone is difficult because known chemical shifts of these units are heavily overlapped and depend on amount of

bridging oxygen and connected species. When the peak around -1 ppm always contributes six or less percent to the overall intensity and its behavior cannot be discussed quantitatively depending on the chemical composition due to its low intensity, ratios and chemical shifts of the peaks at – 10 and – 20 ppm does not show as strong dependency on Al/Si or Al/P ratio as observed for silicon and aluminum signals. When simulation of the spectra could be ambiguous, the center of gravity of the signal could be defined precisely and it is also listed in the Table 17. Center of gravity has more clear tendencies and shift to less negative ppm with growing Al/P ratio and to more negative ppm with growing Si/Al ratio. This might indicate phosphorus incorporation into the structure although dipolar-based experiments are needed to support this hypothesis.

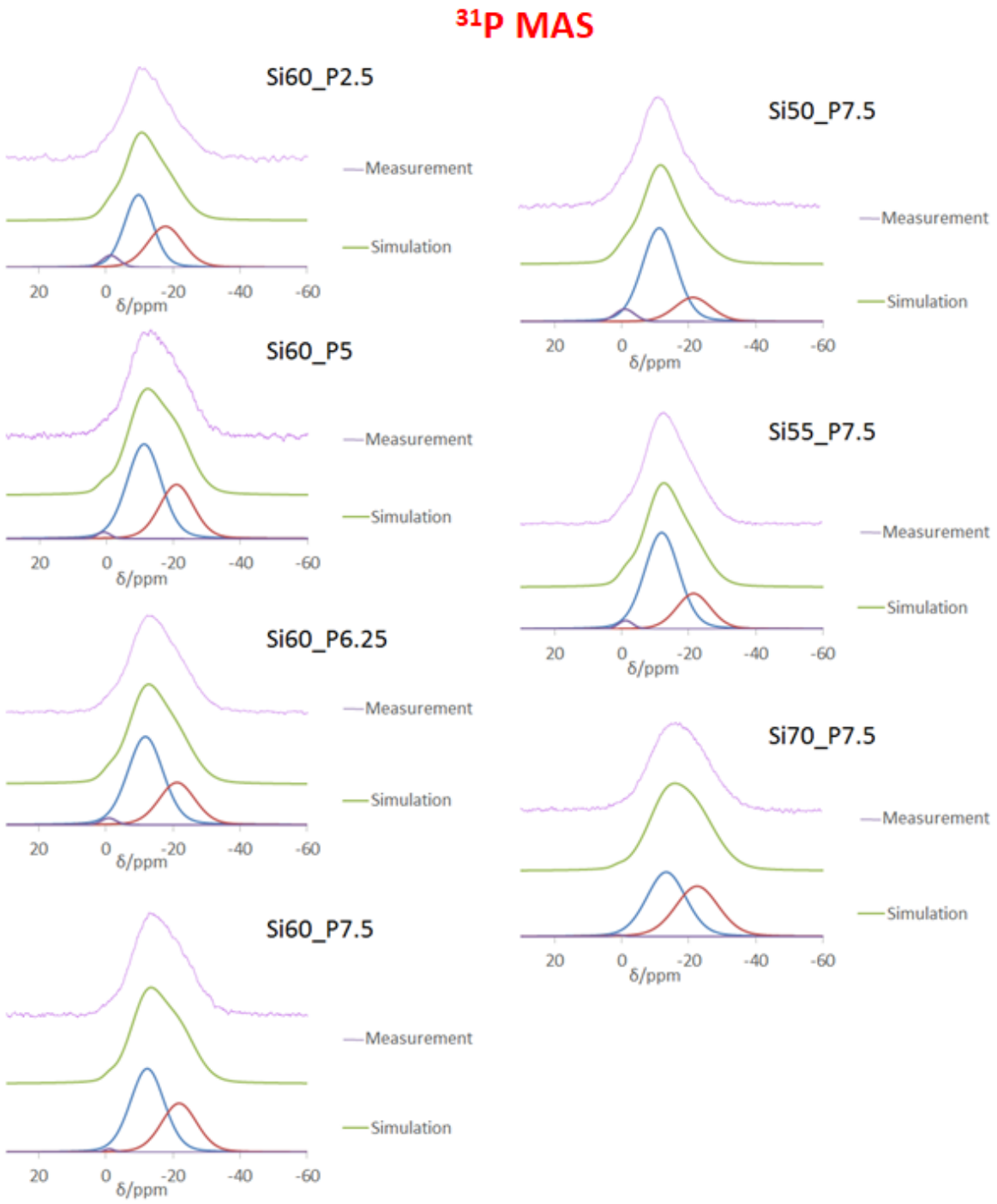

Figure 64. ^{31}P-MAS spectra of the central peak and the results of simulations with DMFIT software of the individual signal components of the glasses Si60 (left) and P7.5 series (right) series obtained at Bo = 7.04 T.

Probe Name	δ_{iso}/ppm Fractional area	δ_{iso}/ppm Fractional area	δ_{iso}/ppm Fractional area	Center of gravity, ppm
Si60_P2.5	-1 (6 %)	-10 (55 %)	-18 (39 %)	-12
Si60_P5	1	-11	-21	-14

	(2 %)	(63 %)	(36 %)	
Si60_P6.25	-1 (2 %)	-12 (66 %)	-21 (32 %)	-15
Si60_P7.5	-1 (1 %)	-12 (62 %)	-22 (38 %)	-16
Si50_P7.5	-1 (6 %)	-11 (74 %)	-21 (20 %)	-13
Si55_P7.5	-1 (3 %)	-12 (71 %)	-21 (26 %)	-14
Si70_P7.5	-1 (0 %)	-13 (54 %)	-22 (46 %)	-17

Table 17. ^{31}P chemical shift values and fractional areas (in brackets). Values are obtained from a simulation of the spectra using the DMFIT software.

MAT MAS NMR. To obtain more information about local phosphorus environment, CSA tensors of phosphorus units were measured by means of Magic Angle Turning experiment (MAT – see 1.2.6) by Dr. Gerrit Schiffmann on the sample Si60_P7.5(A) where shorter relaxation times might be exploited. Such as the signals are broader in the second dimension, a contribution of the signal at -12 ppm might be seen in MAT spectrum of the peak at -22 ppm and vice versa, so the results must be treated with caution. The results of MAT experiment and the slices taken at -12 and -22 ppm are represented in Figure 65. Due to low intensity of the signal around 0 ppm, CSA tensor for this peak is not discussed. The peak around -12 ppm has a CSA shape which might indicate Q^2 or Q^3 phosphorus units and the peak at -22 ppm has very narrow CSA. From the knowledge gained on measurements on P60 and PNa series, it is probable that the signal at -12 ppm might have aluminum neighbors which is reflected in lower CSA values. Dipolar-based experiments (4.1.5-4.1.7) might help to support this hypothesis. The signal at -22 ppm has a very low CSA which might indicate Q^0 units which is not very probable such as the signal from Q^0 units is normally found around 0 ppm or phosphorus environment having four bridging oxygen. The width of CSA tensor and position of the peak propose phosphorus units with four bridging oxygen with mostly aluminum and some silicon in the second coordination sphere.

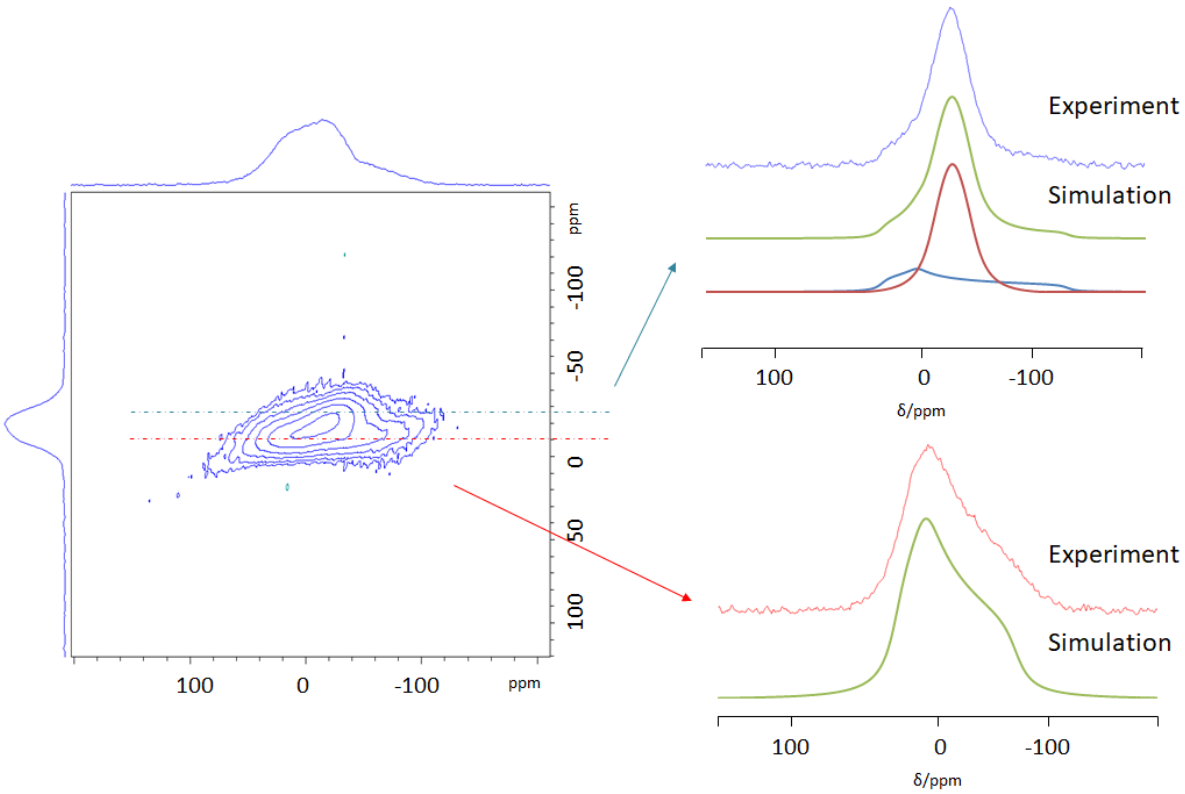

Figure 65. ^{31}P sheared MAT spectrum of the glass Si60_P7.5(A) measured at 200 Hz.

To estimate the relative ratios of the signals observed in MAT NMR measurements, static ^{31}P-echo of Si60_P7.5(A) sample was taken. In Figure 66 results are represented. In Table 18 simulation of this spectrum with DMFIT software using CSA parameters obtained from fitting of MAT measurements and the intensity allowed to be varied are represented. Now an estimation of constituents is possible. As might be seen, the ratio of the signal at -10 ppm to the signal at -21 ppm is approximately 3:2 which is close to the results of single pulse excitation measurements. It is difficult to say which estimation is more precise such as simplified assumptions were taken in both simulations.

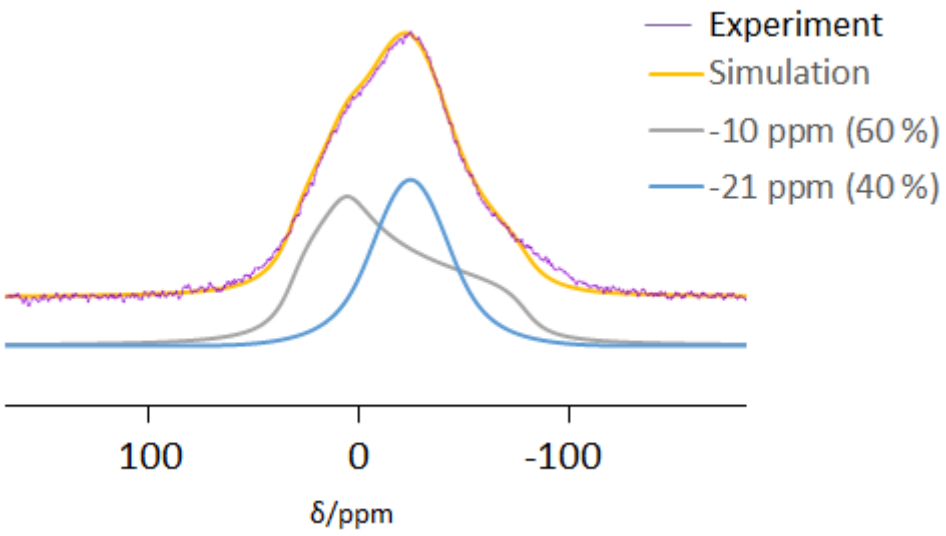

Figure 66. Static ^{31}P echo signal of the sample P60_P7.5(A) and the results of its simulations with DMFIT using parameters obtained from MAT experiments.

Position, ppm	Width of CSA tensor, ppm	η (asymmetry of CSA tensor)	Fraction area
-10	65	0.4	60 %
-21	19	1.0	40 %

Table 18. Results of static echo ^{31}P spectra simulations of the glass Si60_P7.5(A). CSA parameters of individual constituents were taken from MAT spectra of individual signals.

^{31}P{^{23}Na}-REAPDOR NMR. To support assignment of the main signals as $Q^{2/3}$ units and Q^4 unit, ^{31}P{^{23}Na}-REAPDOR measurements were carried out on Si60_P7.5(A) sample. ^{31}P{^{23}Na}-REAPDOR NMR delivers additional information about condensation degree of phosphorus units. According to general phosphorus glass theory (see 2.1.1), Q^3 units do not require charge-compensation cation, Q^2 phosphorus units must be charge-balanced by one and Q^1 by two positive ions. Site-resolved results are compiled in Figure 67. The lines are guides to the eyes representing the results of SIMPSON simulations with indicated dipolar couplings. Such as the peak at 0 ppm contributes less than 6 % to overall spectra and is not properly deconvoluted in all ^{31}P{^{23}Na}-REAPDOR spectra, only the results for the peaks at -11 and -20 ppm are represented. As might be seen, the peak at -10 ppm has more sodium in the surrounding than the peak at -20 ppm. Calculation with two-spin approximation and using $D_{eff} = \sqrt{n}D_{ind}$, where D_{ind} is calculated from ^{31}P-^{23}Na distance 3.2 Å (averaged value over a set of sodium phosphates) delivers 393 Hz for one ^{31}P-^{23}Na connection and 556 Hz for two ^{31}P-

^{23}Na connections. Large measured values of dipolar couplings might be probably explained by the presence of sodium ions around AlO_4 units connected to $Q^{2/3}$ and Q^4 phosphorus species.

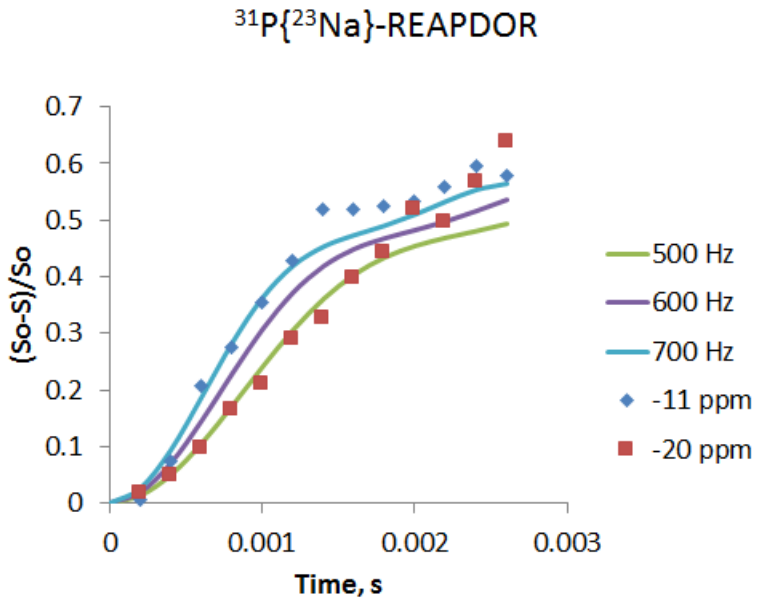

Figure 67. $^{31}P\{^{23}Na\}$ REAPDOR NMR data for Si60_P7.5(A) glass. Red squares: peak at -11 ppm; blue diamonds: peak at -20 ppm. The lines represent results of SIMPSON simulations assuming the indicated effective dipolar couplings.

Combining the results of ^{27}Al, ^{29}Si and ^{31}P measurements, it might be proposed that silicon stays four-coordinated although its environment changes depending on the glass composition which is the subject of further dipolar-based research. Aluminum stays four-coordinated which requires charge-compensation mechanisms. Phosphorus is mainly incorporated as highly symmetrical species (Q^4) giving rise a signal around -22 ppm, which might indicate presence of $AlPO_4$ units as charge-compensating mechanism and as $Q^{2/3}$ species causing peak at -12 ppm. The CSA values of phosphorus suppose presence of aluminum in the second coordination sphere. The insight to connectivity of structural units and information about the presence of triclusters might be gained by means of dipolar-based experiments which are represented in the next chapters. Phosphorus units having in average less connections than four-coordinated aluminum and silicon units might decrease overall network connectivity explaining thereof observed tendencies in Tg and density.

4.2.6. $^{31}P\{^{27}Al\}$-REAPDOR NMR and $^{27}Al\{^{31}P\}$-REDOR NMR

$^{27}Al\{^{31}P\}$-REDOR. To investigate distribution of phosphorus atoms in the network and to gain more information about aluminum environment, $^{27}Al\{^{31}P\}$-REDOR was carried out. The results of $^{27}Al\{^{31}P\}$-REDOR measurements on samples Si60_P7.5, Si60_P5 and Si70_P7.5(A) are shown

in Figure 68. No $^{27}Al\{^{31}P\}$-REDOR effect was detected on sample Si60_P2.5. Lines represent the results of simulations with SIMPSON software with indicated dipolar couplings. In the simulations, the width of CSA tensor was not considered even though each phosphorus unit has distinctly different widths of CSA tensors. The simulations were carried out under assumption that CSA would not affect much the results for this particular case because the widths of all measured CSA tensors are well below 100 ppm and should not affect $^{27}Al\{^{31}P\}$-REDOR curves much as shown by the results of the test SIMPSON simulations (see Appendix 3).

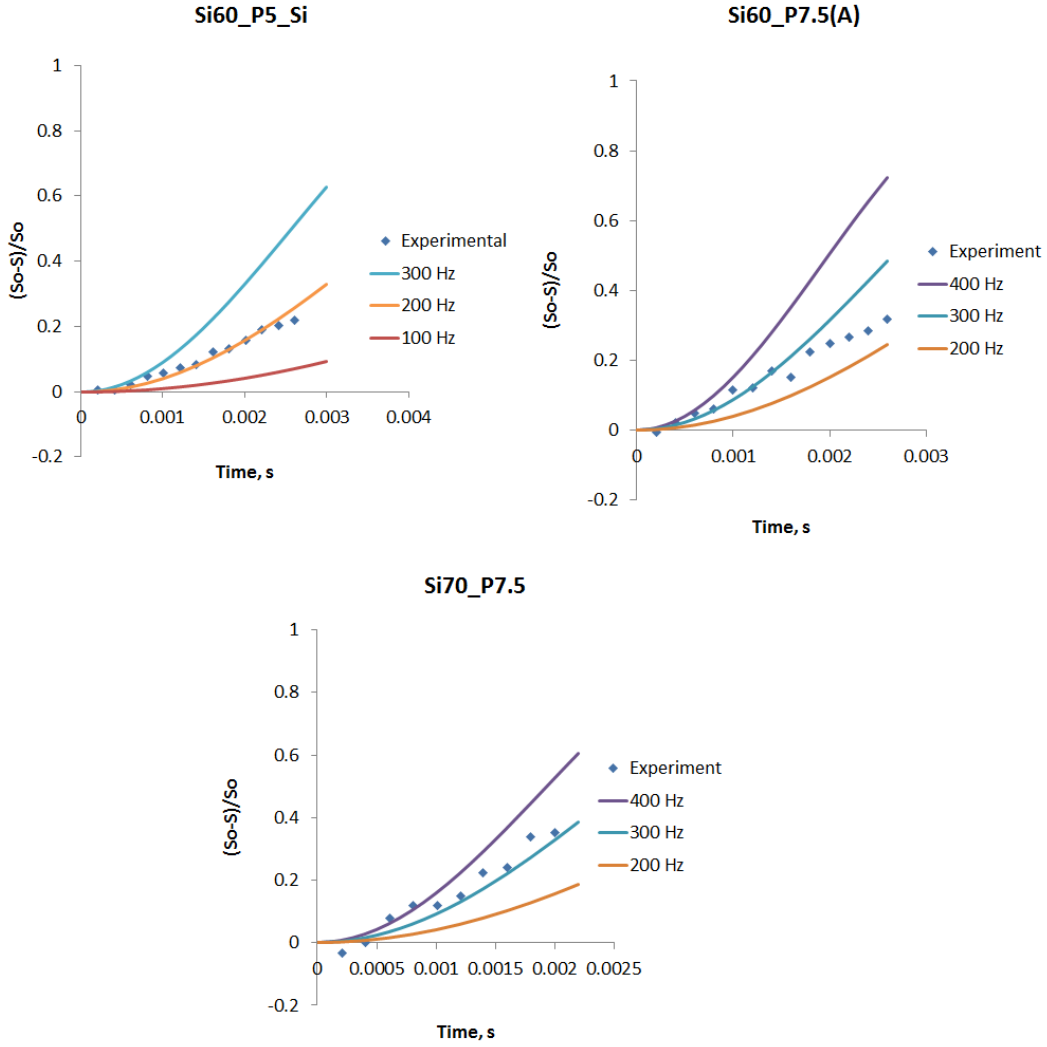

Figure 68. $^{27}Al\{^{31}P\}$ REDOR NMR data for Si60_P5_Si, Si60_P7.5(A) and Si70_P7.5 glasses carried out in the field Bo=7 T. Blue diamonds represent the results of measurements, lines are results of SIMPSON simulations using indicted values of dipolar couplings.

According to the results of the measurements ^{27}Al-^{31}P dipolar coupling steadily increases with growing P/Al ratio in Si60 series being approximately 0, 200, 300 and 350 Hz for the samples Si60_P2.5, Si60_P5_Si, Si60_P7.5(A) and Si70_P7.5, respectively. Assuming 3.1 Å distance for

P-O-AlO_4[122,123] (dipolar coupling of 426 Hz), the amount of the next neighbors obtained by dipolar-based measurements are 0, 0.2, 0.5, 0.7. Steady increase of the dipolar coupling along increasing P/Al ratio speaks for incorporation of phosphorus in the second coordination sphere of aluminum. The results indicate that the shift of aluminum in ^{27}Al MAS spectra with increasing phosphorus content is at least partially caused by the appearance of the phosphorus in the second coordination sphere. The rest of the bridging oxygen of aluminum species is then probably connected to silicon units (due to Löwenstein's avoidance rule) which might be proved by ^{27}Al{^{29}Si}-REDOR (see 4.1.7).

^{31}P{^{27}Al}-REAPDOR. The amount of aluminum in the second coordination sphere might be measured by means of ^{31}P{^{27}Al}-REAPDOR NMR. The results of ^{31}P{^{27}Al}-REAPDOR NMR experiments for the glasses Si60_P2.5, Si60_P5_Si, and Si60_P7.5(A) are represented in the Figure 69. Lines represent the results of SIMPSON simulations with indicated values of P-Al dipolar coupling.

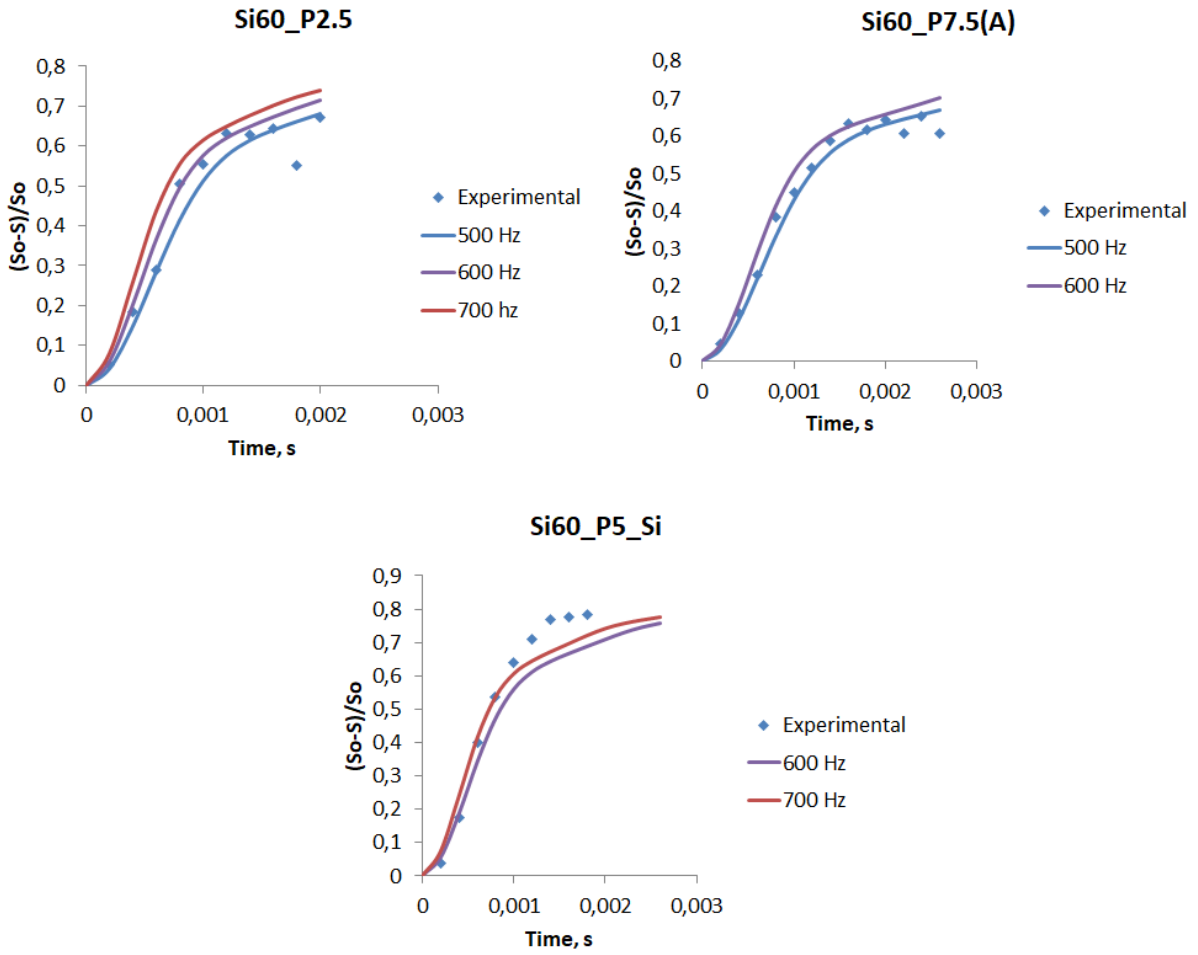

Figure 69. $^{31}P\{^{27}Al\}$ REAPDOR NMR data for Si60_P2.5(top left), Si60_P7.5(A)(top right) and Si60_P5(bottom) glass. Blue diamonds represent experimental data and lines represent results of SIMPSON simulations assuming the indicated effective dipolar couplings.

Due to poor resolution of the phosphorus signals they were treated as one peak in $^{31}P\{^{27}Al\}$-REAPDOR experiments. According to the results of measurements, ^{27}Al-^{31}P dipolar couplings are similar and vary between 600 and 650 Hz for the samples Si60_P2.5, Si60_P5_Si, and Si60_P7.5(A), respectively. Assuming 3.1 Å distance for P-O-AlO_4[122,123] (dipolar coupling of 426 Hz), the amount of the next neighbors obtained by dipolar-based measurements are 2-2.3. This speaks for Al being incorporated in the phosphorus environment and against phosphorus units being distributed in aluminosilicate network. The rest of the bridging oxygen might be occupied with silicon or other phosphorus units which is proved in $^{31}P\{^{29}Si\}$-REDOR (see 4.2.7) and ^{31}P-^{31}P M_2 measurements (see 4.2.9).

4.2.7. $^{31}P\{^{29}Si\}$-REDOR NMR and $^{29}Si\{^{31}P\}$-REDOR NMR

$^{29}Si\{^{31}P\}$-REDOR. To investigate presence of phosphorus in the second coordination sphere of silicon, $^{29}Si\{^{31}P\}$-REDOR experiments were carried out on enriched Si60_P5_Si glass. Exemplary

spectra of $^{29}Si\{^{31}P\}$-REDOR experiment at 40th rotor cycle are represented in Figure 70. As might be seen, only weak effect on the more negative ppm where the signals arousing from re region where Si-P connections are expected, is observed. This small effect might be caused by the bulk effect of phosphorus or indicate small amount of phosphorus in the second coordination sphere of silicon. Overall, phosphorus is not the major coordinator of silicon and silicon is rather surrounded by silicon and aluminum atoms. Therefore, changing Al/Si ratio in the second coordination sphere causes the shift of the silicon signal. To quantify Si/Al ratio in the second coordination sphere of silicon, $^{29}Si\{^{27}Al\}$-REAPDOR were carried out.

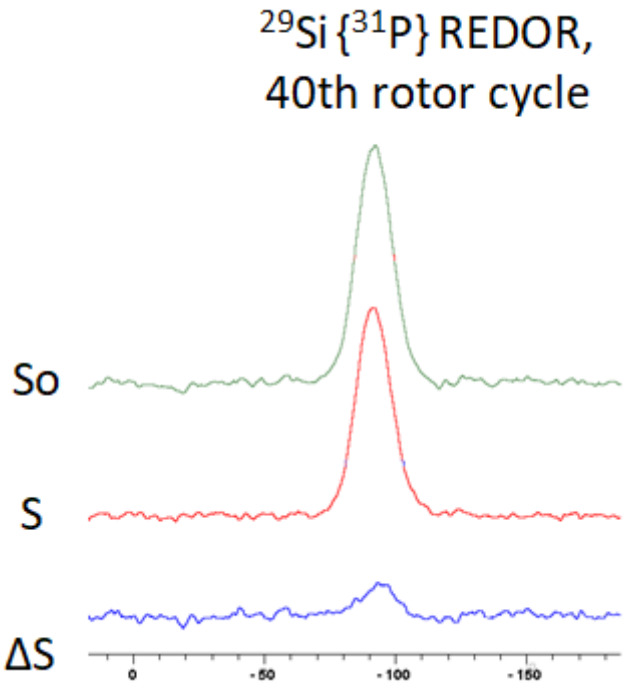

Figure 70. Exemplary $^{29}Si\{^{31}P\}$ REDOR spectra at 40th rotor cycle.

$^{31}P\{^{29}Si\}$-REDOR NMR on Enriched Si60_P5 Glass. $^{31}P\{^{29}Si\}$-REDOR NMR experiments were carried out on enriched Si60_P5_Si sample to investigate network connectivity. The results of the measurements and exemplary $^{31}P\{^{29}Si\}$-REDOR spectra taken at the 20th rotor period are represented in Figure 71. As might be seen from the exemplary spectra, the peaks at -10 and -20 ppm are losing the same fraction of intensity under reintroduction of dipolar coupling between phosphorus and silicon, which speaks for equal amount of silicon close to both phosphorus species. Such as both signals are decaying with equal speed, they were treated as one peak when preparing the data for numerical simulations. The results of SIMPSON

simulation assume one P-Si connection per phosphorus atom assuming P-Si distance of 3.22 Å[124].

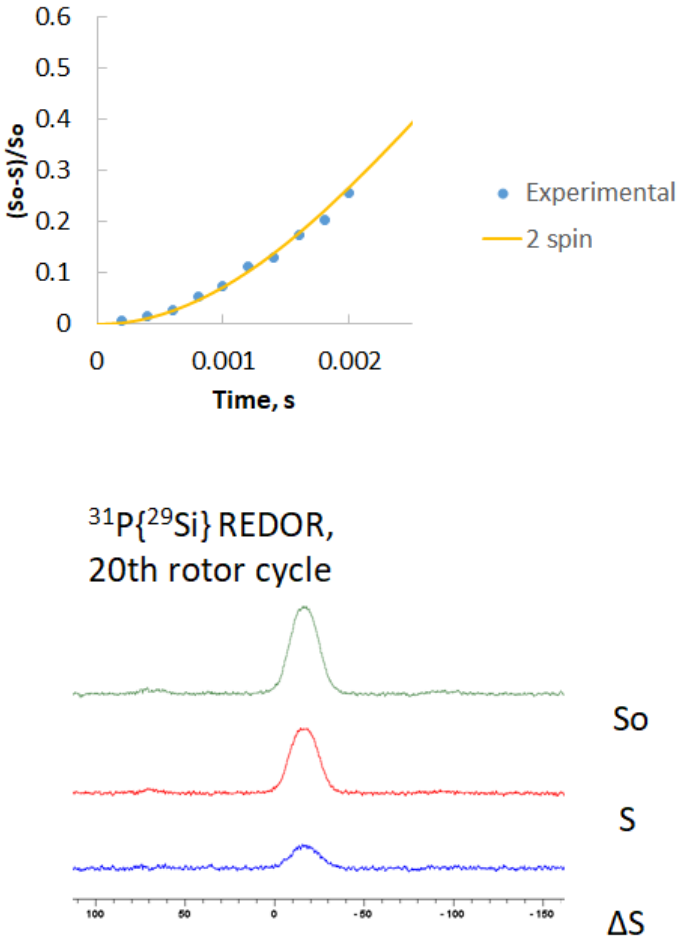

Figure 71. Exemplary $^{31}P\{^{29}Si\}$ REDOR spectra at 20th cycle (bottom) and the results of simulation using two-spin assumption of Si60P5 glass.

4.2.8. $^{31}P\{^{29}Si\}$-REDOR NMR and $^{29}Si\{^{31}P\}$-REDOR NMR

$^{27}Al\{^{29}Si\}$-REDOR. To research aluminum-silicon connectivity, $^{27}Al\{^{29}Si\}$-REDOR was carried out on the enriched Si60_P5_Si sample. In Figure 72 the results of $^{27}Al\{^{29}Si\}$-REDOR measurements are represented. The solid lines are guides to the eyes representing the results of SIMPSON simulation of aluminum having three (4-spin system: one aluminum and three silicon nuclei using 2-spin approximation) and four (5-spin system: one aluminum and four silicon nuclei using two-spin approximation) using Si-Al distance of e. g. 3.22 Å (Si-Al distance in nepheline[124]). As might be seen in Figure 72, aluminum has three to four silicon in the second coordination sphere.

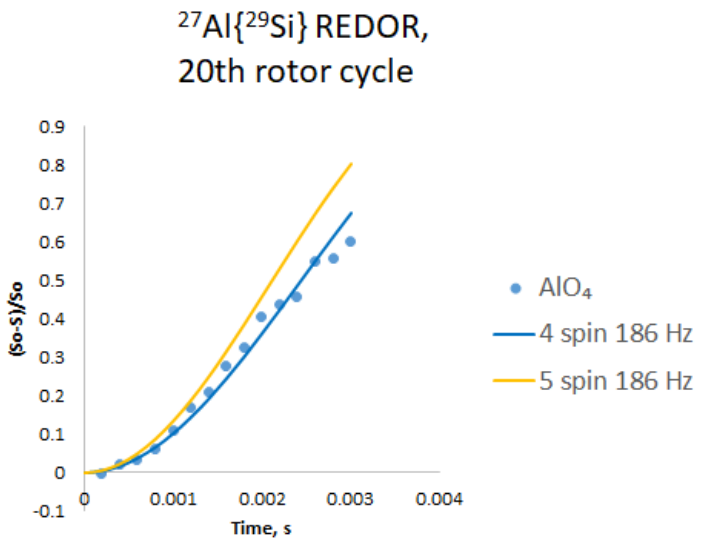

Figure 72. Experimental results of $^{27}Al\{^{29}Si\}$ REDOR. Blue dots represent the results of measurements. The solid lines represent the results of SIMPSON simulation using 4-spin (one Al atom and 3 Si atom) and 5-spin (one Al atom and two Si atoms) systems.

Summing up the results of $^{27}Al\{^{31}P\}$-REDOR and $^{27}Al\{^{29}Si\}$-REDOR experiments, the amount of the neighbors in the second coordination sphere of aluminum is slightly higher than four. First, it indicates low probability of Al-O-Al connections because AlO_4 units are fully coordinated by silicon and phosphorus. Second, the amount of measured neighbors might be explained by small experimental missets, bulk effect, slightly different distances in the glasses comparing with Al-Si distances in crystals or by formation of some amount of Si-O-Al triclusters. Presence of triclusters might be proved by carrying out ^{17}O MQMAS NMR on the samples enriched with ^{17}O NMR[152] although it might be challenging due to low amount of oxygen participating in triclusters building.

$^{29}Si\{^{27}Al\}$-REAPDOR. The results of $^{29}Si\{^{27}Al\}$-REAPDOR experiments carried out on the sample Si60_P5_Si are represented in Figure 73. The lines are guides to the eyes and represent the results of SIMPSON simulations using 3-spin (one silicon and two aluminum nuclei) and 4-spin (one silicon nucleus and three aluminum nuclei using 2-spin approximation) systems using Si-Al distance of 3.22 Å (Si-Al distance in nepheline[124]). From the results of SIMPSON simulations it might be concluded that each SiO_4 unit has two to three aluminum in the second coordination sphere. Additionally, exemplary spectra of Si-Al REAPDOR at the 20th rotor are given in Figure 73. As might be seen, there is no separation of the signal to several peaks having different $^{29}Si\{^{27}Al\}$-REAPDOR effect. This suggests that most of silicon units do not

separate to the pure silica phase (no part of the signal without significant $^{29}Si\{^{27}Al\}$-REAPDOR effect is observed).

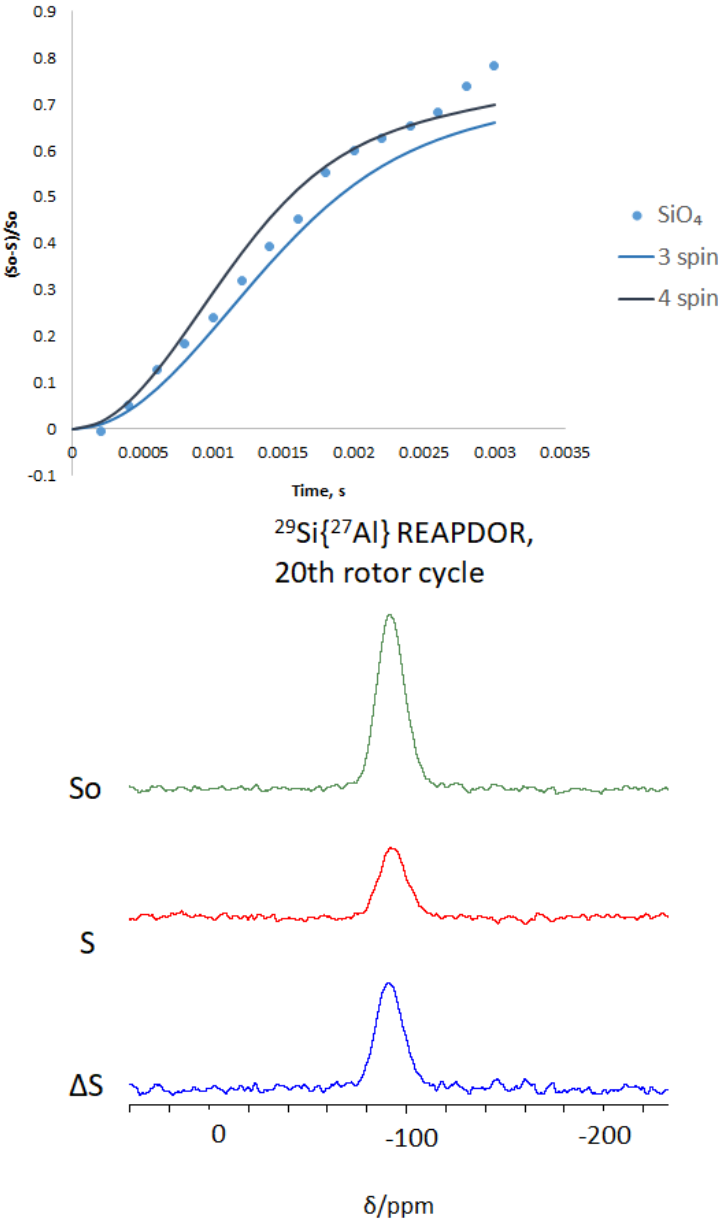

Figure 73. Top: experimental results of $^{29}Si\{^{27}Al\}$ REAPDOR. The solid lines represent the results of SIMPSON simulation using 2-spin (one Si atom and 1 Al atom) and 3-spin (one Si atom and two Al toms) systems. Bottom: exemplary $^{29}Si\{^{27}Al\}$ REAPDOR spectra at 20th rotor cycle.

Based on the results of $^{29}Si\{^{31}P\}$-REDOR, the bonding oxygen of silicon which is not connected to aluminum should connect to other silicon units. If silicon mostly forms connection to silicon and aluminum, the changes of chemical shift of ^{29}Si signal in observed glasses are caused mostly by substitution of silicon by aluminum in the second coordination sphere with increasing Si/Al ratio.

4.2.9. Phosphorus Connectivity

To find out more about connectivity of phosphorus units, M_2 second momentum was measured by obtaining ^{31}P spin echo decays in the samples Si60_P7.5 and Si60_P2.5. Integral intensity of all signals was used to evaluate the data. Experimental points were simulated using equation

$$\frac{I_{2\tau}}{I_0} = \exp\left(-\frac{M_2}{2}(2\tau)^2\right)$$

Where I_0 and $I_{2\tau}$ are the integral intensity of the signal at corresponding time. Experimental points and the results of M_2 simulations are represented in Figure 74. Calculations deliver M_2 values of 1.4 10^6 rad^2 s^{-2} for the sample Si60_P2.5 and 1.8 10^6 rad^2 s^{-2} for the sample Si60_P7.5.

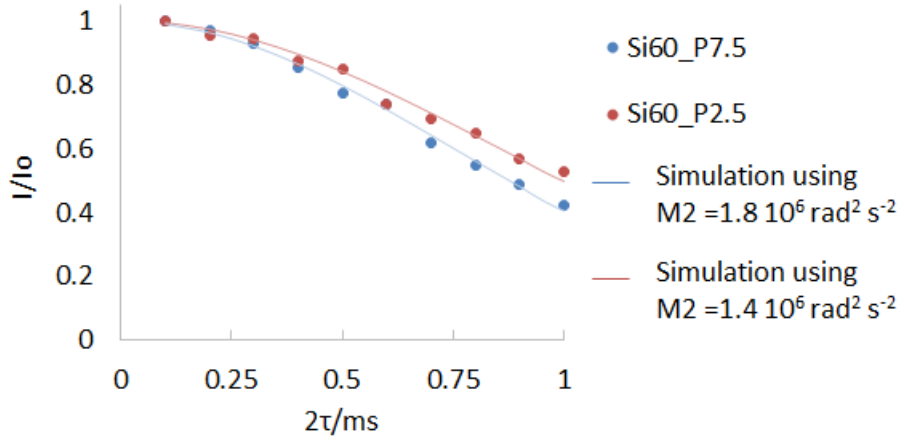

Figure 74. Circles: experimental results of static spin-echo measured on Si60_P7.5 (orange) and Si60_P2.5 (blue) glasses. Lines represent theoretical values fitted with M_2 = 1.4 10^6 rad^2 s^{-2} (orange) and 1.8 10^6 rad^2 s^{-2} (blue).

It is difficult to extract an amount of P-O-P connections from M_2 in this case due to different widths of CSA tensor of $Q^{2/3}$ and Q^4 phosphorus species which affects if the flip-flop transitions should be accounted for[153]. As outlined in 1.1.6, $M_2 = \frac{3}{5}\left(\frac{\mu_0}{4\pi}\right)^2 \gamma_I^4 \hbar^2 I(I+1) \sum_{i \neq j} \frac{1}{r_{ij}^6}$ or $M_2 = \frac{4}{15}\left(\frac{\mu_0}{4\pi}\right)^2 \gamma_I^2 \gamma_S^2 \hbar^2 S(S+1) \sum_S \frac{1}{r_{IS}^6}$ equations might be used to calculate second moment depending if the flip-flop term of the dipole interaction is considered. However, calculations using 2.95 Å P-P distance deliver M_2 between 4.2 10^6 rad^2 s^{-2} and 1.4 10^6 rad^2 s^{-2} which is sufficiently higher than the values observed experimentally which indicates low amount of phosphorus-phosphorus connections. Combining it with previous studies, $Q^{2/3}$ and Q^4

phosphorus species have mostly aluminum and some phosphorus in the second coordination sphere.

4.2.10. *Ex-situ* and *in-situ* ^{23}Na-MAS NMR

Investigation of sodium in the glasses may help to gain more information about glass structure: peak position in ^{23}Na NMR of NAS system spectrum was found to correlate with Na-O distances[154–156] which might relate to macroproperties. Furthermore, *in-situ* NMR investigations of sodium can help to obtain an insight to Na dynamics.

Ex-situ ^{23}Na MAS NMR. ^{23}Na MAS NMR of the glasses Si50, Si60 and Si70 is represented in Figure 75. The peak maximum shifts from -20 to -23 ppm with growing amount of silicon. This shift is in agreement with tendencies in ^{23}Na MAS NMR spectra of the glasses with similar nominal composition[156]. The shift to more negative frequencies with increasing silicon content might be explained by increased Na-O distances[154–156], which might explain the trends observed in macroproperties: the density of phosphate-free silicon-rich glasses decreases with increasing silicon content. To understand better the effect of sodium to the glass structure and to investigate the sodium dynamics, *in-situ* ^{23}Na and ^{27}Al MAS NMR was carried out.

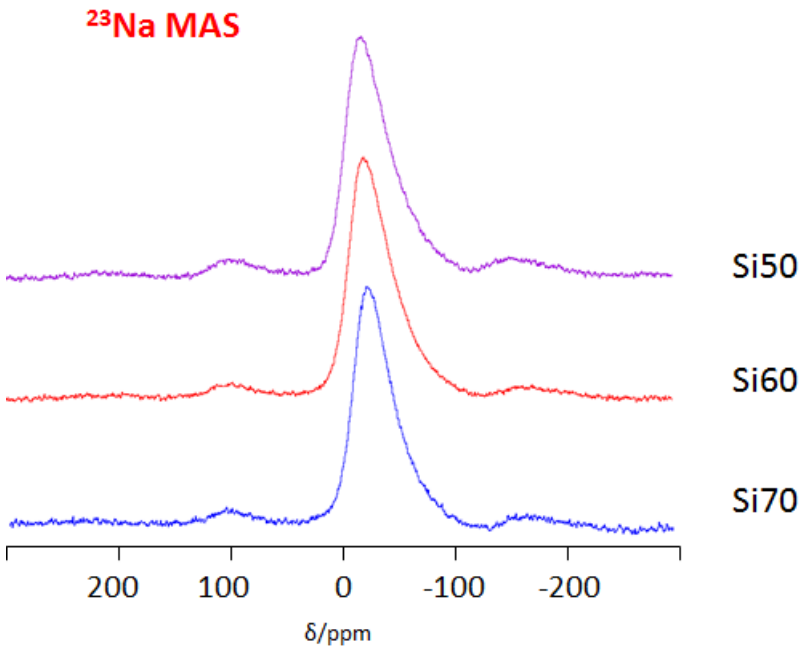

Figure 75. ^{23}Na-MAS NMR spectra of Si50, Si60 and Si70 glasses obtained at Bo = 7.04 T.

In-situ ^{23}Na MAS NMR. To investigate glass dynamics at high temperatures, ^{23}Na and ^{27}Al MAS NMR was measured using novel induction heating method[116]. In Figure 76 and Figure 77 corresponding spectra of the glass Si50 and Si70 at different temperatures are represented. As might be seen, in both glasses shift and width of ^{23}Na is changed during heating and the signal of ^{27}Al does not change even at the maximum possible temperatures. Both glasses show the same trend in the behavior of the ^{23}Na signal: the peak maximum moves initially to the more negative ppm and then the shift to more positive ppm follows. Furthermore, the width of the signal first decreases and then increases with growing temperature. These trends are in agreement with previous investigations of the static in-situ ^{23}Na NMR measurements of the glasses with similar nominal compositions [157,158]. Initial shift to the more negative frequencies might be explained by increasing Na-O distances or by higher coordination number of sodium. The mobility might also cause initial narrowing of the central transition signal (e. g. by averaging of broadening effect of dipolar-dipolar coupling). The shift of the signal to the more positive ppm is probably also connected with mobility of sodium ions: the signal is averaged closer and closer to the isotropic chemical shift by the dynamics[158]. Increasing width of the sodium signal is most probably explained by averaging not only central transition but also satellites by molecular motion[158].

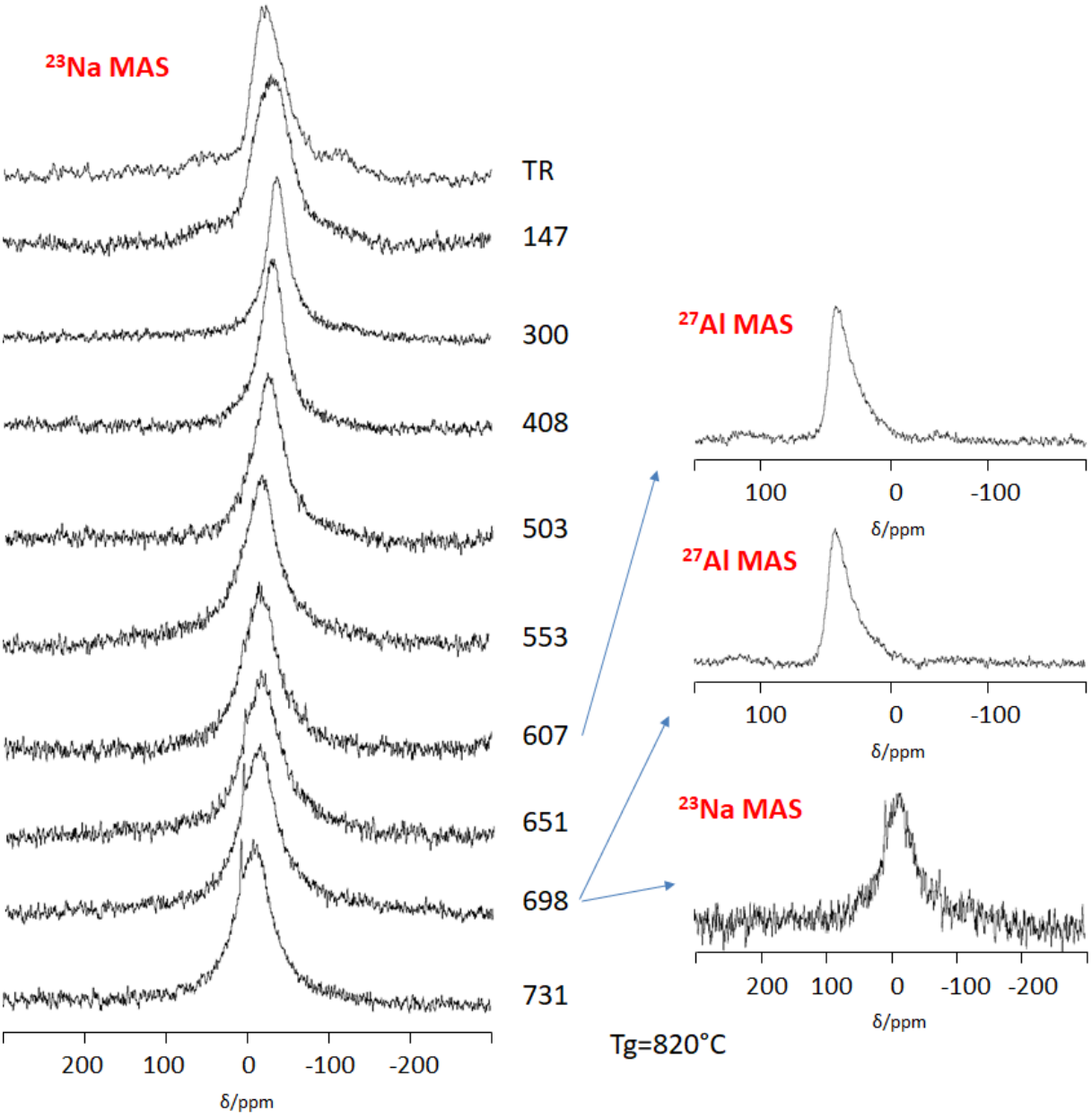

Figure 76. Left: In situ ^{23}Na-MAS NMR spectra of glass Si50, obtained at B0 = 7.04 T and employing repetition times of d1 = 0.1 s. Right: in situ ^{23}Na-MAS NMR spectra employing repetition times of d1=1 s and ^{27}Al-MAS NMR spectra employing repetition times of d1=0.1 s at indicated temperature.

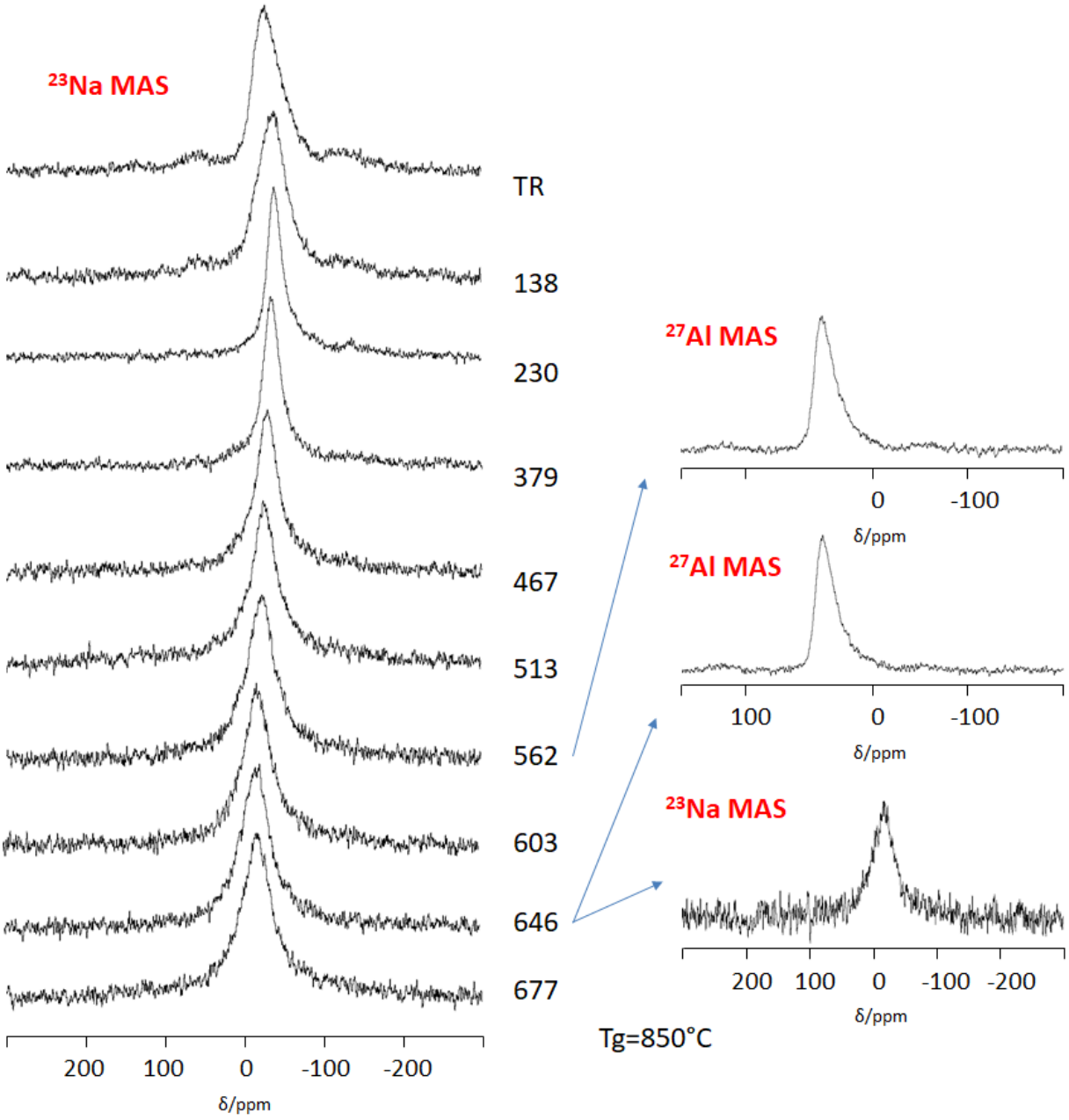

Figure 77. Left: In situ ^{23}Na-MAS NMR spectra of glass Si70, obtained at B0 = 7.04 T and employing repetition times of d1 = 0.1 s. Right: in situ ^{23}Na-MAS NMR spectra employing repetition times of d1=1 s and ^{27}Al-MAS NMR spectra employing repetition times of d1=0.1 s at indicated temperature.

Although the trends in the peak behavior are similar in phosphorus-free silicon-rich glasses, there are some differences which might explain the trends in measured macroproperties. First, there are some additional narrow peak which is most probably cause by some mobile/crystalline fraction (although the latter is less probable such as the narrow peak do not constitute more to the spectra when measuring with longer relaxation times) in the glass Si50 at the higher temperatures. This fraction is not observed when cooling back to the room temperature and do not change the coordination of aluminum but it changes sodium

environment which results in the shift of ^{23}Na spectrum (see Appendix 8). This fraction is not observed in Si70 glass and there are no changes in sodium environment after cooling the sample (see Appendix 8). This might indicate that dynamics of sodium occurs earlier in the Si50 glass. Second, if the position of the peak reflects dynamic processes of sodium ions as discussed above, then it can be plotted against temperature as an indication of sodium mobility as shown in Figure 78. Although initial shift to more negative ppm is more pronounced in Si70 sample which is most probably connected with longer Na-O bonds as discussed above, following shift to more positive frequencies is more pronounced in Si50 sample which correlates with higher mobility of sodium ions. It must be noted that this shift is unlikely to be caused by the changing temperature of the shim coil (see Appendix 8).

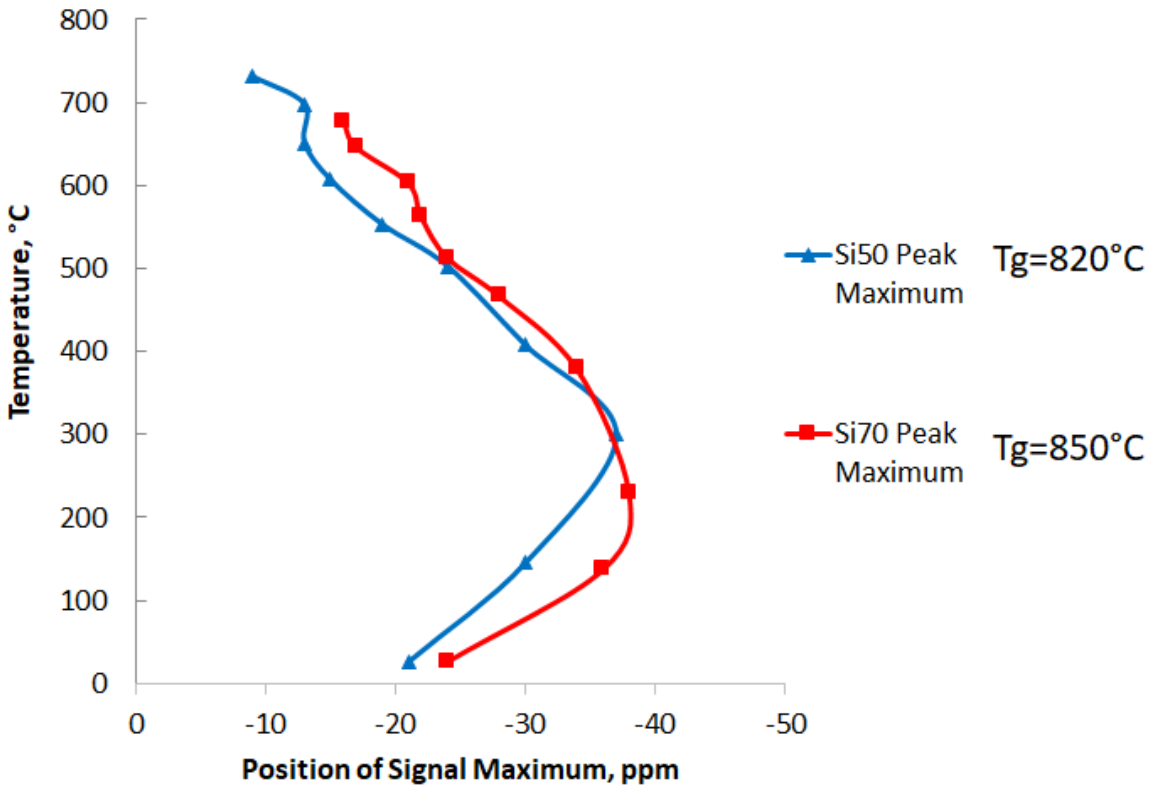

Figure 78. Position of the peak maxima of ^{23}Na signal plotted against temperature in in-situ measurements of the glasses Si50 and Si70.

4.2.11. Glass structure

Based on the results of MAS NMR, MAT, MQMAS and dipolar-based experiments, conclusions about the glass network organizations can be drawn. In the base compositions where only silicon, aluminum and sodium are present, four-coordinated aluminum and silicon units are mixed in the network and sodium charge-balances the aluminum units. If small amount of

phosphorus is added to the network, some sodium ions leave aluminum and partially connect to phosphorus creating two types of phosphorus units: $Q^{2/3}$ and Q^4. They are mostly connected to glass network via P-O-Al bonds although some P-O-Si bonds are also present in the system. Aluminum and silicon are four-coordinated independent of phosphorus content. All three cations are working as network formers. No phase-separation is observed. Charge-compensation mechanism in this system is not similar to those observed in alkali phosphosilicate and aluminosilicate glasses. Charge-balance is preserved by appearance of Q^4 units and, probably by silicon-aluminum triclusters as represented in Figure 79.

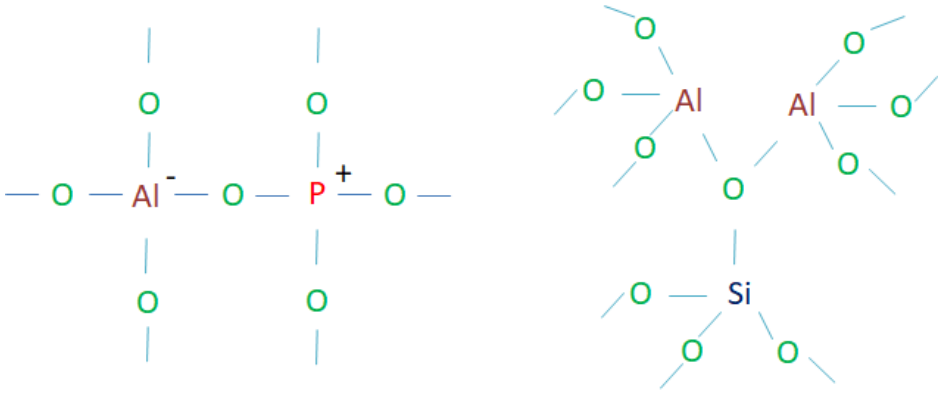

Figure 79. Proposed charge-compensation mechanism in form of Q^4 units (left) and triclusters (right).

From the dipolar-based experiments it follows that silicon is mainly surrounded by other silicon units and partially by aluminum. Si/Al ratio in the second coordination sphere of silicon changes gradually with increasing Si/Al ratio in the base glass composition causing changes of the chemical shift of the silicon signal. Aluminum is surrounded by silicon and phosphorus which implies Al-O-Al avoidance and P/Si ratio in the second coordination increases gradually with increasing P/Si ratio in the glass melting composition. Incorporated phosphorus units mostly connect to aluminum and some silicon.

In the phosphorus-free glasses decreasing density of the glass system with increasing silicon content might be partially explained by longer Na-O bonds as shown by ^{23}Na MAS NMR (peak maximum shift of about 3 ppm was observed). Based on the results of in-situ ^{23}Na MAS NMR, ion mobility is more pronounced in the glasses with higher silicon content at lower temperatures. At the temperatures closer to Tg, the motional averaging of the signal resulting in the chemical shift difference is higher in the sample with lower amount of silicon which is indicated by the position of sodium peak.

4.3. Industrially Produced Fibers from Polyacrylonitrile

Carbon fibers are of importance for modern industry, especially for the areas where lightweight and strong and temperature-resistant solutions are needed due to their combination of high strength and low density. The manufacturing of carbon fibers is a complicated process which is still not fully understood. It consists of many steps including spinning of precursor carbon fibers, stabilization (in air atmosphere), carbonization (in inert atmosphere) and, optionally, graphitization. Finally, in finishing step protective coating also responsible for better adhesion with matrix is applied. The production process of carbon fibers is very energy demanding and final properties of the fibers depend strongly on the manufacturing conditions. Therefore, better understanding of fibers structure transformation during manufacturing might allow to use less energy and obtain high-quality product. Although some attempts to investigate PAN-based fibers with NMR were attempted before [29,31,32,91,159–161], it is still not clear, how far and for which preparation grade of the carbon fibers NMR-spectroscopy could be used. In this study, NMR was attempted on industrially produced carbon fibers at different production steps to find out where its application can help to understand structural reorganization during heating. After that, the approach of applying different NMR methods to the fibers undergone different manufacturing stages was followed in the next chapters.

4.3.1. ^{1}H-MAS NMR

^{1}H-MAS NMR. In Figure 80 central peak of ^{1}H-MAS NMR spectra of non-conductive (non-diluted with silicon dioxide) samples A410-A416 is represented (full-width spectra including sidebands could be seen in Appendix 10). In the first spectra of A410 sample, only one peak is observed in aliphatic region below 5 ppm which corresponds with initial PAN-based copolymer. The sharp peak around 0 ppm might be caused by some coating/solvent/lubrication rests which is difficult to identify. Under manufacturing progress two main changes are observed in the ^{1}H MAS spectra. First, new peaks are appearing and disappearing in the aliphatic regions which indicates ongoing chemical changes. It is difficult to say exactly which chemical moieties cause changes in the spectra such as the peaks are broad and highly overlapping. The second trend in the spectra is the growth of the second major peak centered around 8 ppm which indicates appearance of aromatic moieties and the beginning of polymerization of the network. Comparing the fractional areas of aromatic and

aliphatic peaks it might be concluded that about 40 % of hydrogen atoms are aromatic in the sample A416.

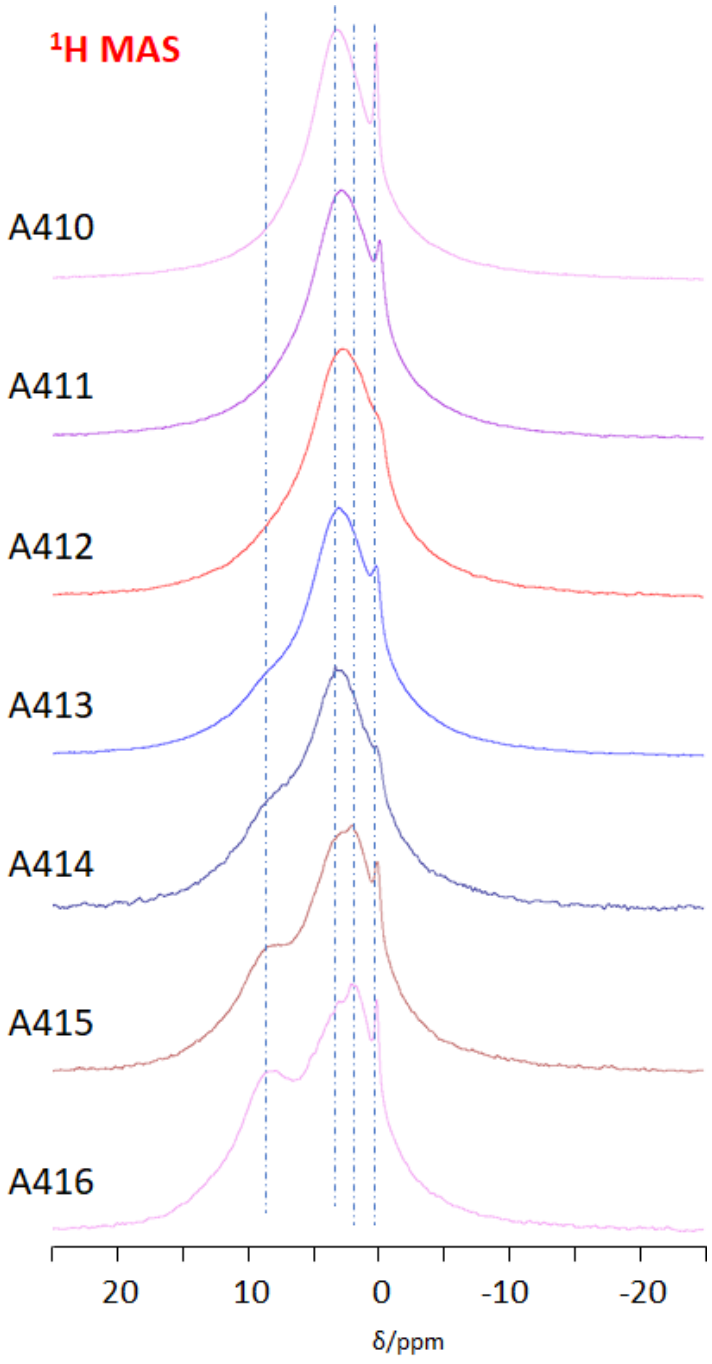

Figure 80. ^{1}H MAS NMR spectra of the central peak of the industrially produced fibers A410-A416.

In Figure 81 the ^{1}H MAS NMR of conductive samples A417-A419 is represented. From the spectra of the sample A417 it might be seen that the sample has mostly aromatic hydrogen in it. If the samples were not conductive, one would expect further increase of the aromatic

signal and decrease/disappearing of the peaks in the aliphatic region with the temperature growth. Contrary to that, the relative area of aliphatic peak is getting higher in the samples A418-A419. That might be explained by skin depth effect of NMR on conductive samples. Probably only the top layers close to the surface are visible in the conductive samples and the penetration depth is decreasing along with increasing conductivity which leads to decreasing aromatic peak. This might open an opportunity to selectively investigate only the surface of industrially produced carbon fibers. Furthermore, the results indicate that, if possible, ^{1}H MAS NMR measurements should be carried out using maximum possible spinning speeds to obtain better spectral resolution by reducing homonuclear dipolar coupling. This would be used later to investigate surface functionalities of differently treated by finishing step fibers (see 4.7.1)

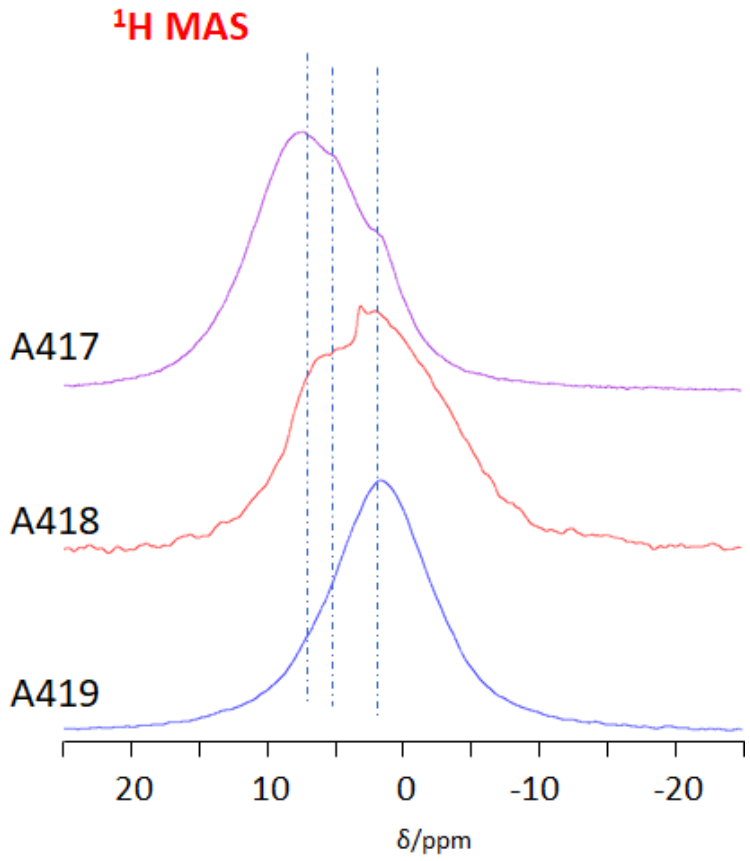

Figure 81. ^{1}H MAS NMR spectra of the central peak of the industrially produced fibers A417-A419.

T_1-Measurements. In Table 19 the results of T_1 measurements of the fibers are shown. Gradually decreasing T_1 values of the samples A410-A416 indicate structural changes. In the conductive sample A 417 the T_1 relaxation time decreases drastically. In the sample A418 and A419 the relaxation time increases again. Based on the results obtained with ^{1}H MAS NMR it could not be said that relaxation times of hydrogen atoms in all fiber volume is increasing.

More probable the penetration depth is decreasing and only T_1 of hydrogen atoms located on the surface layers and having longer relaxation times is measured. Decreasing relaxation times in the samples A410-A416 might reflect structural changes of getting more and more organized polymer network under production steps.

Sample	**Manufacturing Step**	**T_1**
A410	PAN-Fibers	16.8 s
A 411	Stabilization step 1	13.7 s
A 412	Stabilization step 2	8.6 s
A 413	Stabilization step 3	6.0 s
A 414	Stabilization step 4	3.6 s
A 415	Stabilization step 5	2.4 s
A 416	Stabilization step 6	2.9 s
A 417	Carbonization step 1	341 ms
A 418	Carbonization step 2	1.1 s
A 419	Final fibers	1.2 s

Table 19. The results of T_1-measurements of industrially produced carbon fibers.

4.3.2. ^{1}H-^{13}C CPMAS and ^{13}C MAS Investigations

The samples A410-A419 were attempted to be measured using ^{1}H-^{13}C CPMAS NMR. The results are represented in Figure 82. In the sample A410 typical PAN spectra having two peaks centered at 30 ppm (CH and CH_2 group) and 120 ppm (cyano group) could be seen. In the spectra of the sample A416 the spectrum is still similar to the spectrum of original PAN. Additional signal arising from different aromatic carbon constellation is found to the left to the peak of CN group. Furthermore, the signal-to-noise ratio of the sample A416 is worse than in the previous samples which might indicate less hydrogen left in the sample after stabilization process. The spectrum of the sample A417 shows even higher polymerization degree resulting in many peaks in aromatic carbon region although an exact assignment of the

signals is difficult. Furthermore, the relative amount of nitrile groups is reduced drastically in this sample. It is difficult to say if the sharp peak in the aliphatic region corresponds with a lubricant/coating/rests of solvents or with the aliphatic carbon atoms in the fibers. The attempts to obtain sample ^{1}H-^{13}C CPMAS signal from the A418-A419 samples were challenging, probably due to presence of conductive electrons disturbing polarization transfer. The results of ^{1}H-^{13}C CPMAS NMR show that it might be the most suitable method for investigation of carbon environment of non-conductive fibers *viz.* until the end of stabilization step.

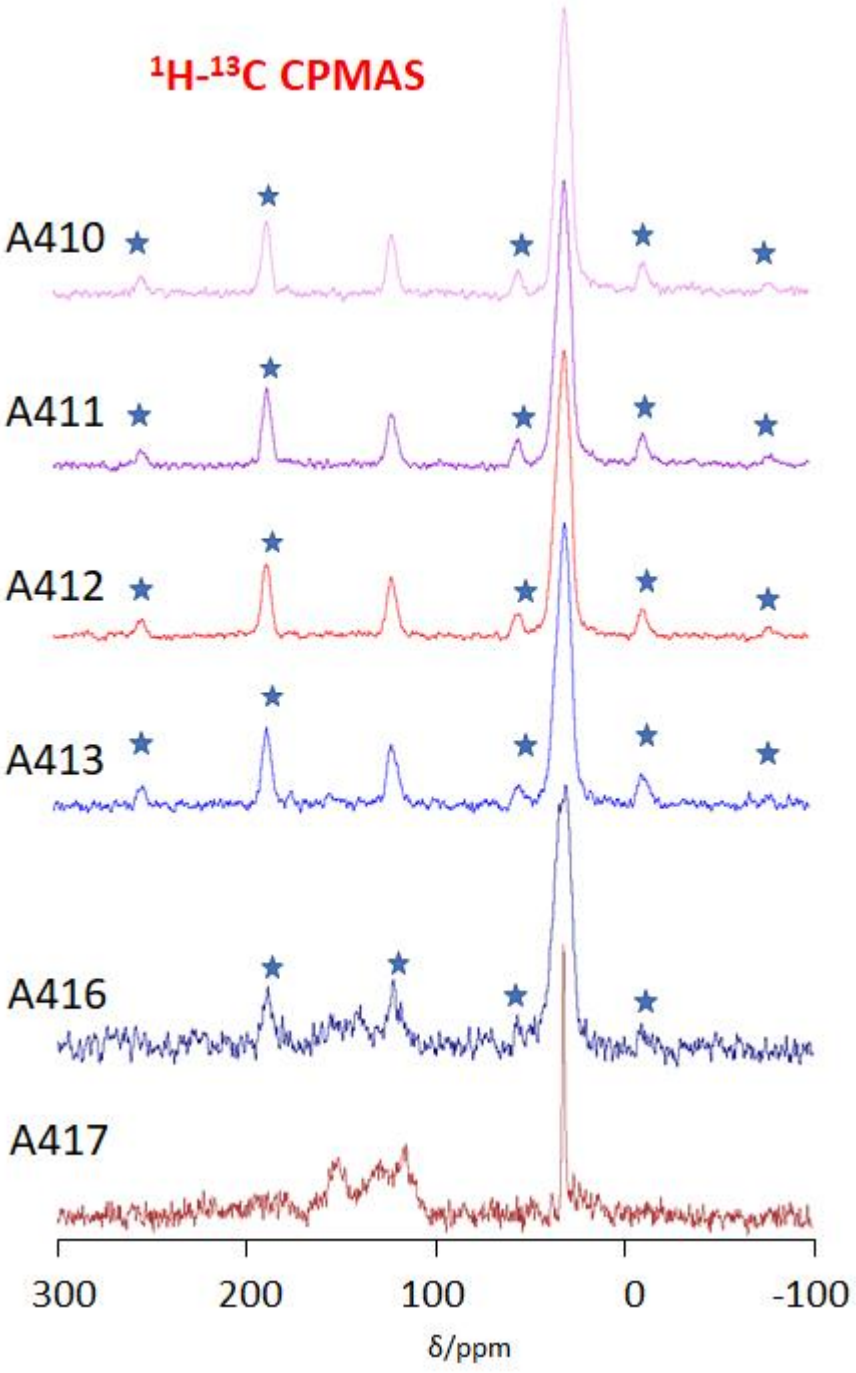

Figure 82. ^{1}H-^{13}C CPMAS NMR of industrially produced carbon fibers.

The spin-echo ^{13}C MAS NMR spectra of the samples A418 and A419 are shown in Figure 83. Broad peaks centered around 120 ppm corresponding with sp^2 carbon are observed in both samples. No other functionalities are observed in the experiment. The signals from the surface chemical groups might be present but not distinguishable in the spectra due to their low intensity.

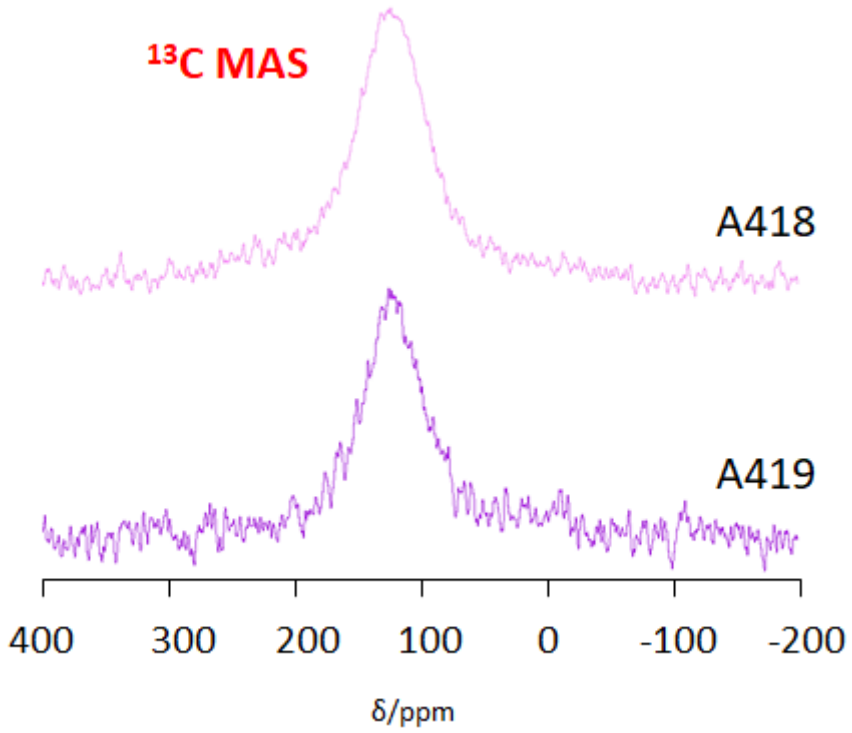

Figure 83. Spin-echo ^{13}C MAS NMR of industrially produced carbon fibers.

4.3.3. Discussion of Application of Solid-State NMR to Industrially Produced Fibers from Polyacrylonitrile at Different Preparation Stages

Two methods were probed in this chapter on the fibers which underwent different production steps. To our best knowledge, that is the first such an attempt to consequently apply solid-state NMR. The results showed that ^{1}H MAS NMR could be used along the whole manufacturing process although an exact assignment of the functionalities giving rise to peaks in spectra is challenging. Maximum possible spinning speeds should be used while recording ^{1}H MAS NMR spectra to obtain better separation of the peaks by reducing homonuclear dipolar coupling (see 4.7.1). Furthermore, ^{1}H MAS NMR might open interesting research opportunities to investigate the carbon fibers at the later production stages when only the surface atoms of the sample could be detected due to their conductivity. ^{1}H-^{13}C CPMAS NMR is the most suitable to be applied on the fibers until the end of stabilization step. Obtaining CPMAS signal on conductive samples is challenging. ^{13}C MAS NMR of conductive samples delivers broad peak caused by sp^2 carbon. Based on the results of these test experiments it was decided to divide further research efforts into two main regions: investigate the initial PAN fibers and their development during stabilization step by means of dipolar-based experiments (chapters 4.4-4.6) and to investigate the surface of industrially produced carbon

fibers by means of single pulse excitation experiments (chapter 4.7.1-4.7.2), although further attempts to use polarization transfer to obtain NMR signal from conductive fibers were made (chapter 4.7.3-4.7.4).

4.4. Investigation of PAN Precursor and Test Substances

As was discussed in previous chapter, NMR methods could be used to investigate the fibers manufacturing process before they become conductive - until first high-temperature furnace. In this chapter, prior to investigation of heat-treated PAN, ^{15}N-enriched PAN and test substances which might be a product of polymerization reaction during stabilization step were investigated by means of solid-state NMR. Obtaining spectra of untreated materials helps to identify chemical shifts of individual molecule components and delivers other important information, for example, CSA values of characteristic molecular components. The information about chemical shift of ^{15}N from the test substances is especially important for correct interpretation of ^{15}N spectra of polymerized fibers where our knowledge of chemical shift positions is limited[162,163].

4.4.1. ^{1}H-^{13}C CPMAS Investigations

The results of ^{1}H-^{13}C CPMAS measurements of PAN are represented in Figure 84. On the left ^{1}H-^{13}C CPMAS spectra at contact time of 1500 us is represented. Two signals can be clearly distinguished around 30 ppm and around 120 ppm. The first one corresponds to alkyl –CH_2- and –CH- groups and the second one corresponds to carbon in nitrile group. The peaks marked with asterisks are sidebands of nitrile signal characterized by its high CSA values. On the right integral intensities of individual signals depending on contact time t_{cp} are shown. The intensity of a signal against the duration of contact pulse follows the equation[49,50]:

$$M(t) = \frac{1}{1 - {T_{IS}}/{T_{1\rho}}}\left(\exp\left(-{t}/{T_{1\rho}}\right) - exp\left(-{t}/{T_{IS}}\right)\right)$$

Where $T_{1\rho}$ is the relaxation time constant of a spin I in the rotating frame and ${1}/{T_{IS}}$ is the cross-polarization rate which is directly connected with the value of dipolar coupling. In agreement with that, alkyl groups show higher ^{13}C-^{1}H coupling as nitrile group.

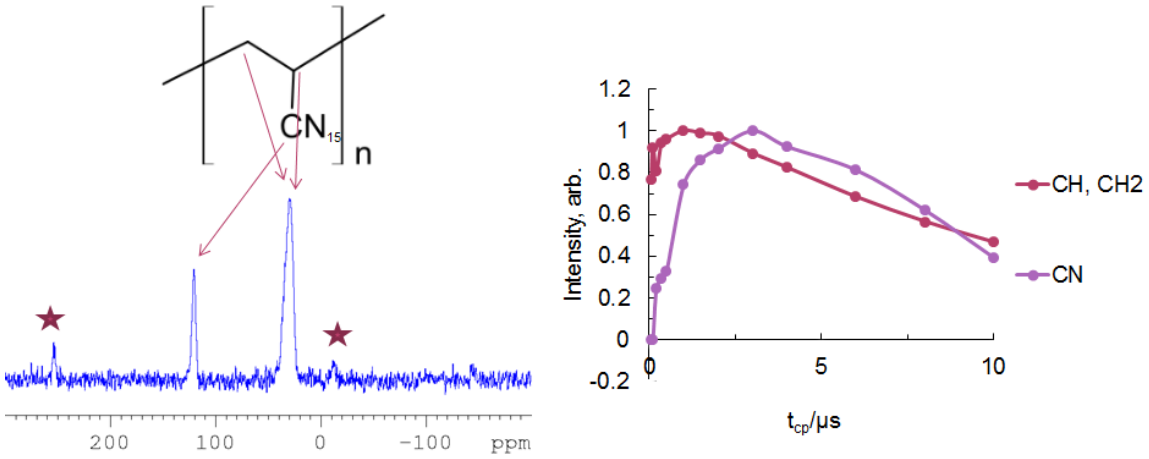

Figure 84. ^{1}H-^{13}C CPMAS spectra of PAN at contact time of 1500 us (asterisks indicate spinning sidebands from the signal at -120 ppm) (left) and intensity dependence of ^{1}H-^{13}C CPMAS signal of PAN on contact time.

Two test substances TS1 and TS2 (1-Amino-2,4-dicyano-6-methylcyclohexene) were prepared by cooperation partner to investigate chemical shifts of carbon and nitrogen in possible reaction products of polymerization. In TS1 nitrogen in one of cyano group and nitrogen in NH_2 group were substituted by N^{15} as shown in Figure 85. In TS2 only nitrogen in amino group was enriched.

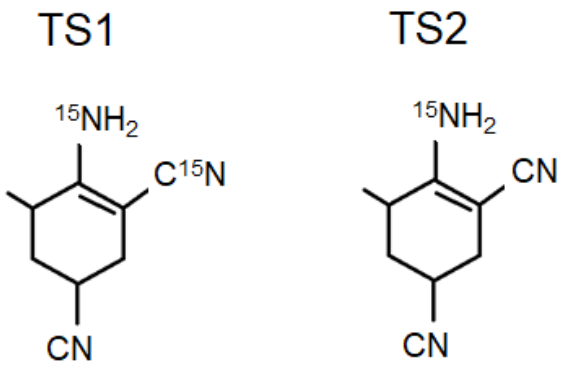

Figure 85. TS1 and TS2 (1-Amino-2,4-dicyano-6-methylcyclohexene) with selectively enriched nitrogen atoms.

In Figure 86 ^{1}H-^{13}C CPMAS spectra of TS1 at contact time 2000 us is shown on the left. Carbon atoms giving rise to the signal at 68 ppm (carbon atom bound to enriched CN group), 120 ppm (CN groups) and 163 ppm (carbon atom next to NH_2 group) can be distinguished. Several overlapping peaks from alkyl groups located between 20 and 30 ppm can also be seen. On the right, dependence of the intensity of resolved signals on contact time is represented. As expected, carbon atoms having no hydrogen in the direct surrounding exhibit slow magnetization build-up. ^{1}H-^{13}C CPMAS spectra obtained from TS2, as expected, are similar to the ^{1}H-^{13}C CPMAS spectra of TS1 and shown in Appendix 13.

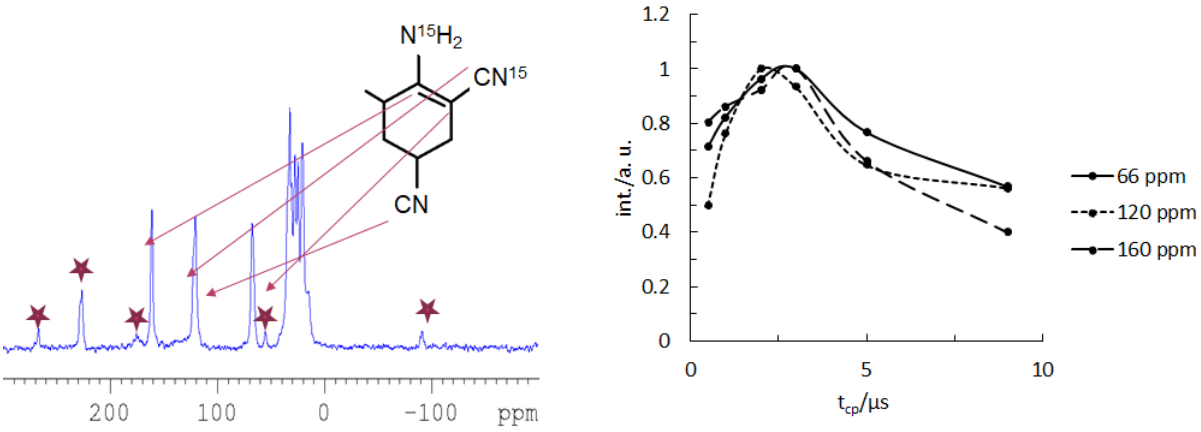

Figure 86. ^{1}H-^{13}C CPMAS spectra of TS1 at contact time of 2000 us (asterisks indicate spinning sidebands) (left) and intensity dependence of ^{1}H-^{13}C CPMAS signal of TS1 on contact time (right).

4.4.2. ^{1}H-^{15}N CPMAS Investigation

In Figure 87 ^{1}H-^{15}N CPMAS signal of PAN and its dependence on contact time is shown. Chemical shift of -128 ppm is in agreement with previous findings[162,163]. Contact time behavior of the signal corresponds with non-protonated carbon exhibiting slow build-up of magnetization.

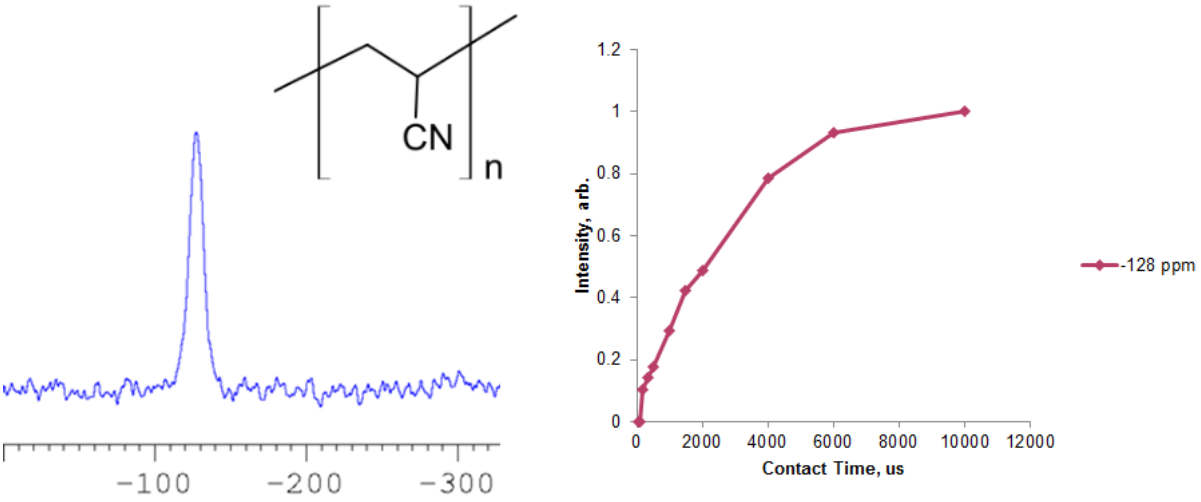

Figure 87. ^{1}H-^{15}N CPMAS spectra of PAN at contact time of 2500 us (left) and intensity dependence of ^{1}H-^{13}C CPMAS signal of PAN on contact time (right).

In Figure 88 ^{1}H-^{15}N CPMAS spectra of TS1 and TS2 are shown. Unambiguous assignment of the peak at -125 ppm to nitrile group and of the peak at -301 ppm to NH_2 group was done based on presence and absence of the signal, chemical shift and distinctly different contact time

behavior of two nitrogen signals. This information might help to understand the signals from heat-treated PAN fibers.

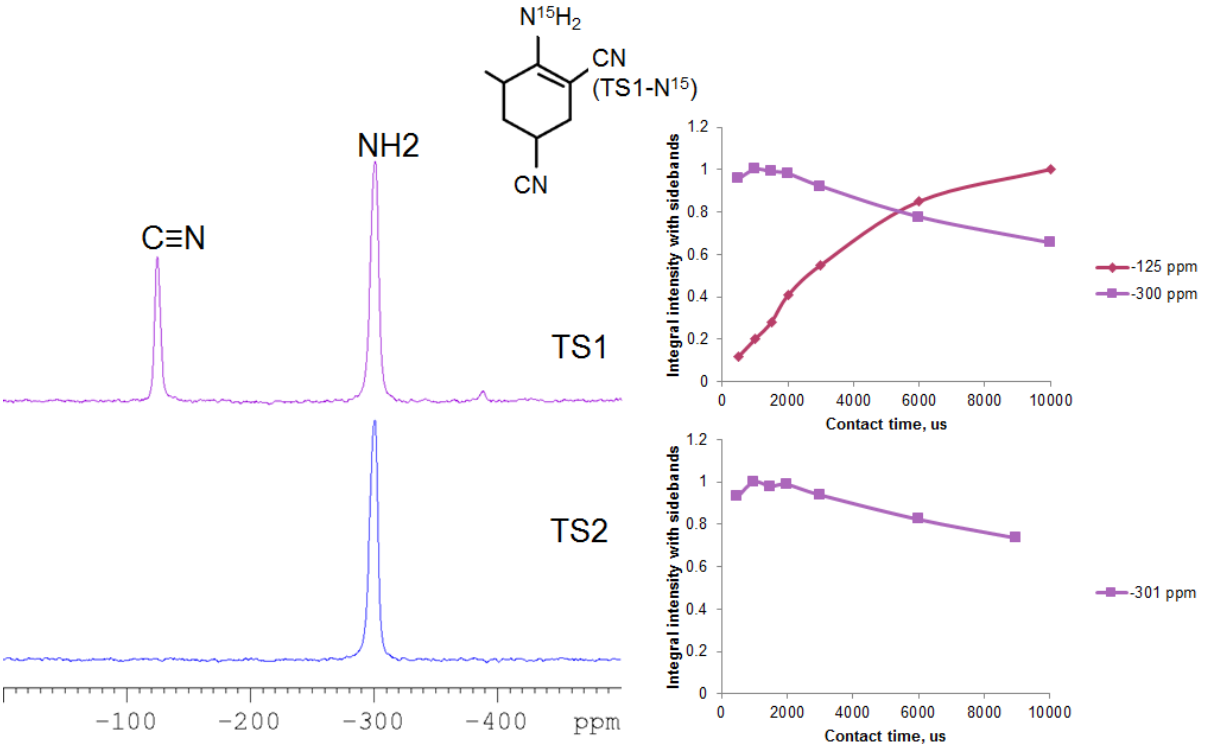

Figure 88. ^{1}H-^{15}N CPMAS spectra of TS1 (top) and TS2 (bottom) at contact time of 2500 us (left) and intensity dependence of ^{1}H-^{13}C CPMAS signal of TS1 (top) and TS2 (bottom) on contact time (right).

4.4.3. ^{13}C{^{15}N} REDOR NMR

Experiments involving ^{1}H-^{13}C CPMAS and ^{1}H-^{15}N CPMAS on the test samples and PAN allowed to gather information about chemical shifts and build-up of the CPMAS curves delivered additional information about bonding to hydrogen. More information can be derived by employing dipolar-based NMR methods between carbon and nitrogen nuclei. In this section, results of ^{13}C{^{15}N} REDOR NMR carried out on control double-enriched glycine sample, PAN and test substance TS1 are represented. To facilitate acquisition of NMR spectra, the magnetization of ^{13}C was prepared by magnetization transfer from hydrogen nuclei. ^{13}C{^{15}N} REDOR experiments were carried out using XY8 phase cycle, dephasing pulses on ^{15}N channel and two-pulse phase-modulated (TPPM) decoupling from protons.

Glycine test measurements. To establish the measurement procedure and estimate experimental error, ^{13}C{^{15}N} REDOR was first carried out on double-enriched glycine sample where nitrogen in amino group and carbon connected to amino group were enriched. Theoretical dipolar coupling between nitrogen and carbon is expected to be 964 Hz.

Experimental results together with simulation using SIMPSON software are represented in Figure 89. Comparison the results of SIMPSON simulations with experimental results delivers slightly lower than theoretical value of dipolar coupling – about 850 Hz indicating an experimental error of about 10%.

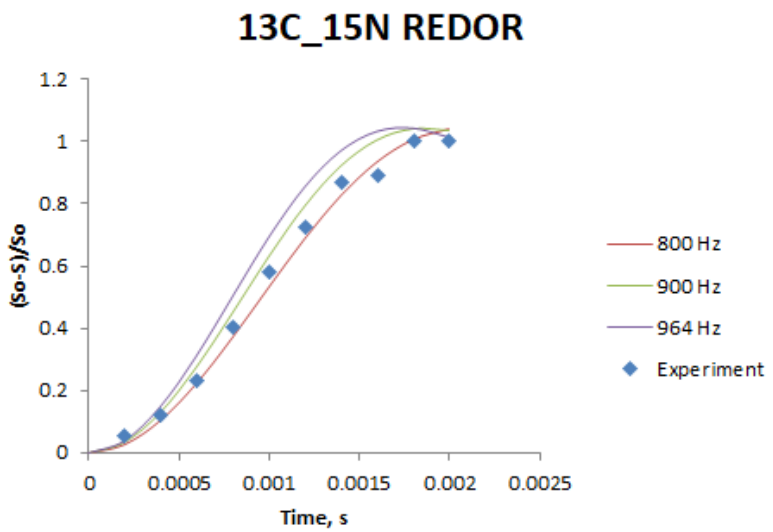

Figure 89. $^{13}C\{^{15}N\}$ test REDOR NMR on double-enriched glycine prior to the measurements on ^{15}N-enriched PAN. Blue diamonds represent experimental data and the lines represent results of SIMPSON simulations assuming the indicated dipolar couplings.

$^{13}C\{^{15}N\}$ REDOR on PAN. Results of $^{13}C\{^{15}N\}$ REDOR NMR on PAN was carried out using spinning speeds of 8 and 16 kHz are shown in Figure 90. Taking C-N distance to be 1.11 Å, dipolar coupling of 2230 Hz is expected. Experimental results show a little smaller dipolar coupling (about 1800-2000 Hz) which might be partially caused by not complete heteronuclear decoupling from hydrogen atoms due to instrumental restriction. Nevertheless, dipolar coupling to hydrogen and instrument mistakes contribute about 10% of the overall REDOR effect, which is comparable with REDOR mistake estimation carried out on double-enriched glycine control measurements (see Figure 89). Further important issue is that due to high dipolar couplings full REDOR-effect is observed after 4-6 rotor periods and the number of points applicable to the comparison with theoretical data is limited. This information would be used later to carry out REDOR measurement on the heated sample (see 4.5.3). Further possibility of evaluating high dipolar coupling might be REDOR experiments under higher spinning speeds while applying high-power dephasing pulses to decrease pulse length or an application of constant time REDOR (CT-REDOR)[164].

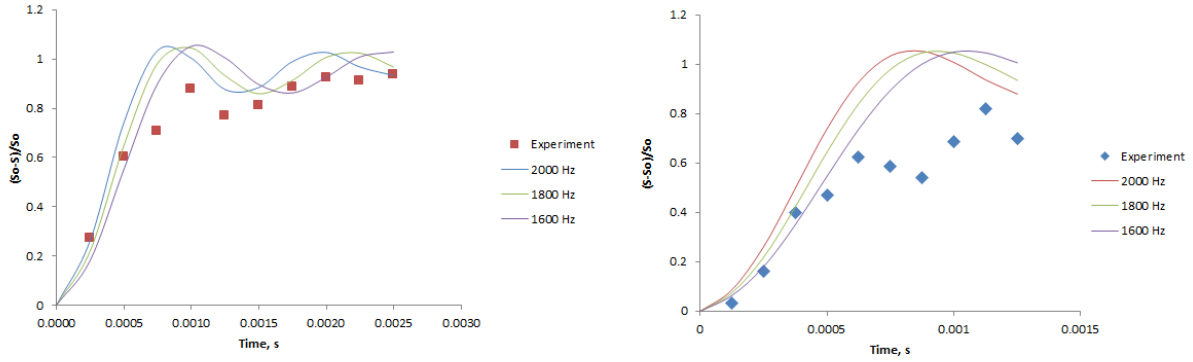

Figure 90. $^{13}C\{^{15}N\}$ REDOR of amorphous PAN sample using spinning speeds of 8 kHz (left) and 16kHz (right). Red squares and blue diamonds represent the experimental results using spinning speeds of 8 kHz and 16 kHz, respectively. Solid lines represent the results of SIMPSON simulations with indicated dipolar couplings.

Further important information, which can be extracted from $^{13}C\{^{15}N\}$ REDOR results and is important in the further analysis of REDOR on the heated samples is the effect of the width of the CSA on REDOR results. It is known that organic molecules with large CSA tensors might pose difficulties when interpreting REDOR results[165,166]. As shown in Figure 91, individual spinning sidebands and the behavior of the central transition during REDOR experiment do not follow the behavior of the integrated REDOR effect (the integrated REDOR effect above in Figure 90 was estimated by summing up the intensities of the central peak and all observed sidebands). This must be considered in the following analysis. Furthermore, large values of CSA tensors lead to appearance of out-of-phase rotational spinning sidebands during measurements as shown exemplary in Figure 147 (see Appendix 11).

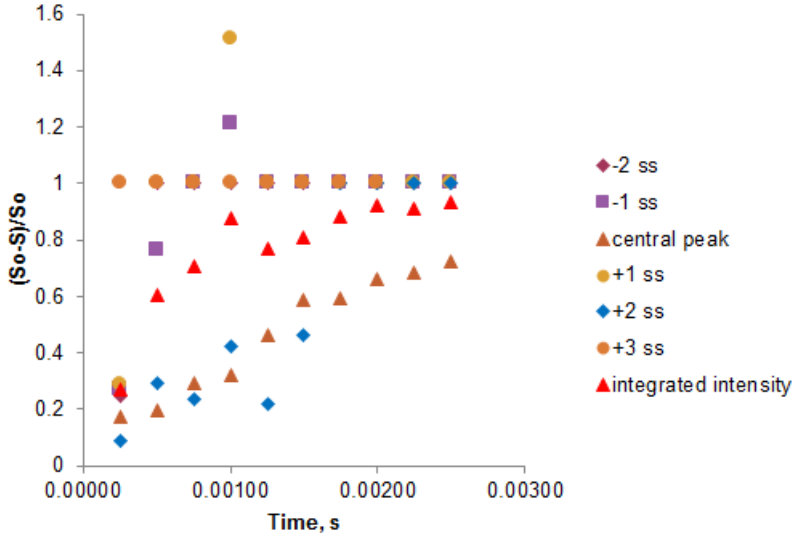

Figure 91. Integrated $^{13}C\{^{15}N\}$ REDOR intensity and individual $^{13}C\{^{15}N\}$ REDOR effects of sidebands using spinning speed of 8 kHz.

As was shown above, the REDOR effect observed on the central transition and the overall effect over all spinning sidebands differ a lot for carbon in nitrile moiety having large CSA tensor. To understand better this effect and to estimate possible implication of it to the analysis of the heated samples, SIMPSON simulations of the full spectra considering the width of CSA tensor and individual effects on sidebands were carried out. Then the REDOR effect was estimated for the central peak and for the integral intensity over all sidebands. Figure 145 in Appendix 9 shows the comparison of these two effects. The higher the dipolar coupling and CSA values, the larger is the difference between REDOR effect on the central peak and integral REDOR effect. This is especially important to consider when interpreting $^{13}C\{^{15}N\}$ REDOR results on the heated PAN samples for the peaks having large CSA (e. g. nitrile group – see Appendix 12) when all sidebands cannot be observed due to low intensity and severe mixing with other signals.

$^{13}C\{^{15}N\}$ REDOR on Test Substances. $^{13}C\{^{15}N\}$ REDOR measurements were also carried out on TS1. The integrated results over central peak and all sidebands are represented in Figure 92 (left). As expected, the ΔS/So values of the peak at 120 ppm (nitrile) does not exhibit full REDOR effect such as only half of the nitrogen atoms in cyano groups are ^{15}N-enriched (see Figure 85). On the right, the ΔS/So values multiplied by two for the nitrile group (such as exactly half of the nitrogen atoms in the cyano groups are enriched and contribute to $^{13}C\{^{15}N\}$ REDOR effect) are represented together with SIMPSON simulations (different widths of CSA tensors of ^{13}C atoms were considered in simulations). The distance expected for these test substance between nitrogen and carbon in C-NH_2 moiety is 1.35 Å[167] and 1.15 Å for nitrile group (due to delocalization of electron density through conjugated pi-orbitals and free electron pair)[167]. This corresponds with dipolar couplings of 1245 Hz and 2014 Hz, respectively. Similar to the results obtained on test glycine measurements and PAN fibers, measured dipolar couplings are slightly lower than theoretical (about 1100 Hz for C-N bond in C-NH_2 moiety and between 1600 Hz and 1800 Hz for nitrile group).

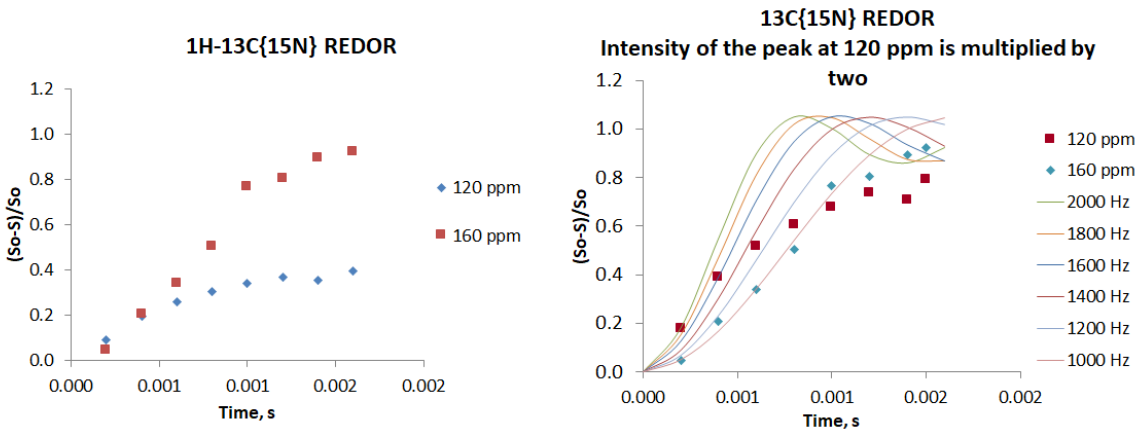

Figure 92. Results of $^{13}C\{^{15}N\}$ REDOR measurements on the test substance TS1. On the left REDOR results are shown as obtained from the experiment. On the right, the intensity of REDOR effect is multiplied by two for the peak at -120 ppm. Lines represent theoretical simulations carried out with SIMPSON software with indicated dipolar coupling.

4.4.4. Discussion of the results of Solid-State NMR Experiments on Unheated PAN and Test Samples

In this chapter, the structure of PAN precursor and test substances before heating was investigated by means of modern solid-state NMR: ^{1}H-^{13}C CPMAS, ^{1}H-^{15}N CPMAS and $^{13}C\{^{15}N\}$ REDOR NMR. This served as preparation for the experiments on the heat-treated samples and helped to understand better how the chemical environment is reflected in NMR spectra. Chemical shifts of the PAN and chemical shifts of carbon and nitrogen in possible reaction products obtained from the test substances were identified. Furthermore, REDOR-experiments on the unheated samples and also on the control samples allowed to estimate possible experimental error and also to understand better the effect of CSA parameters and spinning speed to the results evaluation.

4.5. Evolution of PAN structure Under Heating at Low Temperatures

Stabilization step is the heating of precursor fibers at low temperatures. In this chapter the stabilization step of carbon fibers production is investigated by means of solid-state NMR. After this step, the fibers can be carbonized and/or graphitized without being melted. The stabilization steps affect drastically the resulting structure and properties of the fibers. The polymerization of the PAN during this stage is still not fully understood. There are many proposed possible reaction pathways (see Figure 93) and the literature favors polymerization mechanism with appearance so-called ladder structure of conjugated -C=N-C=N- atoms. In this chapter, polymerization of PAN is investigated by means of *ex-situ* ^{1}H-^{13}C CPMAS, ^{1}H-^{15}N CPMAS and $^{13}C\{^{15}N\}$ REDOR and possible reaction products are proposed. To be able to carry out such an experiment, ^{15}N-enriched PAN-precursor prepared by the cooperation team were used. To our best knowledge, it is the first attempt to follow ^{15}N signal *ex-situ* in PAN during polymerization step.

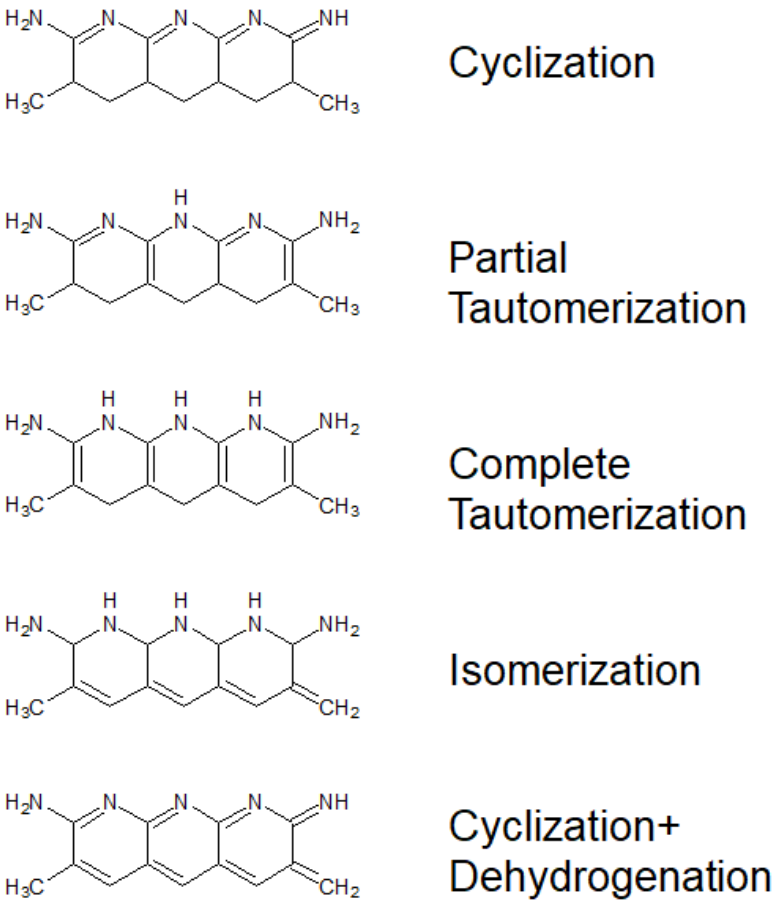

Figure 93.Proposed molecular motifs (left) resulting from different possible PAN polymerization mechanisms (right).

4.5.1. ^{1}H-^{13}C CPMAS Investigation

^{15}N-enriched PAN samples were heated to 268 °C (sample PAN268), 295 °C (sample PAN295) and 395 °C (sample PAN395) and were analyzed *ex-situ* to follow how the signal and, therefore, structure of polymer changes after treatment. Corresponding ^{1}H-^{13}C CPMAS spectra of these samples at contact time of 2000 us and dependence of signal intensity on contact time are shown in Figure 94. The positions of the main peaks are in perfect agreement with those found in the literature[31,32]. Overall signal might be discussed in terms of four distinct regions. The signal in the region C1 (above 140 ppm) could be attributed to aromatic carbon, which is supported by behavior of the signal intensity depending on contact time. Also, the signal of C=N moieties from conjugated -C=N-C=N- ladder structure is expected at this chemical shift range. To find out which chemical environment causes a peak in this region, $^{13}C\{^{15}N\}$ REDOR was performed and the results are discussed later in this chapter. In the region C2, nitrile signal and signal from some aromatic carbon, among other, are expected to be found. This, again, might be cleared by dipolar-based experiments. In the region C3 the signal from carbon C^{1} in enamine nitrile R_2N-C=C^{1}-CN group similar to those in TS1 might be found according to the chemical shifts identified on test substances. The signal in this region is not mixed with spinning sidebands, which was identified by variation of spinning speed during ^{1}H-^{13}C CPMAS experiments. In the region C4, a signal from aliphatic carbon is to be found. It is supported by contact time dependence of the peak at 28 ppm distinctly different from the contact time behavior of the peaks in C1-C3 regions (exhibiting much faster magnetization build-up). Although CPMAS spectra is not quantitative, growth of intensity of non-aliphatic signals comparing with aliphatic carbon signal at the same contact time speaks for polymerization reaction where hydrogen atoms are being removed from the network. Decreasing linewidth of the main peak with growing temperature might be explained by decreased heteronuclear coupling due to slowly removing hydrogen or less disordered structure.

As might be seen, assignment of the signals and conclusion about presence or absence of C-N bonds are difficult based on the chemical shift only. To extract more information, ^{13}C-^{15}N REDOR was carried out (see 4.5.3).

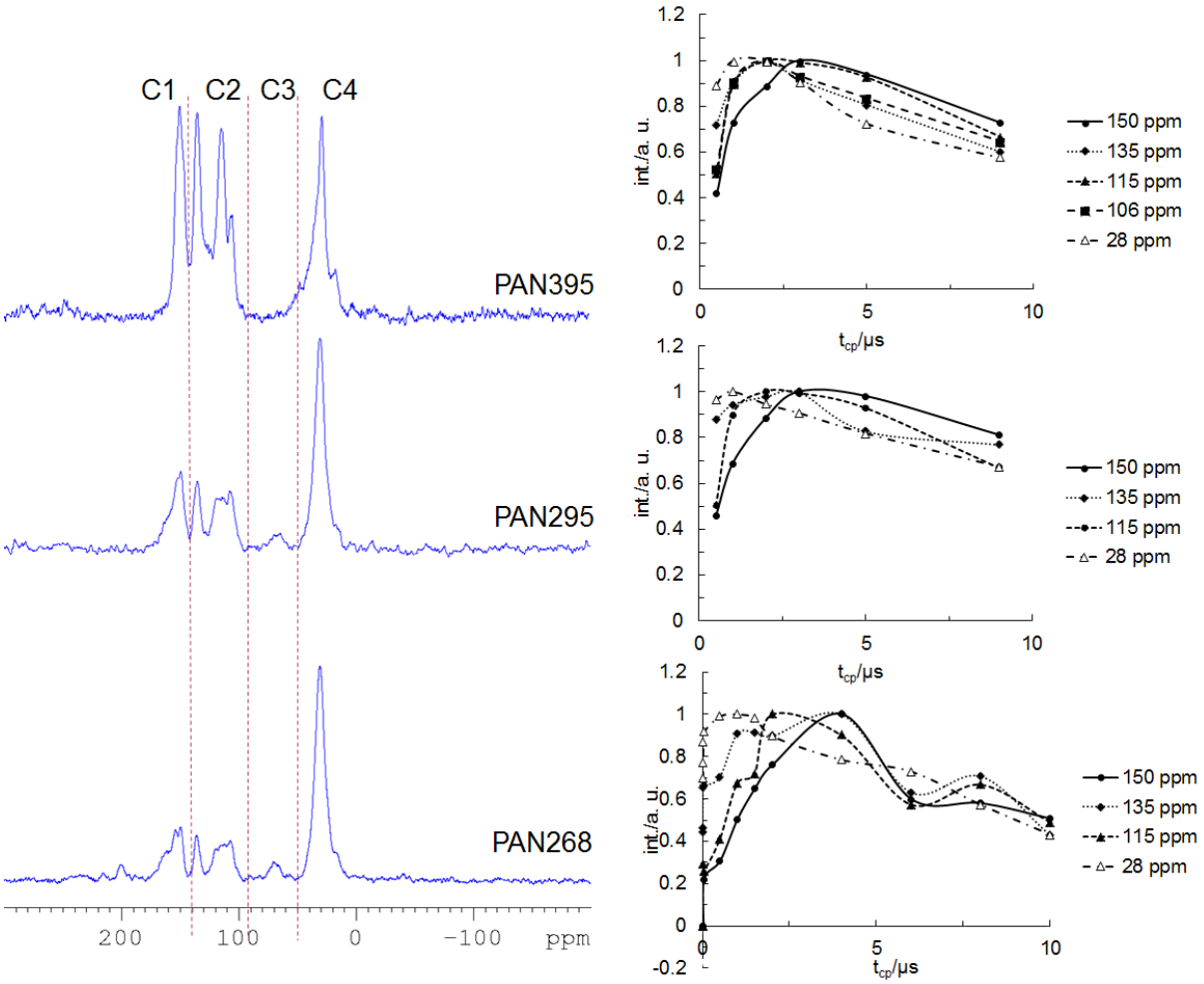

Figure 94. ^{1}H-^{13}C CPMAS (left) and dependence of the intensity of main signals on contact time (right) for the fibers heated to 268 °C (bottom), 295 °C (middle) and 395 °C (top).

4.5.2. ^{1}H-^{15}N CPMAS Investigation

In Figure 95 ^{1}H-^{15}N CPMAS of PAN268, PAN295 and PAN395 and corresponding contact time behavior of the main peaks are represented. Two regions N2 and N3 which exhibit distinctly different magnetization build-up were observed. Additionally, in the region N1, only some low-intensity and difficult to resolve signal growing with increasing temperature is observed. Typically, pyridine and pyrimidine moieties are found in this region[162,163]. According to measurements on PAN, TS1 and TS2, nitrile signal is expected to be found in the region N2. Other moieties also might give rise to the peak in this area as shown in Figure 150. This is supported by CPMAS contact time behavior of two main intensity contributors in this area showing non-hydrogenated environment around nitrogen signal in this area. The peaks in the region N3 probably corresponds to different NH_x moieties as shown in Figure 150. The peak to the right on -300 ppm might be explained by amine moieties both by measurements on test substances and by literature observation.

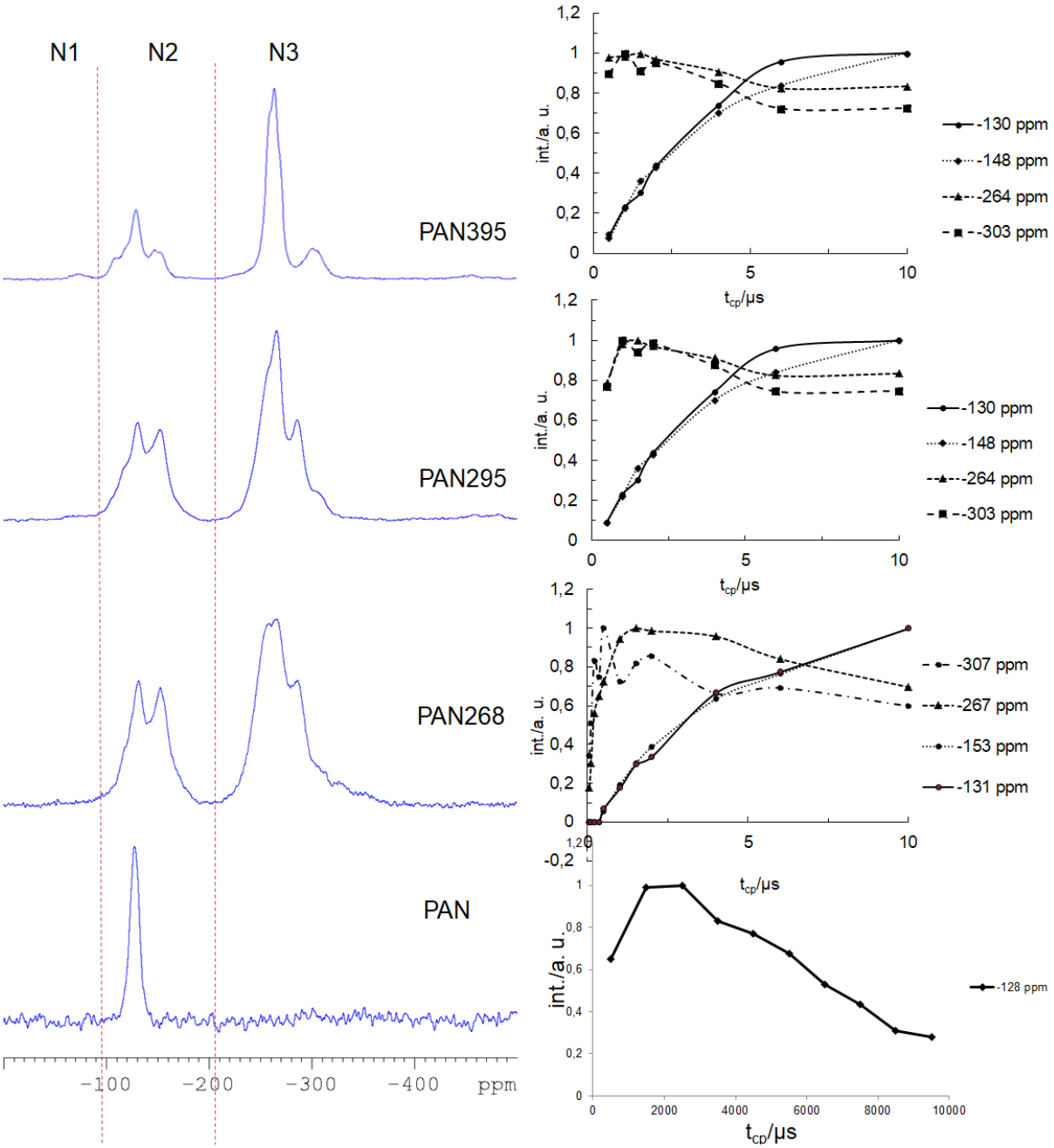

Figure 95. ^{1}H-^{15}N CPMAS (left) and dependence of the intensity of main signals on contact time (right) for the fibers heated to 268 °C (bottom), 295 °C (middle) and 395 °C (top).

The signal to the right of -300 ppm contributes to less than 5% of the whole intensity as estimated by quantitative ^{15}N single pulse experiments which are represented in Figure 96. Also, according to the quantitative single pulse observations, the ratio of the signal intensities in the regions N2 and N3 is about 70:30 in PAN which underwent different temperature treatments. Furthermore, in all experiments a peak located at around -130 ppm (at similar chemical shift as the cyano group observed in untreated PAN) and having similar

magnetization build-up according to the results of ^{1}H-^{15}N CPMAS is observed. This might indicate that nitriles are not consumed fully during reaction.

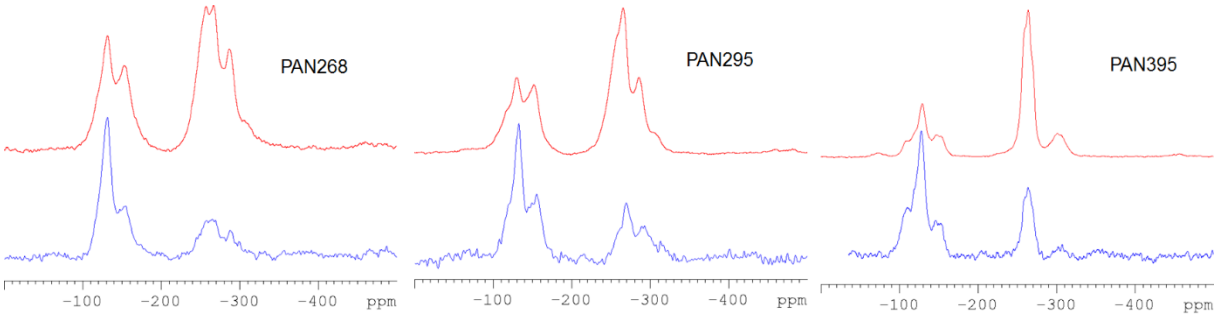

Figure 96. Comparison of ^{1}H-^{15}N CPMAS spectra (red) and onepulse spectra with ^{1}H decoupling (blue) of PAN268, PAN295 and PAN395 fibers.

4.5.3. $^{13}C\{^{15}N\}$ REDOR NMR

When ^{1}H-^{13}C and ^{1}H-^{15}N CPMAS spectra can deliver important information about local hydrogen bonding and structural moieties, dipolar-based ^{15}N-^{13}C correlation experiments might allow to obtain information about dipolar couplings at intermediate scales. To facilitate acquisition of NMR spectra, the magnetization of ^{13}C was prepared by magnetization transfer from hydrogen nuclei. $^{13}C\{^{15}N\}$ REDOR experiments were carried out using XY8 phase cycle, dephasing pulses on ^{15}N channel and two-pulse phase-modulated (TPPM) decoupling from protons. From REDOR measurements on PAN and test substances, it was known that due to high values of ^{13}C-^{15}N dipolar coupling, only first several points are the most important for quantitative evaluation of $^{13}C\{^{15}N\}$-REDOR effect. That is why first several experimental points were taken using large number of repetitions to reach quantitative results and be able to deconvolute individual peaks (further experiments might be carried out using higher spinning speeds while applying high-power dephasing pulses to decrease pulse length or an application of CT-REDOR[164]). Only the peaks in C1 region were $^{13}C\{^{15}N\}$ REDOR effect was sufficient were subjected to quantitative examination. The results of $^{13}C\{^{15}N\}$-REDOR in the regions C2-C4 are discussed qualitatively later in this section. The results of quantitative evaluation of first several points of the samples PAN268, PAN295 and PAN395 are represented in Figure 97, Figure 98 and Figure 99, respectively. Exemplary spectra of further experimental points are given in Appendix 15.

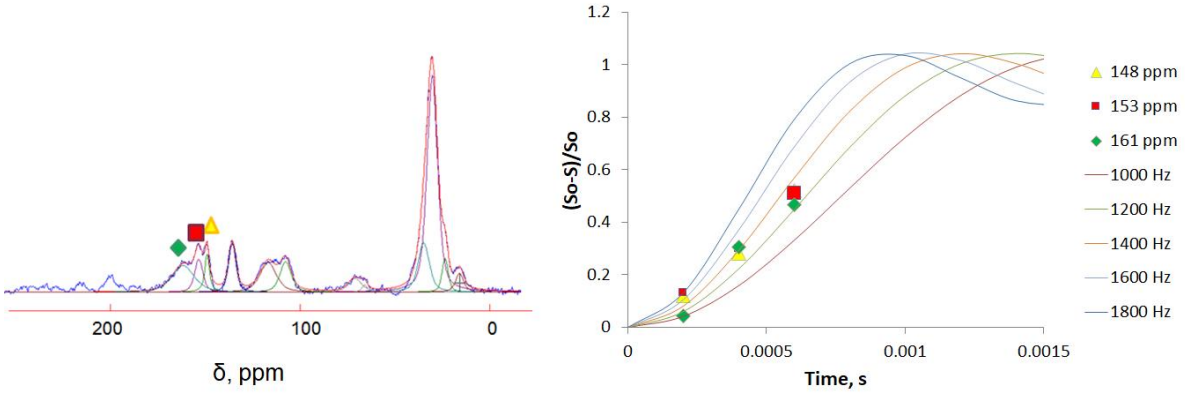

Figure 97. Results of $^{13}C\{^{15}N\}$ REDOR-evaluation of PAN268 sample. Yellow triangles, red squares and green diamonds represent the experimental results. To ease understanding, an exemplary spectrum with corresponding peaks marked is represented above. Solid lines represent the results of SIMPSON simulations with indicated dipolar couplings.

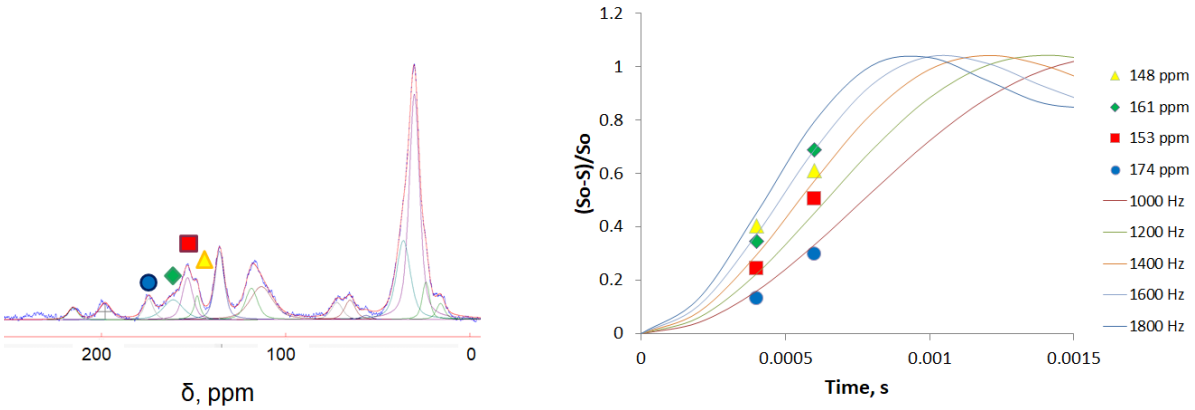

Figure 98. Results of $^{13}C\{^{15}N\}$ REDOR-evaluation of PAN295 sample. Yellow triangles, red squares, green diamonds and blue circles represent the experimental results. To ease understanding, an exemplary spectrum with corresponding peaks marked is represented above. Solid lines represent the results of SIMPSON simulations with indicated effective dipolar couplings.

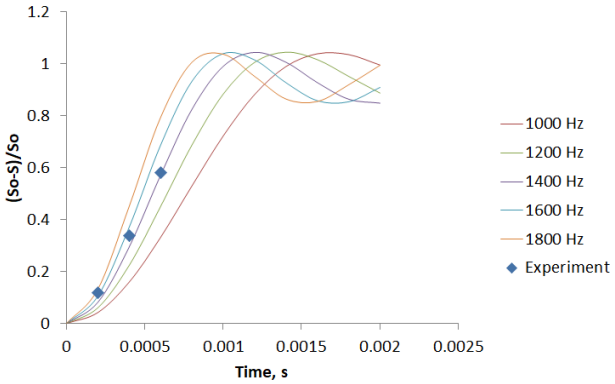

Figure 99. Results of $^{13}C\{^{15}N\}$ REDOR-evaluation of PAN395 sample. Blue diamonds represent the experimental results of the main peak at 150 ppm. Solid lines represent the results of SIMPSON simulations with indicated dipolar couplings.

In the region C1, several peaks are observed at lower treatment temperatures and only one major peak is detected after the heat treatment at 395 °C. In total, it might correspond with different polymerization reaction(s) intermediates leading to the polymerized structure with

one dominating moiety. Peaks deconvolution of PAN268 and PAN295 samples were rather complicated and should be treated carefully such as individual peaks are not resolved enough and alternative ways of spectra deconvolution might be achieved. Furthermore, from theoretical SIMPSON simulations it is known that spinning sidebands must be involved to ^{13}C-^{15}N REDOR effect evaluation (see 4.4.3). It was not possible to be considered for heated PAN samples due to low spinning sideband intensity and highly overlapped signals. Therefore, observed ^{13}C-^{15}N effect might be lower than actual present. Further complications might be mixing of the signal of ^{13}C carbon having ^{15}N nitrogen in environment with non-nitrogenated carbon coming at the same chemical shift, e.g. –C=C-O carbon.

In the sample PAN268, three major peaks were identified. They exhibit similar behavior during $^{13}C\{^{15}N\}$ experiments resulting in ^{13}C-^{15}N dipolar coupling of about 1400 Hz which clearly favors C=N connections. In the sample PAN295 four peaks showing distinct REDOR behavior with ^{13}C-^{15}N dipolar couplings of 1000 Hz, 1300 Hz and 1600 Hz were identified. The latter two clearly favor C=N connection. The first one might be attributed to C-N bond. The major peak in the sample PAN395 is simulated with dipolar coupling of 1500 Hz and indicates C=N connections.

In the region C2, no significant $^{13}C\{^{15}N\}$ REDOR-effect is observed, although signal from nitrile group normally appears in this region (see Appendix 14). On one side, it might be explained by nitrile moieties being fully reacted and transformed immediately at the beginning of the treatment. It contradicts quantitative ^{15}N onepulse measurements showing presence of nitrile group at all investigated temperatures (see 4.5.2). Other possible explanation might be strong mixing of nitrogenated and non-nitrogenated carbon so the resulting ^{13}C-^{15}N REDOR effect from nitrile groups is difficult to detect. That might be fortified by the weak effect on the central transition comparing with overall ^{13}C-^{15}N REDOR effect over all sidebands, which are not detectable in ^{1}H-^{13}C CPMAS spectra due to high CSA tensors of nitrile group (see 4.4.3). Weak effect is observed in the region C3 which corresponds with assumption of the signal being C^1 carbon in enamine nitrile R_2N-C=C^1-CN group. The peak in the C4 region shows very small $^{13}C\{^{15}N\}$ REDOR effect, which indicate that only small fraction of aliphatic carbon, is connected to nitrogen.

Summing up all findings on the heated PAN sample, we might propose that nitrile is not fully consumed during the reaction. Signal typical for pyridine, pyrimidine-like motifs were

observed in ^{1}H-^{15}N CPMAS spectra which disfavors cyclization and isomerization mechanisms although we might not exclude that they might be present as intermediates at lower temperatures. Results of ^{1}H-^{15}N CPMAS NMR suggest presence of NH-moieties in accordance with partial or complete tautomerization and isomerization mechanisms. The observed $^{13}C\{^{15}N\}$ REDOR effect in the aliphatic carbon region is small which disfavors a pronounced contribution of the isomerization mechanism. C=N moieties are suggested by $^{13}C\{^{15}N\}$ REDOR after all treatment temperatures which disfavors complete tautomerization and isomerization mechanisms as final reaction mechanisms. Furthermore, combined results of the existence of small ^{1}H-^{15}N CPMAS signals below -300 ppm where signals of amines are expected to be found, small $^{13}C\{^{15}N\}$ REDOR effect for the carbon in aliphatic region and presence of the signal similar to C^{1} in a moiety R_2N-C=C^{1}-CN in ^{1}H-^{13}C CPMAS spectrum indicates that most of the amines present in the structure exist as enamine nitrile X_2N-C=C-CN. This disfavor the existence of amines connected to aliphatic carbon atoms which speaks against a pronounced contribution of the isomerization reaction. Solid-state NMR results suggest that the X_2N-C=C-CN moiety is present in the structure after heat treatment at lower temperatures, but it is not observed at the samples treated at 395 °C. The combined results obtained by solids-state NMR experiments suggest -C=C-C=N- and -C=C-NH- moieties as main structural motifs. This together with abovementioned reasons against other mechanisms suggest that partial tautomerization and cyclization, followed by dehydrogenation mechanisms seem to be most important for the thermal transformation of PAN homopolymer.

4.5.4. Discussion of the Results of Solid-State NMR experiments on Heat-Treated PAN

In this chapter, the polymerization of PAN was followed by means of modern solid-state NMR: ^{1}H-^{13}C CPMAS, ^{1}H-^{15}N CPMAS and $^{13}C\{^{15}N\}$ REDOR NMR. To our best knowledge, it is the first study involving investigation of ^{15}N NMR signal in heat-treated PAN. Three samples which underwent through temperature treatment at different temperatures were investigated to follow the rection *ex-situ*. The results of ^{1}H-^{13}C CPMAS agree with previous studies indicating subsequent aromatization of the network and several intermediate compounds. Their amount increases and their variety decreases with increasing temperature. Contact-time dependent ^{1}H-^{13}C CPMAS studies allowed to probe the vicinity of the carbon environment to the protons. The obtained ^{1}H-^{15}N CPMAS spectra might be subdivided into three distinct regions. In the area to the left of -100 ppm pyridine and pyrimidine moieties are expected to be found but the peaks in this region are estimated to contribute less than 5% of the overall signal intensity

as propose by single pulse ^{15}N measurements. Presence of this signal disfavors cyclization and isomerization mechanisms as final reaction mechanisms. In the area from -100 to -200 ppm non-protonated nitrogen atoms corresponding with at least three distinct peaks are observed. In the third region to the left to -200 ppm at least four different protonated NH_x signals are observed. The exact assignment is difficult due to the limited knowledge and highly overlapping peaks. Interestingly, the ratios of peak areas of non-protonated to protonated signals does not change much and stays about 70:30 for all investigated samples although the relative ratios of the peaks inside these regions change drastically which probably indicates many intermediate reaction stages. With quantitative ^{15}N MAS NMR it was also found that nitrile moieties are not consumed fully during this polymerization stage. Most of the amines present in the structure exist as enamine nitrile X_2N-C=C-CN at lower temperatures which speaks against a pronounced contribution of the isomerization reaction, but this moiety is not observed at the sample treated at 395 °C. Only the peaks in the region to the left to 150 ppm in carbon spectrum where substantial $^{13}C\{^{15}N\}$ REDOR effect was observed were subjected to the quantitative $^{13}C\{^{15}N\}$ REDOR NMR experiments. All three major peaks of the sample PAN268 show the ^{13}C-^{15}N dipolar coupling of at least 1400 Hz which speaks for presence of C=N connections. PAN295 sample signal delivered dipolar coupling of 1000 Hz which favors single C-N bond and 1300 Hz and 1600 Hz which again clearly favors double C=N bonds. The measurements on PAN395 sample exhibiting only one peak round 150 ppm also propose the dipolar coupling of 1500 Hz which again suggests double C=N connections. The small observed $^{13}C\{^{15}N\}$ REDOR effect in the aliphatic carbon region disfavors a pronounced contribution of the isomerization mechanism. Probably, -C=C-C=N- and -C=C-NH- are the main structural motifs and the results of solid-state NMR Studies suggest partial tautomerization and cyclization followed by dehydrogenation mechanisms of PAN polymerizations.

4.6. Additives and Their Effect on Polymerization of Polyacrylonitrile at Low Temperatures

As outlined in the theoretical section in 2.2.2, copolymers or additives are necessary for the industrial carbon fibers manufacturing. However, the role of additives in polymerization and their effect to chemical reactions is not fully understood. NMR proposes a unique way to follow the reaction mechanism by tracking selectively enriched atoms in the copolymer. Furthermore, based on the experiments on the productions row (see 4.3), NMR is the most suitable technique for investigation of stabilization step where the role of copolymers is especially important. The results of such investigations on selectively enriched samples are represented in this section. First, the sample where some hydrogen atoms are substituted with deuterium are studied. Second, double-enriched copolymers and their effect to the reaction is investigated by means of modern solid-state NMR. At the end of this chapter probable intermediate reaction compound with selectively enriched nitrogen atoms is studied.

4.6.1. Deuterated Samples

As described in 2.2.2, the exact mechanism and role of methacrylate in the production of carbon fibers is still not fully understood. We hope that with the help of solid-state NMR spectroscopy we could propose how MA participates in copolymerization. For that, atoms of hydrogen in MA were substituted through deuterium by cooperation partners and then the polymerization reaction was followed *ex-situ* by means of solid-state NMR spectroscopy.

Test Measurements. Prior to the main measurements, test ^{1}H-^{2}H CPMAS measurements were carried out on the test (co)polymers where certain hydrogen atoms were substituted by deuterium. Test deuterated compounds and the resulting ^{1}H-^{13}C CPMAS spectra are shown in Figure 100. Quadrupole coupling of deuterium depends strongly on the local dynamic resulting in lower quadrupole coupling in CD_3 group due to higher mobility comparing with CD and CD_2 groups. Quadrupole coupling therefore could be used to extract additional information about local chemical environment. That is especially important such as CD_3 and CD and CD_2 groups are difficult to distinguish in solid state NMR based on chemical shift only as shown in Table 20. Further implication important for following research is that the behaviors of intensities of the central peak and the integral intensity over all sidebands are equal under changing contact time (see Appendix 17). To estimate if substitution of hydrogen

by deuterium can affect polymerization path, we carried out *ex-situ* ^{1}H-^{13}C CP-MAS investigations of the sample D1 which underwent temperature treatment (see Appendix 17). The spectrum and magnetization build-up of individual peaks during varied contact time CPMAS experiments is similar to those observed in previous chapter which supposes that substitution of hydrogen by deuterium does not change drastically the polymerization pathway.

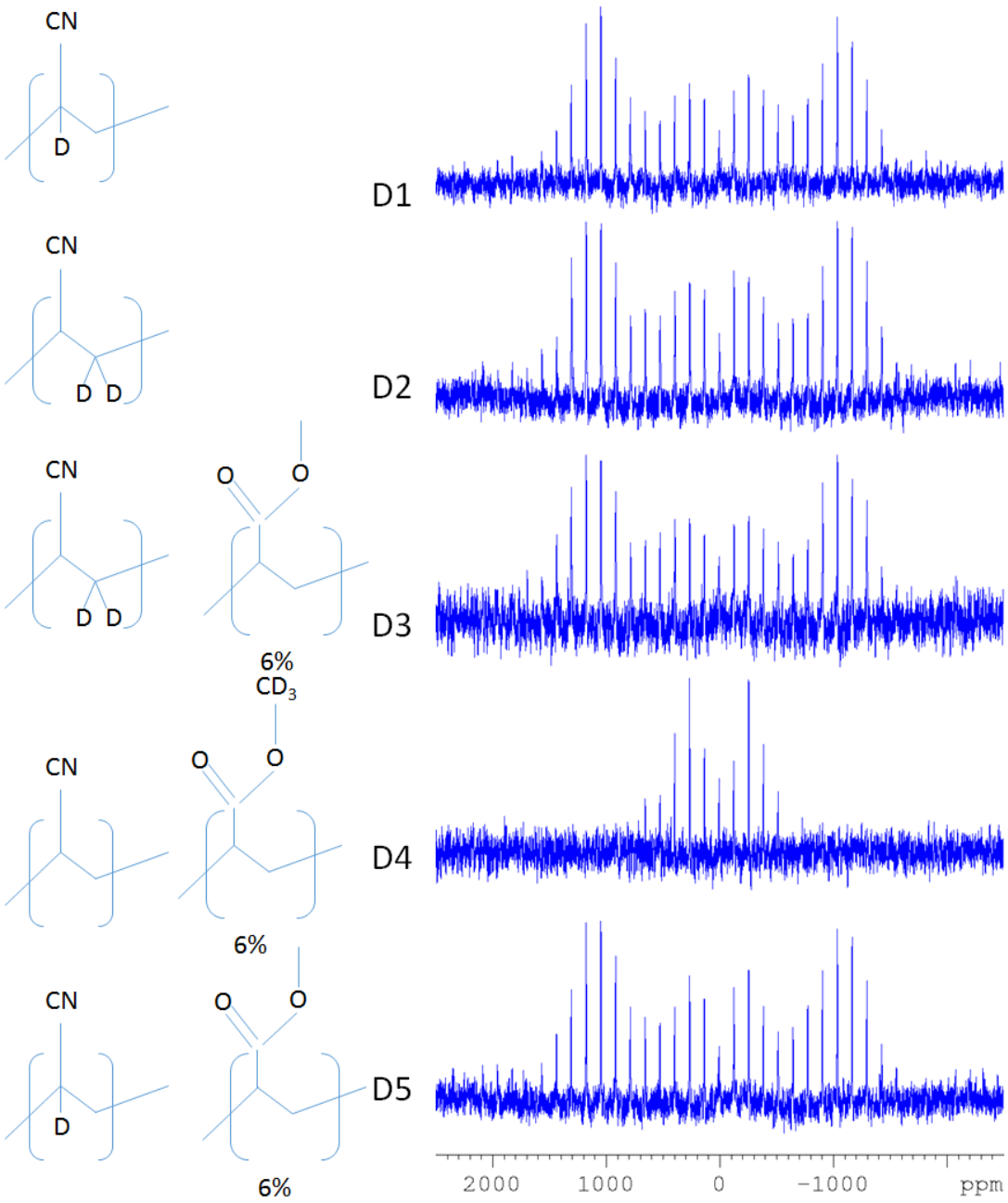

Figure 100. ^{1}H-^{2}H CPMAS spectra of the test deuterated compounds obtained at the contact time t = 1000 us and spinning speeds of 6 kHz.

Sample	Chemichal shift, ppm	C_Q, kHz
D1	4.4	159±6
D2	3.4	163±6
D3	3.6	162±6
D4	4.2	52±6
D5	4.2	160±6

Table 20. Chemical shifts and values of quadrupole couplings of deuterated samples obtained by simulation with DMFIT software [112].

D4 Sample and Its Transformation Under Heat Treatment.

To investigate behavior of acrylate group and its role in polymerization reaction, the sample D4 was heated to 295 °C under argon. In Figure 101 the results of ^{1}H-^{2}H CPMAS (left) and the central transition of ^{2}H MAS (right) are represented. As might be seen from the single excitation measurements, deuterium signal gets broader. It is known that the nuclei with spin I=1 are very sensible to the magic angle settings and that small deviation from the correct magic angle can lead to the broadening or even splitting of the signal. That is why the measurements were carried out with back-to-back MAS setup control to avoid experimental mistakes and to ensure that e. g. line broadening was not caused by maladjustment of the magic angle. Broader peaks after heating might be therefore explained by higher inhomogeneity of environment under polymerization reaction. At the same time chemical shift of deuterium signal changes only moderately staying in the aliphatic region.

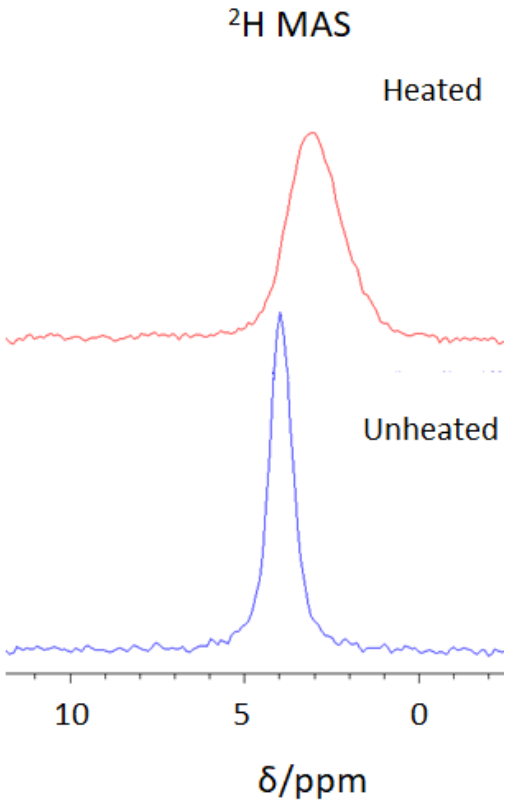

Figure 101. Comparison of the central peaks of ^{2}H MAS taken at 25 kHz (right) of unheated and heated D4 sample.

Aliphatic character of deuterium environment after heating is supported by the results of ^{1}H-^{2}H CPMAS experiments (CPMAS was used to facilitate acquisition of the signal and to employ short recovery times of hydrogen atoms at the lowest possible spinning speeds where intensity is divided over many spinning sidebands to obtain more exact values of quadrupole coupling constant). In Figure 102 on the left it could be seen that quadrupole coupling does not change upon heating (both samples have Cq values of 52±6 kHz according to simulation with DMFIT software). This implies that deuterium is still a part of CD_3 group after heating. Nevertheless, it is still an open question if CD_3 group is still a part of polyacrylate copolymer or if it is a part of some reaction product, which might be chemically or physically attached to the polymer structure.

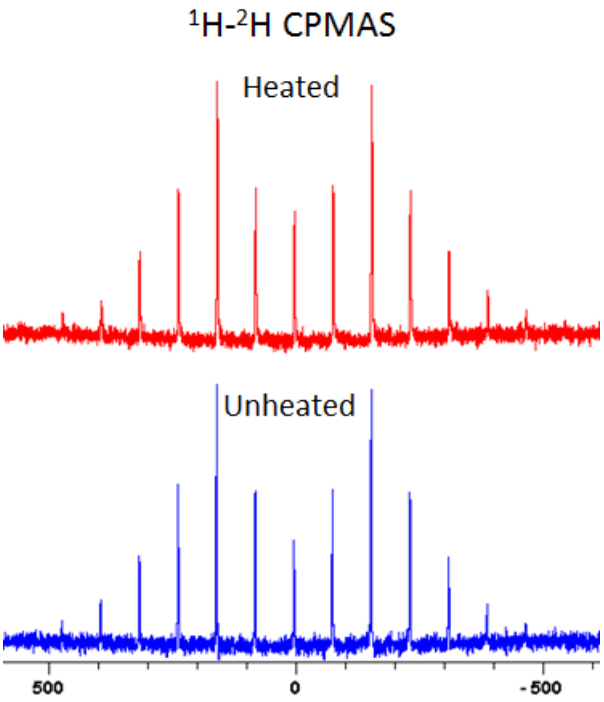

Figure 102. Comparison of ^{1}H-^{2}H CPMAS results taken at 6 kHz unheated and heated D4 sample.

To probe the vicinity to protons (see 1.2.4), ^{1}H-^{2}H CPMAS signal was measured using variable contact times. ^{1}H-^{2}H CPMAS signal applicable to contact time dependent magnetization build-up examination was possible to obtain without using strong hydrogen decoupling which allowed obtaining signal intensity dependence even at advanced contact times. The results are represented in Figure 103. As might be seen, the curve behaviors are nearly identical which speaks strongly for similar hydrogen environment, namely, without direct hydrogen connection (slow magnetization build-up). This implies that CD_3 group is still attached to the polymer backbone and not, e.g. physiosorbed on the surface although it is not clear whether it is still part of methacrylate group or if it is a part of some polymerization reaction product.

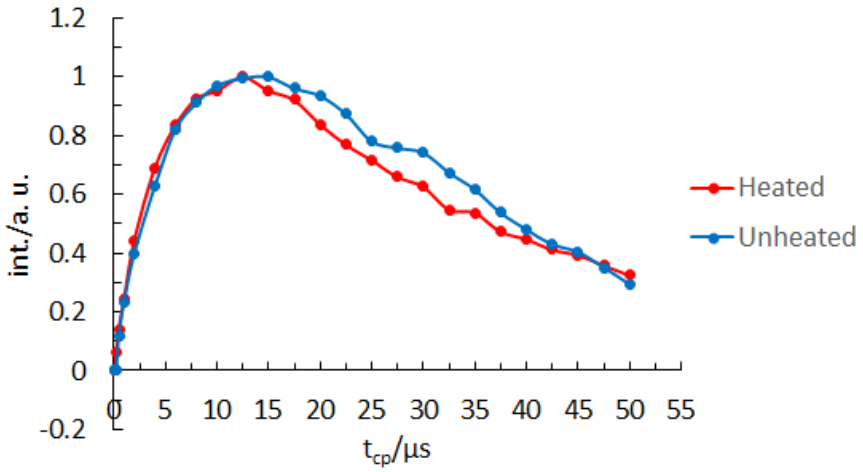

Figure 103. Dependences of ^{1}H-^{2}H CPMAS signal intensities of heated and unheated D4 samples on the contact time.

^{1}H-^{13}C CPMAS spectra of unheated and heated D4 samples were taken to help to identify if the methacrylate copolymer is a part of the structure after temperature treatment. The results are represented in Figure 104. In the spectra of the unheated signals from alkyl carbons and the signal at 120 ppm from nitrile group, which have already been identified in 4.3 are present. Two new signals from carbon in CD_3 group around 55 ppm and from carbon in carbonyl group at 175 ppm are detected. As can be seen from the spectra, these signals are still observed after heat treatment. To avoid misassignment and mixing with spinning sidebands, spectra were taking using different spinning speeds. Presence of these two signals speaks strongly for carbonyl group and CD_3 group being a part of heat-treated copolymer. Unfortunately, it is not clear if they are still the part of the same initial methacrylate group. Aside from these additional two peaks, ^{1}H-^{13}C CPMAS spectra are nearly identical to the spectra observed from the heated PAN copolymer (see 4.5.3). The behavior of the main peaks under changing contact time is essentially similar to those of PAN295 samples and exhibits similar proton environment as shown in Figure 104 which indicate that methacrylate does not alter the structure of polymerized carbon network drastically. Due to low intensity of the new signals (6 mol% of MA in PAN-MA copolymer) and their mixing with other signals and spinning sidebands it was challenging to analyze their magnetization build-up during varied contact time CPMAS experiments.

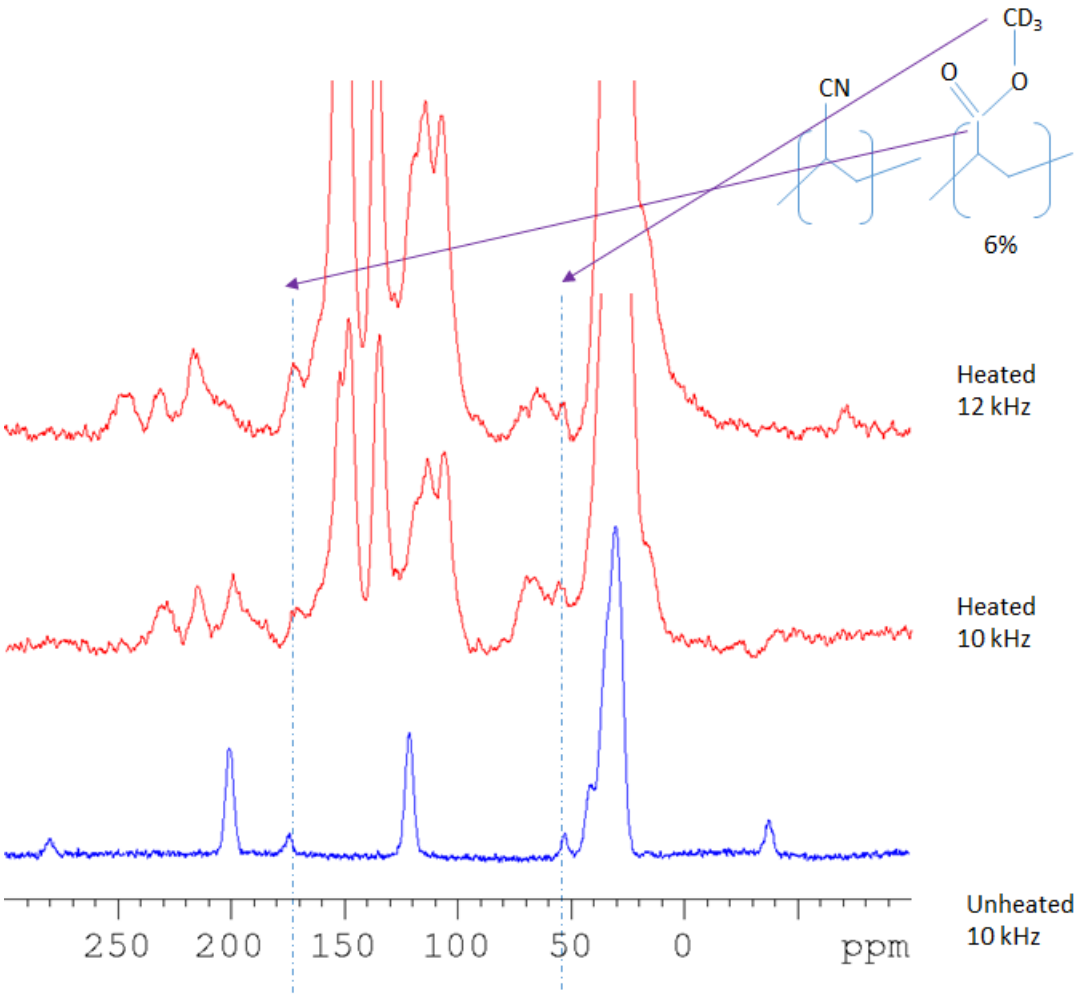

Figure 104. ^{1}H-^{13}C CPMAS spectra of unheated and heated D4 samples. The spectra of heated sample were taken using different spinning speeds to avoid mixing of spinning sidebands and the actual signal.

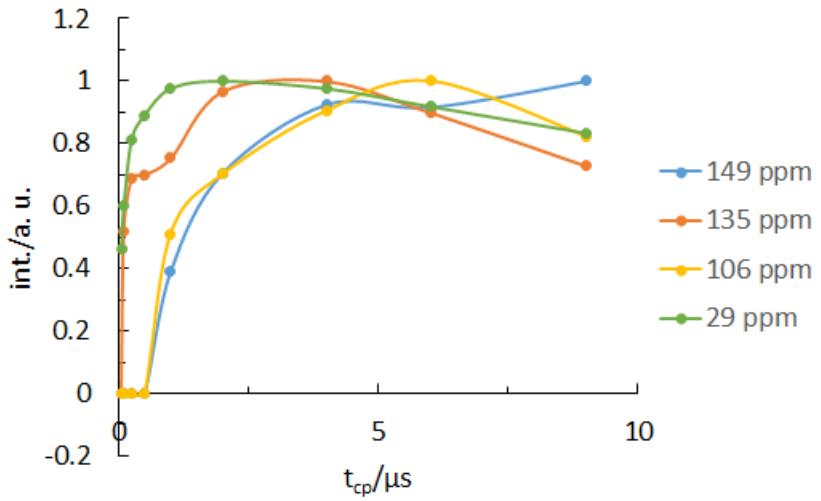

Table 21. Dependence of Intensities of the main ^{1}H-^{13}C CPMAS signals of heated D4 sample on the contact time.

Single pulse excitation NMR allows quantitative measurements to define deuterium amount remaining in the probe after heating. The results show 37 % of initial deuterium still being

present in the structure (see Appendix 18). This corresponds well with the results of IR spectroscopy[111].

Summing up, following results were obtained by NMR investigation of deuterated samples:

- About 37% of the initially selectively enriched deuterium is present in copolymer after heat-treatment;
- After heat treatment deuterium is still the part of CD_3 group;
- CD_3 is the part of polymerized copolymer structure after heating;
- Proton environment of deuterium does not change much after heat treatment.
- At least some part of carbonyl group of the initial methacrylate compound is present in the sample during heating. It is not possible to say if CD_3 is a part of initial methacrylate moiety after heat treatment.
- Methacrylate does not alter the structure of polymerized carbon network drastically.

4.6.2. Double-Enriched Sample

To understand better the role of the copolymer and to attempt to answer some question left open after experiments with deuterated samples, double-enriched samples with ^{15}N-enriched PAN copolymer and ^{13}C-enriched MA-copolymer were prepared by cooperation partner as shown in Figure 105. In this chapter this sample is investigated prior to heating and after undergoing temperature treatment not only by CPMAS NMR but also by 2D ^{1}H-{^{15}N} and ^{13}C{^{15}N}-HETCOR NMR experiments. Possible molecular moieties produced by the reaction of MA copolymer with PAN are then proposed.

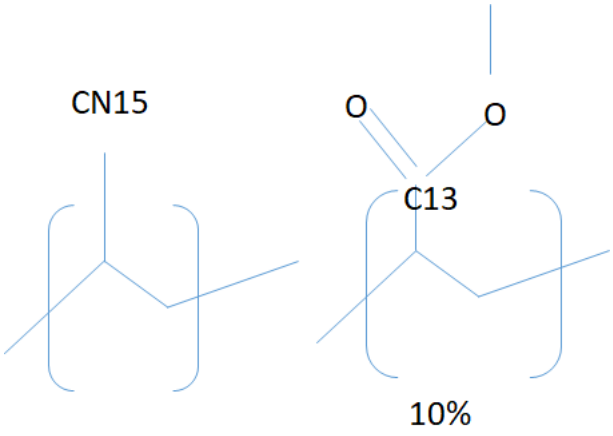

Figure 105. Isotopically labelled (AN-co-MA)-polymers.

^{1}H-^{13}C and ^{1}H-^{15}N CPMAS on Unheated Sample. Labelling of carbon atoms in (PAN-co-MA) polymer opens an opportunity to investigate selectively their chemical environment by means of solid-state NMR. First ^{1}H-^{13}C CPMAS spectra of PAN-MA sample was taken to obtain information about chemical shift and the results are shown in Figure 106. As might be seen the signal from the enriched carbon atom makes the highest contribution to the spectra even considering that the enriched atoms are minority of the overall amount of the carbon in the copolymer. Additionally, the signals from non-enriched alkyl carbons (around 30 ppm), CH_3 group (around 52 ppm) and the carbon in nitrile group (around 120 ppm) could be identified. ^{1}H-^{13}C CPMAS curve behavior is in accordance with hydrogen environment of ^{13}C nuclei showing no directly bounded protons.

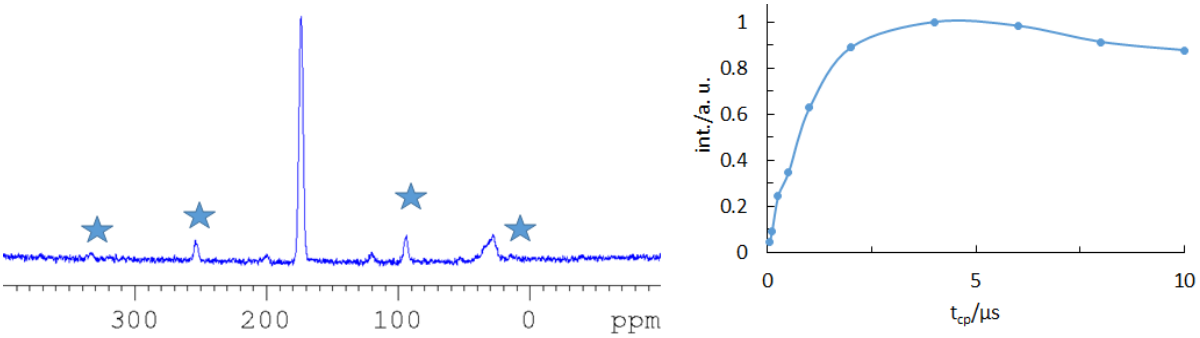

Figure 106. ^{1}H-^{13}C CPMAS spectra (left) and the dependence of ^{1}H-^{13}C CPMAS integrated intensity of the main peak (right) of PAN-MA copolymer. Asterisks indicate spinning sidebands.

As expected, ^{1}H-^{15}N CPMAS NMR of PAN-MA sample has one peak at -120 ppm coming from nitrile group. CPMAS signal dependence shows non-protonated environment and is similar to those observed in PAN and TS1(2) (see 4.4.2)

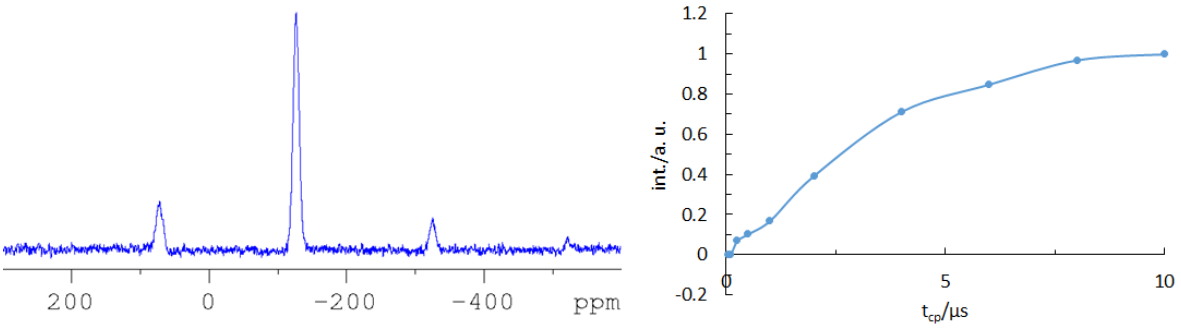

Figure 107. ^{1}H-^{15}N CPMAS spectra (left) and the dependence of ^{1}H-^{15}N CPMAS integrated intensity of the main peak (right) of PAN-MA copolymer.

Comparison of ^{1}H Spectra of Heated and Unheated Samples. First, ^{1}H MAS spectra of double-enriched sample was taken and compared with the spectra obtained from unheated sample. Appearance of aromatic hydrogen signal was expected. The results are shown in Figure 108. Significant structural changes happening during heating result in two additional peaks to the left from aliphatic peak observed in the unheated sample. Individual hydrogen peaks are too poorly resolved to identify if they are caused by aromatic compounds or by aromatic compounds and amine groups. This might be found out by ^{1}H-^{15}N HETCOR (*vide infra*).

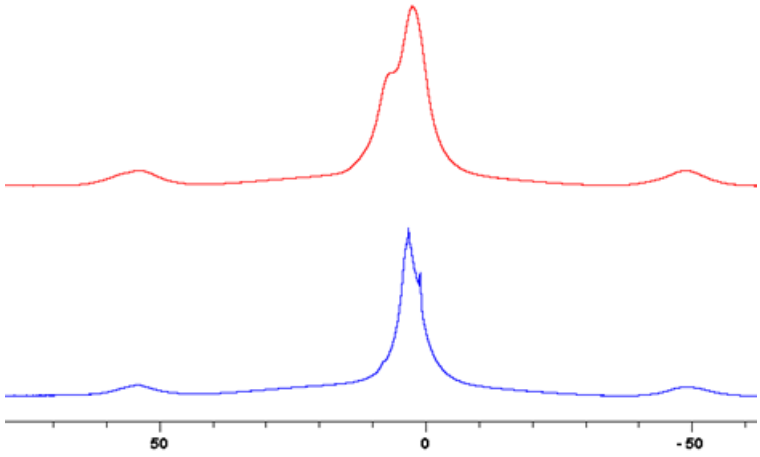

Figure 108. ^{1}H MAS spectra of unheated (blue) and heated (red) PAN-MA sample.

^{1}H-^{13}C CPMAS of Heated Sample. The results of ^{1}H-^{13}C CPMAS NMR are represented in Figure 109. As might be seen, four main peaks at 148, 151, 162 and 172 ppm might be observed. According to CPMAS contact time dependence (the peaks at 148 and 151 ppm were treated as one peak) they are not directly bound to protons. Apart from three main peaks, aliphatic signal from non-enriched carbon nuclei is observed around 30 ppm. Furthermore, small peak at 136 ppm is observed. It is not caused by spinning sidebands as found by measurements employing different rotational speeds (see Appendix 20). It is difficult to say if this is a peak from non-enriched carbon or from some minor reaction product. Both the absence of the pronounced peak at -120 ppm and small CSA values of the main peaks (see Appendix 20) indicate there is either no nitrile group observed or that the amount of nitrile is too low to be detected. This means that nitrile is not a main product of polymerization reaction of MA in PAN-MA copolymer.

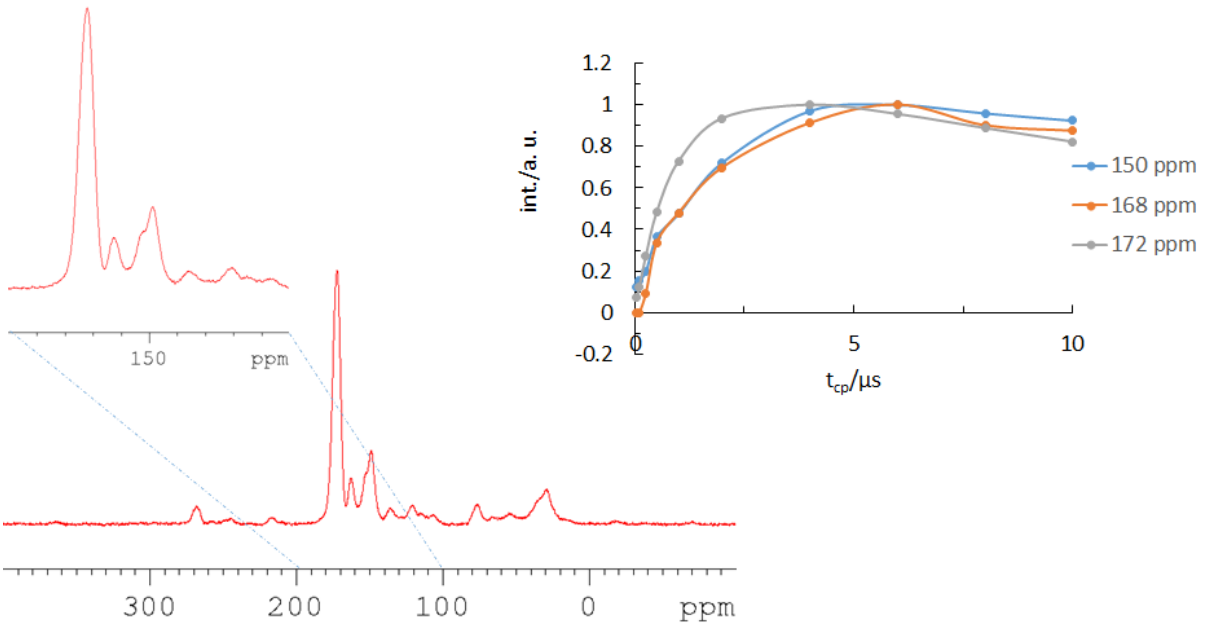

Figure 109. ^{1}H-^{13}C CPMAS signal (left) and dependence of the intensity of main signals on contact time (right) for the heated double-enriched PAN-MA sample.

The signal at 172 ppm has the same chemical shift and the same CSA parameters as ^{13}C carbon in the unheated sample (see Appendix 19 and Appendix 20). Most probably it is the signal from non-reacted part of methacrylate group which is expected from the results from deuterated sample (see 4.6.1) or the peak from ester group where CD_3 was exchanged by some other moiety. This might be found out with carbon-nitrogen dipolar-based experiments. From quantitative single pulse ^{13}C measurements the intensity ratios of the main three peaks at 172, 162 and 150 ppm are 70:5:25 (see Appendix 21). Although some peak intensity might be caused by non-enriched carbon, this contribution is expected to be small (see above for non-heated sample), so there is an indication MA participated in polymerization reaction. This is very important point because it was believed that neutral comonomers do not participate in the reaction and rather play the role of plasticizers (see 2.2.2). Chemical shift and CSA values of the peak at 162 ppm is similar to those of C^1 carbon in $C{=}C^1{-}NH_2$ group in TS1 (see 4.4.1) although it can not be stated that the same chemical environment is causing peak in this region and more investigation are needed.

^{1}H-^{15}N CPMAS of Heated Sample. In Figure 110 the results of ^{1}H-^{15}N CPMAS and corresponding dependencies of the intensities of the main peaks on contact time in CPMAS experiment are represented. As might be seen, the obtained spectrum resembles the one obtained from PAN295 sample (the linewidths are smaller due to higher values of RF-power used in

heteronuclear decoupling from hydrogen). The peaks to the left from -200 ppm show no direct bonding to proton. It is difficult to identify exactly which moieties cause appearance of the signal in this region based on the chemical shift alone and further investigation are needed. The peak to the right from -200 ppm is most probably caused by NH_x group which speaks strongly for at least part of the changes observed in ^{1}H spectrum being caused by appearance of amine group. Again, the intensity of the signal below -300 ppm is low (mixing of the signal with spinning sidebands was verified by variation of spinning speed) which speaks against pyridine, pyrimidine and triazine motifs. The ratio of intensities of non-protonated and protonated regions is 65:35 as identified by ^{15}N single pulse MAS NMR (see Appendix 22). It is slightly lower that the ratio observed in pure PAN fibers (see 4.5.2). Therefore, MA in PAN-MA might participate in the reaction leading to appearance of more NH_x group.

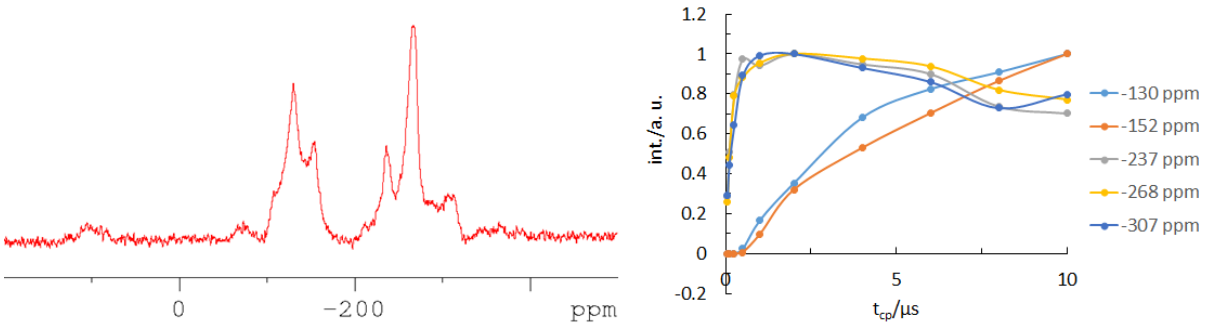

Figure 110. ^{1}H-^{15}N CPMAS signal (left) and dependence of the intensity of main signals on contact time (right) for the heated double-enriched PAN-MA sample.

^{1}H-{^{15}N} HETCOR of Heated Sample. To identify if the additional peak in ^{1}H spectra are caused by amine or some aromatic moieties, ^{1}H-^{15}N HETCOR NMR was carried out. In Figure 111 the results of ^{1}H-{^{15}N} HETCOR experiment are shown. Contact time of the contact pulse was varied and controlled to ensure that only direct ^{1}H-^{15}N bonding is observed. Only part of the nitrogen signal to the left of -200 ppm gives rise to cross-correlation peaks. This together with contact time dependences of ^{1}H-{^{15}N} CPMAS explains that at least some part of the additional peak in hydrogen spectra after heating is caused by NH_x moieties.

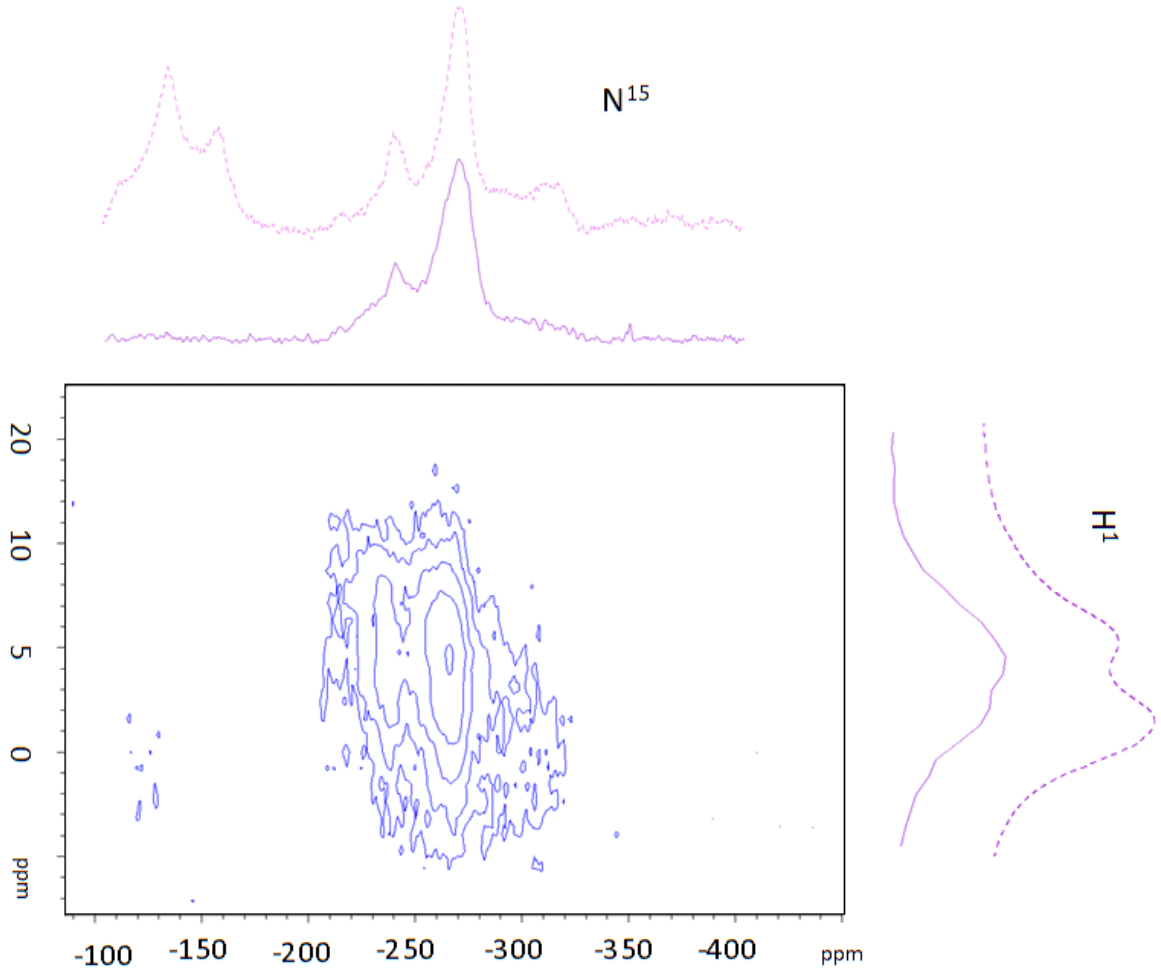

Figure 111. ^{1}H-^{15}N HETCOR of the double-enriched PAN-MA sample. Dotted line shows ^{1}H-^{15}N CPMAS spectra.

$^{13}C\{^{15}N\}$ REDOR of Heated Sample. From the results of ^{1}H-^{13}C CPMAS NMR we could find out that MA copolymer participates in the reaction although an exact assignment of the resulting compounds was difficult. ^{15}N enrichment of nitrile group in PAN polymers allowed to carry out dipole-based experiments and find out if nitrogen atoms in PAN and selectively enriched carbon atoms in MA copolymer are connected through dipolar coupling. To facilitate acquisition of NMR spectra, the magnetization of ^{13}C was prepared by magnetization transfer from hydrogen nuclei. $^{13}C\{^{15}N\}$ REDOR experiments were carried out using XY8 phase cycle, dephasing pulses on ^{15}N channel and two-pulse phase-modulated (TPPM) decoupling from protons.

Test $^{13}C\{^{15}N\}$ REDOR-effect measurement were first carried out on double-enriched glycine samples where nitrogen in amine group and carbon next to amine group were enriched. The results are represented in Figure 112. Theoretical dipolar coupling between nitrogen and carbon is 964 Hz. Comparing the results of SIMPSON simulations (width of carbon CSA tensor

was considered in the simulations) with experimental results delivers slightly lower values of dipolar coupling – about 850 Hz for $^{13}C\{^{15}N\}$ REDOR and about 800 Hz for $^{15}N\{^{13}C\}$ REDOR. This calibration measurements allowed to consider experimental restrictions in the evaluation of $^{13}C\{^{15}N\}$ REDOR on the double enriched PAN-MA copolymers.

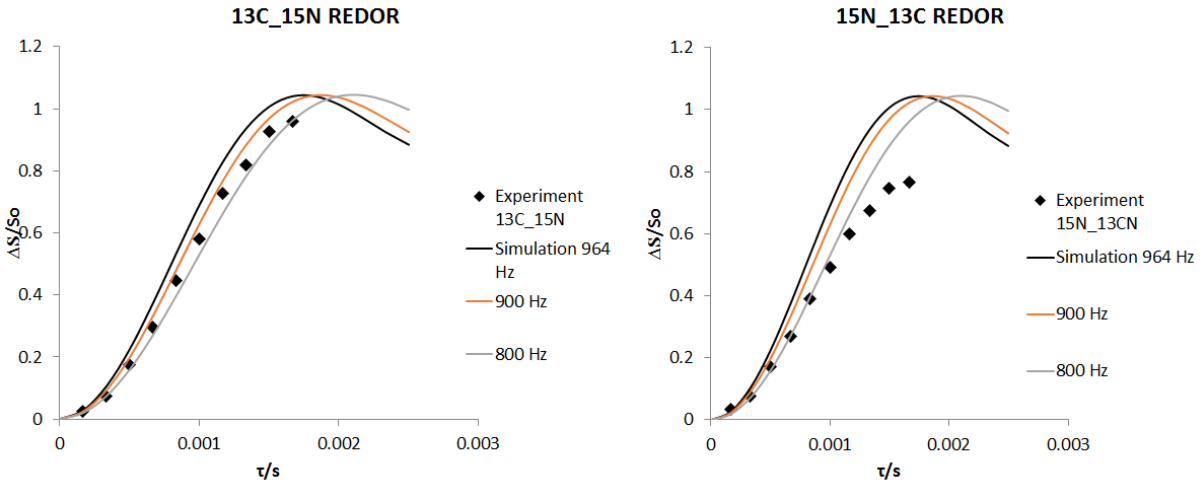

Figure 112. $^{13}C\{^{15}N\}$ (left) and $^{1}H\text{-}^{15}N\{^{13}C\}$ (right) test REDOR NMR on double-enriched glycine prior to the measurements on double-enriched PAN-MA samples. Black diamonds represent experimental data and the lines represent results of SIMPSON simulations assuming the indicated dipolar couplings.

The results of $^{13}C\{^{15}N\}$ REDOR measurements on the double-enriched PAN-MA sample are shown in Figure 113. First important information might be taken from the behavior of experimental points without quantitative fitting: all four major signals observed in $^{1}H\text{-}^{13}C$ CPMAS NMR show significant REDOR-effect, which means that selectively enriched carbon in MA copolymer reacts with nitrogen in PAN. This is very important and contradicts common belief of methacrylate being chemically inert and not playing an important role in polymerization reaction. Most of the enriched carbon reacts with nitrile group forming at least four different carbon-nitrogen surroundings with at least one C-N connection. This also indicates that the signals at 55 and 175 ppm observed in the $^{1}H\text{-}^{13}C$ CPMAS spectra of heated deuterated sample are probably not coming from the part of the same methacrylate group but from the separated ester groups and $CD(H)_3$ groups being still the part of polymer.

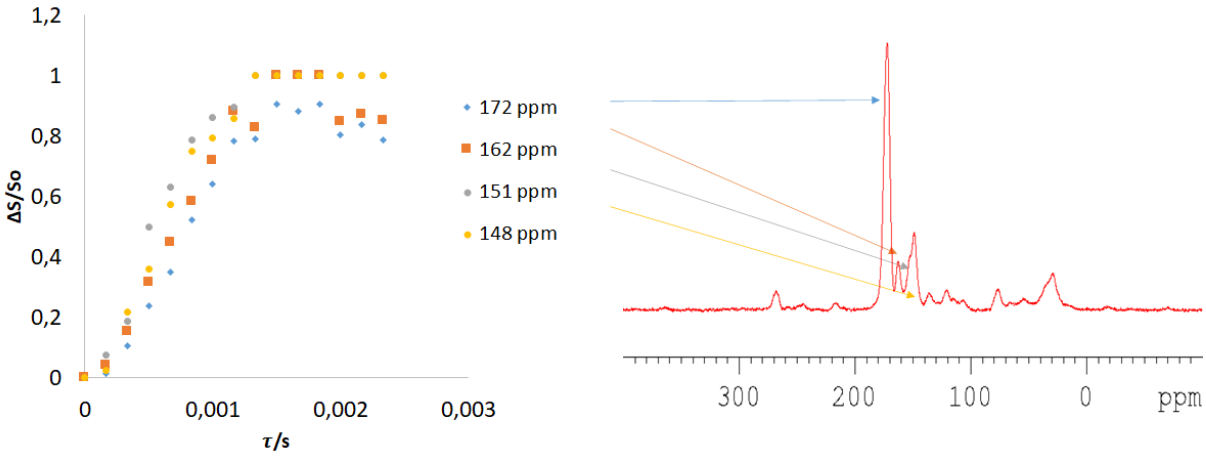

Figure 113. Results of $^{13}C\{^{15}N\}$ REDOR-evaluation of heated PAN-MA sample. Blue diamonds, orange squares and yellow and grey circles represent the experimental results. To ease the understanding, an exemplary spectrum with corresponding peaks marked is represented to the right.

In Figure 114 the results of $^{13}C\{^{15}N\}$ REDOR experiments on PAN-MA sample together with the results of SIMPSON simulations are represented. “A”, “AA” and “AAA” indicated single double and triple-bond of the average length. “R” and “RR” indicate single and double bond of reduced length. Theoretical dipolar couplings used for simulation were multiplied by 964/850 to obtain REDOR curves. Estimated widths of CSA tensor (see Appendix 20) of individual peaks were considered during simulations. Furthermore, such as estimated CSA of the peaks are rather moderate and it is known that nitrile group having the highest CSA is not the main reaction product, quantitative estimation of $^{13}C\{^{15}N\}$ REDOR-effect is possible even if some sidebands could not be considered during analysis. The peaks at 151 and 148 ppm are badly resolved but have similar CSA and decay with the same speed which allowed them to be evaluated together. On the right possible carbon-nitrogen configurations following from quantitative $^{13}C\{^{15}N\}$ REDOR analysis are represented. The behavior of individual peaks with corresponding fits can be found in Appendix 23.

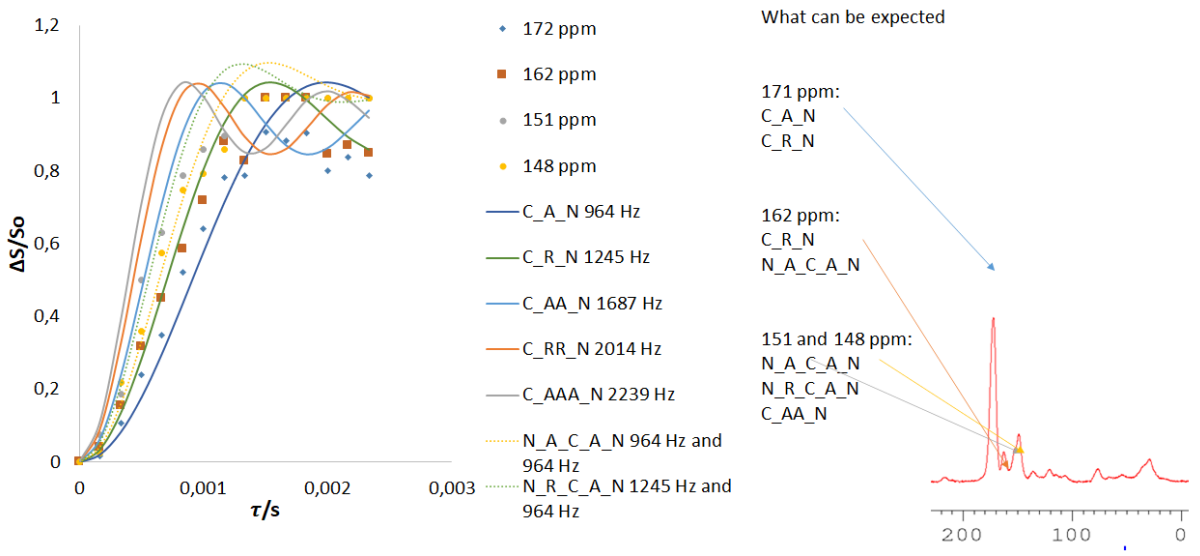

Figure 114. Results of $^{13}C\{^{15}N\}$ REDOR-evaluation of heated PAN-MA sample. Blue diamonds, orange squares and yellow and grey circles represent the experimental results. To ease the understanding, an exemplary spectrum with corresponding peaks marked is represented to the right. Solid lines represent the results of SIMPSON simulations with indicated dipolar couplings. "A", "AA" and "AAA" indicated single double and triple-bond of the average length. "R" and "RR" indicate single and double bond of reduced length.

The peak at 172 ppm correspond the best with single-bond C-N moiety. This is in a perfect agreement with the results of ^{1}H-^{13}C MAS NMR of unheated and heated PAN-MA sample, where it was already proposed that it might be an ester with substituted CH_3 group. The peak at 162 ppm might be caused by the C^1 carbon in $C=C^1$-NH_2 group or N-C-N-C-N carbon. The peaks at 151 ppm and 148 ppm could be attributed to different C=N and N-C=N constellations and more exact proposals cannot be made without further analysis. Only CN nitrile moiety can be excluded due to different chemical shift and drastically different CSA values.

$^{13}C\{^{15}N\}$ HETCOR of Heated Sample. While results of $^{13}C\{^{15}N\}$ REDOR allowed to estimate values of dipolar couplings between nitrogen and carbon atoms, $^{13}C\{^{15}N\}$ HETCOR experiments gives an opportunity to observed cross-correlation peaks in 2D spectra caused by coupled nuclei. To facilitate acquisition of $^{13}C\{^{15}N\}$ HETCOR spectrum, the magnetization of carbon nuclei was prepared by magnetization transfer from hydrogen atoms. Test measurement on glycine were carried out to establish the procedure. The results of $^{13}C\{^{15}N\}$ HETCOR NMR are represented in Figure 115. Contact time of the contact pulse was varied to ensure that only direct ^{13}C-^{15}N bonding is observed. As expected from $^{13}C\{^{15}N\}$ REDOR, all carbon signals are caused by carbon having nitrogen in the surrounding. Interestingly, the small signal corresponding with the peak at -120 ppm in carbon spectrum caused by nitrile group is observed. It is not clear if it is caused

by some minor reaction product or if it is a part of non-reacted amine group connected with non-enriched carbon atoms.

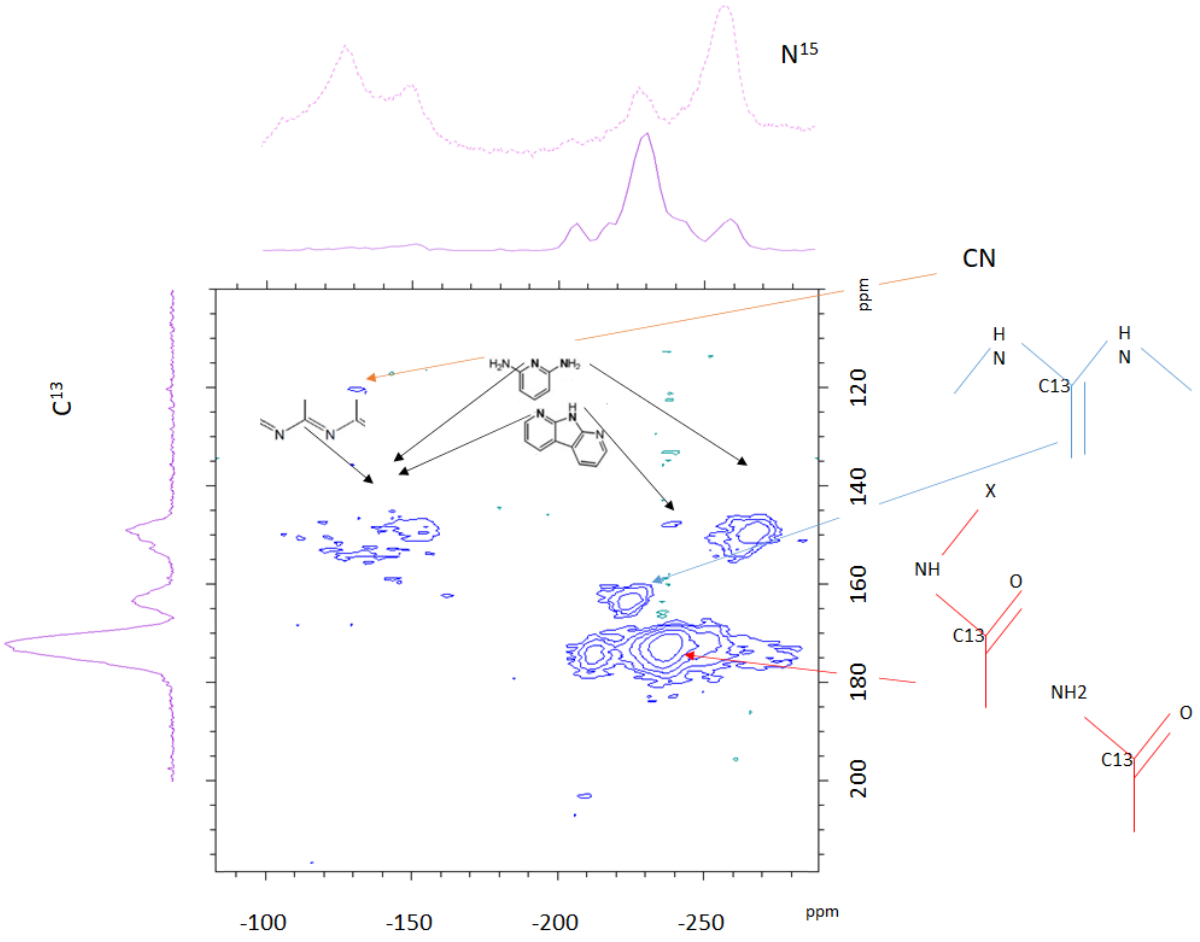

Figure 115. $^{13}C\{^{15}N\}$ HETCOR NMR correlation spectra of double-enriched PAN-MA sample. The dotted lines represent ^{1}H-^{13}C and ^{1}H-^{15}N CPMAS NMR spectra.

The signal at 172 ppm correlates with at least two nitrogen peaks. From ^{1}H-^{15}N HETCOR it is known that these nitrogen atoms should have hydrogen in the surrounding. $^{13}C\{^{15}N\}$ REDOR results suppose single ^{13}C-^{15}N bond. Possible carbonyl hydrogen-containing groups, which might give rise to this signal of the nitrogen at more negative ppm, are shown next to the spectra. The signal at 162 ppm probably comes from single carbon atom connected to the nitrogen, which has some hydrogen in the surrounding. Based on the chemical shift of nitrogen and ^{13}C-^{15}N distance obtained from $^{13}C\{^{15}N\}$ REDOR, it might be assigned to -NH-C-NH- moieties and possible structure is depicted right to the spectrum. The signal at 150 ppm correlated with many different nitrogen environments, protonated and non-protonated. It is possible that the carbon signal is caused by one carbon atoms having different nitrogen neighbors, for example, by amidine-like moieties or that it corresponds to two different C=N

constellations having the same chemical shift. Both structured are allowed by the results of $^{13}C\{^{15}N\}$ REDOR. Some pyridine and pyridine-like structured, which possibly might give rise to the carbon signal around 150 ppm are shown in the Figure 115 next to the spectra.

Solid-state investigation of MA-PAN allowed to find out that MA copolymer, contrary to the common belief, is not just an inert group playing role of a "defect" and therefore improving processability. Results of dipolar-based experiments showed that it actively participates in polymerization process by reaction with nitrogen in nitrile group forming at least four different moieties with at least one C-N connection. Combined results of dipolar-based measurements and correlation experiments suggest that major reaction path involves substitution of CH_3 group in MA ester resulting in appearance of carboxylic amide. Further reaction products might include -NH-C-NH- structures and, possibly, some pyridine or pyridine-like structures.

4.6.3. AN-co-AAM Sample

As proposed by the investigations made in the previous sections, major reaction products of MA-copolymer and PAN might be different carboxylic amides. To obtain more information about the chemical shift and to gain better understanding of the reaction mechanism, a sample of AN-co-AAM (PAN copolymer with 9 mol % of acrylamide) where the nitrogen atoms in the NH_2 group were selectively labelled with ^{15}N was prepared by cooperation partners and investigated by means of solid-state NMR spectroscopy (see Figure 116).

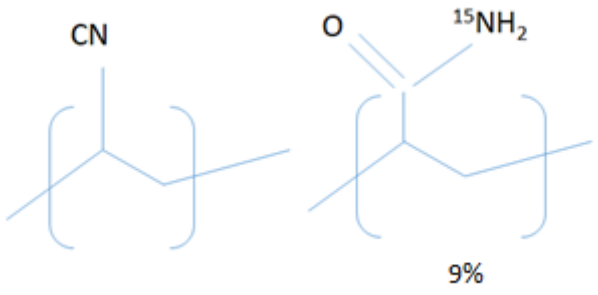

Figure 116. Isotopically labelled AN-co-AAM copolymer.

Unheated AN-co-AAM sample. In Figure 117 the results of ^{1}H-^{13}C CPMAS measurements of unheated AN-co-AAM copolymer are shown. Compared with pure PAN, an expected additional peak corresponding with carboxylic group at about 175 ppm is observed. The dependencies of intensities of the major peaks on the contact time are similar to those observed in PAN and AN-co-AAM samples. The signal of the carboxylic group at about

175 ppm is weak and difficult to be quantified during contact time dependent CPMAS NMR studies.

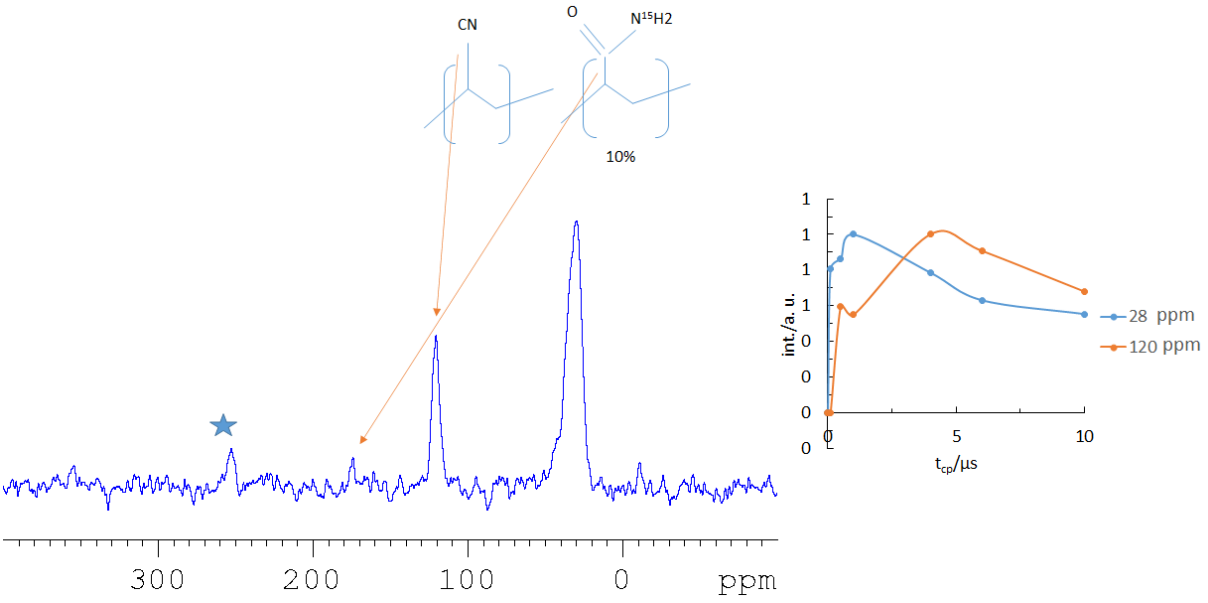

Figure 117. ^{1}H-^{13}C CPMAS spectra (left) and the dependence of ^{1}H-^{13}C CPMAS integrated intensity of the main peaks (right) of unheated AN-co-AAM copolymer. Asterisks indicate spinning sidebands.

In Figure 118 the results of ^{1}H-^{15}N CPMAS investigation of unheated AN-co-AAM sample are shown. The signal of the amide nitrogen is observed at -270 ppm. Fast magnetization build-up of this peak is in agreement with the presence of two hydrogen atoms in the near environment. Combining it with ^{1}H-^{13}C CPMAS and the results of $^{13}C\{^{15}N\}$ HETCOR and $^{1}H\{^{15}N\}$ HETCOR experiments on double isotopically labelled samples, we propose that the part of the intensity of the carbon peak at 175 ppm in heat-treated PAN-MA sample might be caused by such a carboxylic amide group.

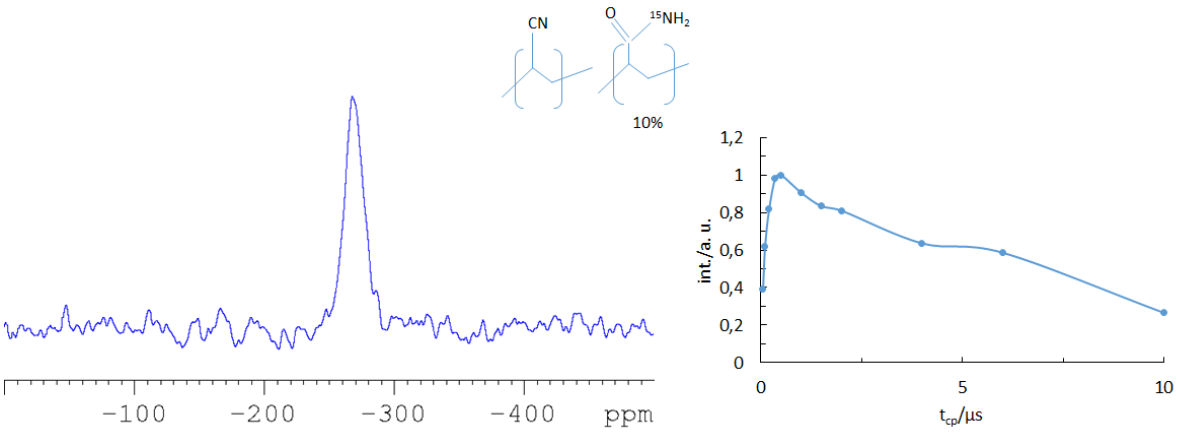

Figure 118. ^{1}H-^{15}N CPMAS spectra (left) and the dependence of ^{1}H-^{15}N CPMAS integrated intensity of the main peak (right) of unheated AN-co-AAM copolymer.

Heated AN-co-AAM sample. ^{1}H-^{13}C CPMAS spectra of the heated samples are shown in Figure 119. They are similar to the spectra of heated PAN and PAN-MA. The dependence of the main signals intensity on the contact time is also similar to PAN and PAN-MA. The similarity of the obtained signals supposes that the incorporated comonomer MA including its follow-up chemistry do not change drastically the structure of the resulting polymer network compared to the PAN homopolymer.

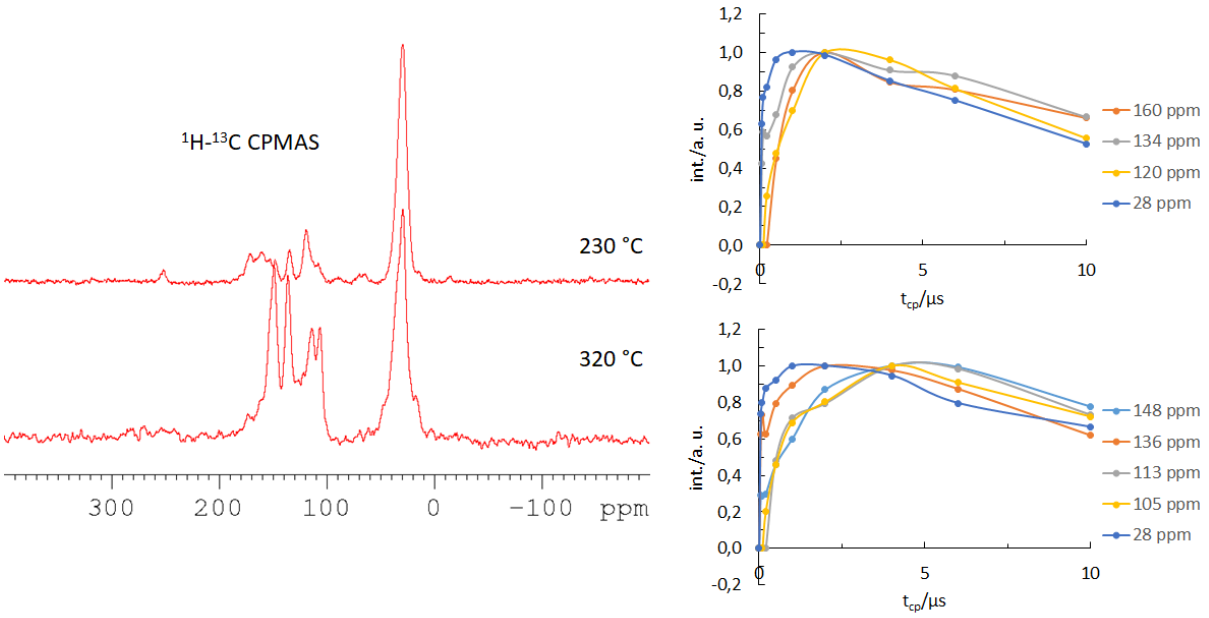

Figure 119. ^{1}H-^{13}C CPMAS spectra (left) and the dependence of ^{1}H-^{13}C CPMAS integrated intensities of the main peaks (right) of AN-co-AAM copolymer heated to 230 °C (top) and 320 °C (bottom).

In Figure 120 the results of ^{1}H-^{15}N CPMAS NMR of heated AN-co-AAM samples is shown. At both treatment temperatures the major signals exhibit fast magnetization build-up which indicates presence of N-H moieties. Only a small signal is observed to the left of -200 ppm where non-protonated nitrogen nuclei are expected to be found based on chemical shift and previous investigations. The relative intensity of this probably non-protonated signal increases with higher temperature indicating possibly nitrogen being introduced to an aromatic carbon network. A peak around -265 - -270 ppm attributed to carboxylic amide NH_2 group is found in both samples. Two additional peaks to the left which might correspond with primary substituted amines in carboxylic amide moieties are observed in both samples.

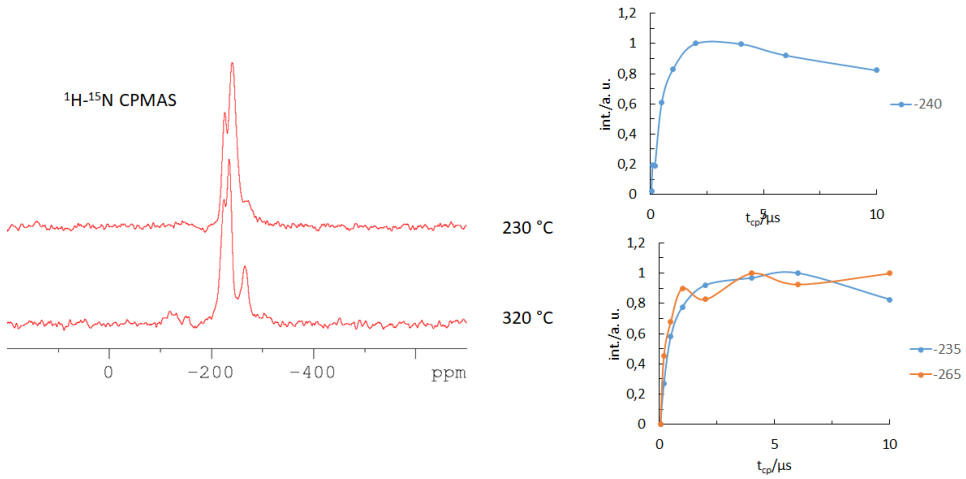

Figure 120. ^{1}H-^{15}N CPMAS spectra (left) and the dependencies of ^{1}H-^{15}N CPMAS signal intensity on the contact time (right) of AN-co-AAM copolymer heated to 230 °C (top) and 320 °C (bottom).

4.6.4. Discussion of the Role of MA Comonomer in the Thermal Transformation of PAN-MA

In this chapter we attempted to find out which role MA comonomer plays in the thermal transformation of PAN-MA. Experiments on the sample where hydrogen was substituted by deuterium in the $CH(D)_3$ group in MA allowed to find out that about 37% of deuterium remains in the sample as a CD_3 group after temperature treatment. Probably, the CH_3 group in MA reacts with PAN comonomer and during these reactions more than half of CH_3 group is removed from the system and the remaining part stays as CH_3 group attached to the polymer. Furthermore, ^{1}H-^{13}C CPMAS experiments on this sample suppose that MA does not change the structure of the heated polymer drastically. Results of dipolar-based experiments on double-enriched samples suppose that the methyl acrylate group plays an important role in the stabilization step switching from a plasticizer during the drawing process to an initiator of the thermal transformation by being transformed to a carboxylic amine contrary to the well-established view of being simply and only a plasticizer. The combined results on PAN-MA and AN-co-AAM samples propose that part of the MA moiety is transformed into a carboxylic amide although the amide might be primary substituted with at least two different functionalities which are difficult to be identified exactly. Further reaction products might include -NH-C-NH- structure motives and, possibly, some pyridine or pyridine-like structures.

4.7. NMR of Industrially Produced Carbon Fibers Having Different Surface Treatment

As found out in 4.3, ^{1}H MAS could be applied to conductive carbon fibers to obtain the signal from the surface layers. In this chapter ^{1}H MAS NMR is applied first to industrially produced carbon fibers in attempt to investigate chemical groups on the surface. Then the same analysis is applied to differently recycled carbon fibers to investigate how well these surface functionalities are preserved in the recycling process. At the end, ^{1}H-^{13}C CPMAS NMR, HETCOR and Xenon NMR are attempted to obtain information about carbon functionalities on the surface.

4.7.1. Single Pulse Excitation on Fibers Having Different Surface Treatment

Spin-echo ^{1}H MAS NMR. In Figure 121 spin-echo ^{1}H MAS NMR spectra of untreated, oxidized and oxidized and sized carbon fibers are represented. In all three fibers the spectrum consists of three major peaks located around 0 ppm, 5 ppm and 8 ppm. An exact assignment of these peaks to certain chemical groups is difficult. The relative intensity of the peak around 8 ppm increases after oxidation followed by increase of relative intensity of the peak at 0 ppm after sizing. This might speak for increasing complexity of the surface functionalities under anodic oxidation and sizing although it is difficult to track the changes exactly.

Although ^{1}H MAS NMR could not be used to exactly define the functionalities on the surface of the carbon fibers, it might be used to track increasing complexity of the surface treatment along with manufacturing. This might open new opportunities to qualitatively control the surface sizing on carbon fibers by comparing the surface areas of different peaks of spin-echo ^{1}H MAS NMR spectra of carbon fibers after surface treatment might.

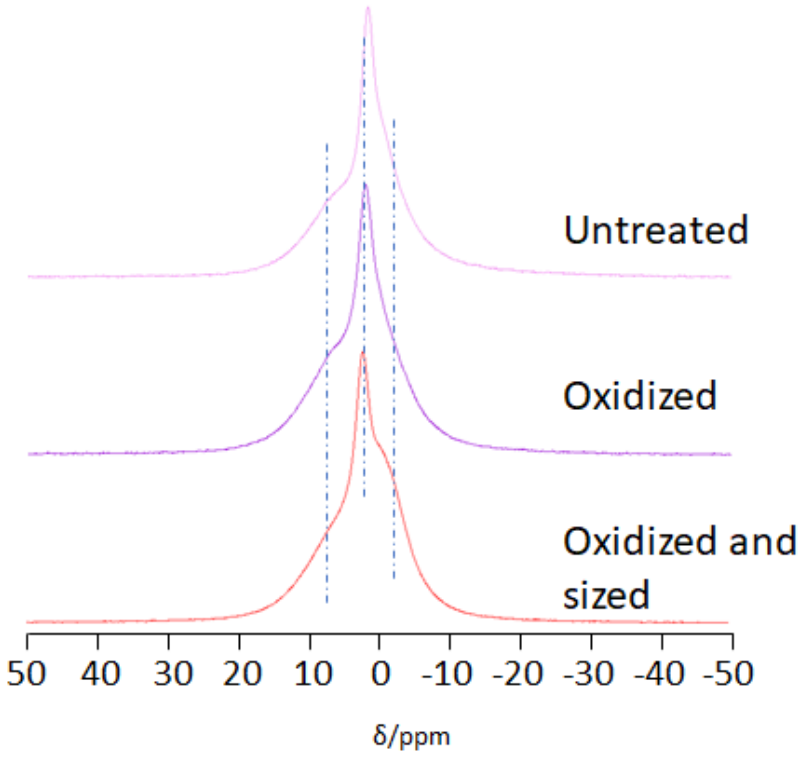

Figure 121. Spin-echo ^{1}H-MAS NMR spectra of untreated, oxidized and oxidized and sized carbon fibers.

Spin-echo ^{13}C MAS NMR. In Figure 122 spin-echo ^{13}C MAS NMR of the fibers having different thermal treatment is represented. Only one peak centered at 120 ppm caused by sp^2 carbon is observed in all three samples. No additional functionalities responsible for surface coating are detected in sized fibers. Probably, the signals from the surface non-aromatic functionalities have relatively low intensities comparing with the signal from aromatic carbon and therefore could not be distinguished.

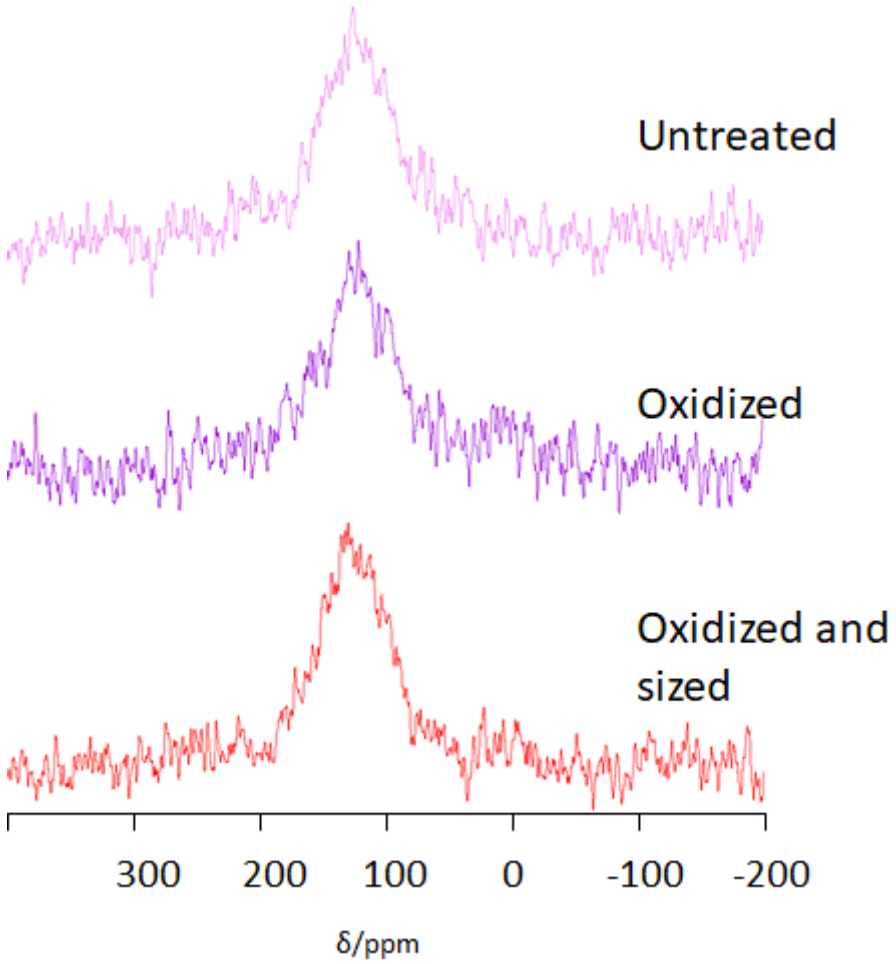

Figure 122. Spin-echo ^{13}C-MAS NMR spectra of untreated, oxidized and oxidized and sized carbon fibers.

4.7.2. Single Pulse Excitation on Fibers after Recycling Treatment

When it is possible to investigate morphology and mechanical characteristics of the fiber by conventional characterization techniques, the functionalities on the surface of the fibers and their retention during process are much harder to assess. Although NMR does not allow quantitative comparison of the surface functionalities because it is very susceptible to the size of the sample, it might deliver qualitative information about the surface chemical composition needed for quality control of the recycled fibers.

Spin-echo ^{1}H MAS NMR. In Figure 123 ^{1}H MAS NMR spectra of original fibers and inductively and chemically recycled fibers are represented. In original fibers three broad peaks centered around 8, 5, and 0 ppm could be distinguished. Although the spectra are not quantitative, the complexity of the signal from recycled fibers are substantially lower than that of original. This most probably indicates loss of the surface functionalities under recycling process. In the recycled fibers the peak around 0 ppm loses some intensity and it is nearly absent in the

inductively recycled sample. The spectrum of chemically recycled fibers resembles most the spectra of original fibers. It might indicate that chemical recycling is better on retaining original functionalities. From spectra comparison it might be concluded that the functionalities giving rise to the peak at 0 ppm are lost or partially removed from the surface and this chemical group, if defined, should be applied by sizing on the surface of the recycled carbon fibers to unsure better adhesion with the new matrix.

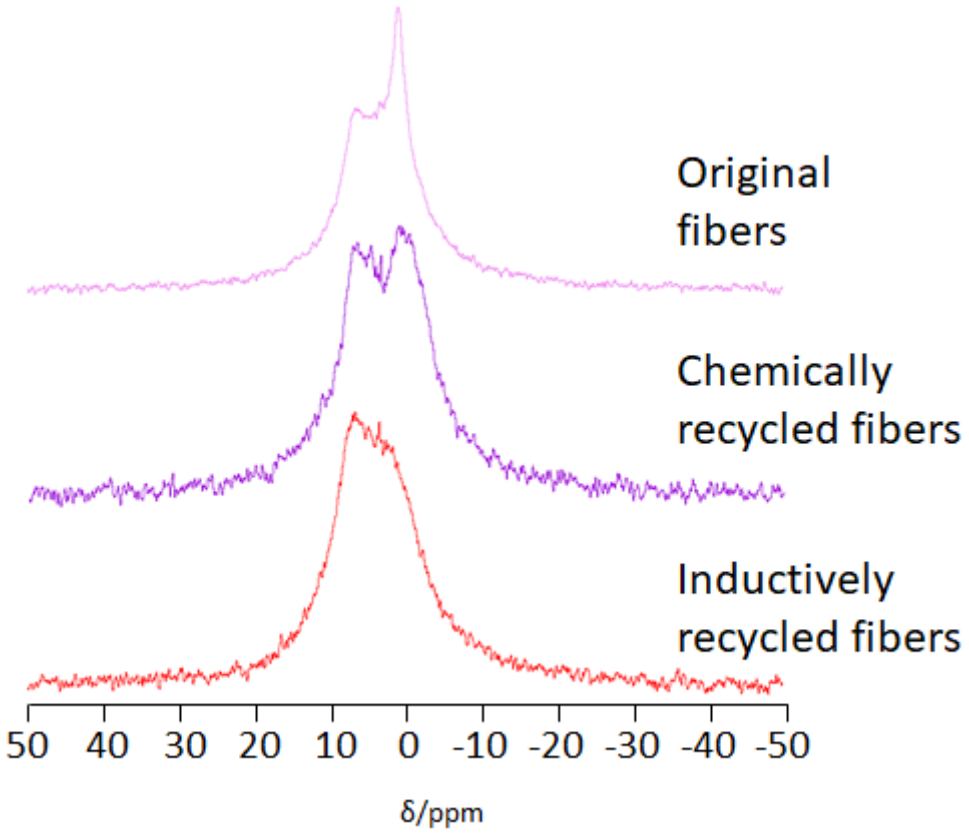

Figure 123. Spin-echo ^{1}H-MAS NMR spectra of original fibers and chemically and inductively recycled fibers.

Spin-echo ^{13}C MAS NMR. In Figure 124 spin-echo ^{13}C MAS NMR of the original fibers and the fibers undergone different recycling procedure are shown. Again, only sp^2 carbon signal is shown and the surface functionalities groups are not distinguishable. Spin-echo ^{13}C MAS NMR does not deliver new information about recycling process.

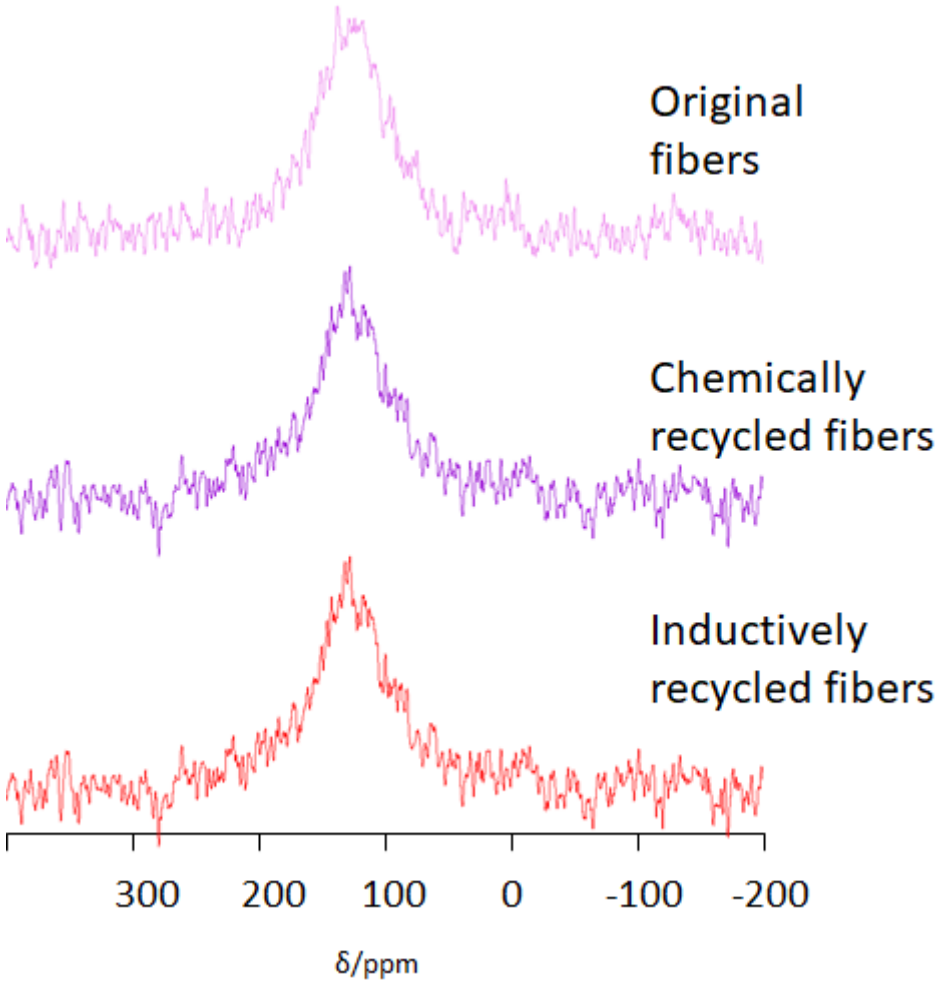

Figure 124. Spin-echo ^{13}C-MAS NMR spectra of original fibers and chemically and inductively recycled fibers.

4.7.3. Polarization Transfer

When ^{1}H MAS NMR spectra deliver qualitative information about functionalities on the surface of the fibers, the exact assignment of the signals is challenging due to strong overlapping of the peaks. ^{1}H-^{13}C CPMAS NMR might open opportunities to assign the functionalities exactly because ^{13}C signal range is much broader than that of hydrogen. Unfortunately, ^{13}C MAS NMR without using polarization transfer delivers only a broad sp^2 carbon peak and the signals from the surface functionalities are too low to be distinguished. In this chapter ^{1}H-^{13}C CPMAS, ^{1}H-^{13}C HETCOR would be attempted on industrially produced fibers having different surface treatment.

^{1}H-^{13}C CPMAS NMR. Although in the chapter 4.3.2 it was found that obtaining ^{1}H-^{13}C CPMAS NMR signal from the conductive samples is challenging, the attempts were continued on the differently treated fibers. As was found out, much higher number of scans (at least 16 k) than that of non-conductive fibers is needed to obtain the signal. It was ensured that the signal

comes from magnetization transfer by running the experiment using a very short pulse on hydrogen channel and by running the control experiment on the spinner filled only with silicon dioxide (see Appendix 24). The results of the measurements are represented in Figure 125. Again, only the signal from sp^2 carbon is observed. Additional signals from the surface functionalities are not distinguishable in the spectra. Small signals around 30 ppm are the spinning sideband which was found out by variation of the spinning speed. The highest signal intensity is observed using length of the contact pulse equal to 5-6 ms. This speaks for non-direct hydrogen-carbon connections.

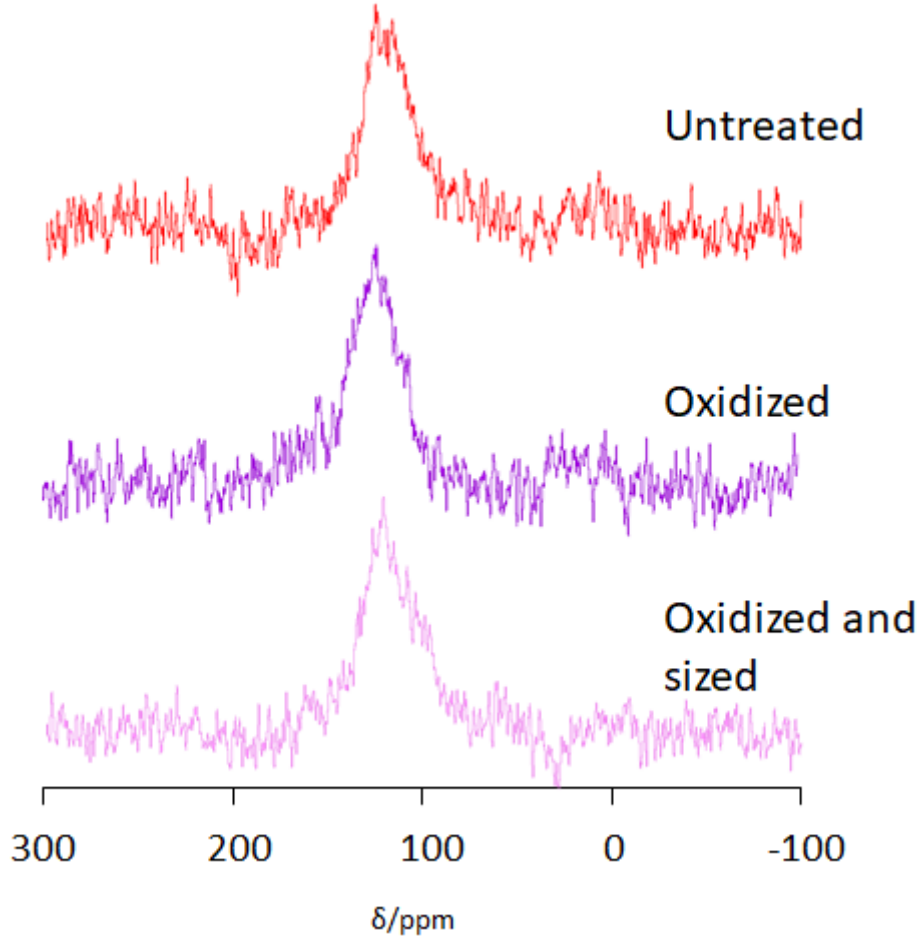

Figure 125. ^{1}H-^{13}C CPMAS NMR spectra of untreated, oxidized and oxidized and sized fibers.

Knowing that there is a lot of carbon and hydrogen atoms in the carbons, such a difficulty to obtain the CPMAS signal might be caused by two reasons. First, most of the carbon and hydrogen atoms might be separated from each other to the distance where polarization transfer through dipole-dipole coupling does not work. This is rather improbable because at least surface functionalities should be organic hydrogen and carbon-based moieties. Second,

the polarization transfer might be disturbed by conductive electrons. This might make the experiments involving dipole-dipole interactions challenging on conductive samples.

^{1}H-{^{13}C} HETCOR of Oxidized and Sized Fibers. Although it was difficult to obtain CPMAS signal from the conductive samples, the existence of the signal means that 2D dipolar-based NMR experiments are in principle possible but might be very time consuming. To find out the connectivity of hydrogen and carbon atoms, ^{1}H-^{13}C HETCOR was carried out on the oxidized and sized fibers. The results are represented in Figure 126. Only sp^2 carbon signal is observed. Although the resolution of the signal is very bad due to hindered polarization transfer, it might be seen that the peak of hydrogen spectra is clearly centered in the aliphatic region. Probably, polarization transfer in the structured aromatic regions of the carbon fibers is disrupted too much by conductive electrons and obtaining of the signal is only possible by polymerization transfer from the surface functionalities or from the defects in the structure.

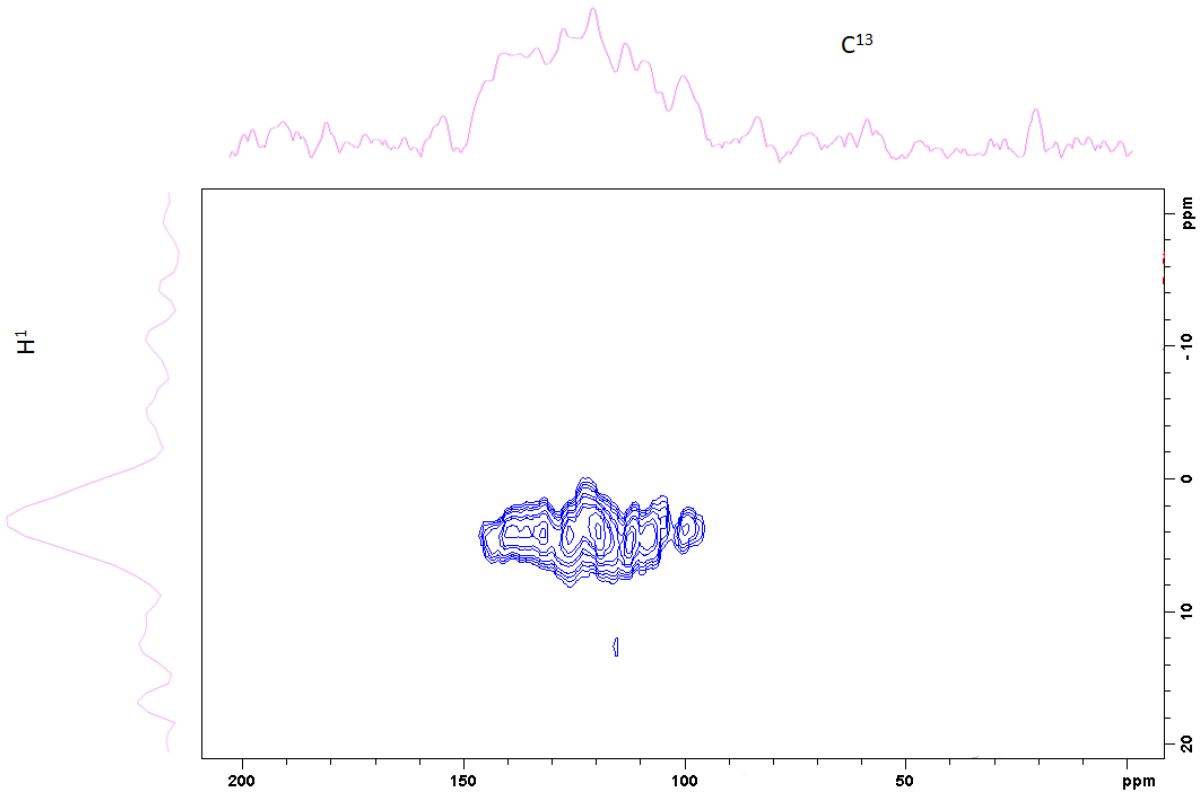

Figure 126. ^{1}H-^{13}C HETCOR of oxidized and sized fibers.

4.7.4. ^{129}Xe NMR

Initially, experiments involving polarization transfer from ^{129}Xe atoms to hydrogen and carbon atoms to facilitate acquisition of spectra were planned together with cooperation partner. Unfortunately, the procedure was very challenging to establish and in this chapter we focus

only on the investigation of NMR signal of ^{129}Xe. Xenon is easily absorbed in the pores on the surface and ^{129}Xe NMR signal depends strongly on the pore environment, especially on the pore size due to large sensitive electron cloud which allows to understand surface properties of the sample. For this work, HP continuous flow ^{129}Xe NMR was measured as a function of the temperature by cooperation partner in the University of Bayreuth. The results are represented in Figure 127. In all three spectra the resonance around 0 ppm correlates with ^{129}Xe gas. As might be seen, in the untreated fibers the structure of the pores is much more complicated than in the oxidized and in oxidized and sized fibers. At the room temperature there are several overlapping peaks which are separated under cooling. Till about 220 °C the chemical shift of absorbed xenon is not changed much. In this temperature range only small fraction of the pore volume is filled with xenon and there is nearly no Xe-Xe interactions which explain the shift of the signal at the lower temperatures and its broadening. At least three different pore varieties having different geometries are present in the untreated fibers. After oxidation the complexity of the pores structure reduces drastically. Only one or maximum two overlapping peaks are detected in the oxidized and oxidized and sized samples at lower temperatures. The shift of the signal and the size of the pores have inversed dependence. The signals having most negative chemical shift are the ones which are first drastically reduced in the oxidized fibers and then disappear in oxidized and sized fibers. This might mean that the smallest pores are successively closed by surface treatment and the larger pores stay unaffected by oxidation and sizing. In the oxidized and sized fibers two pore types having similar size but different geometry are detected. The broader peak corresponds with less ordered pores and the narrower peak correspond with more ordered pores. Probably, this speaks for coating partially filling larger pores making their shape more irregular.

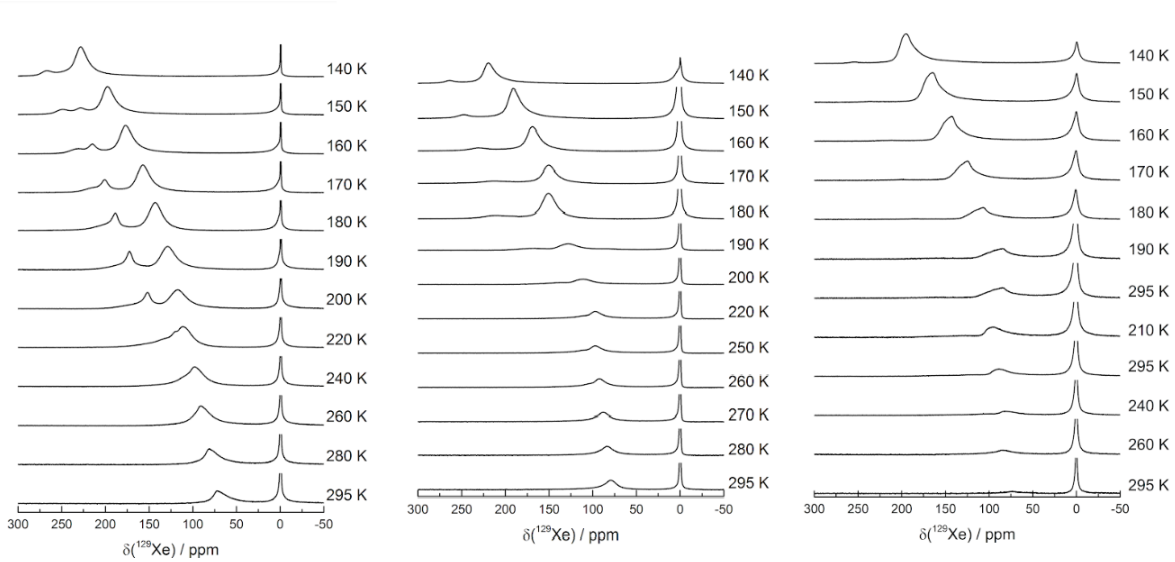

Figure 127. HP continuous flow ^{129}Xe NMR of untreated (left), oxidizes (middle) and oxidized and sized fibers (right).

Summing up, many NMR characterization techniques applied to industrially prepared and recycled carbon fibers have been discussed in this chapter. ^{1}H MAS NMR is a useful tool to track surface functionalities. Subsequent increasing complexity of the signal is observed after surface treatment. Although ^{1}H MAS NMR does not allow to correlate the peaks with certain functionalities, it might open a way to track the quality of the surface covering by comparing the spectra of the samples. Furthermore, ^{1}H MAS NMR opens a possibility to follow chemical changes on the surface of the fibers after recycling. This is important technique for quality and reproducibility control which is difficult to obtain by other methods. ^{13}C MAS NMR is limited in its application and only the signal from *sp*^{2} carbon is detected from all samples. Probably, the signals from the surface functionalities are too weak to be distinguished in the spectra. Polarization transfer using ^{1}H-^{13}C CPMAS NMR is disturbed by free electrons and the enhancement of the signal is very low. Only *sp*^{2} carbon are found by the experiment and the functionalities on the surface cannot be distinguished by measurements

Conclusion

In this work two groups of modern amorphous materials: ultra-strong glasses and carbon fibers were investigated by means of advanced solid-state NMR techniques. ^{29}Si, ^{23}Na, ^{31}P, and ^{27}Al MAS NMR, ^{27}Al MQMAS, ^{31}P{^{27}Al}-REAPDOR and ^{27}Al{^{31}P}-REDOR, ^{31}P{^{29}Si}-REDOR and ^{29}Si{^{31}P}-REDOR, ^{31}P{^{29}Si}-REDOR and ^{29}Si{^{31}P}-REDOR^{27}, ^{27}Al{^{29}Si}-REDOR and ^{29}Si{^{27}Al}-REAPDOR, ^{31}P MAT MAS NMR together with high-temperature in-situ ^{31}P, ^{27}Al, and ^{23}Na MAS NMR were used to investigate two glass system: phosphorus-rich and silicon-rich. ^{1}H, ^{2}D, ^{13}C, and ^{15}N MAS NMR, ^{1}H and ^{13}C spin-echo MAS NMR, ^{1}H-^{13}C, ^{1}H-^{15}N and ^{1}H-^{2}D CPMAS NMR, ^{13}C{^{15}N} REDOR and ^{15}N{^{13}C} REDOR, ^{1}H-{^{15}N} HETCOR, ^{1}H-{^{13}C} HETCOR and ^{13}C-{^{15}N} HETCOR were applied to carbon fibers, PAN precursors and copolymers complemented by HP continuous flow ^{129}Xe NMR.

In the part of this study devoted to the glass materials two glass-forming regions of sodium-aluminum-silicon-phosphorus glass system were selected: phosphorus-rich and silicon-rich. Creation and tailoring of ultra-strong glasses are impossible without understanding the structure of the glass network. That is why the application of NMR as a technique especially suitable for the investigation of amorphous materials was needed. In the phosphorus-rich region the effect of adding aluminum to two base glass composition $60P_2O_5$-$30Na_2O$-$10SiO_2$ (P60 glasses) and $50P_2O_5$-$16.6Na_2O$-$33.3SiO_2$ (P50 glasses) was investigated. In both systems aluminum and silicon cations are distributed in the network, surrounded by phosphorus units and connected through phosphorus chains. Six-coordinated silicon cations are being substituted by six-coordinated aluminum upon addition. This might be explained by the coordination of cations: when SiO_6 units require Q^3 phosphorus around it, AlO_6 units might be surrounded by both phosphorus species. Tendency of SiO_6 units to be coordinated with Q^3 phosphorus might be connected with the charge distribution in SiO_6-O-Q^3 bonds favorable for presence of sodium ions needed to charge-balance SiO_6. In the row P50 number of six-coordinated cations does not change much upon addition of aluminum and in the row P60 the number of six-coordinated cations increases. This relates to P/(Al+Si) ratio – the amount of phosphorus units available to coordinate cations. The trends in the amounts of six-coordinated cations correspond well with observed trends in T_g and Young's modulus. High-

temperature studies of the glasses show that Q^2 phosphorus in P60 glasses species gets mobile first. Addition of aluminum increases the temperatures where dynamics of phosphorus atoms is observed. With increasing temperature structural relaxation or exchange processes of aluminum species are observed. In the silicon-rich glass-forming region small amounts of phosphorus (up to 7.5 %) were added to sodium aluminosilicate glasses with 50 to 70 m. p. of silicon dioxide and the rest equally divided between sodium and aluminum oxides. In the glasses without phosphorus sodium atoms are used to charge-balance four-coordinated aluminum and the glass network consists of silicon and aluminum tetrahedra. If phosphorus is added to the base composition, sodium ions leave aluminum and phosphorus is getting incorporated in form of $Q^{2/3}$ phosphorus units. They are mostly connected to the glass network through P-O-Al bonds, although some P-O-Si bonds were found to be present in the structure. Nevertheless, aluminum and silicon units are four-coordinated independent of phosphorus content and no phase separation is observed. All three cations are working as network formers. The results of solid-state NMR spectroscopy propose that two charge-compensation mechanisms are present at the same time in this system: Q^4 phosphorus units and, probably, silicon-aluminum triclusters.

To investigate carbon fibers, another modern amorphous material, the NMR techniques were applied first to fibers which underwent through different production steps. It allowed to find the regions where the investigation with solid-state NMR might be the most promising. To our best knowledge it was the first attempt to follow complete preparation of carbon fibers with NMR spectroscopy. The results show that ^{1}H MAS NMR could be used for fibers after all manufacturing stages, although the exact assignment of the signal is difficult. Due to conductivity of the fibers after the temperature treatment only the functionalities on the surface are accessible after stabilization step. ^{1}H-^{13}C CPMAS NMR might be successively applied to the carbon fibers until the fibers are getting conductive. Transformation of PAN into aromatic network might be followed.

The stabilization step of carbon fibers manufacturing is of crucial importance for the production and effects drastically the resulting properties of the fibers. At the same time, it is the least understood production step, and many reaction mechanisms are proposed to describe it. In this work NMR characterization of PAN polymer enriched with ^{15}N during stabilization and PAN-MA copolymer with selectively enriched ^{2}H, ^{13}C and ^{15}N were carried

out to obtain new information about reaction mechanisms. To our best knowledge, it is the first study of carbon fibers involving ^{15}N-enriched PAN sample. First, important characteristics needed for NMR investigations such as typical chemical shifts and CSA values, REDOR effect on the molecules having large CSA and estimation of experimenter errors were carried out on PAN precursor and test substances. After that, the ^{15}N-enriched PAN copolymers were stabilized at different temperatures and the reaction was followed *ex-situ* and characterized by MAS NMR and dipolar-based experiments. Transformation of the polymer network was followed first with ^{1}H-^{13}C CPMAS and the results are in agreement with previous studies indicating subsequent polymerization of the network. New information about nitrogen environment during polymerization was obtained: in nitrogen spectrum, two distinct areas with and without hydrogen in the vicinity with relative peak area ratios of about 30:70 which does not change much with increasing temperature were observed together with small amount of pyridine and pyrimidine moieties. We also found out that nitrile moieties are not fully consumed during stabilization step. Dipolar-based experiments allowed to find out more information about C-N connectivity. Combined results of this study propose -C=C-C=N- and -C=C-NH- as main structural motifs which favors partial tautomerization and cyclization+dehydrogenation mechanisms.

Applicability of different polarization transfer methods and dipolar-based experiments to the fibers undergoing stabilization process allowed to follow polymerization of PAN-MA copolymer. The role of copolymers is still not fully understood but it is supposed that they are chemically inert and act rather as plasticizers during polymerization. To investigate it, the polymerization of the network was investigated on the samples with selectively enriched atoms. The results of investigation showed that MA copolymers are not chemically inert and participate actively in the network formation. They fully react with nitrile group in PAN which leads to formation of at least four different moieties with at least one C-N connection. The main reaction product is the result of substitution of CH_3 group in MA with some nitrogen-contained moieties. Probably, it is carboxylic amide group where amide might be primary substituted with at least two different functionalities which is difficult to identify exactly. Further reaction products might include -NH-C-NH- structures and, possibly, some pyridine or pyridine-like structures.

Acknowledgements

First of all, I want to thank my Doktorvater, Prof. Dr. van Wüllen for the chance to work in his group. Without his help, instruction and advices, it would be not possible to create and finish this work. He taught me much more than just applying NMR principles and working with equipment: he taught me the basics of scientific thinking, problem solving and analysis. He taught me always to be critical to the results and to find other ways of interpreting them. He always encouraged me to try new things and not to give up in front of initial difficulties. These lessons are very valuable, and I will apply them not only in my further career but also in private life. He was also always my example of energetic, devoted and diligent scientific work. I want to thank the second referee, Prof. Dr. Höppe for investing his time and efforts needed to read and evaluate the thesis.

I want to thank Dr. Ruhland for his moral support during my PhD, especially during the time when I went through many unsuccessful experiments. I am especially thankful for our collaboration and the idea of working on enriched samples, which eventually became one of the major points of my research. He also always found time to give me the opinion about the work and to support, which is difficult to overvalue.

I want to thank all cooperation partners who supported me with measurements and materials which allowed to support/reject many assumptions: Prof. Dr. Brauer and her group for EDX, elemental analysis and T_g measurements, Prof. Dr. Ruhland for enriched samples, Prof. Dr. Horn and Dr. Moosburger-Will and their group for carbon fibers, Dr. Gutmann for DNP measurements, Prof. Priv.-Doz. Dr. Hans-Albrecht Krug von Nidda and his group for ESR measurements and Tobias Kemnitzer for HP continuous flow ^{129}Xe NMR measurements.

I want to thank my colleagues with whom I worked closely during these years: Dr. Qing Liu, Dr. Gerrit Schiffmann, Holger Kirchhain, Dr. Sabarinathan Venkatachalam and Michaella Rackel. I highly appreciate help of Dr. Tobias Uesbeck on the final correction stage. They do not only help me with research issues but also created fruitful working atmosphere. I also want to thank other colleagues from other chairs/universities with whom we exchanged ideas and worked together: Prof. Dr. Brauer, Prof. Dr. Dominique de Ligny, N. Sawangboon, T. Grammes to name just a few. They all contributed to this research.

Last but not least, I want to thank my family and friends who helped me to go through PhD time. Especially my mother, Raisa Nizamutdinova, who, apart from always being on my side, ensured that I get proper education to be able to start with PhD, and Timofey Yugov, who always respected that I devoted my time to this work and who did everything to create an environment where I could concentrate on my studies and all my friends who supported me when I struggled to combine writing the thesis and full-time job.

Appendix 1. Nominal Composition with and Without Manganese Added and with and Without Thermal Relaxation Treatment

To prove if the structural units of glasses prepared are affected by addition of 0.1 w. p. of $MnCO_3$ and annealing below Tg and if the results obtained on the enriched glasses could be generalized, ^{27}Al, ^{31}P and ^{29}Si spectra were measured on Si60_P7.5(A) and annealed Si60_P7.5(A) glass. The results indicating similarity of structural units are represented in Figure 128.

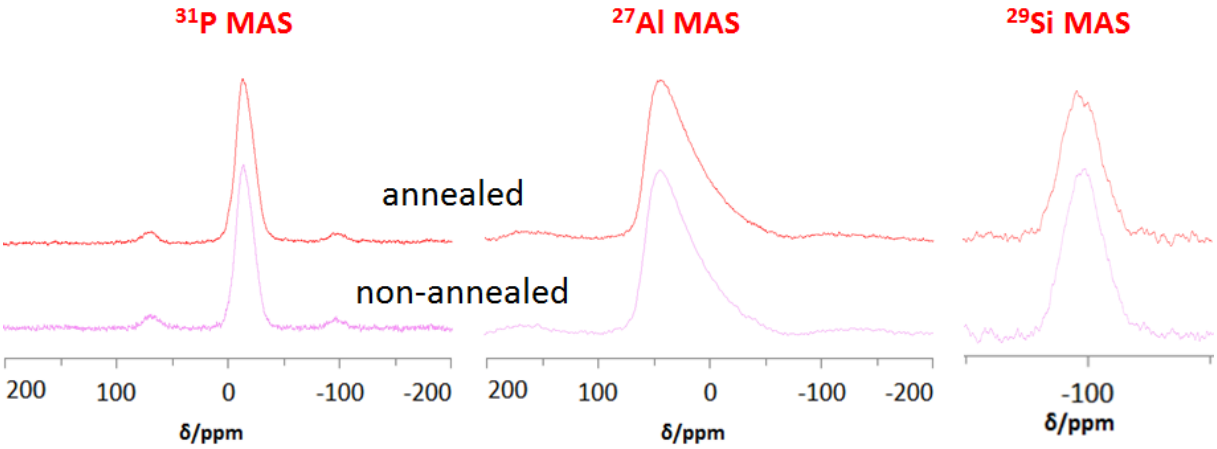

Figure 128. Comparison of ^{31}P (left), ^{27}Al (middle) and ^{29}Si (right) spectra of annealed (top) and non-annealed (bottom) $60SiO_2$-$7.5P_2O_5$-$16.25Al_2O_3$-$16.25Na_2O$ glass prepared with 0.01 w. p. of $MnCO_3$ added to nominal composition measured in the field of 7 T.

Appendix 2. Single Pulse NMR Spectra of ^{29}Si Enriched Glasses

To check if the structural units of glasses prepared with enriched ^{29}Si are similar to those prepared with silicon having natural abundance and if the results obtained on the enriched glasses could be generalized, ^{27}Al, ^{31}P and ^{29}Si spectra were measured on enriched glasses. The results showing similarity of enriched and non-enriched glasses are represented in Figure 129-Figure 131.

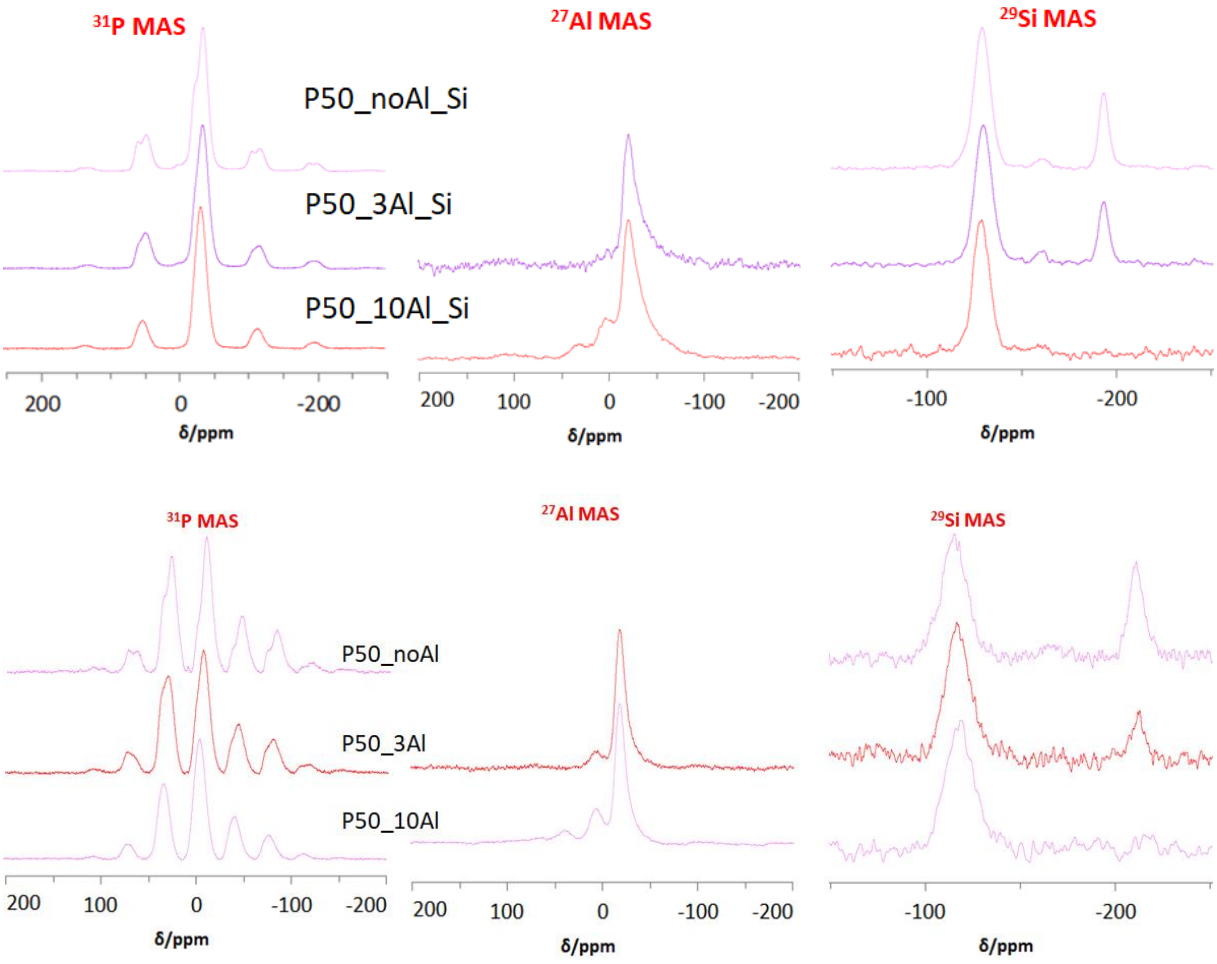

Figure 129. ^{31}P, ^{29}Si and ^{27}Al spectra of the glasses P50_noAl_Si, P50_3Al_Si and P50_10Al_Si measured in the field of 7 T (top) and of the glasses P50_noAl, P50_3Al and P50_10Al measured in the field of 11 T (bottom).

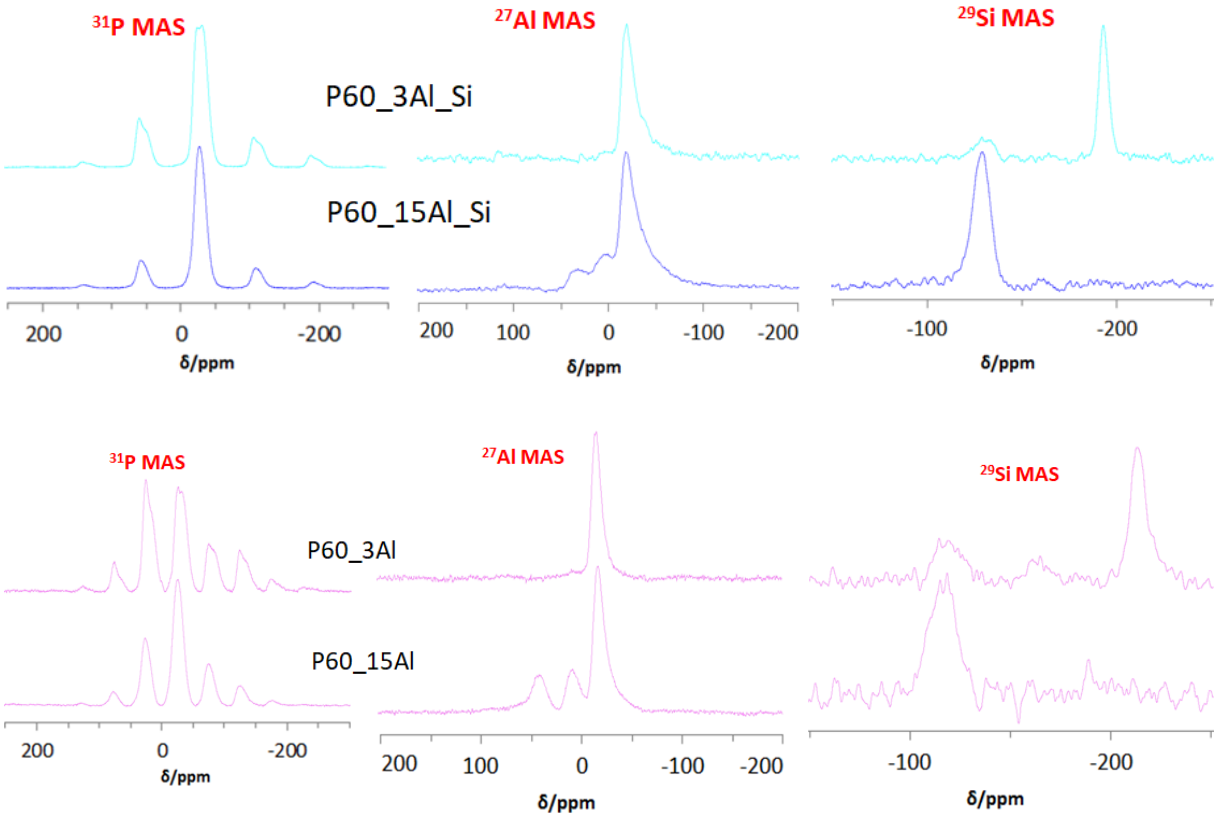

Figure 130. ^{31}P, ^{29}Si and ^{27}Al and spectra of the glasses P60_3Al_Si and P60_15Al_Si measured in the field of 7 T (top) and of the glasses P60_3Al and P60_15Al measured in the field of 11 T (bottom).

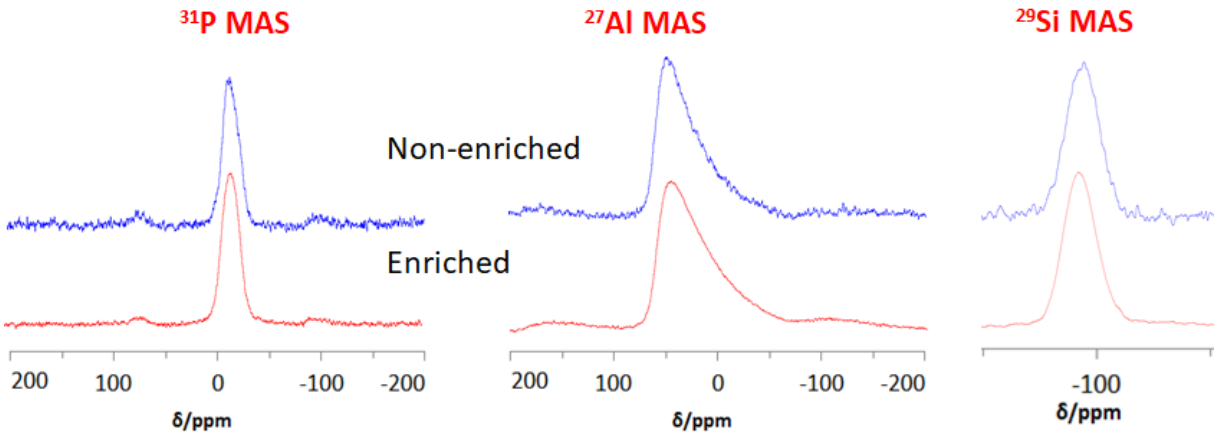

Figure 131. ^{31}P (left) ^{27}Al (middle) and ^{29}Si (right) spectra of glass with nominal composition $60SiO_2$-$7.5P_2O_5$-$16.25Al_2O_3$-$16.25Na_2O$ and 0.01 wp $MnCO_3$ with and without enriched silicon measured in the field of 7 T.

Appendix 3. Effect of CSA of phosphorus signal on $^{27}Al\{^{31}P\}$-REDOR Results

To check how high is the effect of the width of CSA of the phosphorus signal to the results of $^{27}Al\{^{31}P\}$-REDOR, simulations using effective dipolar coupling of 900 Hz and different widths of CSA tensors were run. The results are represented in Figure 132. As might be seen high values of the width of CSA tensor might have significant effect to the results of $^{27}Al\{^{31}P\}$-REDOR measurements. At the same time, values of the widths of CSA tensors below 100 ppm do not affect the results of $^{27}Al\{^{31}P\}$-REDOR measurements much.

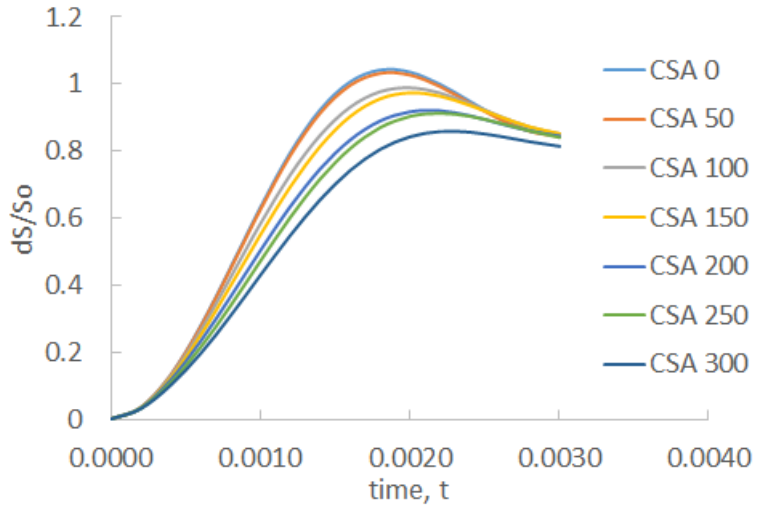

Figure 132. The results of $^{27}Al\{^{31}P\}$-REDOR simulations using effective dipolar coupling of 900 Hz and indicated values of the width of CSA signal on ^{31}P channel in ppm.

Appendix 4. Comparison of Many-spin and Double-Spin Simulation Models

In Figure 133 the results of SIMPSON simulation of ^{29}Si{^{31}P}-REDOR are represented. Comparison was made for 4-spin (one silicon nucleus and three phosphorus nuclei) and 6-spin (one silicon nucleus and five phosphorus nuclei) systems assuming dipolar coupling of 300 Hz and width of CSA tensor of phosphorus of 100 ppm. Solid lines represent the results of simulation using two-spin approximation with effective dipolar coupling $D_{eff} = \sqrt{n}D_{ind}$. Dash-dotted lines represent results of multispin planar systems. Dashed lines represent the results of simulation of multispin system where silicon is located in the center of triagonal-bipyramid system. As might be seen from the graphs, the results are in accordance with each other till ΔS/S values of about 0.5 and 2-spin approximation model might be used for simulation of experimental results. Examples of SIMPSON simulation program for 6-spins are represented below.

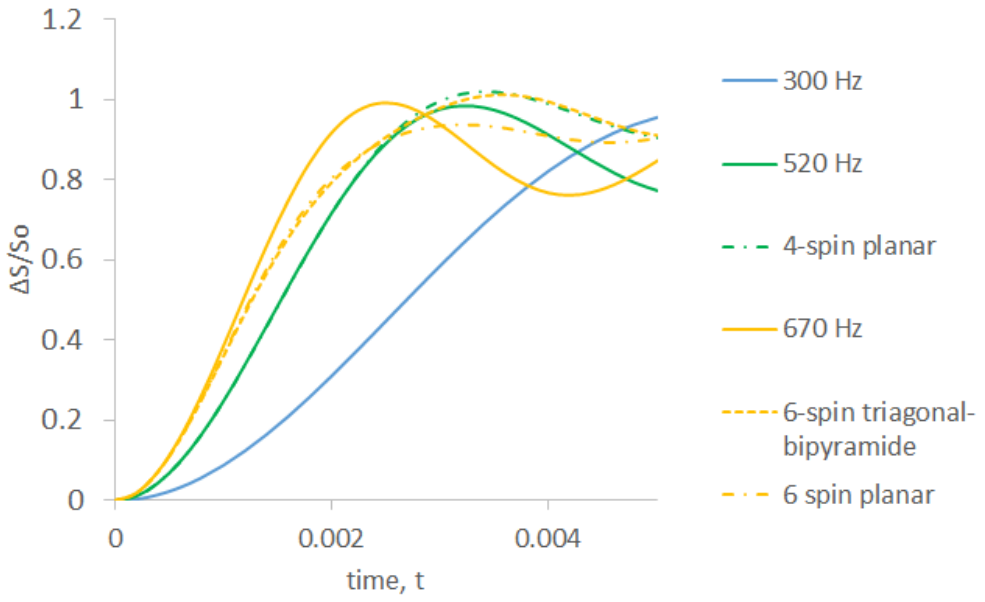

Figure 133. Comparison of the results of SIMPSON simulation of ^{29}Si{^{31}P}-REDOR using two-spin approximation (solid lines) and simulations using multiple dipoles (dashed and dashed-dotted lines).

```
spinsys {
    channels 29Si 31P
    nuclei 29Si 31P 31P 31P 31P 31P
    shift 1  0p 0p 0.2 20 40 60
    shift 2  0p 100p 0.2 20 40 60
    shift 3  0p 100p 0.2 20 40 60
    shift 4  0p 100p 0.2 20 40 60
    shift 5  0p 100p 0.2 20 40 60
    shift 6  0p 100p 0.2 20 40 60
    dipole 1 2 300 0 0 0
    dipole 1 3 300 0 72 0
    dipole 1 4 300 0 144 0
    dipole 1 5 300 0 -72 0
    dipole 1 6 300 0 -144 0


OR

spinsys {
    channels 29Si 31P
    nuclei 29Si 31P 31P 31P 31P 31P
    shift 1  0p 0p 0.2 20 40 60
    shift 2  0p 100p 0.2 20 40 60
    shift 3  0p 100p 0.2 20 40 60
    shift 4  0p 100p 0.2 20 40 60
    shift 5  0p 100p 0.2 20 40 60
    shift 6  0p 100p 0.2 20 40 60
    dipole 1 2 300 0 0 0
    dipole 1 3 300 0 120 0
    dipole 1 4 300 0 -120 0
    dipole 1 5 300 0 90 90
    dipole 1 6 300 0 90 -90

OR

spinsys {
    channels 29Si 31P
    nuclei 29Si 31P
    shift 1  0p 0p 0.2 20 40 60
    shift 2  0p 100p 0.2 20 40 60
    dipole 1 2 520 0 0 0


}

par {

    spin_rate        10000
    np               16
    crystal_file     rep320
    gamma_angles     36
    start_operator   I1x
    detect_operator  I1p
    sw               100000
    method           direct
    verbose          1101
```

```
    proton_frequency       300000000

}

proc pulseq {} {

    global par

    maxdt 0.1

    offset 0 0




    set powerf1 34483
    set powerf2 50000

    set pi1 [expr 0.5e6/($powerf1)]
    set pi2 [expr 0.5e6/($powerf2)]

    #----------------------------
    set pi12   [expr $pi1/2]
    set pi22   [expr $pi2/2]
    set delay1 [expr 1000000.0/$par(spin_rate)/2.0 - $pi22]
    set delay2 [expr 1000000.0/$par(spin_rate)/2.0 -$pi2]
    set delay3 [expr 1000000.0/$par(spin_rate)/2.0-$pi12-$pi22]



    # start block (1 rotor period)
    reset
    delay $delay1
    pulse $pi2 0 0 $powerf2 x
    delay $delay2
    pulse $pi22 0 0 $powerf2 y
    store 1

    # middle block (1 rotor period)
    reset
    pulse $pi22  0 0 $powerf2 y
    delay $delay2
    pulse $pi2 0 0 $powerf2 x
    delay $delay2
    pulse $pi22 0 0 $powerf2  y
    store 2

    # shift refocusing (2 rotor periods)
    reset
    pulse $pi22 0 0 $powerf2 y
    delay $delay2
    pulse $pi2 0 0 $powerf2 x
    delay $delay3
    pulse $pi1 $powerf1 0 0 0
    delay $delay3
```

```
    pulse $pi2 0 0 $powerf2 x
    delay $delay2
    pulse $pi22 0 0 $powerf2 y
    store 3

    # end block (1 rotor period)
    reset
    pulse $pi22 0 0 $powerf2 y
    delay $delay2
    pulse $pi2 0 0 $powerf2 x
    delay $delay1
    store 4

    # collect the first three points separately
    reset
    acq

    reset
    delay $delay1
    pulse $pi2 0 0 $powerf2 x
    delay $delay3
    pulse $pi1 $powerf1 0 0 0
    delay $delay3
    pulse $pi2 0 0 $powerf2 x
    delay $delay1
    acq

    reset
    prop 1
    prop 3
    prop 4
    acq

    for {set j 3} {$j < $par(np)} {incr j} {

        # succesively add a 2 propagator, store in 5
        reset
        if {$j > 3} {
            prop 5
        }
        prop 2
        store 5

        # final pulse sequence
        reset
        prop 1
        prop 5
        prop 3
        prop 5
        prop 4
        acq
    }
}

proc main {} {
```

```
 global par

      set f [fsimpson]
      fsave $f $par(name).fid
      funload $f

}
```

Appendix 5. Glass Series PNA and Effect of Aluminum on CSA Tensors

Glass series PNa with base composition $66P_2O_5$-$33Na_2O$ was prepared using $NH_4H_2PO_4$, Na_2CO_3 and $Al(PO_3)_3$ as precursor. To this composition different amount of aluminum was added to investigate the effect of aluminum to CSA tensors. About 6 g of oxide mixture were slowly heated in platinum crucible to 1200 °C and then cast to copper plate at room temperature. To facilitate acquisition of NMR spectra $MnCO_3$ (0,01 w. p.) was added to the glass compositions to decrease relaxation times. The samples were stored in desiccator. Nominal compositions of series PNa are represented in Table 22.

Glass	P_2O_5	Na_2O_3	Al_2O_3
PNa	66.6	33.3	0
PNa_3Al	64.4	32.2	3.3
PNa_6Al	62.2	31.1	6.7
PNa_8Al	60.7	30.4	8.9
PNa_10Al	29.3	29.6	11.1
PNa_13Al	57.0	28.5	14.4
PNa_15Al	55.6	27.8	16.7

Table 22. Nominal compositions of two series of sodium phosphate glasses.

To prove that CSA tensor of phosphosilicate glasses get smaller under incorporation of aluminum, ^{31}P MAS NMR of PNa series was measured. The results are represented in Figure 134. It might be seen that CSA tensor progressively decreases along with aluminum addition which results on progressively smaller intensities of spinning sidebands. Furthermore, the width of phosphorus peaks is increasing due to increasing diversity of adjustment atoms.

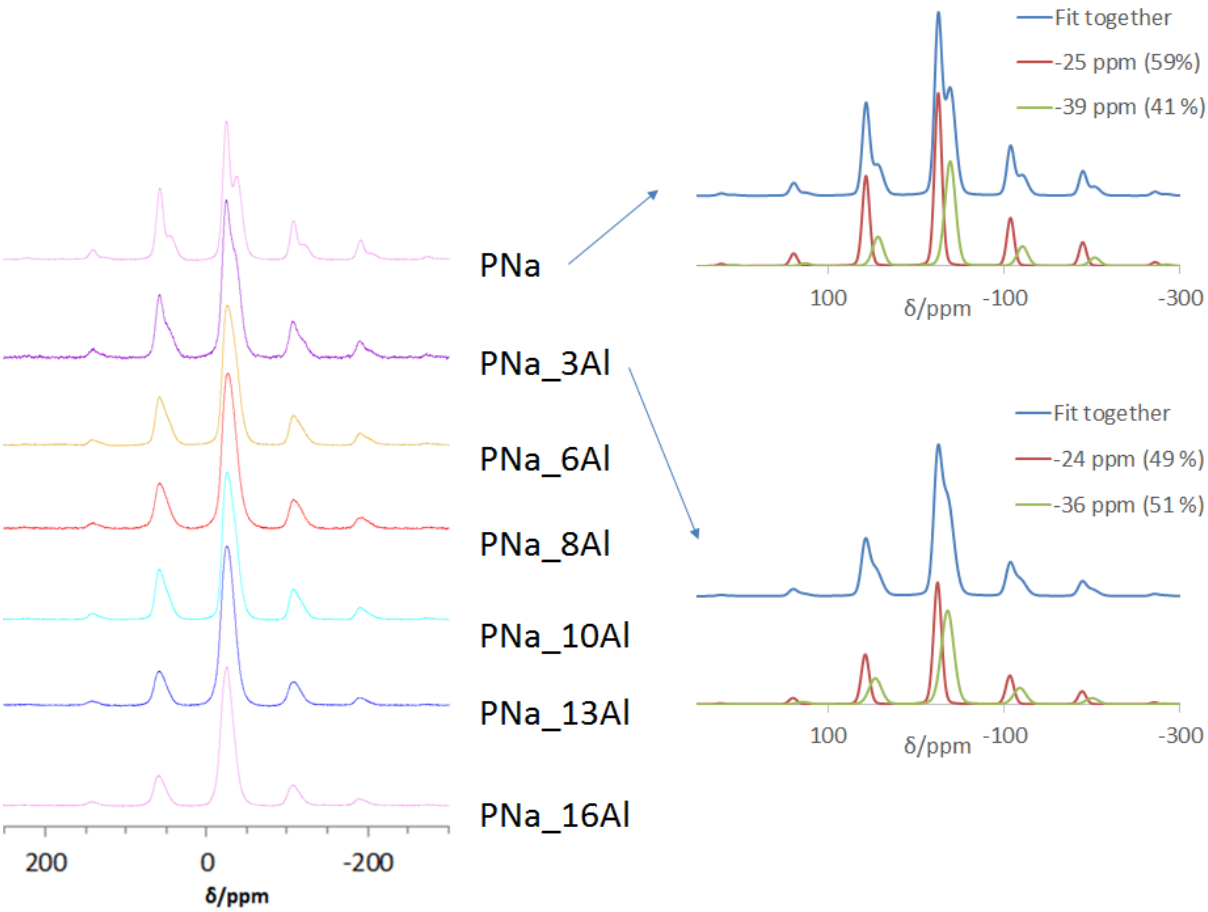

Figure 134. ^{31}P-MAS NMR spectra of glasses of series PNa ((100-x)(0.66P_2O_5-0.33Na_2O)-xAl_2O_3) measured in the field of 7 T.

Appendix 6. Calculation of the Amount of Six-Coordinated Cations in Phosphorus-Rich Glasses

Sample Name	Molar percent of aluminum	N6(Al), amount of six-coordinated aluminum units per (100-x)($60P_2O_5$-$30Na_2O$-$10SiO_2$)-xAl_2O_3 (molar percent of Al_2O_3 * 2 * fractional area of AlO_6 peak)	Molar percent of silicon	N6(Si), amount of six-coordinated silicon units per (100-x)($60P_2O_5$-$30Na_2O$-$10SiO_2$)-xAl_2O_3 (molar percent of SiO_2 * fractional area of SiO_6 peak)	N6, total molar percent of six-coordinated units per (100-x)($60P_2O_5$-$30Na_2O$-$10SiO_2$)-xAl_2O_3
P60_0Al	0.0	0.0	10.0	10.0	10.0
P60_3Al	3.0	5.1	9.7	5.9	11.1
P60_6Al	6.0	9.9	9.4	2.9	12.8
P60_8Al	8.0	13.4	9.2	0.0	13.4
P60_10Al	10.0	15.0	9.0	0.0	15.0
P60_13Al	13.0	17.8	8.7	0.0	17.8
P60_15Al	15.0	18.2	8.5	0.0	18.2

Table 23. Calculation of N6, total amount of six-coordinated species per (100-x)($60P_2O_5$-$30Na_2O$-$10SiO_2$)-xAl_2O_3, in P60 series based on the results of single excitation ^{29}Si and ^{27}Al MAS NMR.

Sample Name	Molar percent of aluminum	N6(Al), amount of six-coordinated aluminum units per (100-x)($60P_2O_5$-$30Na_2O$-$10SiO_2$)-xAl_2O_3 (molar percent of Al_2O_3 * 2 * fractional area of AlO_6 peak)	Molar percent of silicon	N6(Si), amount of six-coordinated silicon units per (100-x)($60P_2O_5$-$30Na_2O$-$10SiO_2$)-xAl_2O_3 (molar percent of SiO_2 * fractional area of SiO_6 peak)	N6, total molar percent of six-coordinated units per (100-x)($60P_2O_5$-$30Na_2O$-$10SiO_2$)-xAl_2O_3
P50_0Al	0.0	0.0	33.3	10.5	10.5
P50_0.25Al	0.3	0.5	33.3	10.8	11.2
P50_1Al	1.0	1.7	33.0	9.3	11.0
P50_3Al	3.0	5.0	32.3	4.2	9.2
P50_6Al	6.0	10.0	31.3	0.0	10.0
P50_8Al	8.0	13.4	30.7	0.0	13.4
P50_10Al	10.0	13.9	30.0	0.0	13.9
P50_13Al	13.0	12.3	29.0	0.0	12.3
P50_15Al	15.0	11.5	28.3	0.0	11.5

Table 24. Calculation of N6, total amount of six-coordinated species per (100-x)($0.5P_2O_5$-$0.33SiO_2$-$0.17Na_2O$)-xAl_2O_3, in P50 series based on the results of single excitation ^{29}Si and ^{27}Al MAS NMR.

Appendix 7. Effect of CSA and Offset on $^{29}Si\{^{31}P\}$-REDOR Results

To investigate possible effect of experimental settings and nuclei environment, series of simulations of $^{29}Si\{^{31}P\}$-REDOR experiments using effective dipolar coupling of 700 Hz was carried out considering phase cycling on the observed channel. In Figure 135 the effect of the width of CSA tensor on $^{29}Si\{^{31}P\}$-REDOR is represented. As might be seen, large width of CSA tensor might have a considerable effect on the results and have to be considered when simulating experimental data. In Figure 136 the effect of offset on the phosphorus and silicon signal on $^{29}Si\{^{31}P\}$-REDOR is shown, respectively. As might be seen, small experimental offsets on phosphorus channel not affect simulation results much but the effects of large offsets must be taken into account. In Figure 137 the results of using pulse length different from ideal π-values on both channels is simulated. Again, small experimental missets do not affect the results of the measurements much but large deviations from π-values on phosphorus channel must be considered. In Figure 135-Figure 138 the results of combined effect of two, three four and five experimental missets and CSA values are shown, respectively. The results indicate that the experiments should be set with maximal caution and that the deviations from ideal setting should be considered in simulations of experimental results. Among all parameters the widths of CSA tensor and large values of experimental offsets and different from π-values pulse lengths on phosphorus channel have the highest effect to the results of simulations alone or combined with other experimental missets. At the end, an example of SIMPSON simulation file for the last Figure is given.

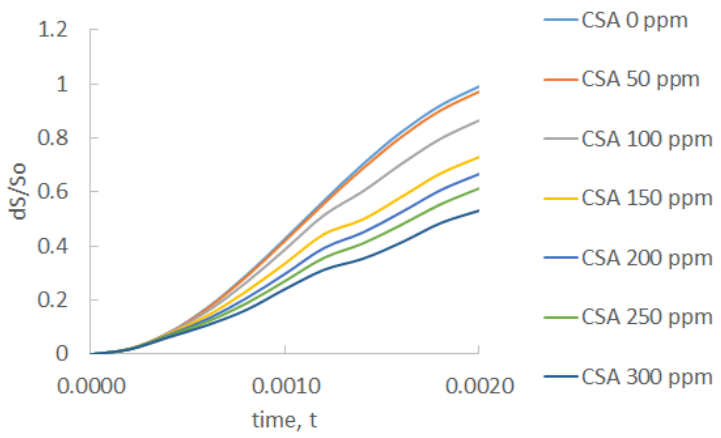

Figure 135. The results of SIMPSON simulations of $^{29}Si\{^{31}P\}$-REDOR using effective dipolar coupling of 700 Hz and indicated values of the width of CSA tensor of phosphorus signal.

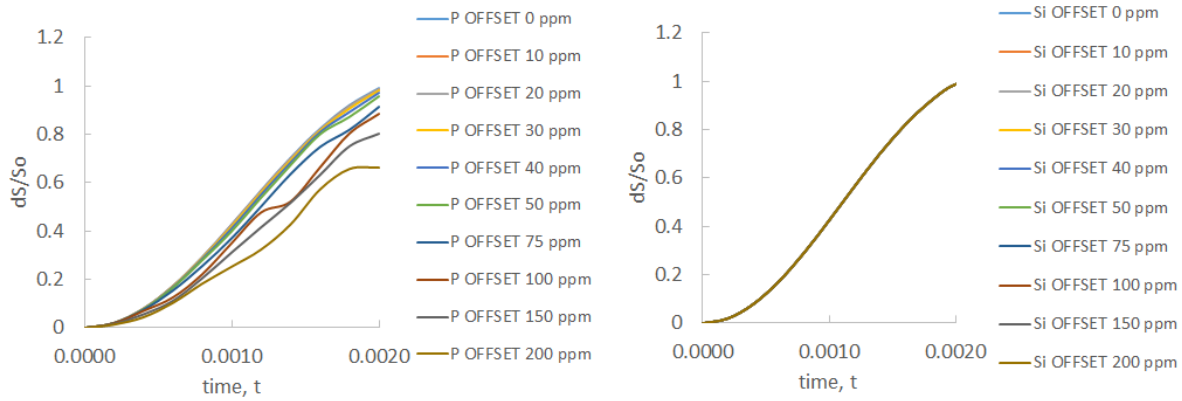

Figure 136. The results of SIMPSON simulations of $^{29}Si\{^{31}P\}$-REDOR using effective dipolar coupling of 700 Hz and indicated values of the offset on phosphorus channel (left) and on silicon channel (right).

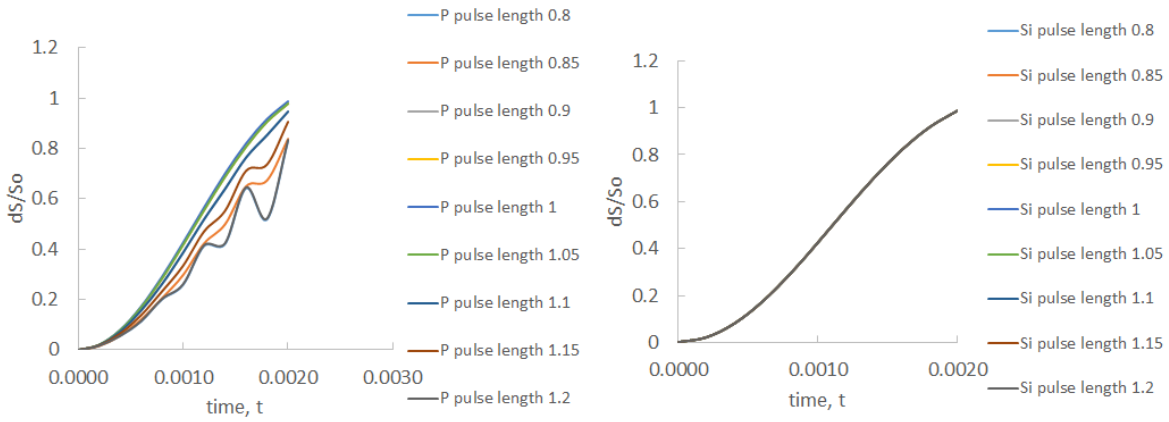

Figure 137. The results of SIMPSON simulations of $^{29}Si\{^{31}P\}$-REDOR using effective dipolar coupling of 700 Hz and indicated values of the ratios of applied pulse lengths to the lengths of π-pulses on phosphorus channel (left) and silicon channel (right).

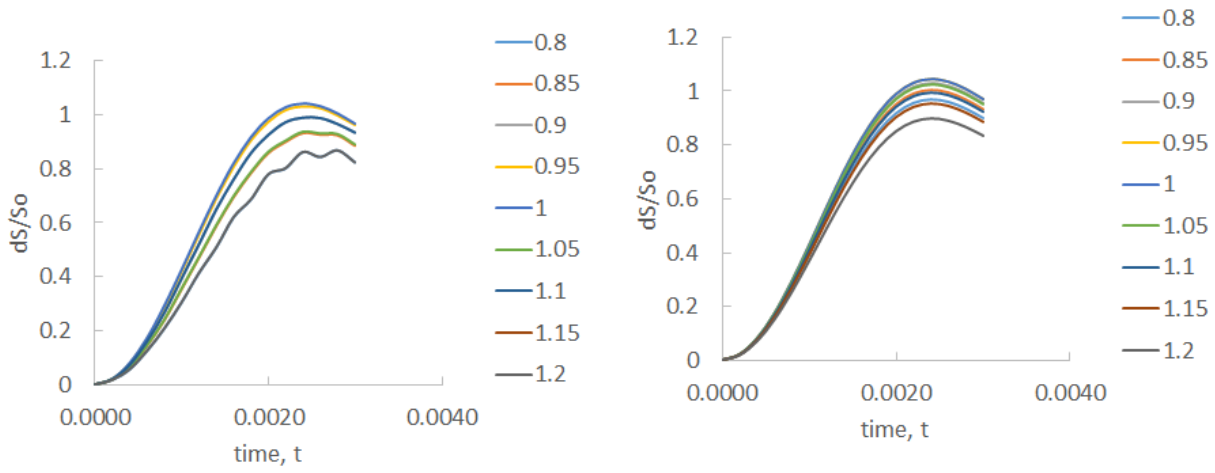

Figure 138. The results of SIMPSON simulations of $^{29}Si\{^{31}P\}$-REDOR using effective dipolar coupling of 700 Hz and indicated values of the ratios of applied pulse lengths to the lengths of π-pulses on left: silicon channel, right: phosphorus channel.

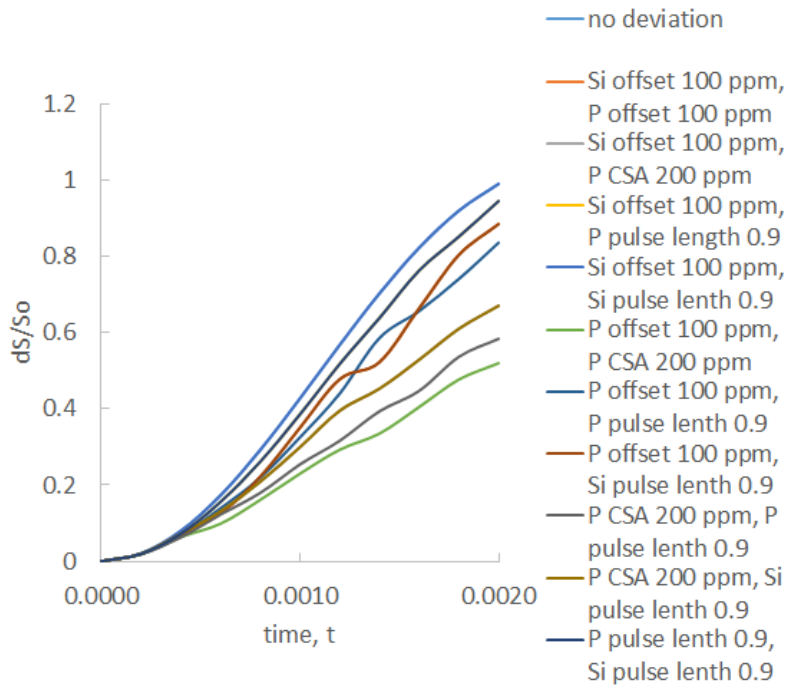

Figure 139. The results of SIMPSON simulations of $^{29}Si\{^{31}P\}$-REDOR using effective dipolar coupling of 700 Hz and combined effect of two indicated factors.

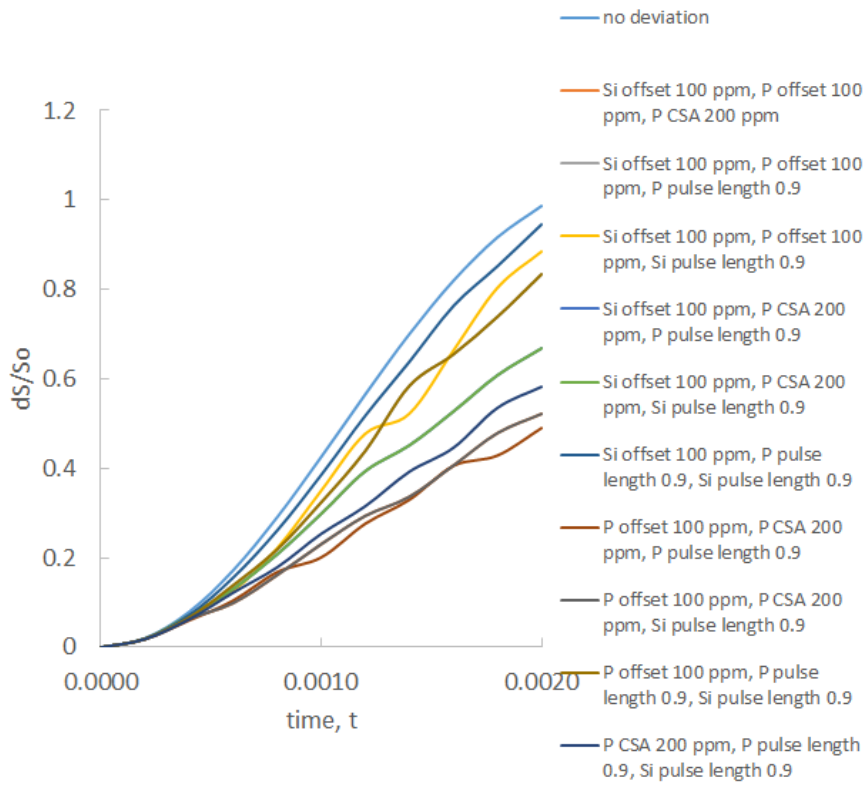

Figure 140. The results of SIMPSON simulations of $^{29}Si\{^{31}P\}$-REDOR using effective dipolar coupling of 700 Hz and combined effect of three indicated factors.

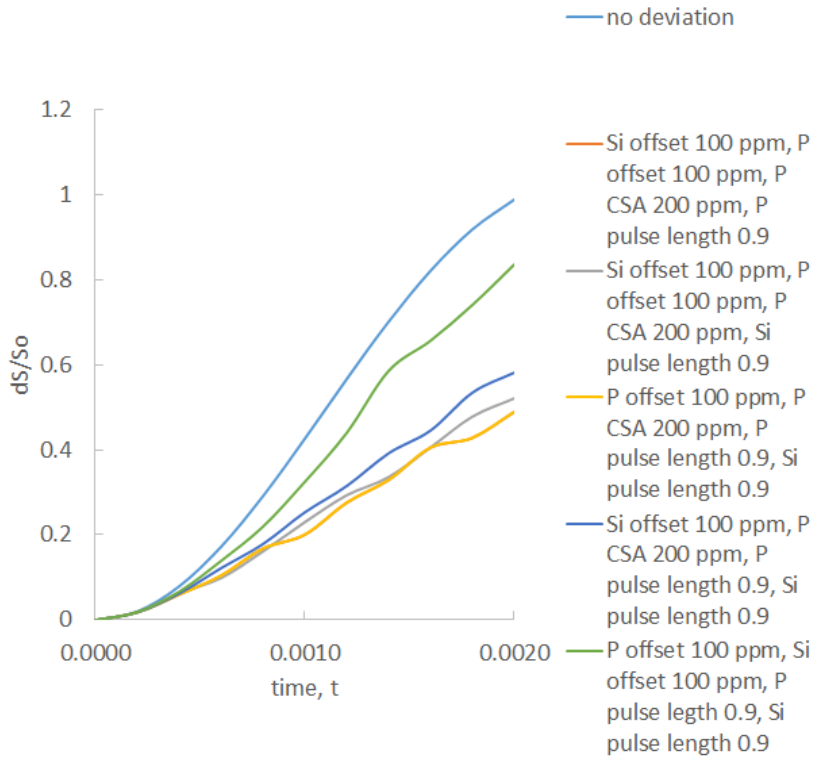

Figure 141. The results of SIMPSON simulations of $^{29}Si\{^{31}P\}$-REDOR using effective dipolar coupling of 700 Hz and combined effect of four indicated factors.

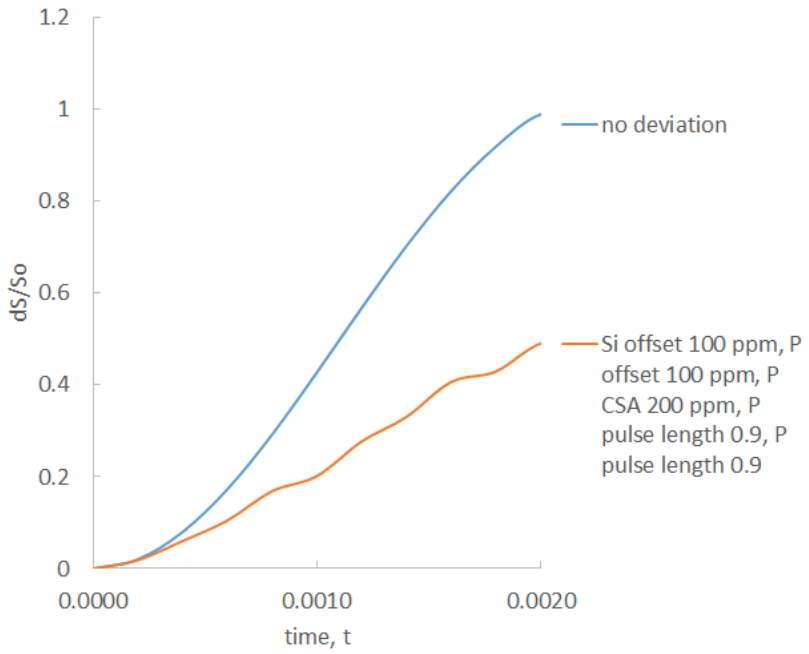

Figure 142. The results of SIMPSON simulations of $^{29}Si\{^{31}P\}$-REDOR using effective dipolar coupling of 700 Hz and combined effect of five indicated factors.

Appendix 8. Effect of the Shim Coil Temperature to the Chemical Shift

In Figure 143 the ex-situ measurements of ^{23}Na spectra of the glass Si50 and Si70 before and after heating with the shim coil having different temperature are represented. The spectra of the glass Si50 is shifted to the less negative frequencies after heating which might be caused by the irreversible new redistribution of the sodium ions probably due to the appearance of a new dynamic fraction at the high temperatures (see 4.2.10), namely changes in the glass structure, irreversible changes in Na-O distances after heating or changed quadrupolar constants of sodium. At the same time, the spectra of the glass Si70 is not shifted much with moderately changed shim coil temperature. Considering that the typical change of the shim coil temperature is lower while using novel induction heating method and that in the case of the current measurement is restricted to the range 301-308 °C (as shown in Figure 144) and the results of the ex-situ measurements, it is not probable that such a large changes in the position of the peak are caused by the different temperature of the shim coil but rather by changing Na-O coordination and averaging out of central transition and satellites due to sodium dynamics as described in 4.2.10.

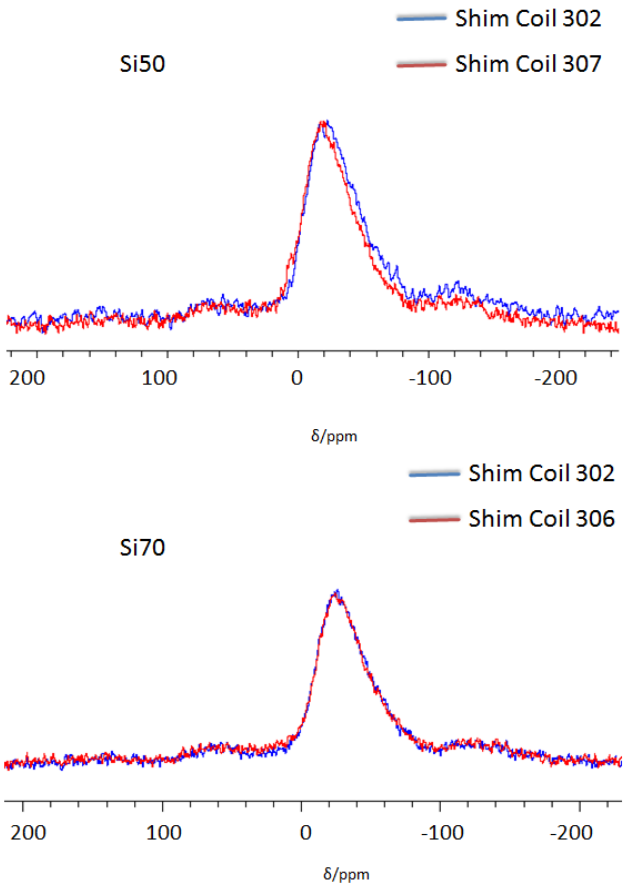

Figure 143. ^{23}Na MAS NMR spectra of Si50 (top) and Si70 (bottom) glasses obtained before and after heat temperature treatment (blue and red lines, respectively).

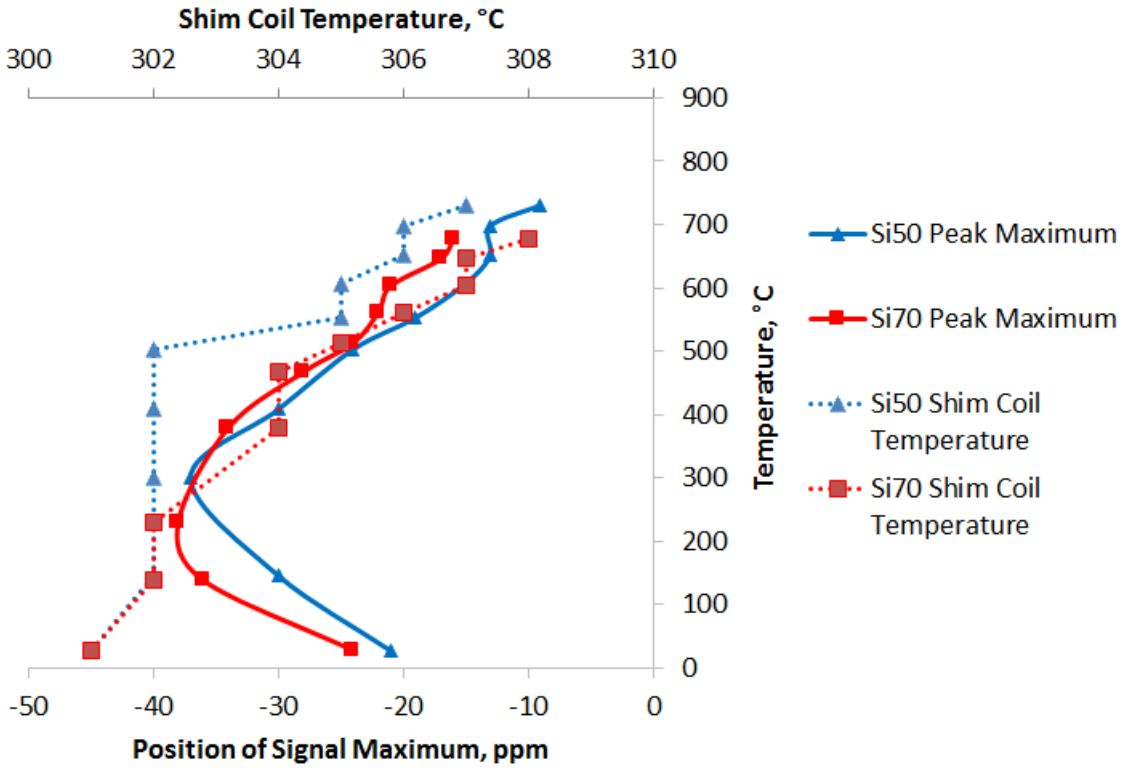

Figure 144. Dependence of the temperature of the shim coil and chemical shift on the in-situ temperature of the sample.

Appendix 9. Simulations of the Effect of the Widths of CSA Tensor and Values of Dipolar Coupling Constants on the REDOR Effect

Simulations of $^{13}C\{^{15}N\}$ REDOR experiments were carried out using simulation program for SIMPSON. CSA of carbon nuclei and effective dipolar coupling were varied as indicated in Figure 145. REDOR-effect was estimated using the intensity of central peak and the integral intensity over all sidebands. The results showed that the REDOR effect on the central peak is smaller than integrated REDOR effect. The discrepancy growths with increasing CSA and dipolar coupling. This implies that intensity of sidebands has to be considered and included in estimation of $^{13}C\{^{15}N\}$ REDOR experiments especially if CSA value on the observed channel are high. An example of SIMPSON simulation program for carbon signal having chemical shift of 120 ppm, CSA width of 200 ppm and dipolar coupling between nitrogen and carbon of 1600 Hz for two rotor periods is represented below.

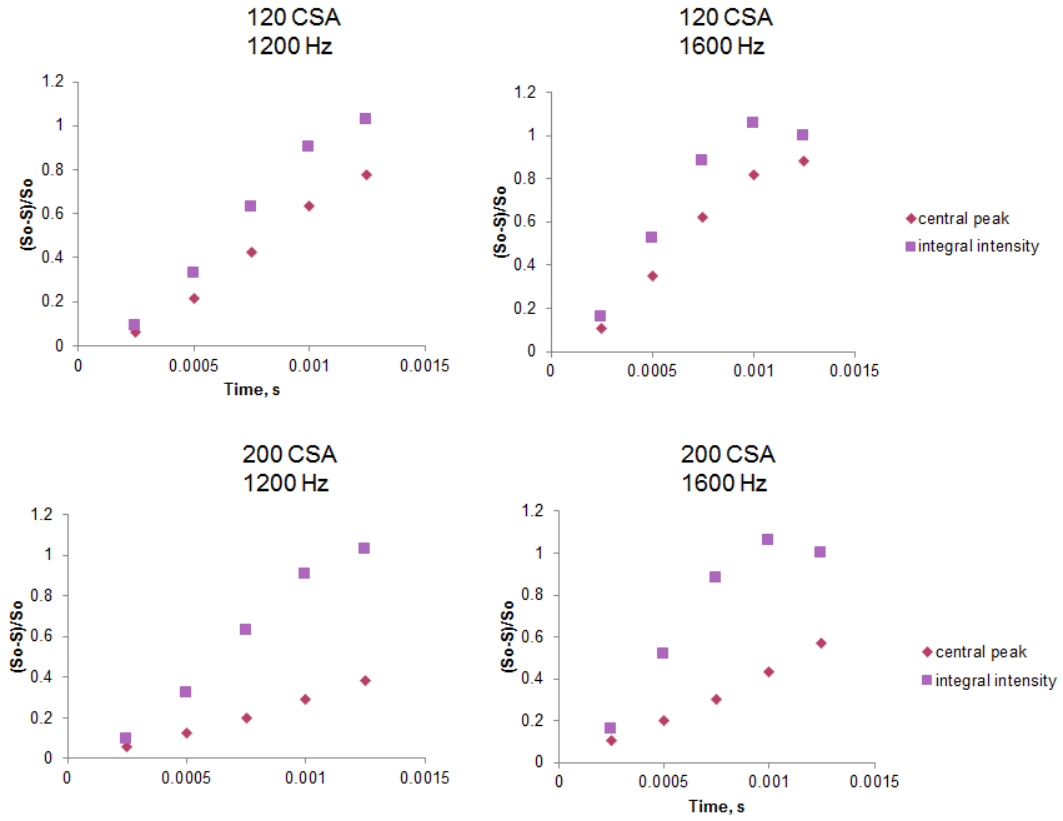

Figure 145. Results of theoretical SIMPSON simulation showing dependence of disagreement of intensity behavior of the central peak and of integral signal intensity depending on dipolar coupling and CSA values.

```
spinsys {
    channels 13C 15N
    nuclei 13C 15N
    shift 1 120p -200p 0.2 20 30 40
    dipole 1 2 1600 0 0 0


}

par {
    use_cluster      1
    cluster_port     4999
    spin_rate        8000
    np  1024
    sw   150000
    crystal_file     rep320
    gamma_angles     36
    start_operator   I1x
    detect_operator  I1p
    method           direct
    verbose          1101
    proton_frequency 500e6
}

proc pulseq {} {
    global par rf1 rf2 rf2_nominal p l0 phz  berp berphas

    maxdt 1
    offset 0 0
# now here the pulse sequence in bruker style. different from the
usual way of calculating redor curves here we are calculating redor
spectra, since
# we are interested in the behaviour of the individual sidebands.

    set tr [expr 1.0e6/$par(spin_rate)]
    set p2 [expr 0.5e6/$rf1]
    set p12  [expr 0.5e6/$rf2_nominal]

    set d25 [expr ($tr/4.0) - 2]
    set d26 [expr ($tr/4.0) - $p2/2]
    set d27 [expr ($tr/4.0) - $p12/2]


set ph8 {0 90 0 90 90 0 90 0}
set ph11 0
set ph3 0
set ph31 0
reset
delay 2
delay $d25

# the next 7 lines define a 180 deg pulse on the dephasing channel
with an appropriate phase propagation for the pulse train. xy_8 is
used.
```

```
set phz 0
for {set j 1} {$j <= $l0} {incr j} {
delay $d27
if {$phz == 7} {set phz 0}
set berp [lindex {0 90 0 90 90 0 90 0} $phz]
incr phz
pulse $p12 0 0 $rf2 $berp
delay $d27
}

# done with the pulse. now we have a fragment d27--p12--d27 which is
looped l0 times. l0 has to be an odd number


# the next three lines define the 180 deg pulse on the observe
channel

delay $d26
pulse $p2 $rf1 $ph3 0 0
delay $d26
# done with the pulse

# now again a d27--p12--d27 fragment, looped l0 times with
appropriate phase propagation within the train.
set phx 0
for {set j 1} {$j <= $l0} {incr j} {
delay $d27
if {$phx == 7} {set phx 0}
set berp [lindex {0 90 0 90 90 0 90 0} $phx]
incr phx
pulse $p12 0 0 $rf2 $berp
delay $d27
}

# done with the pulse


delay $d25
delay 2

# end of sequence. we can now start with the acquisition. since we
need spectra, not only one point is aquired, but the complete fid.

set tdwell [expr 1.0e6/$par(sw)]
acq $ph31
for {set i 1} {$i < $par(np)} {incr i} {
delay $tdwell
acq $ph31
   }
   }
## end of definition of pulse program.
```

```
# main body. important: rf2 and rf2_nominal both denote the power on
the dephasing channel. rf2
# is the value used in the pulse program, rf2_nominal for the
calculation of the durations. so for the s0 experiment, set
# rf2 to zero and rf2_nominal to the value uses in the real redor
experiment.

proc main {} {
    global par rf1 rf2 rf2_nominal p l0

    set rf1  117647
    set rf2  100000
    set rf2_nominal 100000

    set l0 1


      set f [fsimpson]

      fsave $f $par(name).fid
      fzerofill $f 16384
      faddlb $f 200 0
      fft $f
      fsave $f $par(name).spe
      funload $f

}
```

Appendix 10. ^{1}H-MAS NMR Spectra of Fibers

^{1}H MAS spectra of industrially produced carbon fibers including spinning sidebands are represented in Figure 146.

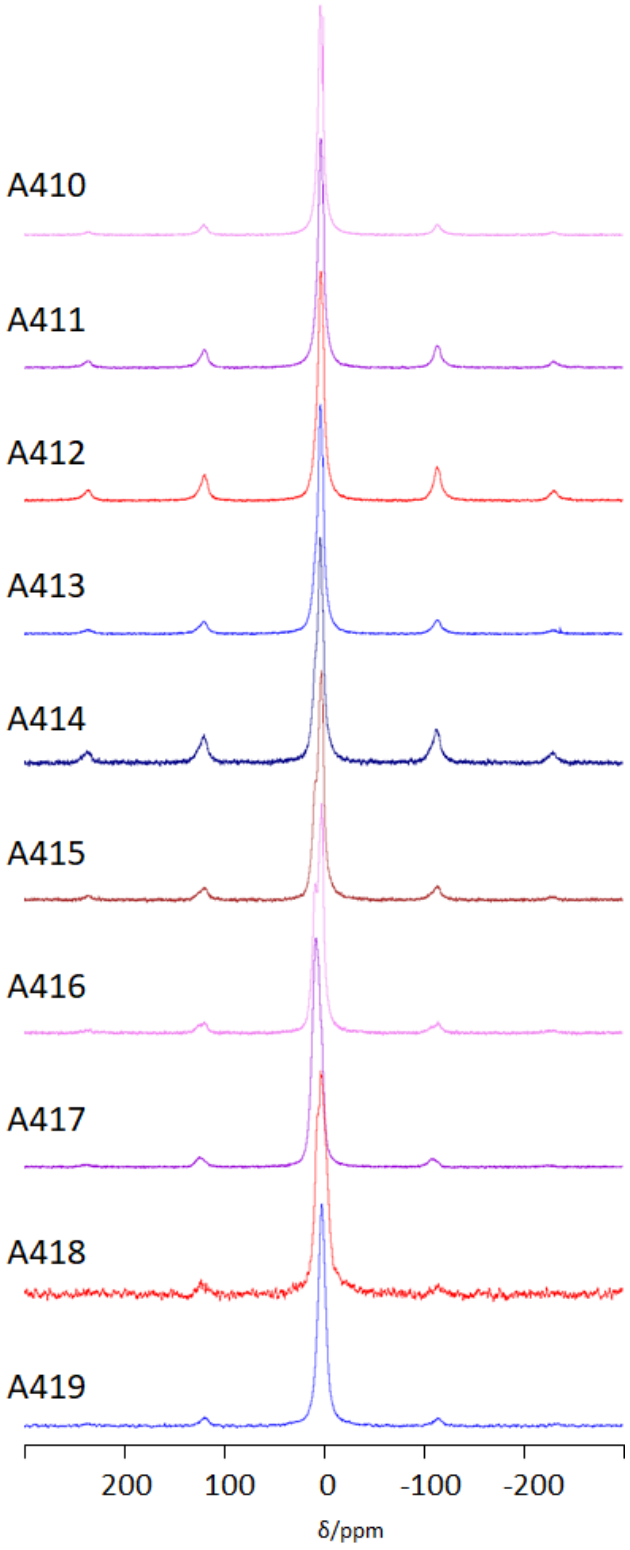

Figure 146. ^{1}H NMR MAS spectra of industrially produced carbon fibers including spinning sidebands.

Appendix 11. Exemplary $^{13}C\{^{15}N\}$ REDOR Spectra of PAN

In Figure 147 an exemplary out-of-phase and negative spinning sidebands intensities caused by large CSA of ^{13}C nuclei is shown.

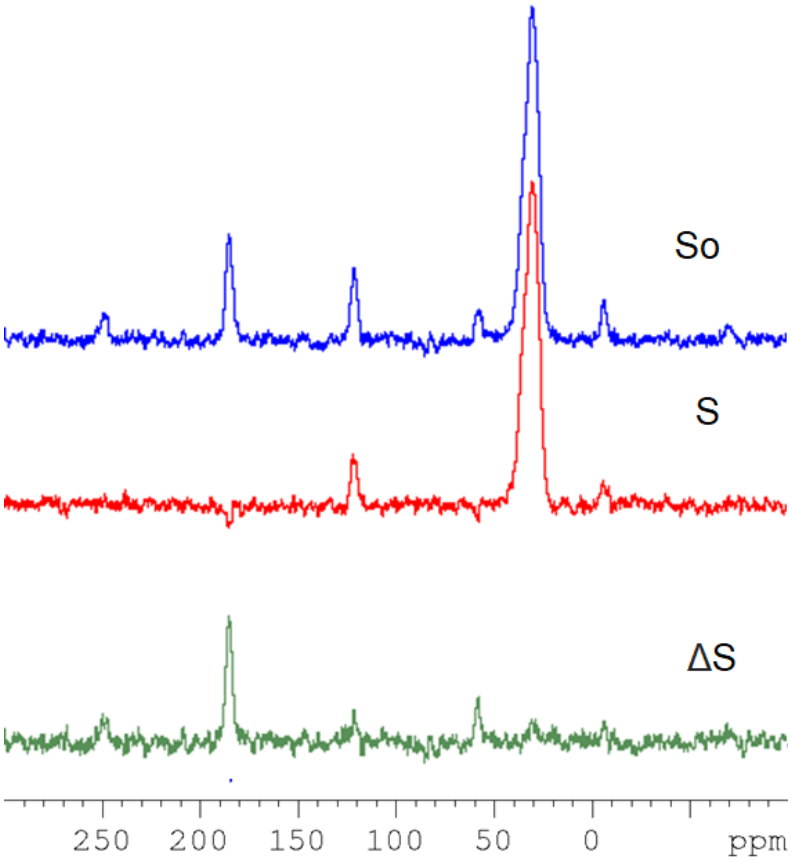

Figure 147. Exemplary $^{13}C\{^{15}N\}$ REDOR spectra of PAN at eighth rotor cycle measured in the field of 11 T.

Appendix 12. Estimations of Individual CSA Components of Carbon Signal of TS1 and Test REDOR Measurements

Such as the widths of CSA tensors are very important for interpretation of $^{13}C\{^{15}N\}$ REDOR effect, the widths of CSA tensors were measured on TS1 using lowest possible spinning speeds. Although more spinning sidebands are needed to define CSA parameters, due to instrumental restriction we could consider only three to six spinning sidebands. Nevertheless, it allowed to estimate minimum width of CSA tensors of individuals peaks. The results are shown in Figure 148. CSA width was estimated using DMFIT software using Haeberlen-Mehring-Spiess convention which is used in both DMFIT and SIMPSON NMR software where the axiality of CSA tensor is defined as $\sigma_{zz} - \sigma_{iso}$. The results imply that great care is to be taken while interpreting the results of $^{13}C\{^{15}N\}$ REDOR on nitrile groups having large CSA.

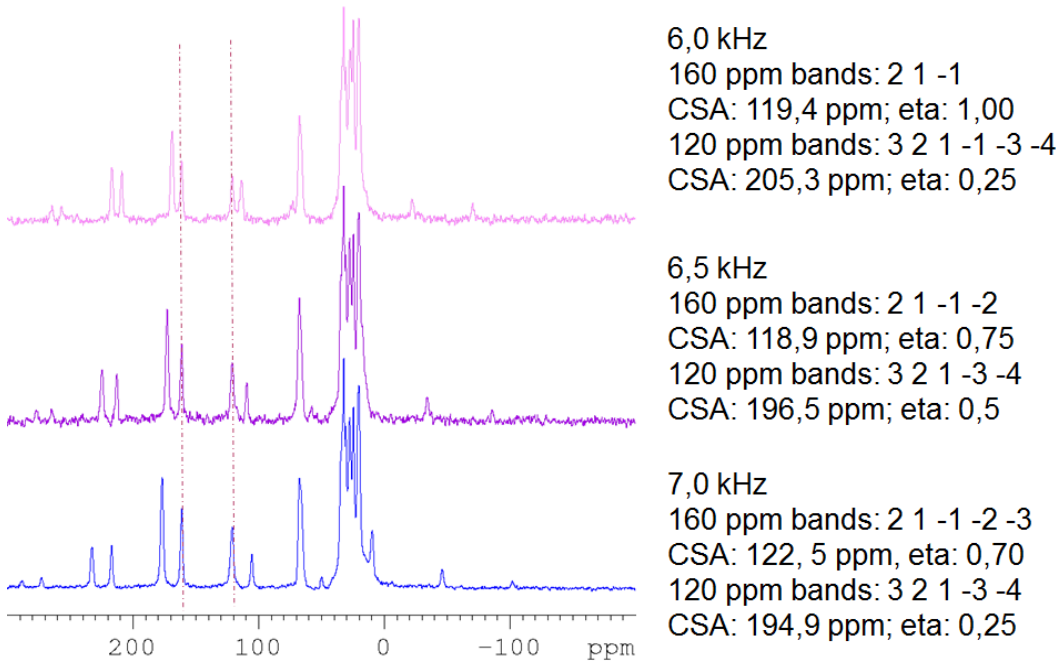

Figure 148. Estimations of individual CSA components of carbon signal of TS1 at lowest possible speed by ^{1}H-^{13}C CPMAS NMR measured in the field of 11 T.

Appendix 13. ^{1}H-^{13}C CPMAS spectra of TS2 and dependence of ^{1}H-^{13}C CPMAS Signal on Contact Time

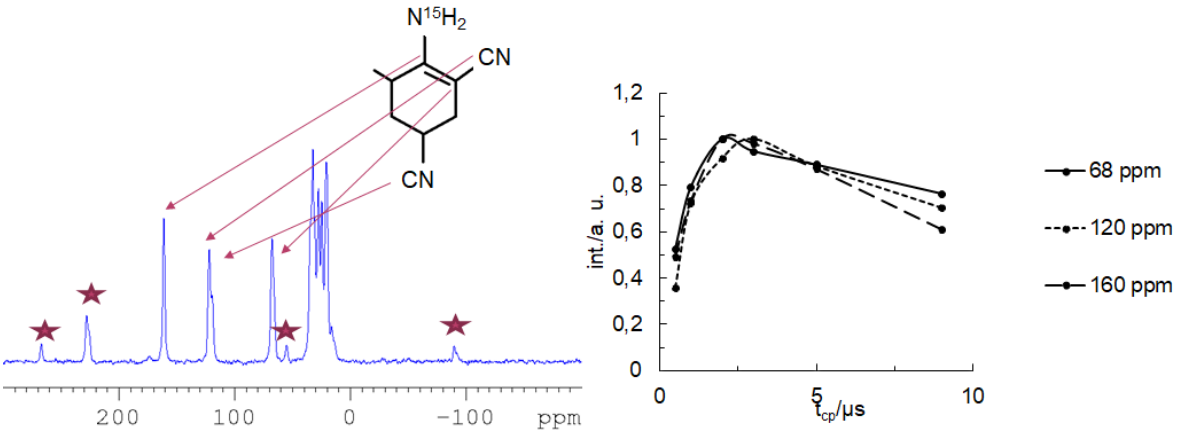

Figure 149. ^{1}H-^{13}C CPMAS spectra of TS2 at contact time of 2000 us (asterisks indicate spinning sidebands) (left) and intensity dependence of ^{1}H-^{13}C CPMAS signal of TS2 on contact time measured in the field of 11 T.

Appendix 14. Typical Chemical Shifts

Typical chemical shift values of ^{13}C and ^{1}H isotopes in organic substances are well known and have been thoroughly researched and tabulated. But for ^{15}N isotopes the situation is different. Such as ^{15}N isotopes have low natural abundance and low gyromagnetic ration, they are very difficult to observe even applying some signal intensity-enhancing techniques such as CPMAS NMR. Therefore, the amount of data about the chemical shift of different molecular moieties is limited comparing to other nuclei investigated in this thesis. In Figure 150[110] the most important information about chemical shift of the moieties, expected to be found in PAN fibers during its polymerization are represented together with an exemplary ^{1}H-^{15}N CPMAS NMR spectra. As might be seen, pyridine and pyrimidine molecules are found to the left of -100 ppm. In the region between-100 and -200 ppm nitrile groups bound to non-hydrogenated carbon, pyridine units with only one amino function in ortho position or triazine derivatives are expected to be found. To the right of -200 ppm different hydrogenated nitrogen moieties can give rise to a signal. Amine moieties are particularly observed in the region right to -290 ppm.

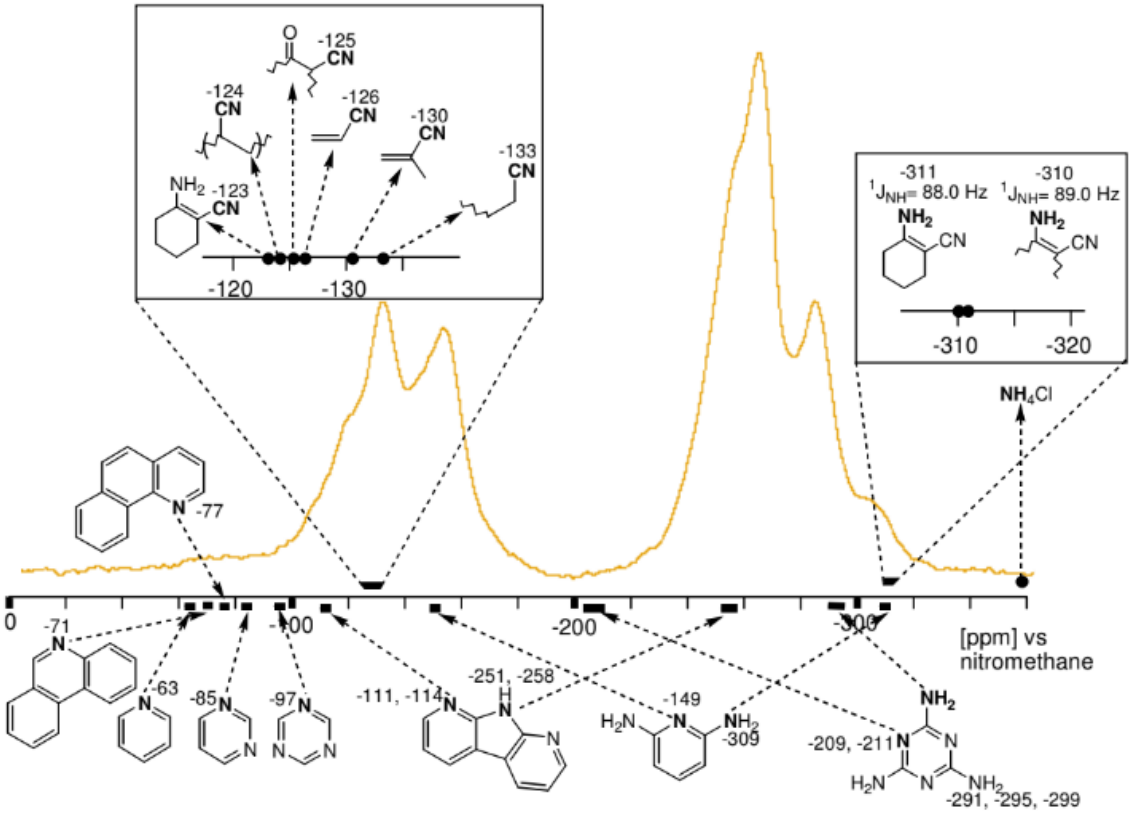

Figure 150[110]. Chemical shift of compounds relevant for the study together with exemplary spectra of PAN295 [168–173].

Appendix 15. Exemplary Spectra of $^{13}C\{^{15}N\}$ Measurements of Heated PAN Samples

An exemplary ^{1}H-^{13}C-$\{^{15}N\}$ REDOR spectrum of PAN268, PAN295 and PAN395 are represented in Figure 151.

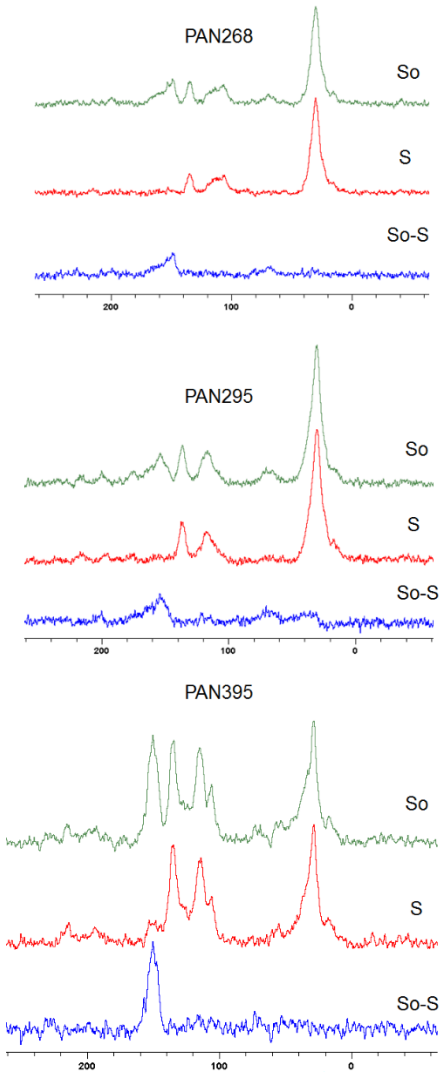

Figure 151. Exemplary $^{13}C\{^{15}N\}$ REDOR spectra of the samples PAN268 (top), PAN295 (middle) and PAN395 (bottom) at t=0.001 s measured in the field of 11 T.

Appendix 16. ^{1}H-^{2}H and ^{1}H-^{15}N CPMAS Measurements on Test Deuterated Samples

In Figure 152 the results of contact time dependent ^{1}H-^{2}H CPMAS and ^{1}H-^{13}C CPMAS experiments of the test substances D1-D5 are represented. The magnetization build-up of individual signals is in agreement with hydrogen proximity. In ^{1}H-^{13}C CPMAS of the signals coming from CH and CD_2 groups complicated magnetization build-up caused by overlapping protonated and non-protonated carbon species is observed.

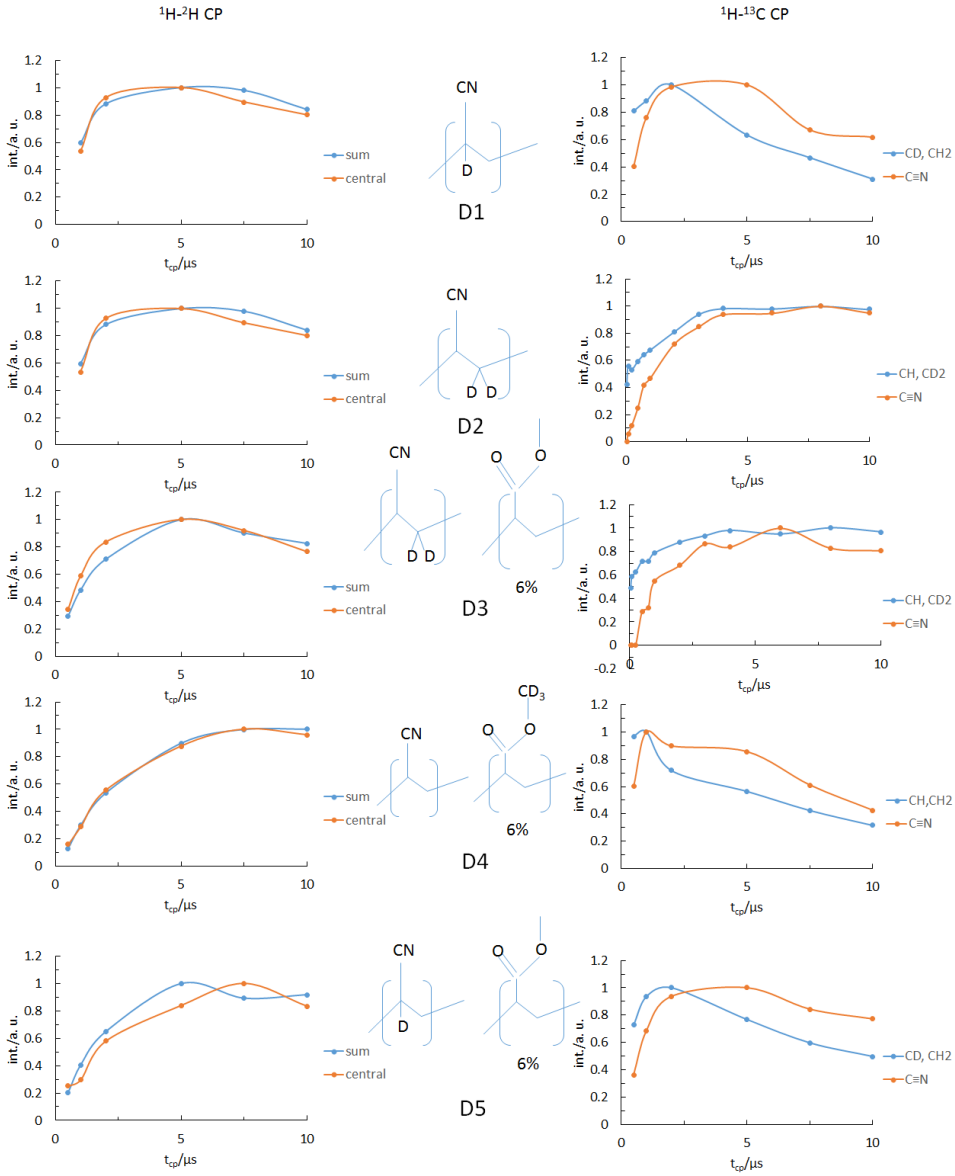

Figure 152. Dependence of signal intensity of ^{1}H-^{2}H CPMAS (left) and ^{1}H-^{13}C CPMAS (right) of test protonated samples measured in the field of 7 T.

Appendix 17. Heated 1D Sample

To find out if substitution of hydrogen by deuterium might have an effect to polymerization, sample D1 was investigated ex-situ after heat treatment. In Figure 153 the results if ^{1}H-^{2}H CPMAS experiments are represented. From the sidebands pattern and magnetization build-up of central peak and integral intensity it is supposed that deuterium might still be a part of -CD- group inside the polymer. ^{1}H-^{13}C CPMAS of the same sample spectra and contact time dependent intensities of the peaks are represented in Figure 154. The spectrum and magnetization build-ups of the individual peaks are in agreement to those observed in polymerized PAN. This supposes that substitution of hydrogen by deuterium dos not change drastically the structure of resulting polymer.

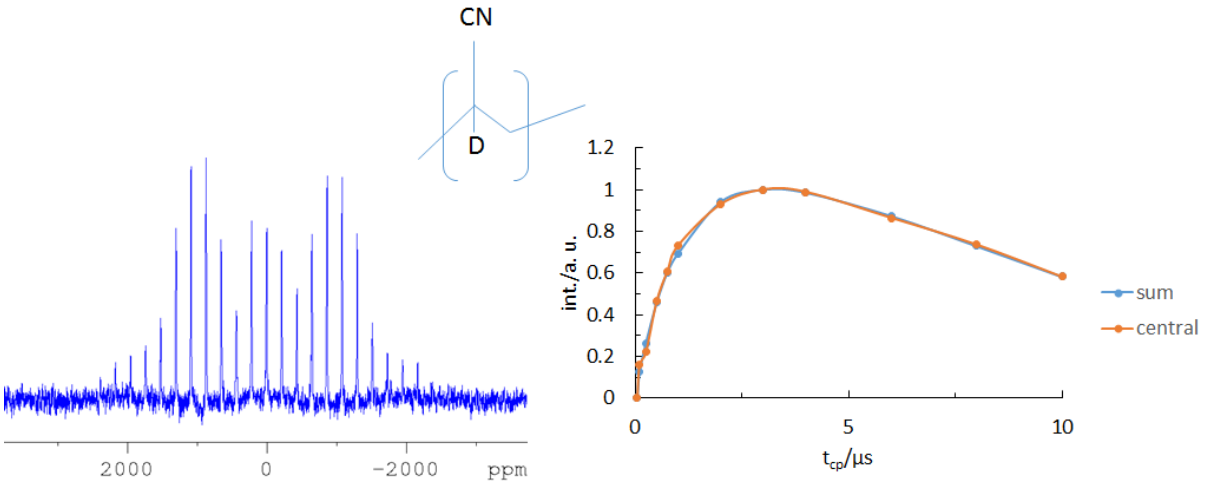

Figure 153. ^{1}H-^{2}H CPMAS (left) and dependence of the signal intensity (right) of heated D1 sample measured in the field of 7 T.

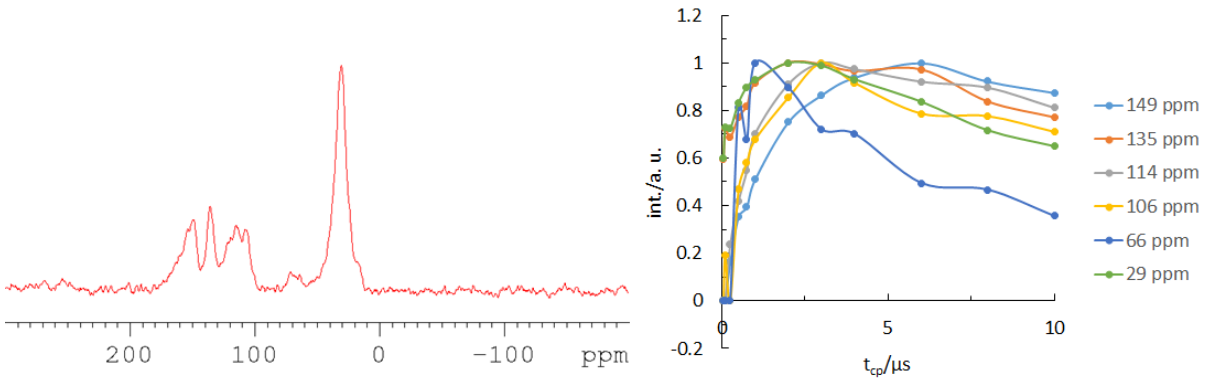

Figure 154. ^{1}H-^{13}C CPMAS (left) and dependence of the signal intensity (right) of heated D1 sample measured in the field of 7 T.

Appendix 18. Quantitative NMR Deuterium Measurements

In Table 25 the results of single pulse quantitative experiments (T1 relaxation times were estimated to be 6.6 s and 5 s for unheated and heated samples, respectively).

	Full rotor, g	Empty rotor, g	Weight of the sample, g	Integral intensity, a. u.	Intensity per gram, a. u.	Percentage
heated sample	0.0967	0.0915	0.0052	3.94691E+11	7.59022E+13	**37**
unheated sample	0.0959	0.0940	0.0019	3.84641E+11	2.02443E+14	

Table 25. Values used in quantitative measurements of heated and unheated D4 sample measured in the field of 11 T.

Appendix 19. Estimations of CSA of Carbon Signal of Unheated Double-Enriched PAN-MA Sample

The results of CSA measurements using lowest possible spinning speed are shown in Figure 148. Although more spinning sidebands are needed to define CSA parameters, due to instrumental restriction we could consider only three to six spinning sidebands. Nevertheless, it allowed to estimate minimum width of CSA tensors of individuals peaks. CSA width was estimated using DMFIT software using Haeberlen-Mehring-Spiess convention which is used in both DMFIT and SIMPSON NMR software where the axiality of CSA tensor is defined as $\sigma_{zz} - \sigma_{iso}$.

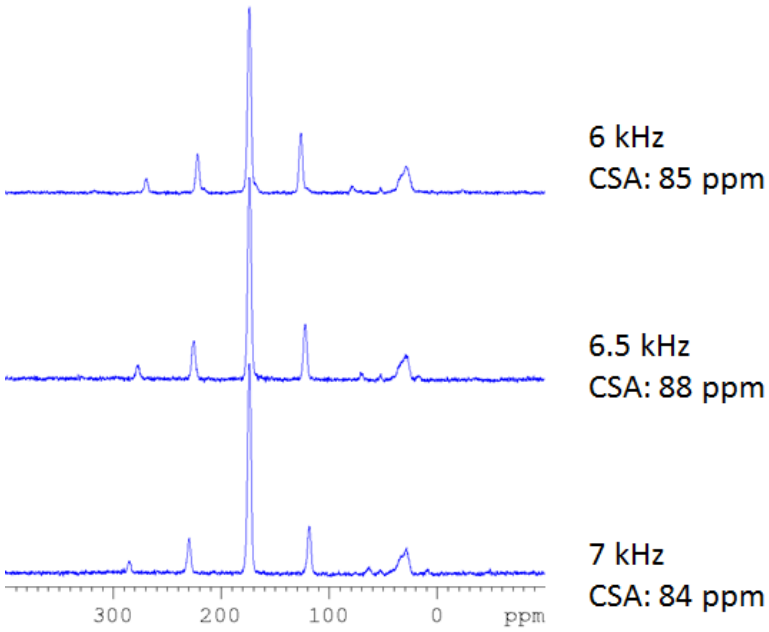

Figure 155. Estimations of CSA components of carbon signal of double-enriched unheated PAN-MA sample at lowest possible speed by ^{1}H-^{13}C CPMAS NMR measured in the field of 11 T.

Appendix 20. Estimations of CSA of Carbon Signal of Heated Double-Enriched PAN-MA Sample

The results of CSA measurements using lowest possible spinning speed are shown in Figure 156. Although more spinning sidebands are needed to define CSA parameters, due to instrumental restriction we could consider only three to six spinning sidebands. Nevertheless, it allowed to estimate minimum width of CSA tensors of individuals peaks. CSA width was estimated using DMFIT software using Haeberlen-Mehring-Spiess convention which is used in both DMFIT and SIMPSON NMR software where the axiality of CSA tensor is defined as $\sigma_{zz} - \sigma_{iso}$. The exact estimation of SCA tensor was difficult due to mixing with the signal from non-enriched carbon and the results should be considered with conscious.

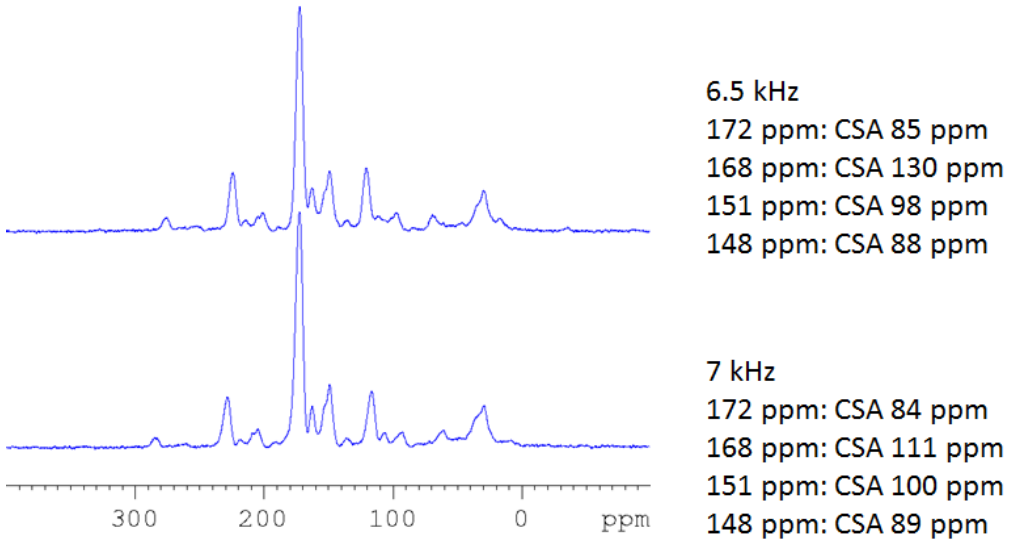

Figure 156. Estimations of CSA components of carbon signal of double-enriched heated PAN-MA sample at lowest possible speed by ^{1}H-^{13}C CPMAS NMR measured in the field of 11 T.

Appendix 21. Quantitative ^{13}C MAS Measurements of Heated Double-Enriched PAN-MA Sample

The results of single pulse ^{13}C MAS NMR measurements with recovery times of 200 s are shown in Figure 157. Due to overlapping of the signal with non-enriched carbon only central peaks were subjected to evaluation, so the results should be treated with caution. Simulation with DMFIT delivered relative integral areas of the peaks 172, 162 and (148 and 151) ppm to be 70:5:25, respectively.

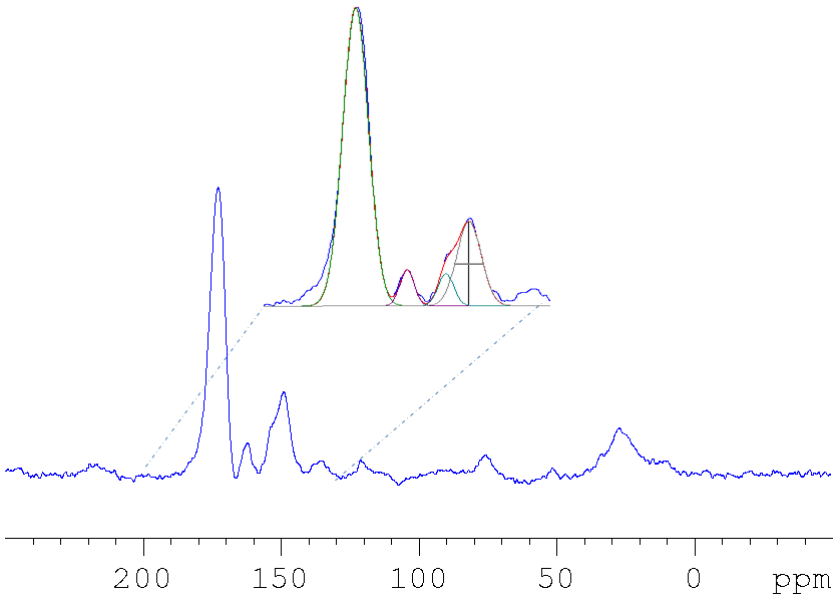

Figure 157. ^{13}C MAS NMR of double-enriched heated PAN-MA sample measured in the field of 11 T.

Appendix 22. Quantitative ^{15}N MAS Measurements of Heated Double-Enriched PAN-MA Sample

The results of single pulse ^{15}N MAS NMR measurements together with results of DMFIT simulations with recovery times of 200 s are shown in Figure 158. The ratio of intensities of non-protonated and protonated regions is about 65:35, but the spectrum has low signal-to-noise ratio and the results should be treated with caution.

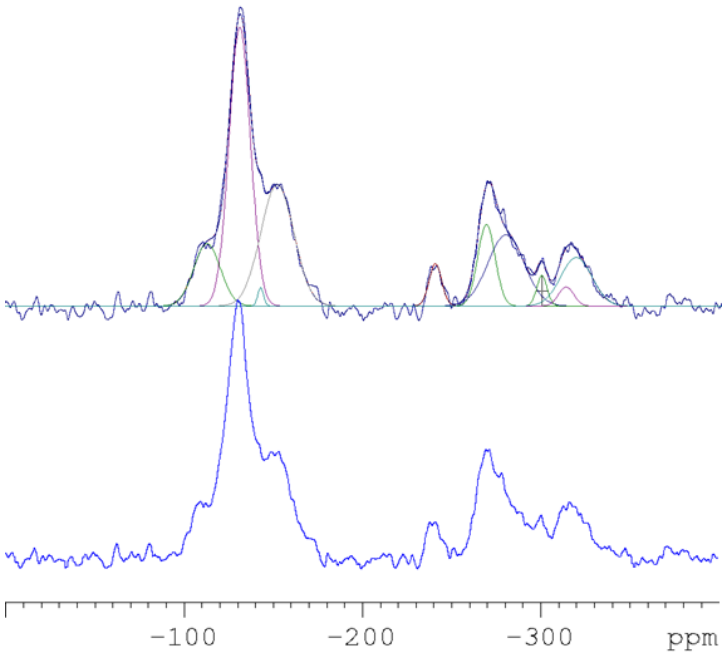

Figure 158. Quantitative ^{15}N MAS NMR of double-enriched heated PAN-MA sample measured in the field of 7 T.

Appendix 23. Estimations of $^{13}C\{^{15}N\}$ REDOR-effect on Individual peaks on heated PAN-MA Sample

The results quantitative estimation of $^{13}C\{^{15}N\}$ REDOR-effect on individual peaks of double-enriched heated PAN-MA sample are shown in Figure 159.

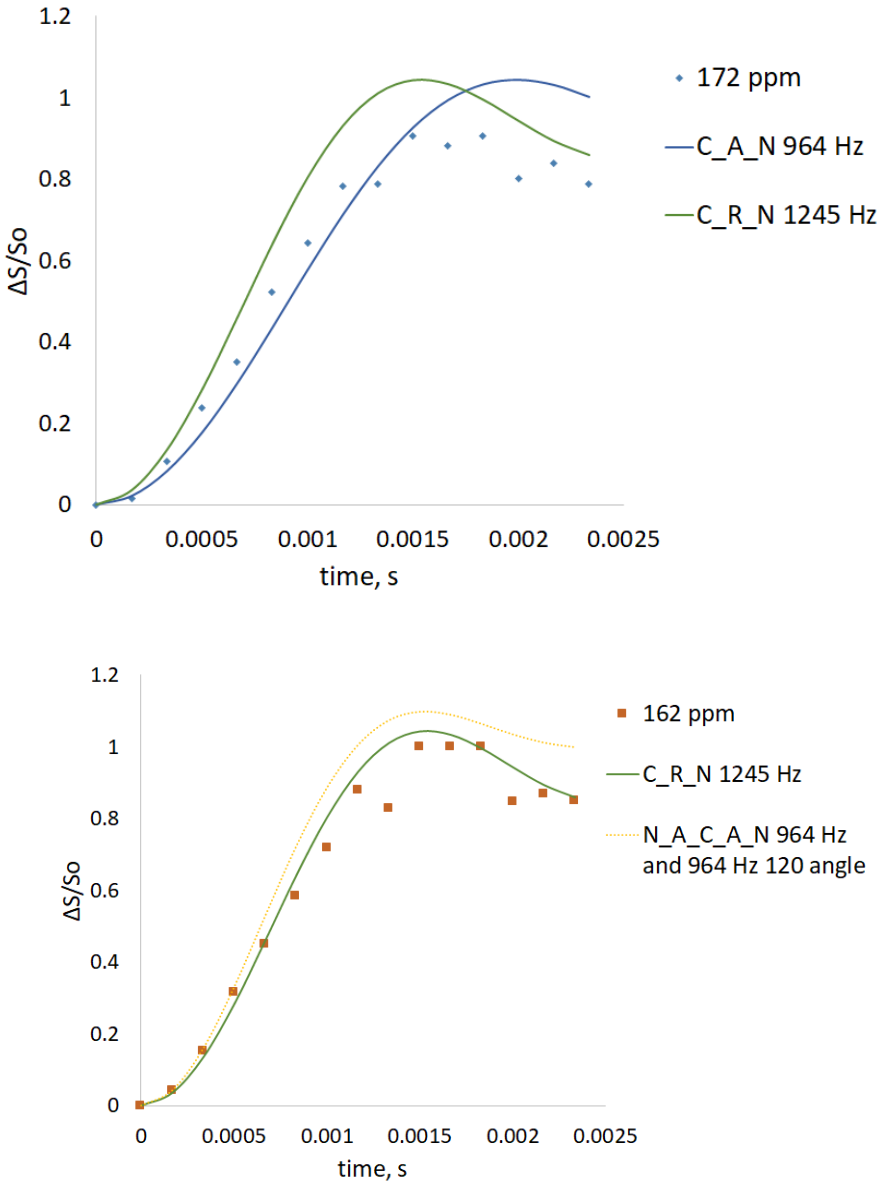

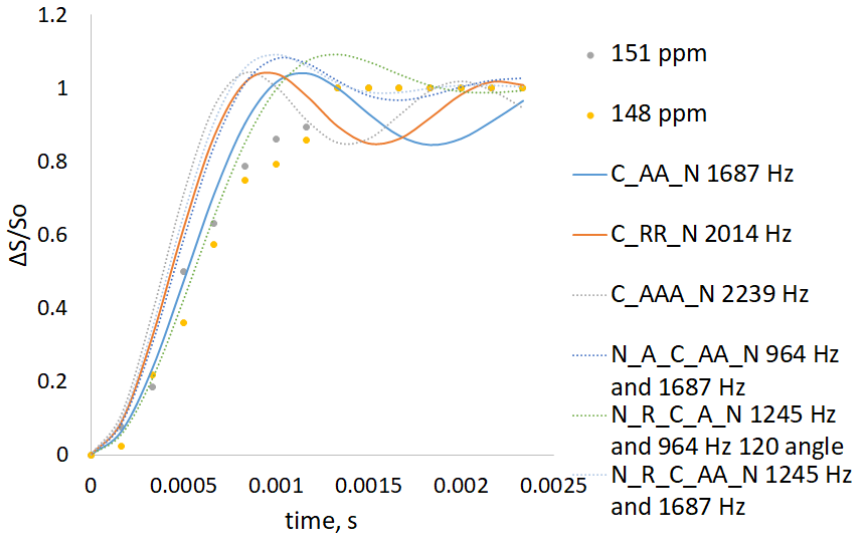

Figure 159. Results of $^{13}C\{^{15}N\}$ REDOR-evaluation of the peaks at 172 ppm (top), 168 ppm (middle) and 151 and 148 ppm (bottom) of heated PAN-MA sample. Blue diamonds, orange squares and grey circles represent the experimental results. Solid lines represent the results of SIMPSON simulations with indicated dipolar couplings. In case of multispin-simulations the bond angle of 120° is assumed. "A", "AA" and "AAA" indicated single double and triple-bond of the average length. "R" and "RR" indicate single and double bond of reduced length.

Appendix 24. Control Experiments for ^{1}H-^{13}C CPMAS NMR on Conductive Samples

In Figure 160 the control experiments which were carried out to ensure, that ^{1}H-^{13}C CPMAS signal comes from polarization transfer are represented.

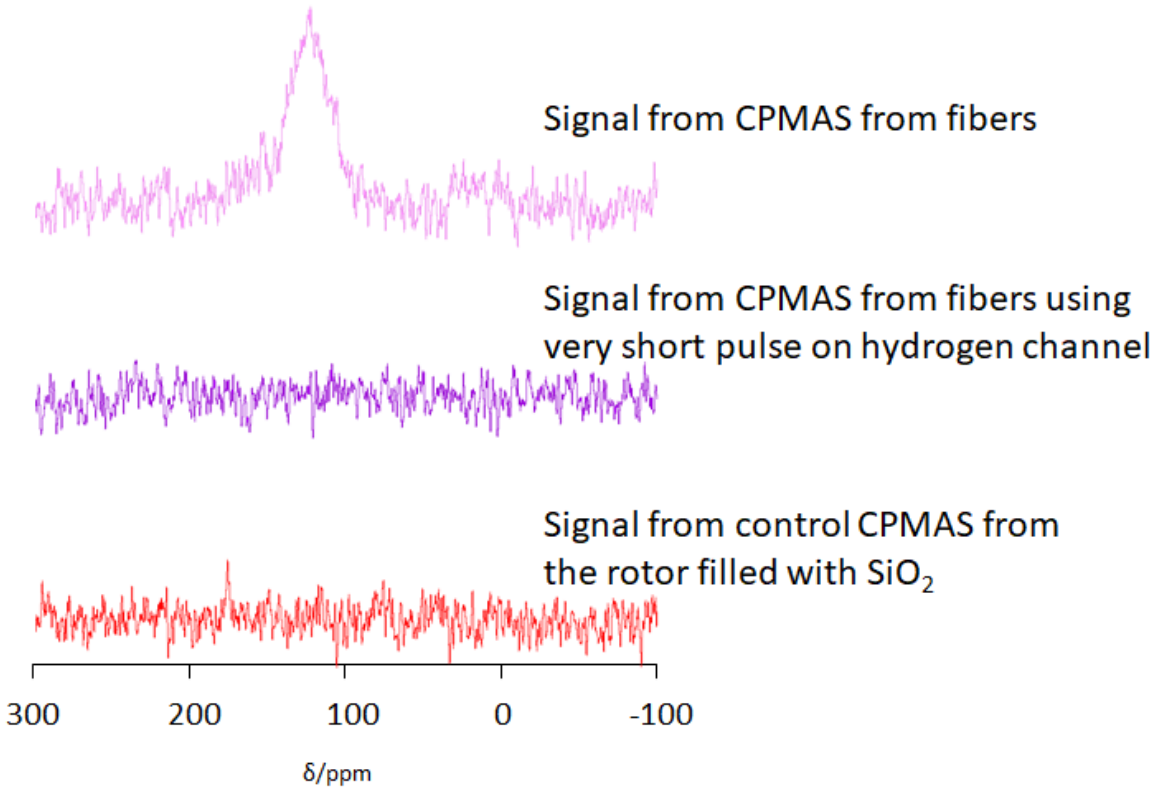

Figure 160. Control experiments to ensure that the signal from ^{1}H-^{13}C CPMAS NMR on conductive samples comes from polarization transfer.

References

1. Medek, A., Harwood, J. S. & Frydman, L. Multiple-Quantum Magic-Angle Spinning NMR: A New Method for the Study of Quadrupolar Nuclei in Solids. *J. Am. Chem. Soc.* **117**, 12779–12787 (1995).
2. Medek, A. & Frydman, L. Multiple - quantum magic - angle spinning NMR: a new technique for probing quadrupolar nuclei in solids. *J. Braz. Chem. Soc.* **10**, (1999).
3. Gullion, T. Introduction to rotational-echo, double-resonance NMR. *Concepts Magn. Reson.* **10**, 277–289 (1998).
4. Gullion, T. & Schaefer, J. Rotational-echo double-resonance NMR. *J. Magn. Reson. 1969* **81**, 196–200 (1989).
5. Pan, Y., Gullion, T. & Schaefer, J. Determination of C-N Internuclear Distances by Rotational-Echo Double-Resonance NMR of Solids. *J. Magn. Reson.* **90**, 330–340 (1990).
6. van Wüllen, L., Tricot, G. & Wegner, S. An advanced NMR protocol for the structural characterization of aluminophosphate glasses. *Solid State Nucl. Magn. Reson.* **32**, 44–52 (2007).
7. Gullion, T. & Vega, A. J. Measuring heteronuclear dipolar couplings for I=1/2, S>1/2 spin pairs by REDOR and REAPDOR NMR. *Prog. Nucl. Magn. Reson. Spectrosc.* **47**, 123–136 (2005).
8. K. Varshneya, A. *Fundamentals of Inorganic Glasses*. (1994).
9. Vogel, W. *Glaschemie*. (Springer, 1992).
10. Weber, M. J. Science and technology of laser glass. *XVth Int. Congr. Glass* **123**, 208–222 (1990).

11. Vogel, W., Höland, W., Naumann, K. & Gummel, J. Development of machineable bioactive glass ceramics for medical uses. *Int. Symp. Glass Proc. Second Beijing Symp. Glass* **80**, 34–51 (1986).

12. Hench, L. L. Bioceramics: From Concept to Clinic. *J. Am. Ceram. Soc.* **74**, 1487–1510 (1991).

13. Kokubo, T. Bioactive glass ceramics: properties and applications. *Biomaterials* **12**, 155–163 (1991).

14. Vogel, J., Wange, P. & Hartmann, P. Phosphate Glasses and Glass-Ceramics for Medical Applications. *Glass Sci. Technol. Glastech. Berichte* **70**, 220–223 (1997).

15. Brow, R. K. & Tallant, D. R. Structural design of sealing glasses. *Pract. Implic. Glass Struct.* **222**, 396–406 (1997).

16. C Sales, B. & Boatner, L. *Lead-Iron Phosphate Glass: A Stable Storage Medium for High-Level Nuclear Waste*. vol. 226 (1984).

17. Donald, I. W., Metcalfe, B. L. & Taylor, R. N. J. The immobilization of high level radioactive wastes using ceramics and glasses. *J. Mater. Sci.* **32**, 5851–5887 (1997).

18. Weber, W. J. *et al.* Radiation Effects in Glasses Used for Immobilization of High-level Waste and Plutonium Disposition. *J. Mater. Res.* **12**, 1948–1978 (1997).

19. Lee, W. E., Ojovan, M. I., Stennett, M. C. & Hyatt, N. C. Immobilisation of radioactive waste in glasses, glass composite materials and ceramics. *Adv. Appl. Ceram.* **105**, 3–12 (2006).

20. Smedskjaer, M. M., Mauro, J. C., Sen, S. & Yue, Y. Quantitative Design of Glassy Materials Using Temperature-Dependent Constraint Theory. *Chem. Mater.* **22**, 5358–5365 (2010).

21. Wondraczek, L. *et al.* Towards Ultrastrong Glasses. *Adv. Mater.* **23**, 4578–4586 (2011).

22. Rouxel, T. Driving force for indentation cracking in glass: composition, pressure and temperature dependence. *Philos. Trans. R. Soc. Math. Phys. Eng. Sci.* **373**, 20140140–20140140 (2015).

23. Rouxel, T. Elastic Properties and Short-to Medium-Range Order in Glasses. *J. Am. Ceram. Soc.* **90**, 3019–3039 (2007).

24. Jiang, Q. *et al.* Tailoring sodium silicophosphate glasses containing SiO6-octahedra through structural rules and topological principles. *J. Chem. Phys.* **141**, 124506 (2014).

25. Zeng, H. *et al.* Anneal-induced enhancement of refractive index and hardness of silicophosphate glasses containing six-fold coordinated silicon. *Appl. Phys. Lett.* **106**, 021903 (2015).

26. Dupree, R., Holland, D., Mortuza, M. G., Collins, J. A. & Lockyer, M. W. G. Magic angle spinning NMR of alkali phospho-alumino-silicate glasses. *Proc. Third Int. Symp. Glass* **112**, 111–119 (1989).

27. Frank, E., Hermanutz, F. & Buchmeiser, M. R. Carbon Fibers: Precursors, Manufacturing, and Properties. *Macromol. Mater. Eng.* **297**, 493–501 (2012).

28. Lee, S., Kim, J., Ku, B.-C., Kim, J. & Joh, H.-I. Structural Evolution of Polyacrylonitrile Fibers in Stabilization and Carbonization. *Adv. Chem. Eng. Sci.* **02**, 275–282 (2012).

29. Dalton, S., Heatley, F. & Budd, P. M. Thermal stabilization of polyacrylonitrile fibres. *Polymer* **40**, 5531–5543 (1999).

30. Kim, J., Kim, Y. C., Ahn, W. & Kim, C. Y. Reaction mechanisms of polyacrylonitrile on thermal treatment. *Polym. Eng. Sci.* **33**, 1452–1457 (1993).

31. Liu, X. *et al.* Stabilization of Atactic-Polyacrylonitrile under Nitrogen and Air As Studied by Solid-State NMR. *Macromolecules* **48**, 5300–5309 (2015).

32. Zhao, J. *et al.* New understanding on the reaction pathways of the polyacrylonitrile copolymer fiber pre-oxidation: online tracking by two-dimensional correlation FTIR spectroscopy. *RSC Adv.* **6**, 4397–4409 (2016).

33. Bashir, Z. A critical review of the stabilisation of polyacrylonitrile. *Carbon* **29**, 1081–1090 (1991).

34. Rahaman, M. S. A., Ismail, A. F. & Mustafa, A. A review of heat treatment on polyacrylonitrile fiber. *Polym. Degrad. Stab.* **92**, 1421–1432 (2007).

35. Roopanwal, A. K. Thermal Stabilization of Acrylic Precursors for the Production of Carbon Fibers: An Overview AU - Bajaj, P. *J. Macromol. Sci. Part C* **37**, 97–147 (1997).

36. Boccara, A. C., Fournier, D., Kumar, A. & Pandey, G. C. Nondestructive evaluation of carbon fiber by mirage-FTIR spectroscopy. *J. Appl. Polym. Sci.* **63**, 1785–1791 (1997).

37. Devasia, R., Nair, C. P. R., Sivadasan, P., Katherine, B. K. & Ninan, K. N. Cyclization reaction in poly(acrylonitrile/itaconic acid) copolymer: An isothermal differential scanning calorimetry kinetic study. *J. Appl. Polym. Sci.* **88**, 915–920 (2003).

38. Jing, M., Wang, C., Bai, Y., Zhu, B. & Wang, Y. Effect of temperatures in the rearmost stabilization zone on structure and properties of PAN-based oxidized fibers. *Polym. Bull.* **58**, 541–551 (2007).

39. Devasia, R., Nair, C. P. R., Sadhana, R., Babu, N. S. & Ninan, K. N. Fourier transform infrared and wide-angle X-ray diffraction studies of the thermal cyclization reactions of high-molar-mass poly(acrylonitrile-co-itaconic acid). *J. Appl. Polym. Sci.* **100**, 3055–3062 (2006).

40. Ouyang, Q., Cheng, L., Wang, H. & Li, K. Mechanism and kinetics of the stabilization reactions of itaconic acid-modified polyacrylonitrile. *Polym. Degrad. Stab.* **93**, 1415–1421 (2008).

41. Hameed, N. *et al.* Structural transformation of polyacrylonitrile fibers during stabilization and low temperature carbonization. *Polym. Degrad. Stab.* **128**, 39–45 (2016).

42. Yu, M. *et al.* Structure and property relations between the polyacrylonitrile-based prestabilized fibers and the partially carbonized fibers. *J. Appl. Polym. Sci.* **124**, 5172–5179 (2012).

43. Meinl, J., Kirsten, M., Cherif, C. & Michaelis, A. Influence of PAN-Fiber Stretching during Thermal Treatment on the Stabilization Reactions. *Am. J. Anal. Chem.* **07**, 282–293 (2016).

44. Nunna, S. *et al.* Investigation of progress of reactions and evolution of radial heterogeneity in the initial stage of thermal stabilization of PAN precursor fibres. *Polym. Degrad. Stab.* **125**, 105–114 (2016).

45. Nunna, S. *et al.* The effect of thermally induced chemical transformations on the structure and properties of carbon fibre precursors. *J. Mater. Chem. A* **5**, 7372–7382 (2017).

46. Morgan, P. *Carbon fibers and their composites*. (Taylor & Francis, 2005).

47. Wangxi, Z., Jie, L. & Gang, W. Evolution of structure and properties of PAN precursors during their conversion to carbon fibers. *Carbon* **41**, 2805–2812 (2003).

48. Frank, E., Steudle, L. M., Ingildeev, D., Spörl, J. M. & Buchmeiser, M. R. Carbonfasern: Präkursor-Systeme, Verarbeitung, Struktur und Eigenschaften. *Angew. Chem.* **126**, 5364–5403 (2014).

49. Kolodziejski, W. & Klinowski, J. Kinetics of Cross-Polarization in Solid-State NMR: A Guide for Chemists. *Chem. Rev.* **102**, 613–628 (2002).

50. Xiaoling, W., Shanmin, Z. & Xuewen, W. Two-stage feature of Hartmann-Hahn cross relaxation in magic-angle sample spinning. *Phys. Rev. B* **37**, 9827–9829 (1988).

51. Anedda, R., Soldatov, D. V., Moudrakovski, I. L., Casu, M. & Ripmeester, J. A. A New Approach to Characterizing Sorption in Materials with Flexible Micropores. *Chem. Mater.* **20**, 2908–2920 (2008).

52. Oschatz, M. *et al.* Structural Characterization of Micro- and Mesoporous Carbon Materials Using In Situ High Pressure 129Xe NMR Spectroscopy. *Chem. Mater.* **26**, 3280–3288 (2014).

53. Cros, F., Korb, J.-P. & Malier, L. Spectroscopic Mesopore Size Characterization and Diffusion Measurement in Closed Porosity by Xenon NMR. *Langmuir* **16**, 10193–10197 (2000).

54. Purcell, E. M., Torrey, H. C. & Pound, R. V. Resonance Absorption by Nuclear Magnetic Moments in a Solid. *Phys. Rev.* **69**, 37–38 (1946).

55. Bloch, F., Hansen, W. W. & Packard, M. Nuclear Induction. *Phys. Rev.* **69**, 127–127 (1946).

56. Duer, J. M. *Introduction to Solid-state NMR spectroscopy*. (Blackwell Pblishing, 2004).

57. Levitt, M. H. *Spin dynamics: basics of nuclear magnetic resonance*. (John Wiley & Sons, 2008).

58. Atkins, P. W. & Friedman, R. S. *Molecular Quantum Mechanics*. (Oxford University Press, 1997).

59. Slichter, C. P. *Principles of Magnetic Resonance*. (Springer, 1990).

60. Keeler, J. *Understanding NMR Spectroscopy*. (Wiley, 2005).

61. Van Vleck, J. H. The Dipolar Broadening of Magnetic Resonance Lines in Crystals. *Phys Rev* **74**, 1168–1183 (1948).

62. Andrew, E. R., Bradbury, A. & Eades, R. G. Nuclear Magnetic Resonance Spectra from a Crystal rotated at High Speed. *Nature* **182**, 1659–1659 (1958).

63. Lowe, I. J. Free Induction Decays of Rotating Solids. *Phys Rev Lett* **2**, 285–287 (1959).

64. Hahn, E. L. Spin Echoes. *Phys Rev* **80**, 580–594 (1950).

65. Mueller, K. T. Analytic Solutions for the Time Evolution of Dipolar-Dephasing NMR Signals. *J. Magn. Reson. A* **113**, 81–93 (1995).

66. Bertmer, M. & Eckert, H. Dephasing of spin echoes by multiple heteronuclear dipolar interactions in rotational echo double resonance NMR experiments. *Solid State Nucl. Magn. Reson.* **15**, 139—152 (1999).

67. Chan, J. C. C. & Eckert, H. Dipolar Coupling Information in Multispin Systems: Application of a Compensated REDOR NMR Approach to Inorganic Phosphates. *J. Magn. Reson.* **147**, 170–178 (2000).

68. R. Hartmann, S. & Hahn, E. Nuclear Double Resonance in the Rotating Frame. *Phys. Rev.* **128**, 2042–2053 (1962).

69. Amoureux, J.-P., Fernandez, C. & Steuernagel, S. ZFiltering in MQMAS NMR. *J. Magn. Reson. A* **123**, 116–118 (1996).

70. Bax, A., Szeverenyi, N. M. & Maciel, G. E. Correlation of isotropic shifts and chemical shift anisotropies by two-dimensional fourier-transform magic-angle hopping nmr spectroscopy. *J. Magn. Reson. 1969* **52**, 147–152 (1983).

71. Gan, Z. High-resolution chemical shift and chemical shift anisotropy correlation in solids using slow magic angle spinning. *J. Am. Chem. Soc.* **114**, 8307–8309 (1992).

72. Szeverenyi, N. M., Bax, A. & Maciel, G. E. Magic-angle hopping as an alternative to magic-angle spinning for solid state NMR. *J. Magn. Reson. 1969* **61**, 440–447 (1985).

73. van Wüllen, L. *et al.* Development and application of novel NMR methodologies for the in situ characterization of crystallization processes of metastable crystalline materials. *Z. Für Krist. - Cryst. Mater.* **232**, (2017).

74. Zachariasen, W. H. THE ATOMIC ARRANGEMENT IN GLASS. *J. Am. Chem. Soc.* **54**, 3841–3851 (1932).

75. Brow, R. K. Review: the structure of simple phosphate glasses. *J. Non-Cryst. Solids* **263–264**, 1–28 (2000).

76. von Wazer, J. R. Phosphorus and its Compounds. *Angew. Chem.* **73**, 552–552 (1961).

77. Van, L., Eckert, H. & Schwering, G. Structure−Property Correlations in Lithium Phosphate Glasses: New Insights from 31 P ↔ 7 Li Double-Resonance NMR. *Chem. Mater.* **12**, 1840–1846 (2000).

78. Brow, R. K., Kirkpatrick, R. J. & Turner, G. L. The short range structure of sodium phosphate glasses I. MAS NMR studies. *J. Non-Cryst. Solids* **116**, 39–45 (1990).

79. Kirkpatrick, R. J. & Brow, R. K. Nuclear magnetic resonance investigation of the structures of phosphate and phosphate-containing glasses: a review. *Solid State Nucl. Magn. Reson.* **5**, 9–21 (1995).

80. Eckert, H. Structural characterization of noncrystalline solids and glasses using solid state NMR. *Prog. Nucl. Magn. Reson. Spectrosc.* **24**, 159–293 (1992).

81. Kreidl, N. J. & Weyl, W. A. PHOSPHATES IN CERAMIC WARE: IV, PHOSPHATE GLASSES*. *J. Am. Ceram. Soc.* **24**, 372–378 (1941).

82. Brow, R. K. Nature of Alumina in Phosphate Glass: I, Properties of Sodium Aluminophosphate Glass. *J. Am. Ceram. Soc.* **76**, 913–918 (1993).

83. Brow, R. K., Kirkpatrick, R. J. & Turner, G. L. Nature of Alumina in Phosphate Glass: II, Structure of Sodium Alurninophosphate Glass. *J. Am. Ceram. Soc.* **76**, 919–928 (1993).

84. Brow, R. K., Kirkpatrick, R. J. & Turner, G. L. Local Structure of xAl2O3· (1 −x)NaPO3 Glasses: An NMR and XPS Study. *J. Am. Ceram. Soc.* **73**, 2293–2300 (1990).

85. Toplis, M. J. & Schaller, T. A 31P MAS NMR study of glasses in the system xNa2O–(1−x)Al2O3–2SiO2–yP2O5. *J. Non-Cryst. Solids* **224**, 57–68 (1998).

86. Hartmann, P., Vogel, J., Friedrich, U. & Jäger, C. Nuclear magnetic resonance investigations of aluminum containing phosphate glass-ceramics. *J. Non-Cryst. Solids* **263–264**, 94–100 (2000).

87. Lang, D. P., Alam, T. M. & Bencoe, D. N. Solid-State 31P/27Al and 31P/23Na TRAPDOR NMR Investigations of the Phosphorus Environments in Sodium Aluminophosphate Glasses. *Chem. Mater.* **13**, 420–428 (2001).

88. Dupree, R., Holland, D., Mortuza, M. G., Collins, J. A. & Lockyer, M. W. G. An MAS NMR study of network - cation coordination in phosphosilicate glasses. *J. Non-Cryst. Solids* **106**, 403–407 (1988).

89. Miyabe, D., Takahashi, M., Tokuda, Y., Yoko, T. & Uchino, T. Structure and formation mechanism of six-fold coordinated silicon in phosphosilicate glasses. *Phys. Rev. B* **71**, (2005).

90. Zeng, H. *et al.* Unique Sodium Phosphosilicate Glasses Designed Through Extended Topological Constraint Theory. *J. Phys. Chem. B* **118**, 5177–5183 (2014).

91. Morita K. *et al.* Characterization of Commercially Available PAN (Polyacrylonitrile)-Based Carbon Fibers.

92. Li, W. *et al.* Structural features of polyacrylonitrile-based carbon fibers. *J. Mater. Sci.* **47**, 919–928 (2012).

93. Houtz, R. C. 'Orlon' Acrylic Fiber: Chemistry and Properties. *Text. Res. J.* **20**, 786–801 (1950).

94. Burlant, W. J. & Parsons, J. L. Pyrolysis of polyacrylonitrile. *J. Polym. Sci.* **22**, 249–256 (1956).

95. Park, S.-J. *Carbon Fibers*. vol. 210 (Springer Netherlands, 2015).

96. Vickerman, J. C. & Gilmore, I. S. *Surface analysis: the principal techniques*. (Wiley, 2009).

97. Wang, T. & Sherwood, P. M. A. X-ray Photoelectron Spectroscopic Studies of Carbon Fiber Surfaces. 17. Interfacial Interactions between Phenolic Resin and Carbon Fibers Electrochemically Oxidized in Nitric Acid and Phosphoric Acid Solutions, and Their Effect on Oxidation Behavior. *Chem. Mater.* **6**, 788–795 (1994).

98. Washer, G. & Blum, F. Raman Spectroscopy for the Nondestructive Testing of Carbon Fiber. *Res. Lett. Mater. Sci.* **2008**, 1–3 (2008).

99. Oliveux, G., Dandy, L. O. & Leeke, G. A. Current status of recycling of fibre reinforced polymers: Review of technologies, reuse and resulting properties. *Prog. Mater. Sci.* **72**, 61–99 (2015).

100. Pimenta, S. & Pinho, S. T. Recycling carbon fibre reinforced polymers for structural applications: Technology review and market outlook. *Waste Manag.* **31**, 378–392 (2011).

101. Pickering, S. J. Recycling technologies for thermoset composite materials—current status. *Compos. Part Appl. Sci. Manuf.* **37**, 1206–1215 (2006).

102. Palmer, J., Ghita, O. R., Savage, L. & Evans, K. E. Successful closed-loop recycling of thermoset composites. *Compos. Part Appl. Sci. Manuf.* **40**, 490–498 (2009).

103. Marsh, G. Reclaiming value from post-use carbon composite. *Reinf. Plast.* **52**, 36–39 (2008).

104. Meyer, L. O., Schulte, K. & Grove-Nielsen, E. CFRP-Recycling Following a Pyrolysis Route: Process Optimization and Potentials. *J. Compos. Mater.* **43**, 1121–1132 (2009).

105. Goto, M. Chemical recycling of plastics using sub- and supercritical fluids. *J. Supercrit. Fluids* **47**, 500–507 (2009).

106. Henry, L. *et al.* Semi-continuous flow recycling method for carbon fibre reinforced thermoset polymers by near- and supercritical solvolysis. *Polym. Degrad. Stab.* **133**, 264–274 (2016).

107. Manis, F., Wölling, J. & Schneller, A. Ganzheitliche Recycling-Prozesskette für Carbonfasergewebe und Gelege. *Lightweight Des.* **9**, 14–19 (2016).

108. Wu, C., Feng, P., Bai, Y. & Lu, Y. Epoxy Enhanced by Recycled Milled Carbon Fibres in Adhesively-Bonded CFRP for Structural Strengthening. *Polymers* **6**, 76–92 (2013).

109. Cholake, S. T. *et al.* Physico-Chemical Characterization of Novel Epoxy Matrix System Reinforced with Recycled Short Milled Carbon Fibre. *J. Miner. Mater. Charact. Eng.* **03**, 373–389 (2015).

110. Ruhland, K. *et al.* Investigation of the chemical changes during thermal treatment of polyacrylonitrile and 15N-labelled polyacrylonitrile by means of in-situ FTIR and 15N NMR spectroscopy. *Polym. Degrad. Stab.* **146**, 298–316 (2017).

111. Ruhland, K., Nizamutdinova, A. & van Wüllen, L. Investigation of the chemical changes during the thermal treatment of AN-co-MA- polymer (PAN-precursor) focusing on the fate of the MA moiety. *Be Submitt. Polym. Degrad. Stab.*

112. Massiot, D. *et al.* Modelling one- and two-dimensional solid-state NMR spectra. *Magn. Reson. Chem.* **40**, 70–76 (2002).

113. d'Espinose de Lacaillerie, J.-B., Fretigny, C. & Massiot, D. MAS NMR spectra of quadrupolar nuclei in disordered solids: The Czjzek model. *J. Magn. Reson.* **192**, 244–251 (2008).

114. Bak, M., Rasmussen, J. T. & Nielsen, N. C. SIMPSON: A General Simulation Program for Solid-State NMR Spectroscopy. *J. Magn. Reson.* **147**, 296–330 (2000).

115. Thurber, K. R. & Tycko, R. Measurement of sample temperatures under magic-angle spinning from the chemical shift and spin-lattice relaxation rate of 79Br in KBr powder. *J. Magn. Reson.* **196**, 84–87 (2009).

116. Kirchhain, H. *et al.* High-temperature MAS-NMR at high spinning speeds. *Solid State Nucl. Magn. Reson.* **78**, 37–39 (2016).

117. Mortuza, M. G., Chudek, J. A., Hunter, G. & Ahsan, M. R. First evidence for the coexistence of four-, five- and six-coordinated silicon in glasses prepared at ambient pressure. *Chem. Commun.* 2055–2056 (2000) doi:10.1039/b006218i.

118. Zhang, L. & Eckert, H. Short- and Medium-Range Order in Sodium Aluminophosphate Glasses: New Insights from High-Resolution Dipolar Solid-State NMR Spectroscopy. *J. Phys. Chem. B* **110**, 8946–8958 (2006).

119. Venkatachalam, S., Schröder, C., Wegner, S. & van Wüllen, L. The structure of a borosilicate and phosphosilicate glasses and its evolution at temperatures above the glass transition temperature: Lessons from in situ MAS NMR. *Phys. Chem. Glas.* **55**, (2014).

120. Tsuchida, J., Schneider, J., Rinke, M. T. & Eckert, H. Structure of Ternary Aluminum Metaphosphate Glasses. *J. Phys. Chem. C* **115**, 21927–21941 (2011).

121. Wegner, S., van Wüllen, L. & Tricot, G. The structure of aluminophosphate glasses revisited: Application of modern solid state NMR strategies to determine structural motifs on intermediate length scales. *J. Non-Cryst. Solids* **354**, 1703–1714 (2008).

122. ICSD collection codes 9641, 16651.

123. ICSD collection codes 170, 26759.

124. Ren, J., Zhang, L. & Eckert, H. Medium-Range Order in Sol–Gel Prepared Al2O3–SiO2 Glasses: New Results from Solid-State NMR. *J. Phys. Chem. C* **118**, 4906–4917 (2014).

125. Ren, J. & Eckert, H. Superstructural Units Involving Six-Coordinated Silicon in Sodium Phosphosilicate Glasses Detected by Solid-State NMR Spectroscopy. *J. Phys. Chem. C* **122**, 27620–27630 (2018).

126. van Wüllen, L., Wegner, S. & Tricot, G. Structural Changes above the Glass Transition and Crystallization in Aluminophosphate Glasses: An in Situ High-Temperature MAS NMR Study. *J. Phys. Chem. B* **111**, 7529–7534 (2007).

127. Wegner, S., van Wüllen, L. & Tricot, G. The structure of phosphate and borosilicate glasses and their structural evolution at high temperatures as studied with solid state NMR spectroscopy: Phase separation, crystallisation and dynamic species exchange. *Solid State Sci.* **12**, 428–439 (2010).

128. Kirchhain, H. Personal Communication.

129. van Wüllen, L. & Venkatachalam, S. Structure and high temperature behaviour of sodium aluminophosphate glasses. *Phys. Chem. Glas. Eur. J. Glass Sci. Technol. Part B* **57**, 173–182 (2016).

130. Peng, M., Chen, D., Qiu, J., Jiang, X. & Zhu, C. Bismuth-doped zinc aluminosilicate glasses and glass-ceramics with ultra-broadband infrared luminescence. *Opt. Mater.* **29**, 556–561 (2007).

131. Shiraki, K. & Ohashi, M. Optical properties of sodium alminosilicate glass. *J. Non-Cryst. Solids* **149**, 243–248 (1992).

132. van Deventer, J. S. J., Provis, J. L., Duxson, P. & Lukey, G. C. Reaction mechanisms in the geopolymeric conversion of inorganic waste to useful products. *First Int. Conf. Eng. Waste Treat. Benef. Use Waste -Prod. WasteEng2005* **139**, 506–513 (2007).

133. Nielsen, K. A. *et al.* Glass composite seals for SOFC application. *Refereed Rep. IX Conf. Exhib. Eur. Ceram. Soc.* **27**, 1817–1822 (2007).

134. Mysen, B. O. & Toplis, M. J. Structural behavior of Al3+ in peralkaline, metaluminous, and peraluminous silicate melts and glasses at ambient pressure. *Am. Mineral.* **92**, 933–946 (2007).

135. Stebbins, J. F. & Xu, Z. NMR evidence for excess non-bridging oxygen in an aluminosilicate glass. *Nature* **390**, 60 (1997).

136. J. F. Stebbins, J. V. Oglesby & S. Kroeker. Oxygen triclusters in crystalline CaAl4O7 (grossite) and in calcium aluminosilicate glasses: 17O NMR. *Am. Mineral.* **86**, 1307–1311 (2001).

137. Kosinski, S. G. *et al.* Raman and NMR spectroscopy of SiO2 glasses CO-doped with Al2O3 and P2O5. *J. Non-Cryst. Solids* **105**, 45–52 (1988).

138. Toplis, M. J., Libourel, G. & Carroll, M. R. The role of phosphorus in crystallisation processes of basalt: An experimental study. *Geochim. Cosmochim. Acta* **58**, 797–810 (1994).

139. Mysen, B. O. Phosphorus solubility mechanisms in haplogranitic aluminosilicate glass and melt: effect of temperature and aluminum content. *Contrib. Mineral. Petrol.* **133**, 38–50 (1998).

140. Gan, H. & Hess, P. Phosphate Speciation in Potassium Aluminosilicate Glasses. *Am. Mineral.* **77**, 495–506 (1992).

141. Glatz, P. *et al.* Different roles of phosphorus in the nucleation of lithium aluminosilicate glasses. *J. Non-Cryst. Solids* **493**, 48–56 (2018).

142. Mysen, B. O., Holtz, F., Pichavant, M., Beny, J.-M. & Montel, J.-M. Solution mechanisms of phosphorus in quenched hydrous and anhydrous granitic glass as a function of peraluminosity. *Geochim. Cosmochim. Acta* **61**, 3913–3926 (1997).

143. Cody, G. D., Mysen, B., Sághi-Szabó, G. & Tossell, J. A. Silicate-phosphate interactions in silicate glasses and melts: I. A multinuclear (27Al,29Si,31P) MAS NMR and ab initio chemical shielding (31P) study of phosphorous speciation in silicate glasses. *Geochim. Cosmochim. Acta* **65**, 2395–2411 (2001).

144. Elliott, S. R. Medium-range structural order in covalent amorphous solids. *Nature* **354**, 445 (1991).

145. Deshpande, R. R. & Eckert, H. Sol-gel preparation of mesoporous sodium aluminosilicate glasses: mechanistic and structural investigations by solid state nuclear magnetic resonance. *J. Mater. Chem.* **19**, 3419 (2009).

146. Deshpande, R. R., Zhang, L. & Eckert, H. Sol-gel synthesis of sodium-modified AlPO4–SiO2 glasses and structural characterization by solid state NMR. *J. Mater. Chem.* **19**, 1151–1159 (2009).

147. Aitken, B. G., Youngman, R. E., Deshpande, R. R. & Eckert, H. Structure−Property Relations in Mixed-Network Glasses: Multinuclear Solid State NMR Investigations of the System xAl2O3:(30 − x)P2O5:70SiO2. *J. Phys. Chem. C* **113**, 3322–3331 (2009).

148. Kubicki, J. D. & Toplis, M. J. Molecular orbital calculations on aluminosilicate tricluster molecules: Implications for the structure of aluminosilicate glasses. *Am. Mineral.* **87**, 668–678 (2002).

149. Toplis, M. J., Dingwell, D. B. & Lenci, T. Peraluminous viscosity maxima in Na2O□Al2O3□SiO2 liquids: The role of triclusters in tectosilicate melts. *Geochim. Cosmochim. Acta* **61**, 2605–2612 (1997).

150. O'Dell, L. A. *et al.* Quantification of crystalline phases and measurement of phosphate chain lengths in a mixed phase sample by 31P refocused INADEQUATE MAS NMR. *Chem. Phys. Lett.* **455**, 178–183 (2008).

151. Ren, J., Zhang, L. & Eckert, H. Sol–gel preparation of mesoporous Al2O3–SiO2 glasses: structural evolution monitored by solid state NMR. *J. Sol-Gel Sci. Technol.* **70**, 482–490 (2014).

152. Lee, S. K. & Stebbins, J. F. Al–O–Al and Si–O–Si sites in framework aluminosilicate glasses with Si/Al=1: quantification of framework disorder. *J. Non-Cryst. Solids* **270**, 260–264 (2000).

153. Lathrop, D. *et al.* Dipolar 31P NMR spectroscopy of crystalline inorganic phosphorus compounds. *Solid State Nucl. Magn. Reson.* **1**, 73–83 (1992).

154. Xue, X. & Stebbins, J. F. 23Na NMR chemical shifts and local Na coordination environments in silicate crystals, melts and glasses. *Phys. Chem. Miner.* **20**, 297–307 (1993).

155. Phillips, B. L., Kirkpatrick, R. J. & Hovis, G. L. 27Al, 29Si, and 23Na MAS NMR study of an Al, Si ordered alkali feldspar solid solution series. *Phys. Chem. Miner.* **16**, 262–275 (1988).

156. Lee, S. K. & Stebbins, J. F. The distribution of sodium ions in aluminosilicate glasses: a high-field Na-23 MAS and 3Q MAS NMR study. *Geochim. Cosmochim. Acta* **67**, 1699–1709 (2003).

157. Maekawa, H., Nakao, T., Shimokawa, S. & Yokokawa, T. Coordination of sodium ions in NaAlO2–SiO2 melts: a high temperature 23Na NMR study. *Phys. Chem. Miner.* **24**, 53–65 (1997).

158. George, A. M. & Stebbins, J. F. Dynamics of Na in sodium aluminosilicate glasses and liquids. *Phys. Chem. Miner.* **23**, 526–534 (1996).

159. Ghoshal, S. *et al.* Solid-state NMR study of spin finish of thermally treated PAN and PAN/CNT precursor fibers. *J. Appl. Polym. Sci.* **131**, n/a-n/a (2014).

160. Foston, M. *et al.* NMR a critical tool to study the production of carbon fiber from lignin. *Carbon* **52**, 65–73 (2013).

161. Hamerton, I. *et al.* Probing the cure of 13C labelled bisphenol A dicyanate ester in carbon fibre reinforced composites using solid state 13C NMR, SEM and FTIR. *Polym. Bull.* **38**, 433–438 (1997).

162. Berger, S., Braun, S. & Kalinowski, H.-O. *NMR-Spektroskopie von Nichtmetallen. 2: 15 N-NMR-Spektroskopie: 71 Tabellen*. (Thieme, 1992).

163. Levy, G. C. & Lichter, R. L. *Nitrogen-15 nuclear magnetic resonance spectroscopy*. (Wiley, 1979).

164. Echelmeyer, T., Wüllen, L. van & Wegner, S. A new application for an old concept: Constant time (CT)-REDOR for an accurate determination of second moments in multiple spin systems with strong heteronuclear dipolar couplings. *Solid State Nucl. Magn. Reson.* **34**, 14–19 (2008).

165. Leppert, J., Heise, B. & Ramachandran, R. Redor in IS1S2 systems. *J. Biomol. NMR* **18**, 153–164 (2000).

166. O'Connor, R. D. & Schaefer, J. Relative CSA–Dipolar Orientation from REDOR Sidebands. *J. Magn. Reson.* **154**, 46–52 (2002).

167. Ruhland, K., Haase, N. & Fischer, A. Detailed examination of nitrile stretching vibrations relevant for understanding the behavior of thermally treated polyacrylonitrile. *J. Appl. Polym. Sci.* **134**, 44936 (2017).

168. Stefaniak, L., Roberts, J. D., Witanowski, M. & Webb, G. A. A 15N NMR study of some azoles. *Org. Magn. Reson.* **22**, 215–220 (1984).

169. Sattler, A. *et al.* Melamine–Melem Adduct Phases: Investigating the Thermal Condensation of Melamine. *Chem. – Eur. J.* **15**, 13161–13170 (2009).

170. Städeli, W., Philipsborn, W. V., Wick, A. & Kompiš, I. 15N-NMR. Studies of Aminopyridines, Aminopyrimidines and of Some Diazine N-Oxides. *Helv. Chim. Acta* **63**, 504–522 (1980).

171. Morales-Rios, M. S., Joseph-Nathan, P., Wrackmeyer, B. & Kupče, Ē. Nitrogen-15 NMR studies of 5-substituted indoles and 4-substituted acetanilides. Evidence for cross-conjugation effects. *Magn. Reson. Chem.* **31**, 238–240 (1993).

172. Kaczmarek, L. *et al.* A 15N NMR study of some fused polyaza heterocyclic ring systems. *Magn. Reson. Chem.* **23**, 853–855 (1985).

173. Lichter, R. L. & Roberts, J. D. Nitrogen-15 nuclear magnetic resonance spectroscopy. XIII. Pyridine-15N. *J. Am. Chem. Soc.* **93**, 5218–5224 (1971).